

General Disclaimer

One or more of the Following Statements may affect this Document

- This document has been reproduced from the best copy furnished by the organizational source. It is being released in the interest of making available as much information as possible.
- This document may contain data, which exceeds the sheet parameters. It was furnished in this condition by the organizational source and is the best copy available.
- This document may contain tone-on-tone or color graphs, charts and/or pictures, which have been reproduced in black and white.
- This document is paginated as submitted by the original source.
- Portions of this document are not fully legible due to the historical nature of some of the material. However, it is the best reproduction available from the original submission.



**ANALYTICAL AND EXPERIMENTAL INVESTIGATION
OF GAS BEARING TILTING PAD PIVOTS**

by

**M.B. Peterson, B.F. Geren, E.B. Arwas, S. Gray
S.F. Murray, J.W. Lund, F.F. Ling**

MECHANICAL TECHNOLOGY INCORPORATED

Prepared for

NATIONAL AERONAUTICS AND SPACE ADMINISTRATION

NASA-Lewis Research Center

Contract NAS 3-7629

H. Cameron, C. O'Dear and H. Tryor. - Project Managers

FACILITY FORM 602

N70-17351

(ACCESSION NUMBER)

302

(PAGE)

NASA-64-472609

(NASA OR TMX OR AD NUMBER)

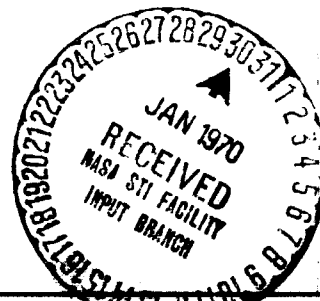
(THRU)

1

(CODE)

15

(CATEGORY)



NOTICE

This report was prepared as an account of Government-sponsored work. Neither the United States, nor the National Aeronautics and Space Administration (NASA), nor any person acting on behalf of NASA:

- A.) Makes any warranty or representation, expressed or implied, with respect to the accuracy, completeness, or usefulness of the information contained in this report, or that the use of any information, apparatus, method, or process disclosed in this report may not infringe privately-owned rights; or
- B.) Assumes any liabilities with respect to the use of, or for damages resulting from the use of, any information, apparatus, method or process disclosed in this report.

As used above, "person acting on behalf of NASA" includes any employee or contractor of NASA, or employee of such contractor, to the extent that such employee or contractor of NASA or employee of such contractor prepares, disseminates, or provides access to any information pursuant to his employment or contract with NASA, or his employment with such contractor.

NASA CR-72609

MTI-69-TR-32

FINAL REPORT

ANALYTICAL AND EXPERIMENTAL INVESTIGATION
OF GAS BEARING TILTING PAD PIVOTS

by

M.B. Peterson, B.F. Geren, E.B. Arwas, S. Gray
S.F. Murray, J.W. Lund, F.F. Ling

MECHANICAL TECHNOLOGY INCORPORATED
968 Albany-Shaker Road
Latham, New York 12110

Prepared for

NATIONAL AERONAUTICS AND SPACE ADMINISTRATION

September, 1969

Contract NAS 3-7629

NASA-Lewis Research Center
Cleveland, Ohio
Space Power Systems Division

Harry M. Cameron
Cecil L. O'Dear
Henry B. Tryon

FOREWORD

The work described herein was performed at Mechanical Technology Incorporated under NASA Contract NAS 3-7629 with Mr. Harry M. Cameron, Mr. Cecil L. O'Dear, and Mr. Henry B. Tryon, Space Power Systems Division, NASA-Lewis Research Center, as Project Managers.

PRECEDING PAGE BLANK NOT FILLED.

TABLE OF CONTENTS

	<u>Page</u>
FOREWORD	11
I. INTRODUCTION -----	1
II. BACKGROUND -----	3
III. PROGRAM SCOPE -----	9
1. Analysis of Pad Motions -----	9
2. Microslip Analysis -----	9
3. Materials and Lubricants -----	9
4. Design and Development of Test Equipment -----	10
5. Screening Tests -----	10
6. Long Term Tests -----	11
7. Special Design Tests -----	11
IV. SUMMARY OF RESULTS -----	12
V. ANALYSIS OF PAD MOTIONS -----	18
VI. GEOMETRIC OPTIMIZATION OF CONCENTRATED CONTACTS FOR MINIMUM MICROSLIPS -----	25
1. Cursory Analysis -----	25
2. Higher Order Surfaces in Contact -----	28
3. Optimized Shapes -----	29
4. Closing-In -----	32
5. Maximum Pressure -----	32
6. Radius of Contact Area -----	32
7. Maximum Microslip -----	33
8. Computer Program for Calculations Sampled Above -----	33
VII. MATERIALS AND LUBRICANTS SELECTION -----	36

	<u>Page</u>
VIII. TEST RIGS -----	42
1. Requirements -----	42
2. Design Approaches -----	43
3. Description of Test Rig -----	49
4. Auxiliary Systems and Instrumentation -----	50
5. Test Rig Calibration -----	53
6. Test Procedure -----	59
IX. OUTLINE OF RESULTS -----	62
X. MATERIAL SCREENING TESTS -----	63
1. Preliminary Tests with M-2 Tool Steel -----	63
2. Preliminary Test with Carbide (K162B) -----	76
3. Conditions Where Damage Occurs -----	77
4. Material Screening -----	79
5. Effect of Shape -----	82
XI. FORMING GAS AND AIR TESTS -----	85
XII. LONG TERM TESTS -----	88
XIII. LUBRICANT TESTS -----	95
XIV. SPECIAL DESIGN TESTS -----	96
1. Tungsten Carbide vs. A286 Flame Sprayed with Tungsten Carbide - Conforming Radius -----	96
2. Sapphire vs. WC (Conforming and Non-conforming Geometry) --	99
3. Carbide and Tool Steel - BRU Conforming Geometry -----	103
XV. 1000 HOUR BRU TEST -----	106
XVI. PIVOT DESIGN -----	109
REFERENCES -----	114

APPENDIX A	The Dynamic Coefficients for the Pad Fluid Film -----	117
APPENDIX B	Dynamic Coefficients for the Tilting Pad Journal Bearing -----	130
APPENDIX C	Microslip Between Contacting Paraboloids -----	138
APPENDIX D	Computer Program for Determining Microslip -----	147
APPENDIX E	Detailed Analysis of Main Test Rig Components ---	155

I. INTRODUCTION

Gas bearings are a very critical component of the Brayton Cycle turbomachinery that is being developed for dynamic power conversion in space vehicles. Because of the high speed of this machinery, bearing selection is dictated by the requirements of rotor-bearing dynamics, rather than by steady-state load capacity. The rotor-bearings dynamics problems are rendered more critical by the fact that the machinery must be capable of operating both in normal gravity and in zero gravity fields. Stability at high speeds, and high stiffness in both the loaded and unloaded states are therefore prerequisites for the gas bearings used in Brayton Cycle machinery. Among the self-acting gas bearings, the tilting-pad type is the one preferred for high speed or for zero G operation.

Because of the freedom of motion of the pads, tilting-pad bearings can tolerate thermal distortions induced by the temperature gradients in high temperature turbomachinery much better than rigid bearings. In addition, properly designed tilting-pad gas bearings have a high stability threshold and possess high fluid film stiffness, even under zero net load on the bearing. High stiffness at zero load is obtained by geometrical preloading. High stability is achieved provided that:

1. The inertia of the pads is low enough that they can track shaft whirl precisely. This requires that the natural frequency of the pads be greater than the running speed.
2. Pivot friction and damage is small so that it does not significantly restrict the freedom of motion of the pads.

To the extent that the above conditions are not satisfied, the advantages of the tilting-pad bearing are lost and it becomes subject to the same problems as rigid bearings, such as half frequency whirl which can rapidly develop destructively high amplitudes.

Depending upon the operating conditions, the pivot motions, and the pivot design,

the pivot members will experience relative rolling and sliding motions. It is necessary to consider what effect these motions would have in causing damage to the pivot and what effect pivot damage has on pad motions.

In order to gain a better understanding of the damage and wear of pivots and to develop design criteria, a theoretical and experimental program was initiated by NASA under Contract NAS3-7629.

The objective of this program is to investigate this problem area by analysis of the pads and pivots motions; by analysis of the elastic and plastic behavior of the pivot-pad combination; and by means of an extensive test program in which actual pivot motions are closely simulated.

II. BACKGROUND

Due to the various factors of misalignment, shock and unbalance a combination of motions can be transmitted from the bearing pads to the pivots. The motions are illustrated in Figure 1.

The pitch motions are the fore to aft rocking of the pads due to the translations of the shaft axis. Roll of the pads arise from the rocking of the shaft axis "end to end" or about its center. Yaw is the twisting of the pad about its center resulting from the rocking of the shaft axis or twisting of the pivot axis. Dynamic loading results when the pad moves parallel to the pivot axis or vice versa. Separation or bounce will occur if the magnitude of the dynamic load is large enough. These motions of the pad will cause a variety of motions within the contact area of the pivot.

Consider the pivot to consist of a ball resting upon a rigid flat plate. When a given load W is applied, an area of contact of radius r and a closure of distance δ is established. The Hertz equations can be used to calculate approximate values of maximum pressure p , and δ . If now any tangential force or twist τ is superimposed on the normal force by the pitch, roll or yaw motions, microslip can occur.

The microslip occurs as a result of the combination of the normal stress, τ_n , and the shear stress, τ_s . The normal stress is a maximum at the center and approaches zero at the contact edge. The shear stresses will be zero at the center and approach a maximum at the edge. Thus at some point on the radius of the contact area (r_c) the ratio of the stresses $\tau_s/\tau_n > f_s$ (where f_s is the static friction coefficient for the material pair) and microslip will occur. When $\tau_s/\tau_n < f_s$ then only elastic deformation will occur and the two surfaces are locked together. If $\tau/w > f_s$ slip will occur over the whole contact region and gross sliding will

occur. Thus for a ball resting on a plate with a given load w , one can define a locked region and a slipped region as shown in Figure 2. The question then arises "what happens to these regions as pitch, roll, yaw, and dynamic load are induced"?

Pure pitch will cause body B to rotate about body A and have the same effect as a change of load. Slippage will increase in the direction of the pitch motion particularly in the regions of P and P'. The amount of motion will be extremely small (10^{-6} in.) for the amount of pad motions considered. The basic dimensions of the locked regions, r_e , and slip regions $r - r_e$ will change only slightly.

Roll motion will have a similar effect to pitch but in the direction RR'.

Motions in the normal direction due to dynamic loading will produce changes in slippage. In this case the slip will be symmetric to the axis, equal at both P and R. If the dynamic load motions are greater than δ , separation may occur. For a 1/2" diameter ball a 30# load gives a δ of only .0003. Thus very small motions in the vertical direction can result in a large amount of microslip.

Yaw motion results in a direct application of shear stress to the contact area and will cause slippage about the pivot axis. As the yaw motion increases a point will be reached where nearly the full contact area will slip.

Thus in the contact area, for small motions in any direction, the result will be elastic deformation with a small amount of scrubbing action or microslip within a well defined slip region. The basic area of contact will remain in the same position.

Thus one can consider two types of motion:

1. Gross Sliding

By gross sliding is meant that the whole contact area is experiencing slip in the same direction. This will result if the yaw motion becomes large enough. It will also take place with the fully conforming socket and ball

since there can be no rolling action. Gross sliding will also result from large tangential forces particularly with a ball on flat geometry.

2. Rolling Motion with Elastic Deformation and Microslip

This will be the predominate form of motion due to normal shaft and pad motion. It will consist of a scrubbing action within a well defined contact region. The amount of microslip will be small.

If there is gross sliding, damage and wear will be severe. This can be established by considering the wear rates in typical fretting experiments using the equipment shown schematically in Figure 3.

A hardened dry, 52100 steel sleeve was loaded against a hardened 52100 steel ball by means of a spring. This permitted the bearing to roll with the ball to some extent, a condition which simulated the motion in the actual application. The center of the ball was located at the node point of the second mode of the rod. After approximately 20×10^6 cycles, no damage could be detected. The contact areas were smooth and polished. Substitution of a glass-reinforced Teflon-lined bearing for the steel bearing also showed no damage, only a faint polished area on the Teflon sleeve.

When the test was set up with a fixed bearing sleeve, so that most of the motion was sliding rather than rolling, damage was severe. The amplitude in this case was reduced to 0.2 mils because of the restraint on the bearing. Within a few hours, a conspicuous wear area was observed with the typical reddish-brown debris which is characteristic of fretting damage.

These results indicated that surface damage could be produced in a fairly short period of time if pure sliding conditions were imposed. This can be avoided by appropriate pivot design. Pure rolling without microslip is almost impossible to achieve. The question then remains as to the methods of selecting materials, lubricants and pivot designs for the conditions of rolling with microslip.

The experimental work on all these lines is almost non-existent. Johnson (Ref. 2)

demonstrated that the slip region exists and fretting will result in the contact of a steel sphere with a plane surface. Burton (Refs. 3, 4, 5) has studied the case of oscillating normal load for the case of a ball on a flat. Much of this work was lubricated, however, some data were reported on the unlubricated condition with 52100 steel. Severe damage was reported after 30×10^6 cycles at

$$\frac{\sigma_{\max}}{\sigma_{\min}} = \frac{750,000 \text{ psi}}{460,000 \text{ psi}}.$$

Although this is a higher stress level and variation than would be used in a pivot, the required life of the pivot is of the order of 3.6×10^{10} cycles. Klint (Ref. 6) investigated the "limits of elastic behavior" and found that without gross slip there was no wear for stainless steel specimens after 2×10^6 cycles at stresses high enough to produce plastic deformation. However, when the limit was exceeded wear and damage was observed in a few seconds of operation. In this case only an oscillatory tangential force was considered.

Somewhat more information is available on actual pivots operated at low temperature. Pivots lubricated with oil in tilting pad journal and thrust bearings operate with little difficulty over long periods of time. Where fluid lubricants can not be used a set of design specifications has been developed (Ref. 7). In essence, they prescribe a ball and cylinder configuration where the stress is less than 120,000 psi and the difference in radii large enough to insure a rolling action at the pivot. Pivots designed in accordance with these specifications have shown no wear (or at least insignificant wear) over very long periods of operation. Operating results are shown in Table I. It was felt that the main reason for the successful operation of these pivots is that they were lubricated and that the motion was primarily rolling. The extent of microslip within the area of contact was not determined.

At temperatures above 600°F, the use of solid film lubricants is limited, and at temperatures above 1000°F, the hardness of available materials is reduced. Under these conditions, additional difficulties can be anticipated. At high frequencies, the solid film lubricants could be more rapidly removed and appreciably more heat would be generated. This may increase the wear and damage appreciably. There

needs to be a clearer understanding of the effect of variables on the fretting damage, particularly with principally rolling motions and outside the limited conditions listed above. Accordingly a program was initiated by NASA under Contract No. NAS-7629 to Mechanical Technology Inc. The scope of this program is described in the following section.

TABLE I

ACCUMULATED OPERATING HOURS ON SOME MTI COMPRESSORS WITH
TILTING-PAD, GAS LUBRICATED, JOURNAL BEARINGS

Machine	Bearing Size D x L in.	No. of Pads	Speed RPM	Bearing Temp. °F	Pivot Dimensions			Ratio	Operating Time Hours	Material	Lubricant
					Gas	Ball in ⁴	Cylinder in ⁴				
LASL-Main Circulator	3-3/4 x 2-1/2	4	12,000	270	He	.375	.3875	1.03	>10,000	M-2	Electrofilm 4396
	2-1/2 x 2-1/2										
LASL-Clean Up Hoop	2-1/2 x 1-3/4	4	12,000	100	He	.4997	.5107	1.02	>10,000	52100	Electrofilm 4396
BuMines	2-1/2 x 1-3/4	4	18,000	300	He	.4997	.5107	1.02	70	52100	Electrofilm 4396
NASA Turbo- Compressor Simulator	2-1/8 x 2-1/8	4	50,000	200	Argon	.375	.3824	1.02	100	M-1	Electrofilm 4396
	1-1/2 x 1-1/2					.250	.255	1.02			
Rotor Test Rig	2-1/2 x 1-3/4	4	18,000	100	Air	.4997	.5107	1.02	100	52100	Electrofilm 4396
BuMines Turbo- Compressor	2-1/4 x 2-1/4	4		250	N ₂ Argon	.423	.4515	1.07	> 300	M-2	Electrofilm 4396
	3 x 2-3/8	4	24,000		Air						

III. PROGRAM SCOPE

In order to gain a better understanding of the wear and surface damage in pivots a theoretical and experimental program was conducted. The purpose of this program is to suggest design criteria for maximum pivot life. In order to obtain this information the program was divided into the following parts.

1. Analysis of Pad Motions

Information was required to determine the magnitude of motions to be used in the experimental portion of the program. An analytical investigation was conducted using as a model the 50,000 RPM axial flow, Brayton Cycle turbocompressor designed by P&WA and MTI. The pitch, roll and yaw aspects of the pad motions were calculated for both bearings of the turbocompressor, over the speed range from 12,000 to 60,000 RPM, as functions of a mechanical unbalance in the turbine wheel plane, and these were used to establish realistic amplitudes of motion on the test program.

2. Microslip Analysis

It would be expected that the wear and surface damage of the pivot could be directly correlated to the amount of microslip which results from the pad motions and that different pivot designs would result in different amounts of microslip. Accordingly, an analytical investigation was undertaken to determine surface geometry for minimum microslip and the microslip which would result from several conventional geometric pivot shapes. The intent of this portion of the program was to determine the optimum pivot shape. This work was performed at Rensselaer Polytechnic Institute under the direction of F. F. Ling.

3. Materials and Lubricants

Present and future Brayton Cycle Space power units will operate in the 400 to 1400°F range. As a part of this program, it was necessary to select from the literature those materials and lubricants with the greatest potential for

successful pivot operation within this temperature range. The most appropriate materials would be evaluated in the experimental portion of the program.

4. Design and Development of Test Equipment

In order to evaluate the materials and designs selected above, it was necessary to develop a test rig which simulated the rolling and yaw motions of gas bearing tilting pad pivots. The following requirements were specified:

Motion	- Independent rotary oscillation about 3 orthogonal axis
Motion Amplitude	- .0015 inches
Frequency	- 200 and 1000 cps
Atmosphere	- Argon or air
Load	- 2 to 30 pounds
Temperature	- 80 to 1400°F

5. Screening Tests

A series of short term tests was first run to select the appropriate materials.

With closely fitting machine surfaces, welding can result. In selecting materials for a given application the first step is to choose materials which slide or roll without damage. Since it is not possible to theoretically determine when damage will occur, screening tests must be used. Such a test may be of short duration since damage, if it is to take place, will occur almost immediately. For this program a 12 hour test was selected. The operating conditions were selected to duplicate those for the bearing pivot as closely as possible.

With selected motions, pivot shapes and materials, 12 hour screening tests were run using the test rigs developed for the purpose. The purpose of the screening tests was to select the best materials based on damage in three temperature ranges: 80 - 400°F, 80 - 1000°F, 80 - 1400°F. The range of operating conditions was as follows:

Temperatures - 80 to 1400°F
Loads - 2 to 30#
Frequency - 200 and 1000 cps
Pivot Shape - .250 radius ball versus flat, .256, .375, .750 pocket
and .256, .375 cylinder
Motion - Pitch .0005 in/in to .0015 in/in.
Roll .0005 in/in to .0005 in/in.
Yaw .0005 in/in to .003 in/in.
Atmosphere - Argon

6. Long Term Tests

Once materials are selected which are not damaged by this type of motion it is necessary to determine their long term behavior with respect to wear or surface fatigue. Several of the materials which were most promising from the screening test were run for 2000 hours within the conditions tested above. 2000 hours represents 20% of the expected design life of 10,000 hours. This is a sufficient percentage of the life for realistic extrapolation.

7. Special Design Tests

During the course of the program a number of special designs were evaluated. These were pivots which were being contemplated for use in various prototype machinery. The tests consisted of 1/2 inch balls mated with either conforming or non-conforming sockets. In most cases 100 hour evaluations were made at various temperatures. A final test was run for 1000 hours.

IV. SUMMARY OF RESULTS

An analytical and experimental investigation of pivots for tilting-pad gas bearings has been conducted. Six rigs have been constructed which simulate the motions in the pivot. These rigs give pure rolling motions in two directions when applied independently. A twisting or yaw motion can also be applied. The test rigs allow the testing of pivots at temperatures to 1400 F in a various atmosphere at loads to 30 pounds. Various combinations of pitch, roll, and yaw can be applied at frequencies of 200 and 1000 cps. The systems have been set up for the unattended operations. The investigation results are as follows:

1. A study has been conducted to determine the pad motions due to the rotation of a typical compressor shaft rotating at speeds between 12,000 and 60,000 rpm.
 - a. The amplitudes of the pad oscillation in the pitch, roll and yaw directions are limited in magnitude due to the fluid film damping. No resonant peaks due to individual pad-gas film resonances were encountered with the speed range (10,000 to 60,000 rpm) investigated. This may be due to the fact that the film damping is sufficient to completely suppress any such individual pad resonances.
 - b. The calculated pitch amplitudes were about 1 to 1.5 milliradians at the system critical speeds, dropping rapidly to about 0.1 to 0.3 milliradians, away from the critical speeds. Roll and yaw oscillation amplitudes were of about equal magnitudes through the speed range, being everywhere below .1 of the pitch amplitude.
2. An analytical investigation was conducted to determine the amount of microslip which occurs with various contact geometries. A computer program was developed which allows the determination of microslip for 4th order contact surfaces as well as the pressure.

3. An analysis was also carried out to examine what can be done geometrically to minimize microslips. It was found that an optimum geometry does exist where the microslip is essentially eliminated.
4. A series of 12 hour screening tests has been conducted with various materials, pivot shapes, under various types of motions, amplitudes, frequencies, temperatures and loads which simulate gas bearing tilting pad pivots. The following results were obtained:
 - a. Under the most severe conditions of the above variables damage was insignificant in the 12 hour test with most materials. The damage consisted merely of a darkened ring of metal at the periphery of the area of contact. This damage pattern corresponds to the slip region predicted by theoretical considerations. No overall wear was evident.
 - b. The tests indicated that the most suitable materials for the selected temperature ranges are as follows:

<u>400F</u>	<u>1000F</u>	<u>1400F</u>
M-2 Tool Steel vs. Itself	M-2 Tool Steel vs. Itself	
Stellite Star J vs. Stellite 19	Stellite Star J vs. Stellite 19	Stellite Star J vs. Stellite 19
SAE 52100 Steel vs. Itself		
Stellite 6B vs. Stellite 6B		
K 96 Tungsten Car- bide vs. Itself		
K 162B Titanium Carbide vs. Itself	K 162B vs. Itself	K 162B vs. It- self
Carboloy 608 vs. Itself		

400F

Cemented Oxide
vs. Itself

HP Al_2O_3 vs.
Itself

1000F

Cemented Oxide
vs. Itself

1400F

- c. Pure ceramic materials, hot and cold pressed Al_2O_3 gave surface fracture pits in the contact area.
 - d. Severe damage to the pivots was found under the following conditions:
 - dynamic load
 - yaw (twist) motion of 3.2 mil/inch of radius
 - specimens free to turn in holder.
 - e. No effect of pivot shape was evident with the following exception: Increased damage was noted with the .256" radius (nearly conforming). This was attributed to the filling of the clearance with wear debris.
 - f. No difference in the wear, surface damage, or appearance of the slip area was evident after running tool steel, stellite, or titanium carbide specimens after running in an air, argon, or reducing (93 N_2 7 H_2) atmosphere at 500F and 900F.
5. A series of 2000 hour tests run at 900F using the .250 radius ball vs. various socket geometries showed the following:
- a. There was no significant increase in the wear or surface damage as compared with the 12 hour tests.
 - b. The carbide, tool steel, and stellite performed satisfactory.

Some microdamage was evident but appeared to be insufficient to seriously affect pivot motion. It is concluded that these materials are suitable for long term service.

- c. In contrast to the short term tests, no effect of the following shapes could be detected:

.250" radius vs.	{	flat .256 radius socket .256 radius cylinder .750 radius socket
------------------	---	--

6. Four tests were run with two solid film lubricants (MoS_2 bonded with sodium silicate and the NASA fused fluoride). Neither lubricant was worn away after 3.6×10^8 cycles (100 hours).
7. A series of 100 hour tests was run at 500 F with a variety of special materials and shapes. The following results were obtained:
 - a. Six tests with the combination WC ball-WC sprayed A-286 steel conforming socket indicated that the sprayed coating was removed from the socket and transferred to the ball during the test. The depth of the damage area was .0003 in. This damage induced changes in the pivot motions. It was concluded that this material combination was inadequate.
 - b. Eight tests were run with the sapphire ball-WC sockets with both the conforming and non-conforming geometries. In all cases some damage was evident. The non-conforming geometries with the center hole showed damage at the hole edge. The conforming geometries showed micro-transfer from one surface to the other with no edge effect. Fracture cracks were noted on the sapphire ball; accordingly it was concluded that this material combination was inadequate.
 - c. Eight tests were run with the BRU pivot design (conforming geometry) used in the Brayton Rotating Unit (BRU)*

* A single-shaft, turbocompressor alternator presently being tested at NASA-Lewis.

With both carbide (the BRU pivot material) and tool steel, micro-damage occurred. This damage consisted of removal of material from each surface and transfer to the other at isolated contact spots. The depth of the damage was approximately 20 microinches. This did not interfere with the motions and no overall wear could be detected. This type of damage was characteristic of all conforming geometries.

8. Two of the carbide BRU pivots described above were run for an additional 1,000 hours. The micro-damage at the conclusion of the test was more general, covering most of the surface. The extent of the damage however, was still small enough so it did not affect the motions of the pivots in the test rig. No significant wear was detected. It was concluded that the conforming surface pivots that were tested will operate successfully in an otherwise properly designed pivoted pad gas bearing, at least for the order of one to several thousand hours.
9. It is concluded that when using the proper materials and lubricants that pivot fretting is not a significant problem area. The sliding motions in the contact area are not large enough to produce significant damage or wear even when the imposed motions are 10 times that expected in a properly designed bearing.
10. Within the limits of these experiments the shape of the test specimens was an insignificant variable except that there was more surface damage with the more conforming geometries (radius ratios of 1 or 1.02).
11. For minimum damage and wear the following recommendations are made:
 - a. Materials

Temperatures to 900 F	M-2 Tool Steel vs. M-2 Tool Steel hardened to 58 RD
Temperatures to 1200 F	Stellite Star J vs Stellite 19
Temperatures to 1400 F	Titanium Carbide K 162B vs. Itself

- b. Materials ideally should be coated with a solid film lubricant which will withstand that temperature range. (Silicate bonded MoS_2 and the NASA fluoride performed satisfactorily; undoubtedly others will too.)
- c. The following pivots are recommended for design limits given:

<u>Radius of Pivot</u> <u>in.</u>	<u>Radius of Socket</u> <u>in.</u>	<u>Material</u>	<u>Temp.</u> <u>°F</u>	<u>Load</u> <u>#</u>
.125	.1625	M-2 Tool Steel	900	32
.125	.1625	K162B Carbide	1400	8
.250	.375	M-2 Tool Steel	900	52
		K162B Carbide	1400	41
.375	.5625	M-2 Tool Steel	900	66
		K162B Carbide	1400	50

V. ANALYSIS OF PAD MOTIONS

The purpose of this task has been to calculate the pitch, roll and yaw components of the oscillations of the gas bearing pads, in response to rotor unbalance. To this end, the analysis of the pad oscillations was made and introduced in the previously existing rotor response computer program (Ref. 9), so that the modified program calculates the amplitudes of the pad oscillation, in addition to the whirl amplitudes of the rotor. Calculations were then made using as a model the rotor and tilting pad journal bearings of the NASA's Brayton Cycle axial flow turbocompressor. The dynamic simulator of this rotating unit was at the time under test at MIT.

Calculation Procedure

The bearing pads are separated from the journal surface by a thin gas film. The pressure generated in the film by the rotation of the journal depends not only on the speed and the gas viscosity but also on the whirling motion of the journal. This latter dependency may conveniently be expressed in terms of a set of spring and damping coefficients which relate the generated dynamical forces to the amplitudes and velocities of the journal. The coefficients are calculated from lubrication theory as described in Appendix A. On this basis, a model of the rotor-bearing-pad system can be set up where the flexible rotor is supported in bearings represented by spring and damping coefficients, and each bearing pad is connected with the journal through another set of spring and damping coefficients. The system is excited by the rotor unbalance forces. Thus, the motions of the bearing pads are determined by a four step procedure: 1) calculate the spring and damping coefficients for the fluid film of the bearing pads, 2) combine the pad coefficients to obtain the resulting spring and damping coefficients for the complete bearing, 3) calculate the rotor motion due to a specified rotor unbalance, and 4) calculate the corresponding motion of the pads.

To determine the gas film stiffness and damping consider a single pad which is held fixed. With respect to the center of the pad, the journal center position is defined through the polar coordinates ϵ_0 and ϕ_0 under static conditions, (see

Fig. A-1). Under dynamic conditions the journal center whirls in an orbit around the steady-state position. The coordinate system for this motion is a cartesian coordinate system, with origin in the steady-state position with a ξ -axis parallel to the load direction and with a η -axis perpendicular to the ξ -axis, see Fig. A-1. Thus, relative to the pad the journal center amplitudes are ξ and η . The forces F_ξ and F_η generated in the gas film by this motion can be expressed as:

$$\begin{aligned} F_\xi &= -K_{\xi\xi}\xi - B_{\xi\xi}\frac{d\xi}{dt} - K_{\xi\eta}\eta - B_{\xi\eta}\frac{d\eta}{dt} \\ F_\eta &= -K_{\eta\xi}\xi - B_{\eta\xi}\frac{d\xi}{dt} - K_{\eta\eta}\eta - B_{\eta\eta}\frac{d\eta}{dt} \end{aligned} \quad (1)$$

These equations assume that the motion is reasonably small. The four spring coefficients, $K_{\xi\xi}$, $K_{\xi\eta}$, $K_{\eta\xi}$, and $K_{\eta\eta}$, and the four damping coefficients $B_{\xi\xi}$, $B_{\xi\eta}$, $B_{\eta\xi}$, and $B_{\eta\eta}$, are known when the steady-state operating conditions are given. In other words, for fixed bearing dimensions, bearing load and lubricant properties the coefficients depend only on the speed of the rotor. The coefficients are calculated as Taylor series coefficients of the hydrodynamic bearing film forces as shown in detail in Appendix A.

Once the eight gas film coefficients have been determined for each of the four bearing pads, they can be combined to yield similar coefficients representing the complete tilting-pad bearing. Equation (1) is used in combining the pad coefficients where, now, the journal amplitudes ξ and η define the relative motion between the journal center and the pad center such that the pitch motion of the pad and the radial motion of the pad on its flexure is included. In this way eight new coefficients are obtained, valid for the complete bearing. If any x-y coordinate system is introduced with the origin in the center of the bearing, with the x-axis vertical and the y-axis horizontal, the journal center motion can be defined by the amplitudes x and y. The corresponding dynamic forces become:

$$F_x = -K_{xx}x - B_{xx} \frac{dx}{dt} - K_{xy}y - B_{xy} \frac{dy}{dt}$$

(2)

$$F_y = -K_{yx}x - B_{yx} \frac{dx}{dt} - K_{yy}y - B_{yy} \frac{dy}{dt}$$

where the K's are the four bearing spring coefficients and the B's are the four bearing damping coefficients. They are calculated from the spring and damping coefficients of the individual pads, and include the effect of pad inertia and pad flexure as explained in detail in Appendix B.

With the 8 bearing coefficients known as defined by Equation (2), a rotor unbalance response calculation can be performed. In this calculation the rotor is represented by a series of mass points, simulating the mass distribution of the actual rotor, and the mass points are connected by weightless shaft sections which have the same stiffness as in the actual rotor. This way of simulating the rotor for calculation purposes is the conventional one used in the Prohl method (sometimes called the Holzer method for flexural vibrations) which is the method employed in the present analysis. At the bearing locations this idealized rotor model is supported by the 8 bearing coefficients, and the whole system is forced to vibrate by the rotor unbalance. The calculations are performed on a digital computer, and the details of the analysis and the computer program are given in Reference 9. For the present purpose, the computer program in Reference 9 has been revised to calculate automatically the 8 bearing coefficients based on the gas film coefficients for the individual bearing pads as defined by the analysis in Appendix B. The pad coefficients must be given as input to the program, and they are obtained from a separate program which is based on the analysis given in Appendix A.

The rotor response computer program calculates the journal amplitudes and the slope of the whirling shaft at the bearings. Knowing these quantities, and the dynamic coefficients for the bearing pads, the analysis in Appendix B can be used to calculate the resulting motions of the individual bearing shoes. This analysis is incorporated into the rotor response computer program.

Each bearing pad has four degrees of freedom: a) the radial motion of the pad on its flexure, b) the pitch motion of the pad around an axial axis through the pivot, c) the roll motion of the pad around a tangential axis through the pivot, and, d) the yaw motion of the pad around a radial axis through the pivot. The rotor response computer program calculates the amplitudes of these motions. Thus, by specifying a rotor unbalance, the program can be used to calculate the pad motions as a function of rotor speed, and with these results it is possible to establish a typical pad motion to be considered in the pivot performance tests.

Calculation of Pad Motions

Reference 10 describes in detail the analysis, design and experimental evaluation of the dynamic simulator and its bearings. Figure 4, reproduced from Reference 10, shows the cross sectional view of the rotor. Its principal characteristics are:

Material - Steel (heat treated AMS 6415F, AISI 4343)
Rotor weight - 10.62 lbs.
Polar moment of inertia - 12.7 lb.in^2
Transient moment of inertia (about c.g.) - 243 lb.in^2
Location of centerline of the compressor end bearing - 1.42 inches*
Location of c.g. - 8.75 inches
Location of centerline of the turbine end bearing - 11.47 inches*
Total rotor length - 15.51 inches

The journal bearing characteristics used in the calculations were as tabulated on the next page. The pad and its pivot are illustrated in Figure 5.

* Measured from the forward-most face of the thrust runner.

	<u>No. 1 Bearing (compressor end)</u>	<u>No. 2 Bearing (turbine end)</u>
Diameter, inches	1.5	2.125
Length, inches	1.5	2.125
Machined, radial clearance [*] , inches	0.00135	0.00319
Set-up, radial clearance ^{**} , inches	0.000675	0.00158
Number of pads	4	4
Pad arc length, degrees	80	80
Pivot position (arc length from leading edge to pivot centerline, expressed as a fraction of the pad arc length)	0.65	0.65
Pad weight, lbs.	0.14	0.21

 * This is the difference between the radius of curvature of the pad and the shaft radius.

** In order to insure that all the bearing pads, including the ones in the bearing half directly opposite from the direction of load, may form a convergent wedge and generate hydrodynamic pressures, the bearing pads are assembled so that their centers of curvature lie on a circle of radius "a". The radial clearance of the bearing at set-up is then: $C_B = C - a$, where C is the machined radial clearance. This is referred to as "pre-loaded" bearing, where the preload coefficients defined as: $m = a/C$. In the pad motion calculations reported here, the tabulated values of the set-up clearance was used. In the simulator test program, however, it was necessary to reduce set-up radial clearance of the turbine end bearing to 0.00068 inches to insure rotor-bearing stability over the complete speed range as discussed in Reference 10. The larger, design objective value of the turbine end bearing clearance tabulated above was nevertheless used, as it will yield larger values of pad oscillation amplitudes than the one used in the simulator tests.

The two rigid body critical speeds of the drive rotor-bearings system occur at about 20,000 and 30,000 rpm, while the third critical speed (flexural) is at about 85,000 rpm*. The mode shapes at the two rigid body critical speeds are shown in Figure 6, reproduced here from Reference 10. These mode shapes are straight lines, as the two critical speeds are rigid body criticals. Note that for this particular rotor-bearings system, the node point of the first critical speed mode occurs very near the No. 1 bearing and that the node point of the second critical speed mode occurs very near the No. 2 bearing. This characteristic of the particular rotor-bearings system used in the pad motion calculations will be referred to again in discussing the calculated pad motions in the pitch direction.

Using the pad motion calculation procedure described earlier and in Appendices A and B of this section, the pad motions were calculated for the following conditions.

Lubricant Argon at 400°F

Ambient Pressure: 12 psia

Speed Range: 10,000 to 60,000 rpm

Orientation: horizontal

Direction of Static Load Vector: midway

Unbalance Load: 0.01 oz.in. in the turbine plane

A horizontal orientation was used as this gives the largest pad motion amplitudes, in the case of the pads located in the upper half of the bearing, i.e., the bearing half 180° away from the load direction. With a vertical rotor, the amplitudes would be equal in all four pads.

The calculated pad motions are shown in Figures 7 through 10. Figures 7 and 8 are for the upper and lower pads respectively of the No. 1 bearing. Figures 9 and 10 are for the upper and lower pads respectively of the No. 2 bearing.

* In actual turbocompressor simulator, these rigid body critical speeds were lowered to about 11,000 and 18,000 rpm by the use of flexure supports under the pads, as described in Ref. 10. The third (flexural) critical speed is not significantly changed by the use of pad support flexures.

The calculated results in all cases show that the pad motion amplitudes peak at the rotor-bearing system critical speeds and are limited in amplitude due to the gas film damping. The gas film damping suppresses any individual pad gas film resonances that may occur within the speed range that was investigated.

The pitch motions of the pads track the whirl orbit of the rotor in the bearing. Since, as noted above (and as shown in Figure 6), the node point of the first rigid body critical speed is very near the No. 1 bearing, the rotor whirl amplitudes at this speed will be very small at the No. 1 bearing location. Thus, as Figures 7 and 8 show, there is no peak in the pitch amplitude curve at this critical speed which occurs at about 20,000 rpm. There is, however, a peak at the second critical speed which occurs at 20,000 rpm. Similarly, as also noted earlier and in Figure 6, the node point of the second critical speed occurs very near the location of the No. 2 bearing. Accordingly, it would be expected that the curve of the pitch motions for the No. 2 bearing pads would exhibit a peak at the first critical speed (20,000 rpm), but not at the second critical speed (30,000 rpm). This is in fact the case as illustrated in Figures 9 and 10.

The roll and yaw motions, on the other hand, will reflect the conical (angular) motions of the shaft about the center plane of the bearing. Accordingly, the roll and yaw oscillation amplitudes should exhibit peaks at both critical speeds, in each bearing, as is shown in Figures 7 through 10.

Figures 7 through 10 indicate that the pitch oscillations are considerably larger than either the roll or the yaw oscillations. The latter two are of about the same magnitude and are closely coupled, throughout the speed range.

Based on the calculations, it appears that oscillation amplitudes in pitch will be about 1 to 1.5 milliradians at the system critical speeds. Gas bearing turbomachinery is normally designed to operate away from system critical speeds. Under normal design conditions, therefore, the calculation results indicate that pitch amplitudes will be of the order of 0.1 to 0.3 milliradians.

Roll and yaw oscillation amplitudes on the other hand are considerably smaller, being of the order of .05 milliradians or less throughout if critical speeds are avoided.

VI. GEOMETRIC OPTIMIZATION OF CONCENTRATED CONTACTS FOR MINIMUM MICROSLIPS

It is a reasonable assumption that by changing the radius of curvature or other variables that the amount of microslip in the slip region would change. It is also a reasonable assumption that the amount of wear and surface damage will be proportional to the amount of microslip.

Accordingly, an analytical investigation was conducted to calculate the amount of microslip which occurs in curved contacts and also to determine that geometry where microslip will be at a minimum. Results of this investigation are described in the following sections.

1. Cursory Analysis

For bodies with axial symmetry and second order surfaces, Hertz-Mindlin theory [1] applies. The simplest case is shown in Fig. 11a in which L is the load normal to the interface, T is the load tangent to the interface and R is the radius of the identical pair of spherical surfaces in contact. Figure 11b, shows an enlargement of the contact area in which a is the radius of the contact region, c is the radius of the sub-region known as the locked region. The remaining region is the slip region. ρ is a generic radius. For this classical case, within classical contact theory, the following formulae are applicable:

$$p = \frac{3L}{2\pi a^3} (a^2 - \rho^2)^{1/2} \quad (1)$$

$$c = a \left(1 - \frac{T}{fL}\right)^{1/3} \quad (2)$$

$$\delta_x = \frac{3(2 - \nu)fL}{8Ga} \left[1 - \left(1 - \frac{T}{fL}\right)^{2/3}\right]^{1/2} \quad (3)$$

where p is the pressure distribution, δ_x is the relative horizontal displacement

between points, far removed from the contact zone, on the two bodies, L is the total load, f is the static friction coefficient, ν is Poisson's ratio, and G is the shear modulus.

Using the dimensionless quantities:

$$\tilde{p} = \frac{2\pi a^2 p}{3L}, \quad \tilde{c} = \frac{c}{a}, \quad \tilde{\rho} = \frac{\rho}{a}, \quad \tilde{\delta}_x = \frac{8Ga\delta_x}{3(2-\nu)fL},$$

$$\tilde{T} = \frac{T}{fL} \quad \text{and} \quad \tilde{T}_s = \frac{T_s}{f_s L},$$

where T_s is that portion of T which is directly associated with slippage, the above formulae become:

$$\tilde{p} = (1 - \tilde{\rho}^2)^{1/2} \tag{4}$$

$$\tilde{c} = (1 - \tilde{T})^{1/3} \tag{5}$$

$$\tilde{\delta}_x = 1 - (1 - \tilde{T})^{2/3} \quad (0 \leq \tilde{T} \leq 1). \tag{6}$$

Since T_s by definition is $\int_c^a 2\pi p f p dp$, therefore carrying out the integration and putting in dimensionless terms,

$$\tilde{T}_s = (1 - \tilde{c}^2)^{3/2} = \left[1 - (1 - \tilde{T})^{2/3} \right]^{3/2} = \tilde{\delta}_x^{3/2} \quad (0 \leq \tilde{\delta}_x < 1).$$

Also from the last two of the set of three equations above,

$$\tilde{T} = \begin{cases} 1 - (1 - \tilde{\delta}_x)^{3/2} & (0 \leq \tilde{\delta}_x < 1) \\ 1 & (\tilde{\delta}_x > 1) \end{cases} \quad (8)$$

Figure 12 shows a master plot of \tilde{T} , \tilde{T}_s vs. $\tilde{\delta}_x$. That is, it shows, for each value of $\tilde{\delta}_x$, that portion of \tilde{T} which is directly associated with slippage. All these quantities are in dimensionless measures, of course.

It should be noted that \tilde{T} is the measure of the ratio of rolling to static friction, i.e., T/fL . Thus at $\tilde{T} = 1$ gross sliding will take place. Also, at $\tilde{T} = .1$, approximately one-third of \tilde{T} is directly associated with slippage, etc. Figure 13 shows several sample geometries and their equivalent ones within the contact theory. The equivalent ones are used so that the simple formulae above can be used. The alternative method, though equivalent, would lead to more complicated formulae. Now, since $a \sim R^{1/3}$ according to Hertz theory, where R is the radius of the contacting spheres used in the equivalent geometries for which the formulae were derived, it can be said that

$$a_1 \sim 2.7, a_2 \sim 1.59, a_3 \sim 1, a_4 \sim .91, a_5 \sim .791 \quad (9)$$

where a_1, \dots, a_5 refer to the five radii of curvature for the five cases shown in Fig. 13. By definition, $\tilde{\delta}_x = 8Ga\delta_x/3(2 - \nu)fN$; everything else being equal, the geometrical difference, which causes a 's to be different, affect δ_x 's for a given \tilde{T} . This is so since for all levels of $\tilde{T} \leq 1$, $\tilde{\delta}_x$ has a unique value according to Fig. 11. This means, under this condition

$$\delta_x \sim \frac{1}{a} \quad (10)$$

Therefore, combining equations (9) and (10),

$$\delta_x^{(1)} : \delta_x^{(2)} : \delta_x^{(3)} : \delta_x^{(4)} : \delta_x^{(5)} = 1 : 1.7 : 2.7 : 3 : 3.5 . \quad (11)$$

Since δ_x is proportional to slip, i.e., δ_x is also proportional to the energy dissipation by microslip, it can be seen that the first case is better than the second, etc., in the order arranged, insofar as dissipation due to microslip is concerned. In this consideration, everything else is kept constant. This conclusion, moreover, is general, in that it is not dependent upon any fixed set of values of f , L , v , G .

In the above, for spherical surfaces in contact, a semi-quantitative comparison has been made of the geometries with regard to microslips without actually evaluating the microslips.

2. Higher Order Surfaces in Contact

Since it is known that microslips do occur with second order surfaces (e.g., spherical surfaces) in contact, one natural question which arises in design is what can be done geometrically to minimize microslips. To this end, an analysis has been carried out to examine the contact of higher order surfaces, in particular fourth order surfaces (Appendix C). This analysis entailed a generalization of the Hertz problem for fourth order paraboloidal surfaces in contact. Microslips and annulus of slip were sought. For this purpose, an inverse method was devised. Based upon this analysis, which shows how the geometry can be optimized for minimum microslips, the following data for design are shown in subsequent sections: Microslip data for spherical surfaces in contact; Optimized shapes; Closing-in; Maximum pressures; Radius of contact area; Maximum microslip; Computer program for the above.

The general analysis referred to above (Appendix C) is concerned with surfaces of fourth order and the contact region which are ellipses. Spherical surfaces

are, of course, special cases. Using the theory and letting τ be the ratio of the applied traction T to the load L , the following microslip data for various radii balls on socket are shown:

- Fig. 14 - Microslip vs. Angular Position for $1/4''^R$ Ball on Flat.
- Fig. 15 - Microslip vs. Angular Position for $1/4''^R$ Ball on $1''^R$ Socket.
- Fig. 16 - Microslip vs. Angular Position for $1/4''^R$ Ball on $3/4''^R$ Socket.
- Fig. 17 - Microslip vs. Angular Position for $1/4''^R$ Ball on $1/2''^R$ Socket.
- Fig. 18 - Microslip vs. Angular Position for $1/4''^R$ Ball on $0.256''^R$ Socket.

The number on the curves refers to $1/4$, $1/2$, $3/4$ and the full distance between the radii of the slip region. α_1 is the maximum Hertz pressure and δ_x as defined earlier. The microslip in the transverse direction is several magnitudes lower than those in the loading direction. Figure 19 shows the effect of equivalent radius, R_e , on maximum microslip, where

$$\frac{1}{R_e} = \left(\frac{1}{2R_b} - \frac{1}{2R_s} \right)$$

R_b and R_s are the radii of the ball and socket, respectively.

3. Optimized Shapes

Table 2 shows calculated, optimized shape data. Consider a ball with radius R_b in a socket with radius R_s . Then using the equation $C = 1/2R$, the geometries are:

$$f_b = C_b(x^2 + y^2)$$

$$f_s = C_s(x^2 + y^2)$$

TABLE 2
OPTIMIZED SHAPE DATA

Ball	Socket	$\frac{\theta_b + \theta_s}{2\pi} A_b = \frac{1}{2R_b}$	$\frac{\theta_b + \theta_s}{2\pi} A_s = \frac{1}{2R_s}$	$\frac{\theta_b + \theta_s}{2\pi} B$	
				L = 2 lb.	L = 30 lb.
.125 in.	.131 in.	4 in. ⁻¹	3.817 in. ⁻¹	- 1.05 x 10 ³ in. ⁻³	- 1.7 x 10 ² in. ⁻³
.125	.25	4	2	- 5.6 x 10 ⁴	- 9. x 10 ³
.125	.375	4	1.33	- 9. x 10 ⁴	- 1.45 x 10 ⁴
.125	flat	4	0	- 1.77 x 10 ⁵	- 2.9 x 10 ⁴
.25	.256	2	1.953	- 1.15 x 10 ²	- 17.5
.25	.5	2	1	- 1.75 x 10 ⁴	- 2.9 x 10 ³
.25	.75	2	.667	- 2.9 x 10 ⁴	- 4.7 x 10 ³
.25	flat	2	0	- 5.6 x 10 ⁴	- 9. x 10 ³
.375	.381	1.33	1.312	- 30.3	- 4.6
.375	.75	1.33	.667	- 9. x 10 ³	- 1.5 x 10 ³
.375	1.125	1.33	.445	1.45 x 10 ⁴	- 2.4 x 10 ³
.375	flat	1.33	0	- 2.9 x 10 ⁴	- 4.7 x 10 ³

where f_b and f_s are the distances, for a given (x,y) , from the ball and socket surface to the plane of the interface (an assumption of the classical contact theory). The apparent geometry is given by

$$f_a \equiv f_b - f_s = (C_b - C_s)(x^2 + y^2) = \frac{\theta_b + \theta_s}{2\pi} A(x^2 + y^2)$$

where

$$A = 2\pi(C_b - C_s)/(\theta_b + \theta_s)$$

and

$$\theta_b + \theta_s = \frac{1 - \nu_b}{G_b} + \frac{1 - \nu_s}{G_s}$$

The modified apparent geometry which includes fourth order terms is

$$f_m = \frac{\theta_b + \theta_s}{2\pi} [A(x^2 + y^2) + B(x^4 + 2x^2y^2 + y^4)].$$

Given $(\frac{\theta_b + \theta_s}{2\pi}) A$, $(\frac{\theta_b + \theta_s}{2\pi}) B$, may be found from a $(\frac{\theta_b + \theta_s}{2\pi}) B$ vs. $(\frac{\theta_b + \theta_s}{2\pi}) A$

graph (note that $(\frac{\theta_b + \theta_s}{2\pi}) B$ is negative). Note $\frac{\theta_b + \theta_s}{2\pi} A_b + \frac{\theta_b + \theta_s}{2\pi} A_s = \frac{\theta_b + \theta_s}{2\pi} A$.

There are an infinite number of ways to break up $\frac{\theta_b + \theta_s}{2\pi} B$, but only two are shown below:

1. Modified ball-spherical cup:

$$f_b^{(1)} = C_b(x^2 + y^2) + \frac{\theta_b + \theta_s}{2\pi} B(x^4 + 2x^2y^2 + y^4)$$

$$f_s^{(1)} = C_s(x^2 + y^2).$$

2. Spherical ball-modified cup:

$$f_b^{(2)} = C_b (x^2 + y^2)$$

$$f_b^{(2)} = C_s (x^2 + y^2) - \frac{\theta_b + \theta_s}{2\pi} B (x^4 + 2x^2y^2 + y^4) .$$

The results in Table 2 are also plotted in Fig. 20. Figure 21 shows a typical cross-section of ball and socket as modified. Originally, it was intended to build and evaluate such a pivot combination; however, since the results of the screening and long-term tests showed very little damage with simple shapes, this added complexity was not necessary.

4. Closing-In

The effect of the geometric parameter $\frac{\theta_b + \theta_s}{2\pi} A$ on the closing-in δ_z for steel is shown in Fig. 22.

5. Maximum Pressure

Figure 23 shows the effect of the geometric parameter $\frac{\theta_b + \theta_s}{2\pi} A$ on the maximum pressure for steel. It is provided to aid in design. The maximum pressure of the modified case is only some eight percent of the maximum pressure of the ball-socket counterpart.

6. Radius of Contact Area

Figure 24 shows the effect of the geometric parameter $\frac{\theta_b + \theta_s}{2\pi} A$ on the radius of contact area for steel. It should be consulted to determine the extend of the modification, i.e. how large x and y may be before interference occurs between the two surfaces. Interference begins at a radius equal to approximately 120 percent of the radius of the contact area. Therefore, the modification should end at values of x and y which are within the interference circle, such as

$$(x_{\max}^2 + y_{\max}^2)^{1/2} = 110 \text{ percent of the contact area radius.}$$

7. Maximum Microslip

The chart for maximum microslip as a function of the geometric parameter $\frac{\theta_b + \theta_s}{2\pi} A$ for steel is shown in Fig. 25. $\alpha_2/\alpha_1 = 0$ is the case of Hertz-Mindlin and $\alpha_2/\alpha_1 = -1$ is the optimized case.

8. Computer Program for Calculations Sampled Above

The program is written for an IBM 360 computer using Fortran IV language (see Appendix D). The input variables are:

NQ = number of Q's
 NA1 = number of α_1 's
 NA2 = number of ratios α_2/α_1
 MS = number of τ 's
 NT = control number for checking the size of A
 AMIN = minimum size of A
 AMAX = maximum size of A
 Q = load in pounds
 A01 = α_1
 A02 = α_2/α_1
 U = coefficient of friction
 PR = Poisson's ratio
 TAU = τ = shear force/normal force

The values for NQ, NA1, NA2 need no explanation other than $NQ \leq 10$, $NA1, NA2 \leq 100$. MS also acts as a control statement as well as providing the number of τ 's. If $MS = 0$, the microslip and locked displacement will not be computed and will be listed as zero in the output. Unless the microslip and locked displacement are absolutely necessary, it is urged that they not be computed because they increase

the computation time by about 50 times. If $0 < MS \leq 10$, then the microslip will be computed. In order to eliminate unwanted output, and especially unnecessary computation when $MS \neq 0$, NT, AMIN and AMAX are provided to check the size of A. Since values of B, maximum pressure, etc., are usually only wanted for a certain range of A, the lower and upper limits of A are provided by AMIN and AMAX, respectively. If $NT \geq 1$, the value of A will be checked to see if $AMIN \leq A \leq AMAX$. If $NT = 0$, A will not be checked. The range of α_1 used for the graphs in this paper is $10^3 < \alpha_1 < 10^6$. The ratio $\alpha_2/\alpha_1 = 0$ corresponds to the simple Hertz case of two concentric spheres and the ratio $\alpha_2/\alpha_1 = -1$ yields the minimum slip case. If $\alpha_2/\alpha_1 = 0$, then the maximum pressure is equal to α_1 ; otherwise it is given in the output under PMAX. U, PR and TAU are provided only if $MS \neq 0$, otherwise they are omitted.

The format information is as follows:

NQ, NA1, NA2, MS, NT, AMIN, AMAX	- 5I5, 5X, 2F10.
Q's	6F10
A01's	6E10
A02's	6F10
U, PR	6F10
TAU's	6F10

Note: AMIN and AMAX are required only if $NT \neq 0$ and U, PR and TAU's are required only if $MS \neq 0$.

The output headings are:

A	= coefficient of second order terms in the apparent geometry function which <u>does not</u> include the material constants
B	= coefficient for fourth order terms
DEL	= closing in $(\theta_b + \theta_s)$

PMAX = maximum pressure in the area of contact in psi (only if $\alpha_2/\alpha_1 \neq 0$)

SMAX = $2\pi G \times$ maximum slip between the two bodies in lb./in.

UL = $2\pi G \times$ displacement of locked region in lb./in.

RAD = radius of contact area in inches

A1 = α_1 (equals maximum pressure if $\alpha_2/\alpha_1 = 0$)

A02 = α_2/α_1

VII. MATERIALS AND LUBRICANTS SELECTION

There is very little published information to define the requirements for pivot materials at high temperatures. However, since a pivot is primarily a rolling contact the information based on rolling contact bearings can be used. The most important of these material requirements are as follows:

1. A high yield strength at the maximum operating temperature (high hardness)
2. Dimensional stability
3. Corrosion resistance to the environment
4. Good sliding compatibility in the environment
5. Relative ease of fabrication to the desired configuration
6. Adequate shock resistance (thermal and mechanical)

Actually the requirements of high strength, corrosion resistance, and shock are so limiting at temperatures to 1400°F that they are given primary consideration. A number of surveys have been published (Reference 11 to 14) on the status of materials for rolling contacts. The most recent by Glaeser (12) makes the following recommendations.

<u>Temperatures</u>	<u>Material</u>
900°F	M-2, M-50, T1 Tool Steel
1400°F	K-162B carbide
1600°F	Stellite Star J, Stellite 19
2000°F	α - Al_2O_3 , Stabilized ZrO_2

Bisson and Anderson (reference 11) recommend that the minimum hardness level of rolling bearings be Rockwell C55. If the hardness level drops below this value, an increase in the wear and a shortening of the fatigue life could be expected. Since the stresses in bearings are generally higher than those used in pivots, this value should be considered more of a goal than a requirement. On this basis, SAE 52100 steel and 440 C stainless steel are recommended to 450°F. Tool steels M1, M2, M10 and T1 are suitable to approximately 1000°F.

In an Air Force program two tool steels were developed WB-49 and WACD-65 which have better hot hardness than the M or T series tool steels at 1000°F. These have proven to be satisfactory for certain applications but are not widely used as yet (16).

In general, the M-series tool steels have been found to be satisfactory at temperatures up to 800°F to 900°F. In the temperature range below 900°F there are few reasons to consider materials other than the M series tool steels. In Reference 15 rolling tests were run on potential high-temperature bearing materials, both dry and lubricated with silane. In the unlubricated tests, Stellite and 440 C stainless were both inferior to M1 steel. Al_2O_3 and synthetic sapphire gave high wear either lubricated or unlubricated. Of the M series tool steels T5 and M2 showed the best hot hardness at 800°F (16). Stellite has been used to 1200°F. For higher temperatures there has been little experience. Titanium carbide, hot and cold pressed Al_2O_3 , ZrO_2 and a chrome carbide appear to be the most promising. Tungsten carbide can be used at high temperatures in an inert environment but will oxidize rapidly in air at temperatures above 900°F. Thus recommendations for material to be used above 1200°F are primarily based upon the availability, reliability and experience with the materials and their fabrication rather than experience of sliding and rolling behavior.

For the temperature range above 1000°F to 1200°F the Stellite materials seem most appropriate. They have more ductility and are easier to fabricate than the carbides or ceramic but maintain higher hardness levels than the tool steels. It would be desirable to use the Stellite to 1400°F to avoid the use of carbides if possible. To do this it is necessary to select the materials with the maximum high temperature hardness. Data from Reference 17 indicate that this would be alloys 3, 19, Star J and 98 M-2 of the standard materials. Of these the standard bearing materials have been Star J balls and Stellite 3 races which have found some success in marginal lubrication applications such as water. In high temperature roller tests, Reference 18, Murray found that Star J, 3, and 19 gave satisfactory performance to stresses of 300,000 psi and 1200°F. Further, Stellite 19 appeared to be the most ductile member of the group. At high stresses to 500,000 psi the 19 alloy failed because of excessive deformation while the others cracked. Stellite 19 was thus selected over Stellite 3. Star J was selected because it is a standard ball material. Stellite 6B was added to include a wrought Stellite alloy.

Although rolling tests and bearing tests have been run with the carbides and ceramic at high temperatures, there is insufficient evidence to select materials on that basis. Rather than that, the approach used was to select the conventional materials for initial evaluation. There is considerable question whether such materials can be used in a pivot which is subjected to shock loads. Since they are difficult to fabricate they would be used only for those temperature ranges where the metals are inadequate. The primary advantage of these types of materials has been found to be effective (Reference 19) in a number of sliding applications. It was selected primarily on this basis. The ceramic material hot and cold pressed Al_2O_3 were selected as those for which there has been maximum performance in inert environment, (Reference 20).

SAE 52100 and 440C stainless were selected for comparison purposes. A flame plated tungsten carbide was also added since this is being used in a current pivot design.

The list of selected materials is shown in Table 3.

The effect of the lubricant and the life of the lubricant in a pivot application is difficult to estimate since the number of cycles is far beyond the life of the films in pure sliding contact. Data is not available on pure rolling contacts. If we assume that the life of the film will be determined by the microslip in the area of contact then the lubricant film would be only considered as a "break in" film. In this program this approach was taken. Consideration was given primarily to selecting the materials which would operate unlubricated. The lubricant would be added to extend the life.

A review was made of the high temperature solid lubricants which could be used for various temperature ranges (References 21 to 28). The candidates are shown in Table 4.

TABLE 3
MATERIALS

<u>Temperature Range</u>	<u>Ball Material</u>	<u>Hardness</u>	<u>Socket Material</u>	<u>Hardness</u>
80 - 450°F	52100 Steel	59-61 RC	Same as Ball	Same as Ball
80 - 800°F	M-2 Tool Steel	60-62 RC	Same as Ball	Same as Ball
80 - 1100°F	Stellite Star J	59-62 RC	Stellite 19	56-58 RC
80 - 1200°F	Stellite Star J	59-62 RC	Carboloy 608 (Chromium carbide + Ni Binder)	70 RC
80 - 900°F Air	Kennametal K196	91 RA	Same as Ball	Same as Ball
80 - 1200°F Argon	(Tungsten carbide + Co-binder)			
80 - 1600°F	Kennametal 162B (Titanium carbide + Ni Binder)	89 RA	Same as Ball	Same as Ball
80 - 1800°F	Cold Pressed Al_2O_3	80 R _{45N}	Same as Ball	Same as Ball
80 - 1800°F	Hot Pressed Al_2O_3	80 R _{45N}	Carboloy Ce- mented Oxide	90 RA
80 - 1800°F	Hot Pressed Al_2O_3		Hot Pressed Al_2O_3	
80 - 450°F	440 C Stainless Steel		440 C Stainless Steel	Same as Ball
80 - 1000°F	Kennametal K196	91RA	Flame LINW40	Same as Ball

TABLE 4
LUBRICANTS

Lubricant	Temperature Range F	
	<u>Air</u>	<u>Inert</u>
MoS ₂	750	1200
Resin Bonded MoS ₂	600	600
Silicate Bonded MoS ₂	800	1200
Metal Bonded MoS ₂	800	----
WS ₂	800	> MoS ₂
CdO + Graphite	800	1400
PbO	1200	1200
PbO SiO ₂	1250	1250
Ceramic Bonded CaF ₂	500 - 1400	500 - 1400
AgPb Alloy	600 - 1400	600 - 1400
PbMoO ₄	1000 - 1400	1000 - 1400
Glasses	1000 - 1400	1000 - 1400

The following lubricant films were selected based upon known lubricating properties and the availability of reliable means of application; preference was given to lubricant films which would be suitable in both air and argon environments and suitable on both metal and ceramic specimens:

	<u>1st Choice</u>	<u>Other</u>
1400°F	Ceramic Bonded CaF_2	AgPd , PbMoO_4
1200°F	PbSiO_2	PbO
800°F	Silicate Bonded BoS_2	Silicated Bonded Graphite
600°F	Resin Bonded MoS_2	

VIII. TEST RIGS

1. Requirements

In order to adequately evaluate the effect of pivot motions it was necessary to construct an apparatus which simulated the pad motions and conditions. This meant a rig which would hold a ball and a socket and impose a rotary motion between the two in three orthogonal axes; that is pitch, roll and yaw (Figure 26). The necessary operating conditions are given in Section III, "program Scope". These conditions imposed some difficult design problems. They are discussed in the following sections.

A diagrammatic sketch of the resulting test rig is shown in Figure 27. Essentially it consists of a rigidly held ball. The socket is mounted on the flat face of a spherical seat. In operation the spherical seat is floated on a gas bearing. Motion is imparted to the spherical seat by means of a pendulum at its base. This is driven by three electromagnetic drivers shown in Figure 29. This test device is described in greater detail in a later section. Six of these test rigs were constructed and used during the test program.

A second rig was designed during the course of this program. It was intended that it be used for the study in subsequent programs of the effects of dynamic and shock loading.

A sketch of this rig is shown in Figure 28. Essentially it uses the same test specimens as the previous test rig. The important feature of the rig is that the desired motions are separated into two different dynamic components, pitch and dynamic load. The pitch motion is provided by angular oscillation of a

preloaded rigid rocking bar supported on knife edges. The other motion consists of direct loading coupled with reciprocating dynamic loading on an axis at right angles to the pitch motion axis. The steady load is applied by pneumatic means. A shock load or alternating dynamic load is applied by a commercial electromagnetic drive. The temperature and other requirements conform to those specified for the present test device.

2. Design Approaches

In the design of the pivot-fretting test rig, some difficult problems were encountered. These are discussed in the following sections. A more detailed design analysis is given in Appendix E.

a. Drive Systems

In the preliminary design study, several methods of driving the lower test specimen at high frequency and small amplitude motions were reviewed. Two were considered to offer the best potential solutions, pneumatic drives and electromagnetic drives.

The pneumatic drive represented a new concept based on gas bearing technology. The drive consisted of establishing a pair of opposed hydrostatic gas bearing thrust pads on either side of the lever arm for each axis of motion and achieving a condition of controlled pneumatic hammer.

The advantages of this system include the following:

1. Drives can be completely contained in the heated tests zone of the rig with the only drive energy requirement being a supply of preheated and pressurized gas.
2. Since no mechanical drive linkages are involved there is a maximum freedom for establishing pure multiple motions.

Because of the newness of the concept, a room temperature demonstration model of the basic drive principle was built.

This model demonstrated that while the motions and amplitudes could be achieved, extensive development would be necessary in order to resolve the following problem areas:

1. Excessive drive gas flow
2. Control of amplitudes of motion, which could only be achieved by the use of mechanical end stops.
3. Mechanical stops represented a material selection and wear problem for long term testing particularly at high temperature and influenced the form of motion achieved since a bounce occurred at each contact.
4. The motions would change as the specimen friction increased as a result of damage.

In order to apply electromagnetic drives the following major factors had to be considered:

1. The availability of a suitable driver
2. The drives would have to be located outside of the test zone of the rig because of the high test temperature involved.
3. The linkage system between the drives and lower specimen would have to penetrate the furnace, would have to be of light weight, would have to be non-sensitive to distortion effects and be suitable for permitting the three motions required without undesirable interactions.

A careful survey was made of commercially available vibration generators and vibration table drives. It was found that reasonably sized units had inadequate output at the high frequencies. This was mainly because of the inherent internal mass of the machines which absorbed a portion of the available power. Drives of adequate power output were extremely bulky and presented problems of interference when for example three units had to be mounted in close proximity beneath the rig. More remote mounting involved long heavy linkages with their several problems.

The fundamental requirement for the drive was that the smallest size unit was needed with the largest possible ratio of power output to internal mass. The only pieces of equipment which would meet this requirement were high powered speaker drives such as used in horns. In these devices the only internal moving parts necessary for functional performance are a plastic diaphragm and a light-weight coil.

Consideration was given to several models of different design and power output.

Tests were conducted to verify its applicability in the test rig drive system. In these tests, a series of simulated loads representative of the linkage and specimen reaction forces were achieved by cementing weights to the diaphragm. Figure E-4 of Appendix E shows some typical performance curves.

These performance curves were correlated with the minimum linkage masses that could be designed for the requirements as is discussed under driver performance.

On the basis of these studies and tests it was decided to proceed using the electromagnetic drives of the speaker unit type.

b. Specimen Support

Because of the small amount of motion it was necessary to hold one specimen rigid and to move the second. A simpler design would result if the ball was held stationary. Accordingly the upper ball specimen support assembly is rigidly positioned in all radial directions but has axial freedom for the

application of the test load. The system uses two well spaced thin circular diaphragm plates with very high radial stiffness and low axial stiffness to support the upper specimen shaft assembly. (See Figure 27).

c. Drive Linkages

A lightweight linkage system was necessary in order to obtain adequate motions (see Figure 29) which consisted of a thin walled aluminum cone made by spinning which was cemented directly to the diaphragm and a light aluminum horizontal push rod connecting to a thin steel horizontal push-rod. The steel rod operates in the hotter zone at the extremity of a hemispherical gas bearing specimen support member. The thin steel push-rod provides the transverse flexibility necessary for the motions imposed in other planes.

Recognizing that the electromagnetic drives were not designed for this type of application, that consistency between these commercial units was an unknown and that their capability of extended continuous operation was also an unknown, it was decided that a study of the possibility of operating the driver and linkage close to resonance should be undertaken. Operating close to resonance had the potential advantages of reducing the power output required and internal heating of the drivers.

Resonance was to be achieved by building an adjustable spring in the lower horizontal linkage. A convenient design solution was to make the flexure support bearing act as this spring. A detailed Design Analysis is given in Appendix E.

The motion is imposed on the lower specimen holder. This holder must provide accurate positioning with negligible friction and no wear while being subjected to high frequency pitch, roll and yaw motions. The ideal solution to this problem was to support the specimen on a hemispherical gas bearing of high radial stiffness, so this approach was adopted. The design of this bearing is given in Appendix E.

d. Thermal Control

Heating of the test specimen followed the conventional procedure of providing a group of controllable high wattage cartridge heaters in the rig housings and of preheating incoming environmental and gas bearing gases. Containment of the heat is assisted by external high temperature insulating material.

It is essential that the lower drive linkages and electromagnetic drives be at a temperature as close to room temperature as possible. This means that a temperature gradient of about 1300°F may exist at the lower zone of the rig.

This temperature gradient was effectively achieved with the minimum of thermal distortion by a combination of high temperature insulating materials and a copper shunt taking heat to a water cooled ring at the lower end and surface of the rig. Provisions were also included for local air cooling.

Thermal expansion differences between the heated test rig and the cold base plate which supports both the rig and the three electromagnetic drivers could affect the test motions. This problem was solved by providing a support structure between the rig and base plate very close to the vertical centerline in which all thermal growths in the horizontal plane are radial. The drive linkage settings are made when the selected test temperature condition has been achieved.

e. Sealing

A condition of testing is that the specimens be operated in a closely controlled atmospheric environment such as argon, without any possibility of contamination from the external gases or gas bearing exhaust.

Consideration was given to positive seals such as a bellows connecting the upper specimen holder to the lower dynamic specimen holder. Problems of temperature, fatigue life of the bellows and drive power showed this to be impractical.

The design accepted was a staggered type of radial labyrinth seal set to the

minimum practical clearance. Details of the analysis of the labyrinth are given in Appendix E.

The feed supply of the environmental gas into the test zone was injected between the two support diaphragms and through the vertical specimen support shaft. Operational experience has established the minimum pressure difference and flow necessary for satisfactory environmental testing and conservation of gas supply.

f. Specimen Retention

Retention of specimens under very high frequency excitation and over a range of temperatures represents a classical problem. This is particularly true if one of the specimens is a precise, highly finished ball and materials of varying thermal expansion rates are involved.

The lower specimen which is in the basic form of a flat disk is mounted with a high interference fit into a small specimen holder which has a thread shaft extension. This shaft extension screws into a high temperature self-locking insert.

The more difficult problem is locking the ball. The technique used varies depending on whether the ball is made of high or low expansion rate material. The specimen holding cover is provided with a conical seat for accurately locating the lower portion of the ball. Tightening of the cover loads the ball against an upper Stellite block. In the case of a high expansion rate material specimen, the spring tension in the cover plus the matching thermal expansion rates will maintain a clamping force on the ball with changing temperature. For low expansion rate material specimens an additional spring washer plate is put in series with the Stellite block in order to maintain the clamping action.

As an extra precaution and for extended testing at temperatures where metal creep might relax the clamping action, an anti rotation flat is ground to provide a side surface on the ball and is engaged by a small set screw through

the wall of the cover.

3. Description of Test Rig

A schematic diagram of the test rig is shown in Figure 27. A photograph of the test rig is shown in Figure 30 and of the overall system for two rigs in Figure 31. The panel control system is shown in Figure 32. The test rig provides the mountings for a ball loaded against a flat, socket or cylindrical lower specimen. A photograph of the test specimens is shown in Figure 33. The lower specimen and its holder are screwed into a spherical seat. This seat rests in the base socket which is floated as a gas bearing. A pendulum at the bottom is driven to impart rocking motions to the bottom specimen about the circumference of the ball. At the base of the pendulum is a flat plate. Connected to this plate are three 75 watt electromagnetic drivers (as shown in Figure 29) whose outputs are combined to obtain pitch, yaw and roll motions. For driver 1 and 2 "out of phase" 180° pure pitch will be obtained. If they are "out of phase" with a different amplitude some yaw will be introduced. If drivers 1 and 2 are "in phase" pure yaw will be obtained. Roll about an axis 90° to the pitch motion is introduced by driver 3. It can be "in phase" or "out of phase" with the pitch motion. If it is "in phase" the direction of pitch is merely shifted through some angle. If it is "out of phase" a rolling motion is obtained about the contact point on the ball. For these tests the roll driver was always used "out of phase" to simulate the bearing motion.

The ball is held rigidly in a holder which is mounted on the bottom of a hollow rod. The rod is held in place by two diaphragms. These diaphragms prevent lateral motion of the ball but are thin enough to allow for radial or vertical motion. A load is applied to the top of this rod with air pressure into a bellows section.

The test specimens atmosphere is contained by two labyrinths with a ten mil clearance. Argon admitted to the top of the rig passes the heaters and enters the hollow specimens rod by a series of passages. From here it passes across the specimens and out through the labyrinth. A positive pressure prevents the

back flow of air into the specimen area.

Eight cartridge heaters which allow heating the rig to 1400°F are mounted in the rig housing. The temperature of the rig is controlled by a thermocouple next to the heaters; the specimen temperature is measured by a thermocouple mounted on the labyrinth.

Air is supplied to the gas bearing after passing by the cartridge heaters. This insures uniform temperatures throughout the rig necessary to maintain the small clearance in the gas bearing. The gas pressure from the bearing is exhausted to atmosphere.

Insulation surrounds the outside of the rig to further insure uniform temperature. The test rig is also mounted on a base plate which contains a water jacket. This protects the drivers from the rig heat.

In all, six such rigs were constructed for running the tests. In addition a number of auxiliary systems were necessary. These are described in the following section.

The primary measurements made upon the specimens are wear and surface damage. The wear is measured with a capacitance probe by measuring the position of the load stem as a function of time. However, in these experiments the wear was generally negligible so the results are presented as observed surface damage or Talysurf traces after a given period of running. An indication of surface damage is also obtained by monitoring the motions with the probes at the base of the pendulum. With undamaged specimens a smooth sine wave is obtained on the scope. If damage results this trace becomes distorted with frequent shifts in the amplitude.

4. Auxiliary Systems and Instrumentation

The gas system is shown in Figure 34. Essentially it consists of a supply line from an air compressor and from an eight bottle argon manifold. The air is used

for the load bellows and the gas bearing. The argon is used as an atmosphere blanket for the specimens. The air is filtered in a commercial 5 microinch filter which removes moisture and other impurities. From the filters which are part of the test system the air is piped to the rigs. An auxiliary standby system of N_2 is provided to protect the rig in case of a loss of gas pressure. Three air and three argon lines each shared by two rigs are heated by passing them through a coil inside a tubular furnace. The air for the loading system is not heated since the flow to the load bellows is very small.

For all tests the commercially pure argon was used. An analysis of the gas is given in Table 5. Some initial tests were run in high purity argon. Since the results were essentially the same as the commercially pure argon the latter was used because of its availability and lower cost.

TABLE 5
SPECIFICATION NO. L-108

<u>PRODUCT</u>	Argon
<u>PHYSICAL STATE</u>	Argon gas, A.
<u>GUARANTEED MINIMUM PURITY</u>	99.998 percent
<u>TYPICAL PURITY</u>	99.999 percent
<u>NORMAL DEWPOINT</u>	Below - 90°F (less than 5 ppm moisture by volume)
<u>MAXIMUM IMPURITIES</u>	Oxygen ≤ 5 ppm by volume Nitrogen ≤ 10 ppm by volume

The heating system for the gas and test rigs are shown in Figure 35. The test rig contains 6 cartridge heaters. Three from each rig are connected to a separate 100 volt variac. The three gas heaters are each heated with a 220 volt variac. Also shown is the time contact system which will shut the rig off at the desired time. This was used primarily in the screening tests where it was necessary to shut the tests off at 5 A.M.

The temperature measurement and recording system is also shown in Figure 35. The gas temperature and the test temperature are continuously recorded throughout the test. Temperature is controlled by a thermocouple near the heater elements to prevent large temperature cycling. Actually by calibration and by experience the variac settings were found which maintained the desired temperature. The heaters rarely cycled on or off.

The most important system is, of course, that used to obtain the desired motions and to measure them. The complete system is shown in Figure 36. The system consists of two oscillators, which can be set at any frequency. For these tests two frequencies were used, 1000 cps and 200 cps. The desired frequency could be selected with the proper switching device.

Three 75 watt amplifiers were used for each rig, one for each driver. Two phase shifters were also used for one pitch amplifier and one for a roll amplifier.

In order to determine and adjust the motions three 10 mil capacitance probes were mounted, one opposite each probe. These probes were connected to an oscilloscope on the panel board to monitor motions.

All variations of the motions could be detected by combining any two of the probes on the x, y of the scope. Typical patterns for the various motions are shown in Figure 37. Pure pitch motion is detected by monitoring probes x_1 and x_2 . First, equal amplitudes are set on each driver. If they are "in phase" the motion will be as shown in trace 1A. The angle α then would equal 45° . For pure yaw 3A and 3B the same pattern is obtained but shifted 90° into the first quadrant. Any combination of pitch and yaw 4A, will also give a similar pattern with an angle β somewhere in between the pitch and yaw pattern. In each of these cases pattern B remains the same showing x_1 varying with y_1 constant. The most significant pattern is that of a 7A and B since this is the test condition. 7A shows that there is a combination of pitch and yaw; 7B shows an ellipse. The y_1 direction indicates the amount of roll the x_1 direction indicates the amount of pitch at that end of the driver.

The important fact to note is that for each type of motion a unique pattern exists which can be readily identified.

Test Rig Calibrations

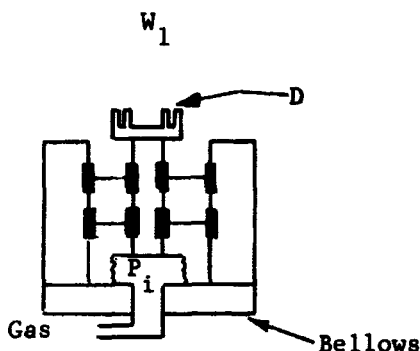
After the test rigs were set up a number of calibrations were necessary to test the rig performance. These calibrations are described in the following sections.

The most critical part of the rig was the gas bearing. The two surfaces were lapped together, assembled in the test rig, and the gas flow determined at a given load. This was repeated until further lapping produced no further decrease in flow. The minimum film thickness was desired to minimize the gas usage but primarily to obtain the maximum bearing stiffness. Once this had been accomplished the bearings were calibrated by measuring bearing lift for a given amount of preload. To obtain this data only the base of the apparatus was used. A capacitance probe was mounted at the center of the spherical socket and the bearing lift determined for at various pressures. The data obtained for 25 pounds for rig one is shown in Figure 38. It can be seen that in the low pressure region there is a linear relationship between load and lift. Then at a given pressure, in this case 75 psi, there was a large increase to lift. Thereafter the relationship again became linear. It was determined that there was still contact below 75 psi, therefore, it would be necessary to operate with a lift of approximately .001 inch. The reason for this behavior could not be exactly determined, however, it was felt to be due to the small inaccuracies in the conformity of the ball and the socket. The bearing lift curves for Rigs 1 and 2 for various preloads are shown in Figures 39 and 40. It can be seen that in all cases the behavior is essentially the same. These curves then established the pressure necessary to float the bearing for a given load. Usually, however, it was not necessary to refer to such curves since the large increase in lift made audible changes in the gas flow pattern.

The remaining four rigs did not have the same characteristic behavior. Because of the improved lapping procedures much closer tolerances could be held between the seat and the socket. As a result the linear portion of the lift pressure

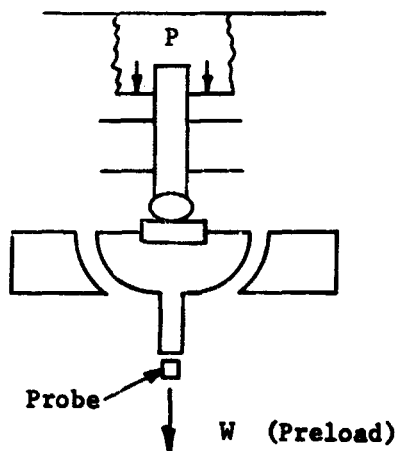
curve was shifted from the starting point of 80 psi and 1.0 mil to 50 psi and .1 mil. A typical curve is shown in Figure 41. This behavior allowed these rigs to be operated at a much smaller film thickness.

It was also necessary to calibrate the load bellows on the test rigs. To do this several methods were tried; two were successful. The primary method used was with dead weights. To do this the rig was turned upside down as shown below:



A dial indicator was placed on the labyrinth at point D. The gas pressure was determined which would give a positive indication of motion. The amount of motion was noted. A given weight was then added to the top of the labyrinth and the pressure determined to bring the indicator to the same reading. Using this method the six were calibrated as shown in Figure 42. The differences in the calibration of Rigs 1 and 2 and the remainder reflect small modifications made in the design of the rig.

Another check of the load was carried out by a different method illustrated below.



With the bearing floating two forces act in opposition to the gas pressure, the load pressure P and the preload W . To maintain the same position as indicated by a probe on the bottom of the pendulum any decrease in W must be balanced by an increase in P . Thus a direct calibration can be obtained. Calibration checks using this method gave essentially the same results as previously shown.

Considerable attention was given to the motion of the spherical socket in the design and calibration of the test rig. The center of the specimen was to be placed at the exact center of the spherical socket; this would insure a pure rolling motion about the ball specimen. Secondly, the bearing was designed to be extremely stiff to minimize radial motions. It was found that with the bearings floating with the correct lift that the lateral clearance was of the order of .2 mils. Particular attention was also given to the thermal expansions in order that alignment be maintained.

It was desired to obtain a system which gave independent motions in pitch, roll, and yaw; that yielded no motions perpendicular to the plane of the specimens, whose pivot point in yaw was at the center of the contact area, and which had a common axis, for both the top half of the rig containing the ball specimen and the bottom half containing the flat specimens. Actually these conditions were closely approached with two limitations:

1. The alignment would change due to wear and distortion to high temperatures.
2. The push rods added stiffness to the system and some combinations of motion were difficult to obtain.

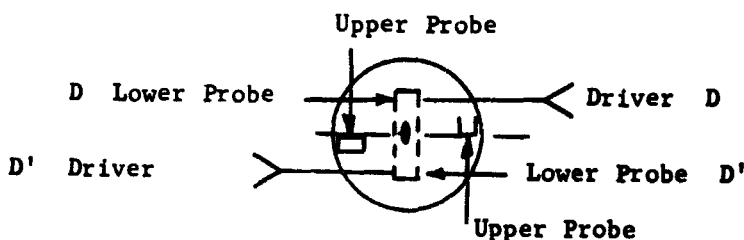
Ideally, it would be desirable to measure the motions inside the rig; this, however, was impossible because of space limitations and because of the high temperatures. Accordingly, it was necessary to check the motions inside the rig to compare with those measured on the pendulum.

Initially only the pitch and yaw drivers were used on the 200 cps calibration

tests. The calibration curve and the location of the probes is shown in Figure 43. These experiments were carried out with only the bottom half of the test rig. This method had some limitation in that the stability of the seat was dependent to a large extent upon the friction of the specimens. However, an independent loading system was devised which simulated this condition. In Figure 43 is shown two input pitch motions at D and D'. The two lines represent what this motion should be at different distances from the pivot point O. Probes were placed at positions A, A', B, B', and (1) and (2). In one case shown here the input motions were 1.76 mils on one driver and 1.8 mils on the other driver. At A and A' motions of .84 were obtained which was essentially the same as that of .86 which would be expected based upon the lever arm distance of .9". No motion could be detected at B and B' in the roll direction.

In order to determine if the spherical socket was pivoting about the center measurements were taken at positions (1) and (2). If motion was pivoting, that at (1) should be less than that at (2). If horizontal motion resulted then (1) and (2) should be equal. As shown in Figure 43, the motions indicate pivoting and the amount is what would be expected based upon the lever arm distance. Thus for two input amplitudes the motions are reproduced at the pivot point.

For yaw motions a different arrangement was necessary as shown below:



Here two small flags were placed in positions A and A' of Figure 43 and observed perpendicular to the line of pitch motion. These probes should give the magnitude of the motion and should be 180° out of phase for yaw motion. The following table shows the motions which were measured in this series of calibrations.

YAW MOTIONS

<u>D</u> <u>Input</u>	<u>D'</u> <u>Input</u>	<u>Predicted Motion</u>	<u>Measured Motion</u>
1.6 mil	2.1 mil	4.3 mil	3.9 mil
.7 mil	.7 mil	1.7 mil	1.5 mil
.5 mil	.6 mil	1.2 mil	1.0 mil

It can be seen that the yaw motions are also reproduced within the accuracy of the measuring techniques.

The calibration at 1000 cps was much more difficult to do because any additional flags added to detect motion, reduced or modified the overall motion. Furthermore unless extreme care was taken the flags themselves would vibrate and give erroneous data. Care also had to be taken that the probes themselves were not in resonance or in motion. Here a series of experiments was run to obtain the desired information. In this case all three drivers were connected and the drive system points epoxied in place.

For the pitch and roll motions measurements were taken at the points A and B shown in Figure 43. These data are shown below. The input motions D_1 , D_2 and D_3 are the motions at the base of the pendulum for each driver.

1000 CPS PITCH AND ROLL MOTION

<u>Input (mil)</u>			<u>Predicted (mil)</u>		<u>Measured (mil)</u>	
D_1	D_2	D_3	A	B	A	B
1.5	1.4	0	.62	0	.70	0
3.2	2.2	0	1.15	0	1.1	0
4.4	3.4	0	1.67	0	1.8	.1
0	0	.7	0	.30	0	.30
0	0	.4	0	.16	0	.20

These calibrations were run with a 20 pound preload on the spherical seat and a 3 pound load on the pivot position. Thus the average total load on the bearing is essentially the same as in the tests. In the tests a 5 pound preload is used with a load of 15 to 30 pounds; the standard condition being 15 pounds. Thus it can be seen that the pitch motions and roll motions induced by the drivers are reproduced at the pivot.

In the 1000 cps tests the yaw motion is applied in conjunction with the pitch motion by setting different amplitudes on D_1 and D_2 , the two pitch drivers. Measurements were taken in the same way as that described for the 200 cps tests. That is with two flags mounted on the surface of the spherical seat on an axis parallel to the pitch motion. Motion is observed 90° to the pitch. Photographs of the scope traces of the driver probes and the measurement probes are shown in Figures 44 and 45. The input motions are apparently sine waves, slightly out of phase of amplitudes 2.9 mil and 1.7 mils. The output motions are distorted waves of amplitudes .16 and .10 mil and "in phase". The phase relationships are correct in prediction of yaw however, the amplitude measured is much smaller than would be predicted if the straight lever arm relationship held. If this were so a 1.2 mil difference in amplitude should give a 1.2 mil motion at a distance of .75 in. rather than the .16 and .10 mil measured. Studies of the motions at various frequencies indicated that the yaw motion was reproduced up to a frequency of 350 cps where it went through a resonance peak; thereafter the amplitude of yaw decreased. Thus the loss of yaw motion was due to operating above the natural frequency of pendulum in torsion. Therefore it was necessary to calibrate for the yaw motion. This calibration of the yaw motion is shown in Figure 46 for 200 cps and 1000 cps.

Thus it was established that the input motions on the pendulum were reproduced above except for the 1000 cps yaw condition. Here it was necessary to calibrate to obtain the correct amplitude of motion.

It was also desired to know the nature of the yaw motion. To determine this a plot was made of the motion of the bottom pendulum plate from the photographs of the two scope traces of the pitch shown in Figure 44. By plotting the position

of each end of the plate at the same time the motion could be determined. A graph of the motion is shown in Figure 47 for an amplitude of 3 mil on one driver and 2 mil on the other driver.

In the figure the dotted line represents the motion in one direction and the solid lines motion in the other. It can be seen that the yaw is not continuous throughout the cycle but comes primarily at the end of the cycle in each direction. The reason for this behavior has not been firmly established but is probably due to the fact that the roll driver gives some restraint to the system. However, the important fact is that the yaw motion is present and it has been found that this motion is transmitted to the contact surface of the spherical socket.

6. Test Procedure

Essentially the same procedure was used for running all the screening tests. The specimens were made to finished dimensions; drawings of the specimens are shown in Figure 48 and 49. Immediately prior to the test the flat specimen was pressed into the holder. The specimen holder, the flat specimen and the ball were then cleaned according to the procedure specified in Table 6. They were then placed in the apparatus and fastened securely. A five pound preload was added and the bearing floated with the desired gas pressure based upon the total load. It was generally set to give a bearing lift of .3 to .5 mil with the combined load and preload. This would mean that the clearance would be something less than .3 mil. The .3 mil would be the clearance change at the bottom of the socket; on the side the clearance would not change. Since the bearing is supported at the bottom the lift could be close to the actual clearance change. The argon atmosphere was then introduced and the temperature controller set to the desired level.

When the temperature had stabilized the desired motions were set on the pendulum. This was done by increasing the power gradually to both drivers until the correct pitch and yaw motions were obtained. The yaw motion was determined by the difference in amplitude of the two drivers; the average of the motion of the two

TABLE 6
NASA SPECIFIED
CLEANING PROCEDURES

- 1) Thoroughly solvent clean the metal surfaces by alternately scrubbing with a solvent-soaked soft cloth and rinsing with a stream of solvent. Repeat procedure with alcohol, then acetone. Avoid the halogenated solvents commonly used in degreasers except as possibly a first step to remove heavy oil or grease. (Hot halogenated solvents can leave residue films that may interfere more with friction measurements than the original contaminants.
- 2) Polish with a paste of water and levigated alumina (very fine polishing grade of aluminum oxide) on a soft cloth. Rinse and repeat several times using a clean area of cloth each time. Final rinse should be with distilled water.
- 3) During final rinse, specimen should pass the "water-wet" test. The distilled water should form a thin film over the entire metal surface. If it does not wet (pulls away from) any area (especially edges) of the specimen, alumina polishing followed by rinsing must be repeated until complete surface is wettable with distilled water.
- 4) Drying may be hastened by blotting the surface with filter paper or by using warm water prior to the final distilled water rinse. The latter method warms the metal surface and promotes rapid evaporation. It is important that distilled water be used in final rinse to avoid formation of water "marks" of mineral deposits on the polished metal.
- 5) If specimens are stored after cleaning, they should be kept in an evaporated chamber such as a vacuum desiccator.

General Note:

Contamination with oils from the hands must be avoided by wearing rubber gloves or by handling specimen only with tongs. (Oils from the skin are highly polar organic materials that are strongly absorbed on metal surfaces.)

drivers determined the pitch. After these motions were set the roll motion was increased to the desired level. The test was then run for a period of 12 hours. It was started at approximately 4 P.M., the motions monitored til 5 P.M. and then run until 4 A.M., where it was timed to shut down. The automatic shut down stopped the motions and turned off the heaters. The argon flow was maintained and manually shut off when temperatures reached approximately 200°F. The test rig was then disassembled; the specimens removed and inspected for damage. Photographs were made of the specimens to indicate the damaged areas. If there were no damage the specimens were set aside for reuse after relapping; if there were damage they were reground to a depth of 10 mils if reused.

When the tests using shaped sockets were run it was necessary to insure alignment. This had been, of course, not critical with the ball on flat combination. It was found that with time of operation, at high temperatures, certain distortions and wear would take place which would modify the original alignment. Thus it was necessary to find a method to align each test immediately prior to each run. Several methods were attempted. The one found most suitable was to mount a gage in the top of the rig which could detect the vertical displacement of the ball holder and stem. The bearing was floated and the load applied. By moving the top half of the rig the point of optimum alignment could be easily detected as the lowest point in the indicator as the ball rested lower in the socket. The rig halves were then bolted in this position. This technique also allowed the load to be calibrated for each test. This method will not eliminate thermal distortions; however, the rig was designed to minimize this effect. Although considerable effort has been expended to align the specimens there is no assurance that such alignment will take place in an actual tilting-pad pivot. For other tests longer running times were used; the set-up procedure however remained the same. Monitoring of these tests was done several times a day.

IX. OUTLINE OF RESULTS

During the course of this investigation a large number of tests were run. A complete list of the tests is given in Table 7. They have been divided into the following categories:

<u>SECTION</u>	<u>TEST</u>	<u>PURPOSE</u>	<u>TIME(hrs)</u>
X	Material Screening	Select Materials and Shapes	12
XI	Air & Forming Gas Tests	Effect of Atmosphere	12
XII	Long Term Tests	Effect of Time	100,2000
XIII	Lubricant Tests	Effect of Solid Film Coating	100
XIV	Special Design Tests	Evaluation of Special Shapes	
	(a) WC vs Sprayed WC		117
	(b) Sapphire vs WC		100
	(c) BRU Design		100
XV	1000 hour BRU Test	Effect of Time with Conforming Radius	1000

The results for these tests are discussed in the following sections.

As will be noted from the table the effects of almost all the variables were studied, that is, materials, shape, frequency, load, amplitude, time, and temperature. Since little damage resulted however, most of the later evaluations were made under the most severe conditions of operation, that is high temperatures, large amplitudes and high frequencies. In all the tests the 1/2" ball was used as a test specimen.

X. MATERIAL SCREENING TESTS

The purpose of this phase of the investigation was two fold: first it was desired to determine those operating conditions which induced damage, secondly it was desired to screen a number of materials which could reasonably be considered for pivots. In accordance with this approach, tests were first run under the least severe operating conditions, that is 200 cps, low amplitude of motion and low temperature. Since very little damage was noted as conditions became more severe, the screening tests were eventually run under the most severe conditions required. A large number of tests were run at various operating conditions. From these a number were selected for discussion which best illustrate the effect of several variables. These are described in the following section.

1. Preliminary Tests with M-2 Tool Steel

a. Pure Pitch

The initial tests were run with hardened M-2 tool steel, 80°F, in pure pitch at 200 cps. The geometry used in all the tests was a 1/2" diameter ball loaded against a flat. A series of tests was run at three loads and three amplitudes. The conditions as well as the figure numbers of photographs of the damage are shown below:

<u>Amplitude</u>	<u>Load</u>		
	<u>2#</u>	<u>15#</u>	<u>30#</u>
.6 mil	-	Fig. 51a	Fig. 52a
1.2 mil	Fig. 50 a	Fig. 51b	Fig. 52b
1.7 mil	Fig. 50 b	Fig. 51c	Fig. 52c

Photographs of both the ball and the flat are shown

No test was run under the 2# load .6 mil amplitude condition.

It can be seen that in all cases the damage consisted of a small darkened ring as would be expected based upon the micro slip concepts (8). A surface profile trace

across the diameter of the ring pattern is shown in Figure 53a. A diameter of this particular ring was 8 mils. No wear or surface damage is evident. The ring itself is approximately .01 mil in height and .4 mil in width. The composition of the ring was not identified chemically. It was presumed and appeared to be oxide. Although there was an argon atmosphere, the argon contains several parts per million of oxygen or carbon dioxide. At the flow rate of the argon this would be sufficient to produce oxidation.

While the ring patterns were somewhat irregular, it is clear that there is no significant difference in the width of the rings as a function of either amplitude or load. There were two important characteristics which should be noted: the diameter of the rings increased with load and secondly the ball and flat photographs are mirror images of each other. This can best be seen in Figure 51c where the ring bulges out in several areas, in Figure 52a where the ring is broader on one side than on the other and in Figure 52b where a scratch on the flat is evident on the ring of the ball. In examining photographs of almost all tests, this conclusion was firmly established. The fact that they are mirror images indicates that the slippage is extremely small, that there are no gross motions, and that the damage is insignificant or it would obliterate the points of similarity.

The increase in the size of the rings with increased load would be expected based on elastic contact theory. Measurements were made of the ring diameters where there was a definite pattern. The measured radius is compared with predicted areas based upon the Hertz equation in Figure 54. Although there are differences in several points the agreement is as good as could be expected.

Thus it can be seen that under the maximum conditions of load and amplitude at 200 cps there was no significant surface damage. The investigation was then directed to investigate the effect of other variables.

TABLE 7
TEST RESULTS

Ball Vs. Flat - 12 Hours - Screening Test

Test No.	Material	Temp. (°F)	Frequency (cps)	Load (lbs)	Amplitude (mils) P + R + Y (inch)	Test Rig
2-3	M2 vs. M2	80	200	15	.5	1
2-4	M2 vs. M2	80	200	15	1.0	1
2-5	M2 vs. M2	80	200	15	1.5	1
2-6	M2 vs. M2	80	200	15	.5	1
2-7	M2 vs. M2	80	200	15	1.5	1
2-8	M2 vs. M2	80	200	15	1.0	1
4-21B	M2 vs. M2	80	200	2	1.0	2
4-22A	M2 vs. M2	80	200	30	.0005	2
4-22B	M2 vs. M2	80	200	30	.001	2
4-24	M2 vs. M2	80	200	30	1.5	2
4-24X	M2 vs. M2	80	200	2	1.5	2
4-38	M2 vs. M2	1000	200	15	1.0	1
3-15	M2 vs. M2	80	200	15	1.0 & .5	1
M-38	M2 vs. M2	1000	1000	15	1.5 + .5 + .25	1
M-42	M2 vs. M2	1000	1000	15	1.5 + .5 + .25	2
M-43	M2 vs. M2	400	1000	15	1.5 + .5 + .25	3
M-45	M2 vs. M2	1000	1000	15	1.5 + .5 + .25	3
PHT-3	M2 vs. M2	1000	200	15	1.0	1
PY-1	M2 vs. M2	80	200	15	.5 + .1	2
PY-2	M2 vs. M2	80	200	15	1.0 + .1	2
PY-3	M2 vs. M2	80	200	15	1.5 + .15	2
PY-4	M2 vs. M2	80	200	15	1.5 + .5	2
PR-1	M2 vs. M2	400	1000	15	.5 + .5	2
PR-2	M2 vs. M2	80	1000	15	1.0 + .5	2
Y-1	M2 vs. M2	80	200	15	1.0	2
Y-2	M2 vs. M2	80	200	30	1.0	2
Y-3	M2 vs. M2	80	200	15	.5	1
Y-4	M2 vs. M2	80	200	15	.5	1
YHT-1	M2 vs. M2	1000	200	15	1.0	1
PRY-1	M2 vs. M2	400	200	15	1.5 + .5 + .25	1
PRY-2	M2 vs. M2	400	1000	15	1.5 + .5 + .25	2
PRY-3	M2 vs. M2	80	1000	15	1.5 + .5 + .25	2
PRY-4	M2 vs. M2	400	1000	2	1.5 + .5 + .25	2
PRY-5	M2 vs. M2	400	1000	30	1.5 + .5	2
PRY-7	M2 vs. M2	400	1000	30	1.5 + .5 + .25	2
PRY-8	M2 vs. M2	300	1000	15	1.5 + .5 + .25	1
P-19	M2 vs. M2	80	1000	15	1.0	2
P-20	M2 vs. M2	80	1000	15	1.0	2
P-22	M2 vs. M2	80	1000	15	1.5	1
P-24	M2 vs. M2	80	1000	15	1.5	1
P-26	M2 vs. M2	80	1000	15	.5	1

Test No.	Material	Temp. (°F)	Frequency (cps)	Load (lbs)	Amplitude (mils) P + R + Y inch	Test Rig
P-29	M2 vs. M2	80	1000	30	1.5	2
P-30	M2 vs. M2	400	1000	30	1.5	2
P-25	M2 vs. M2	80	1000	15	1.5	2
4-29	KB162B vs. KB162B	80	200	2	.5	2
4-29B	KB162B vs. KB162B	80	200	15	1.0	2
4-29C	KB162B vs. KB162B	80	200	15	1.5	2
4-30	KB162B vs. KB162B	80	200	15	.5	2
4-46	KB162B vs. KB162B	1000	200	15	.5	1
4-46B	KB162B vs. KB162B	1400	200	15	1.0	1
4-46C	KB162B vs. KB162B	1000	200	15	1.0	1
4-46D	KB162B vs. KB162B	1000	200	15	1.5	1
4-47	KB162B vs. KB162B	1000	200	30	1.0	1
4-34B	KB162B vs. KB162B	80	200	30	1.0	2
PHT-1	KB162B vs. KB162B	1400	200	15	1.5	1
PHT-2	KB162B vs. KB162B	1000	200	15	1.5	1
PHT-4	KB162B vs. KB162B	1000	200	30	1.5	1
P-18	KB162B vs. KB162B	80	200	30	1.5	2
P-21	KB162B vs. KB162B	400	1000	15	1.0	2
P-23	KB162B vs. KB162B	400	1000	15	1.5	2
P-27	KB162B vs. KB162B	80	1000	15	1.5	1
P-28	KB162B vs. KB162B	400	1000	30	1.5	2
PRY-6	KB162B vs. KB162B	400	1000	30	1.5 + .5 + .25	2
YHT-2	KB162B vs. KB162B	1000	200	15	1.0	1
M-2	KB162B vs. KB162B	400	200	15	1.0	2
M-34	KB162B vs. KB162B	1000	1000	15	1.5 + .5 + .25	1
M-36	KB162B vs. KB162B	1400	1000	15	1.5 + .5 + .25	1

Test No.	Material	Temp. (°F)	Frequency (cps)	Load (lbs)	Amplitude (mils) P + R + Y (inch)	Test Rig
M-37	KB162B vs.					
	KB162B	80	1000	15	1.5 + .5 + .25	2
M-1	STEL.6B vs.					
	STEL.6B	1000	200	15	1.0	1
M-3	STEL.6B vs.					
	STEL.6B	1000	200	15	1.0	1
M-4	STEL.6B vs.					
	STEL.6B	400	200	15	1.0	2
M-4B	STEL.6B vs.					
	STEL.6B	400	200	15	1.0	2
M-18	STEL.6 vs.					
	STEL.6	400	1000	15	1.5 + .5 + .25	2
M-19	STEL.6 vs.					
	STEL.6	1000	Ball Turned In Holder			1
M-5	K162B vs.					
	C608	1200	200	15	1.0	1
M-6	K162B vs.					
	C608	400	200	15	1.0	2
M-7	K162B vs.					
	C608	1400	200	15	1.0	1
M-14	K162B vs.					
	C608	400	1000	15	1.5 + .5 + .25	1
M-16	K162B vs.					
	C608	400	1000	15	1.5 + .5 + .25	2
M-17	K162B vs.					
	C608	1000	1000	15	1.5 + .5 + .25	1
M-8	440C vs. 440C	400	1000	15	1.5 + .5 + .25	1
M-21	440C vs. 440C	1000	1000	15	1.5 + .5 + .25	1
M-9	H.P.AL203 vs.					
	C.P.AL203	400	1000	15	1.5 + .5 + .25	2
M-10	52100CAS vs.					
	52100CAS	400	1000	15	1.5 + .5 + .25	2
M-10B	52100CAS vs.					
	52100CAS*	400	1000	15	1.5 + .5 + .25	2
M-15	STARJ Vs.					
	STELLITE 19	400	1000	15	1.5 + .5 + .25	1
M-27	STARJ vs.					
	STELLITE 19	1400	1000	15	1.5 + .5 + .25	1
M-30	STARJ vs.					
	STELLITE 19	1000	1000	15	1.5 + .5 + .25	1
M-31	STARJ vs.					
	STELLITE 19	1400	1000	15	1.5 + .5 + .25	1
M-20	M-50TS vs.					
	M-50TS	400	1000	15	1.5 + .5	2
M-25	44A vs. LWIN 40	1000	1000	15	1.5 + .5 + .25	1
M-26	44A vs. LWIN 40	400	1000	15	1.5 + .5 + .25	2
M-33	44A vs. LWIN 40	1000	1000	15	1.5 + .5 + .25	1
M-35	44A vs. LWIN 40	400	1000	15	1.5 + .5 + .25	2
M-46	44A vs. LWIN 40	1000	1000	15	1.5 + .5 + .25	4

Test No.	Material	Temp. (°F)	Frequency (cps)	Load (lbs)	Amplitude (mils) P + R + Y / inch	Test Rig
M-23	HPAL203 vs. HPAL203	1000	1000	15	1.5 + .5 + .25	1
M-24	HPAL203 vs. HPAL203	400	1000	15	1.5 + .5 + .25	2
M-29	HPAL203 vs. HPAL203	1400	1000	15	1.5 + .5 + .25	1
M-39	HPAL203 vs. HPAL203	1000	1000	15	1.5 + .5 + .25	1
M-11	44A vs. 44A	400	1000	15	1.5 + .5 + .25	2
M-22	CPAL203 vs. CPAL203	400	1000	15	1.5 + .5 + .25	2
M-40	CPAL203 vs. CPAL203	1000	1000	15	1.5 + .5 + .25	1
M-13	STEL6 vs. STEL19	400	1000	15	1.5 + .5 + .25	2
P-31	M2 vs. K162B	80	1000	15	1.0	2

<

Shape Test - 12 Hours - Screening Test

Test No.	Material	Temperature	Frequency	Load	Amplitude $\left(\frac{\text{mils}}{\text{inch}}\right)$ P + R + Y	Test Rig	Pivot Shape	Socket Shape
SS-1	M2 vs. M2	400° F	1000 cps	15 lbs	1.5 + .5 + .25	3	.250"SP R	.256"SP. R.
SS-2	M2 vs. M2	400	1000	15	1.5 + .5 + .25	3	.250	.256 SP. R.
SS-6	M2 vs. M2	400	1000	15	1.5 + .5 + .25	4	.250	.256 SP. R.
SS-7	M2 vs. M2	400	1000	15	1.5 + .5 + .25	2	.250	.256 SP. R.
SS-12	M2 vs. M2	1000	1000	15	1.5 + .5 + .25	4	.250	.256 SP. R.
SS-13	M2 vs. M2	1000	1000	15	1.5 # .5 + .25	3	.250	.256 SP. R.
SS-14	M2 vs. M2	400	--	15	-----	3	.250	.256 SP. R.
SS-16	M2 vs. M2	1000	--	15	-----	3	.250	.256 SP. R.
SS-19	M2 vs. M2	400	1000	--	-----	5	.250	.256 SP. R.
SS-5	M2 vs. M2	400	1000	15	1.5 + .5 + .25	3	.250	.375 SP. R.
SS-8	M2 vs. M2	400	1000	15	1.5 + .5 + .25	4	.250	.375 SP. R.
SS-11	M2 vs. M2	1000	1000	15	1.5 + .5 + .25	3	.250	.375 SP. R.
SS-15	M2 vs. M2	400	--	15	-----	4	.250	.375 SP. R.
SS-23	K162B vs. K162B	1000	1000	15	1.5 + .5 + .25	4	.250	.375 SP. R.
SS-22	M2 vs. M2	900	1000	15	1.5 + .5 + .25	5	.250	.375 SP. R.
SS-21	M2 vs. M2	400	1000	15	1.5 + .5 + .25	6	.250	.375 SP. R.
SS-3	M2 vs. M2	400	1000	15	1.5 + .5 + .25	3	.250	.750 SP. R.
SS-4	M2 vs. M2	400	1000	15	1.5 + .5 + .25	3	.250	.750 SP. R.
SS-9	M2 vs. M2	400	1000	15	1.5 + .5 + .25	2	.250	.750 SP. R.
SS-10	M2 vs. M2	400	1000	15	1.5 + .5 + .25	2	.250	.750 SP. R.
SS-17	M2 vs. M2	1000	--	--	-----	4	.250	.750 SP. R.
SS-20	M2 vs. M2	400	--	--	-----	5	.250	.750 SP. R.
CS-1	M2 vs. M2	400	1000	15	1.5 + .5 + .25	3	.250	.256 CLY. R
CS-2	M2 vs. M2	400	1000	15	1.5 + .5 + .25	4	.250	.750 CLY. R
CS-3	M2 vs. M2	400	--	15	-----	2	.250	.256 CLY. R
CS-4	M2 vs. M2	400	--	15	-----	5	.250	.750 CLY. R
CS-5	M2 vs. M2	1000	1000	15	1.5 + .5 + .25	3	.250	.256 CLY. R

Forming Gas Tests - 12 Hours

Test No.	Material	Temperature	Frequency	Load	Amplitude (mils/inch)	Test Rig	Pivot Shape	Socket Shape
FG 1	M2 vs. M2	500°F	100 cps	15lbs	1.5 + .5 + .25	6	.250"SP.R.	
FG 2	M2 vs. M2	900	1000	15	1.5 + .5 + .25	6	.250	
FG 3	K162B vs. K162B	500	1000	15	1.5 + .5 + .25	6	.250	
FG 4	K162B vs. K162B	900	1000	15	1.5 # .5 # .25	6	.250	
FG 5	STARJ vs. STEL. 19	500	1000	15	1.5 + .5 + .25	6	.250	
FG 6	STARJ vs. STEL. 19	900	1000	15	1.5 + .5 + .25	6	.250	
FG 4A	K162B vs. K162B	900	1000	15	1.5 + .5 + .25	6	.250	
FG 7	M2 vs. M2	500	1000	15	1.5 + .5 + .25	5	.250	.375"SP. R.
FG 8	M2 vs. M2	900	1000	15	1.5 + .5 + .25	5	.250	.375 SP. R.
FG 9	K162B vs. K162B	500	1000	15	1.5 + .5 + .25	5	.250	.375 SP. R.
FG 10	K162B vs. K162B	900	1000	15	1.5 + .5 + .25	5	.250	.375 SP. R.
FG 11	STAR J vs. STEL. 19	500	1000	15	1.5 + .5 + .25	5	.250	.375 SP. R.
FG 12	STAR J vs. STEL. 19	900	1000	15	1.5 + .5 + .25	5	.250	.375 SP. R.
Air Test - 12 hours								
AT 1	M2 vs. M2	500	1000	15	1.5 + .5 + .25	5	.250	.375 SP. R.
AT 3	M2 vs. M2	900	1000	15	1.5 + .5 + .25	5	.250	.375 SP. R.
AT 2	M2 vs. M2	500	1000	15	1.5 + .5 + .25	6	.250	
AT 4	M2 vs. M2	900	1000	15	1.5 + .5 + .25	6	.250	

Long Term Test

Time	Material	Temperature	Frequency	Load	Amplitude (mils) inch	Test Rig	Pivot Shape	Socket Shape
100 Hrs.	M2 vs. M2	400°F	200 cps	15 lbs	1.0	2		
100 Hrs.	K162B vs. K162B	1000	200	15	1.0	1		
1345 Hrs.	K162B vs. K162B	900	1000	15	1.5 + .5 + .25	5	.250 "SP.R.	
2000 Hrs.	K162B vs. K162B	900	1000	15	1.5 + .5 + .25	1	.250	.750 "SP.R.
2000 Hrs.	K162B vs. K162B	900	1000	15	1.5 + .5 + .25	3	.250	.256
2000 Hrs.	K162B vs. K162B	900	1000	15	1.5 + .5 + .25	2	.250	.256
1950 Hrs.	M2 vs. M2	900	1000	15	1.5 + .5 + .25	4	.250	.750
1105 Hrs.	M2 vs. M2	900	1000	15	1.5 + .5 + .25	5	.250	.256
1105 Hrs.	M2 vs. M2	900	1000	15	1.5 + .5 + .25	6	.250	.256
2000 Hrs.	M2 vs. M2	900	1000	15	1.5 + .5 + .25	4	.250	.256
1950 Hrs.	STAR J vs. STEL. 19	900	1000	15	1.5 # .5 # .25	1	.250	.750
1950 Hrs.	STAR J vs. STEL. 19	900	1000	15	1.5 + .5 + .25	3	.250	.256
1950 Hrs.	STAR J vs. STEL. 19	900	1000	15	1.5 + .5 + .25	2	.250	.256
1950 Hrs.	M2 vs. A-286	900	1000	15	1.5 + .5 + .25	6	.250	.256

Lubricant Tests - 100 Hour Test - M2 Tool Steel

Test No.	Solid Film Lube.	Temperature	Frequency	Load	Amplitude	(mils) Test inch Rtg	Pivot Shape	Socket Shape
SFL 2	None	500°F	1000 cps	15 lbs	1.5+.5+.25	6	.250 "SP.R.	.375 "SP.R.
SFL 4	None	900	1000	15	1.5+.5+.25	6	.250	.375
SFL 5	Fused Fluoride	500	1000	15	1.5+.5+.25	6	.250	.375
SFL 6	None	500	1000	15	1.5+.5+.25	5	.250	.375
SFL 7	Fused Fluoride	900	1000	15	1.5+.5+.25	5	.250	.375
SFL 8	None	900	1000	15	1.5+.5+.25	5	.250	.375
SFL 1	MoS ₂	500	1000	15	1.5+.5+.25	6	.250	.375
SFL 3	MoS ₂	900	1000	15	1.5+.5+.25	5	.250	.375

Test No.	Material	Temperature	Hours	Load	Amplitude		Rig	Test	Pivot Shape	Socket Shape
					(mils)	Inch				
001	WC vs. Sprayed WC	95°F	117-1/4	15lbs	1.5+	.5+.25	6		.250"SP.R.	.250"SP.R.
002	WC vs. Sprayed WC	490	117-1/4	15	1.5+	.5+.25	6		.250	.250
003	WC vs. Sprayed WC	490	16	15	1.5+	.5+.25	5		.250	.250
003	WC vs. Sprayed WC	480	117-1/4	15	1.5+	.5+.25	5		.250	.250
004	WC vs. Sprayed WC	500	16	15	1.5+	.5+.25	6		.250	.250
005	WC vs. Sprayed WC	95	117-1/4	15	1.5+	.5+.25	5		.250	.250

Non-Conforming Radius, Set E, Sapphire Pivot Tungsten Carbide Socket

1	Sapphire vs. WC	500	100	15	1.5+	.5+.25	1		.375	.500
2	Sapphire vs. WC	500	100	15	1.5+	.5+.25	1		.375	.500
3	Sapphire vs. WC	500	100	15	1.5+	.5+.25	1		.375	.500
4	Sapphire vs. WC	500	100	15	1.5+	.5+.25	1		.375	.500

Conforming Radius - Set A - Sapphire Pivot Tungsten Carbide Socket

A	Sapphire vs. WC	500	100	15	1.5+	.5+.25	2			
B	Sapphire vs. WC	500	100	15	1.5+	.5+.25	2			
C	Sapphire vs. WC	500	100	15	1.5+	.5+.25	2			
D	Sapphire vs. WC	500	100	15	1.5+	.5+.25	2			

Test No.	Material	Temperature	Hours	Load	Amplitude ^(mils) in./h	Rig	Test	Pivot Shape	Socket Shape
8X115	W Carbide	500°F	100	151bs	1.5+.5+.25	1	1	.25"SP.R.	.25"SP.R.
8X113	W Carbide	500	100	15	1.5+.5+.25	1	1	.25	.25
Ser. #3	M2 vs. M2	500	100	15	1.5+.5+.25	1	1	.25	.25
Ser. #2	M2 vs. M2	500	100	15	1.5+.5+.25	1	1	.25	.25
8X111	W Carbide	500	100	15	1.5+.5+.25	2	2	.25	.25
8X114	W Carbide	500	100	15	1.5+.5+.25	2	2	.25	.25
Ser. #5	M2 vs. M2	500	100	15	1.5+.5+.25	2	2	.25	.25
Ser #1 & 4	M2 vs. M2	500	100	15	1.5+.5+.25	2	2	.25	.25

b. Pure Yaw

The second variable investigated was that of pure yaw. The tests were run with M-2 tool steel, 80°F, 15# load and 200 cps, the same as the previous tests. The initial test was run with a yaw motion of 1.6 mils/inch of radius. Under these conditions no damage resulted as shown in Figure 55a. Only the flat surface is shown since the ball surface looks exactly the same. Since no damage was observed the exact same test was run with the amplitude of yaw motion increased to 3.2 mil/inch. Two tests were run 15# load and 30# load. Photographs of the flat specimens are shown in Figures 55b and c. Indications of damage are apparent at this amplitude. A test at 1000°F also gave the same result. A photograph at a higher magnification is shown in Figure 56. Tearing of the material and metal transfer is evident. A surface profile trace is shown in Figure 53b. The area of contact has remained essentially the same. Wear is evident to a depth of .04 mil. In 10,000 hours, the required pivot life wear would be excessive. It would be desirable to know at what yaw amplitude between 1.6 mil/inch and 3.2 mil/inch damage began. However, because this amount of motion is approximately ten times that which would be expected in a bearing pivot further consideration was not given to the damage in pure yaw.

c. Combined Motions

Tests were run with M-2 tool steel at 200 cps with a load of 15 pounds to determine the effect of combined motions. The following tests at the maximum conditions of motion illustrate the results.

<u>Pitch</u>	<u>Motion</u> <u>Roll</u>	<u>Yaw</u>	<u>Temperature</u>	<u>Damage on Flat</u>
1.7 $\frac{\text{mil}}{\text{inch}}$.59 $\frac{\text{mil}}{\text{inch}}$	0	400°F	Fig. 57a
1.7 $\frac{\text{mil}}{\text{inch}}$	0	.48 $\frac{\text{mil}}{\text{inch}}$	80°F	Fig. 57b
1.7 $\frac{\text{mil}}{\text{inch}}$.59 $\frac{\text{mil}}{\text{inch}}$.48 $\frac{\text{mil}}{\text{inch}}$	400°F	Fig. 57c

Although the width of the rings varied it can be seen that there is no significant difference with the combinations of motions and that the total damage is insignificant during the course of the 12 hour test.

d. Elevated Temperature and 1000 cps Tests

Attention was directed to the effect of higher frequency and high temperatures, the maximum limits being 1000 cps and 1400°F. Photographs of the 1000 cps test in pure pitch of 1.7 mil/inch are shown in Figures 58a and 58b for 15# and 30# loads, respectively. By comparing these photographs with those of Figures 51c and 52c, it can be seen that there is no significant increase in surface damage. In Figures 59a and 59c is shown the damage with M-2 tool steel, 15# load, 1000 cps, 1.7 $\frac{\text{mil}}{\text{inch}}$ pitch, at three temperatures, 80°F, 400°F and 1000°F. It can be seen that at 1000 cps the damage pattern is essentially the same as at 200 cps. Increasing the temperature did not change this behavior significantly except that at 1000°F there was evidence of metal transfer. This damage was small and hard to separate from the buildup of surface oxide. An overall photograph of the damaged areas for the 1000°F, 1000 cps test is shown in Figure 60. Although there is damage on a micro scale, it is doubtful that this could interfere with the operation of the pivot.

Thus it has been concluded that even with the maximum conditions of frequency, amplitude, load, and temperature expected in a pivot that the amount of damage is insignificant for M-2 tool steel during the course of a 12 hour test.

2. Preliminary Test with Carbide (K162B)

A similar series of tests was conducted with a nickel bonded titanium carbide. The conditions of these tests and photographs of the ball and flat surfaces for pure pitch motion at 200 cps are listed on the following page.

<u>Amplitude</u>	<u>80°F</u>			<u>1000°F</u>			<u>1400°F</u>		
	<u>2#</u>	<u>15#</u>	<u>30#</u>	<u>2#</u>	<u>15#</u>	<u>30#</u>	<u>2#</u>	<u>15#</u>	<u>30#</u>
.59 $\frac{\text{mil}}{\text{inch}}$	61a	62a	-	-	64a	-	-	-	-
1.2 $\frac{\text{mil}}{\text{inch}}$	-	62b	63b	-	64b	65b	-	66b	-
1.7 $\frac{\text{mil}}{\text{inch}}$	-	62c	-	-	64c	65c	-	67c	-

A photograph of the 1000 cps at the maximum amplitude at 400°F is shown in Fig. 68a for 15# load and 68b for 30# load.

From these photographs it is clear that the same conclusion can be drawn as for the M-2 tool steel. Although the nature of the surface traces change at higher temperatures, there is no significant damage; the motion has primarily a polishing effect on the surface.

A photograph of the ball and flat area of K162B run with pure yaw of 3.2 $\frac{\text{mil}}{\text{inch}}$ at 200 cps, 15# load and 1000°F is shown in Fig. 69. Even with this amount of yaw no surface damage is observed as was found for M-2 under identical conditions. Thus it has been concluded that even with the most severe operating conditions no damage is observed with K162B in the 12 hour test.

3. Conditions where Damage Occurs

It was found in the previous tests that the only severe damage occurred when the amount of yaw motion was 3.2 mil/inch of radius for tool steel. However, due to unusual operating conditions some other forms of damage were detected.

a. Damage from Impact Loading

When tests were first run at 1000 cps it was found that under a particular set of conditions of load and gas bearing pressure, hammer resulted in the

vertical direction. This condition resulted in a dynamic load between the ball and the flat at a frequency of 1000 cps. The vertical motion of the ball was approximately 1.2 mils, however, the relative motion between the ball and the flat could not be determined. Thus, it was not known if separation occurred. However, the extent of the damage was large. Photographs of the surface of the M-2 tool steel and the K162 ball and flat are shown in Fig. 70. It can be seen that the damage area is three times the normal size and is much more severe than that encountered in pure yaw. A surface profile trace of the M-2 tool steel is also shown in Fig. 53c. The depth of the damage is 1.5 mils, this is very much greater than that which was found in pure yaw. The mean normal stress was 286,000 psi and the number of cycles was 432×10^6 . From these results it is obvious that this is a condition which must be avoided. The main question is the extent of dynamic load in gas bearing machinery. Load variations will occur to the extent of 50 percent variation about a static load due to misalignment. Here no separation will occur. If the stress and the stress variations are kept low then based on bulk fatigue behavior, adequate life would undoubtedly result. However, minimizing the load increases the probability of slippage and separation. Also, fatigue failures occur much more readily at the surface. Southwest Research(3-5) have reported some dynamic load data at 25 KC. Severe damage was found after 30×10^6 cycles at $\frac{\sigma_{max}}{\sigma_{min}}$ of 750,000 psi / 460,000 psi. Although this is a higher stress level and variation than would be used in a pivot, the required life of a pivot is much longer, that is 3.6×10^{10} cycles. Clearly more data is needed to understand the severity of this problem.

During normal operation separation is unlikely in a properly designed pivot because of the preload; but it can occur for example, if the system were subjected to high "g" forces in "lift-off" or start-up. The duration of the motion need not be long, for damage to be incurred, as some simple bench tests have shown. More information is also needed to better understand the load conditions where damage will occur from separation. Because of this condition the dynamic load rig was designed for subsequent evaluations.

b. Sliding

Another type of severe damage occurred when one of the specimens was free to rotate. Occasionally, because of the differential thermal expansion of the specimens and their holders and because of forces due to surface damage, one of the specimens would be free to move during the test. Under these conditions much more damage and wear would result presumably from the sliding action. Photographs of the surfaces of such a test are shown in Fig. 7, for tool steel at 400°F. Although these tests were run at the most severe conditions of motion and load, damage would also occur under less severe conditions. Although it is unlikely that such sliding motions would occur in a bearing pivot, these tests do illustrate what can happen if these conditions do exist.

4. Material Screening

From the previous tests it was concluded that little damage would result from short term operation with M-2 tool steel and K162B under the most severe conditions of operation. Although these are suitable materials, it was desired to evaluate the other material combinations which might be used for certain applications. The approach used in running these tests was to screen the materials for damage at 400°F. For those materials which appeared promising at that temperature successively higher temperatures were used. The test conditions for all tests were the following:

frequency	-	1000 cps
load	-	15 pounds
pitch motion	-	1.7 mil/inch
roll motion	-	.59 mil/inch
yaw motion	-	.25 mil/inch
atmosphere	-	argon
time	-	12 hours

The following materials were tested. The figure numbers relate to photographs of the flat specimen. The damage to the ball specimen is essentially the same.

TABLE OF MATERIAL SCREENING TESTS

<u>Material Combination</u>		<u>Figure Number</u>		
<u>Flat</u>	<u>Ball</u>	<u>400°F</u>	<u>1000°F</u>	<u>1400°F</u>
M-2 Tool Steel	M-2 Tool Steel	59b	59c	
Stellite 6B	Stellite 6B	72a		
440C Stainless	440C Stainless	72b		
SAE 52100 Steel	SAE 52100 Steel (annealed)	72c		
SAE 52100 Steel	SAE 52100 Steel	72d		
Stellite 6B	Stellite 19	72e		
Stellite Star J	Stellite 19	72f	75b	77a
K162B Carbide	C608 Carbide	73a		
K96 Carbide	K96 Carbide	73b		
K162B Carbide	K162B Carbide	73c	75a	77b
Hot Pressed Al_2O_3	*Cemented Oxide	74a		
Hot Pressed Al_2O_3	- Hot Pressed Al_2O_3	74b	75d	
Cold Pressed Al_2O_3	- Cold Pressed Al_2O_3	74c	75c	
K96 Carbide	- Sprayed WC	74d	76	

In general the results were similar to that found for M-2 tool steel and K162B carbide. At 400°F indentations resulted with the Stellite 6 and the annealed SAE 52100 steel. This resulted in a larger area of contact and in some cases an oblong shape (Fig. 72c). Of the metals the 440C stainless steel gave somewhat more damage than the others. For the carbides the damage was less severe than the metals. Satisfactory performance was obtained with tungsten carbide (K96), titanium carbide (K162B) and chrome carbide (C608). For the ceramic materials excellent results were obtained with the cemented oxide (Fig. 74a) and the hot pressed Al_2O_3 (Fig. 74b). With the cold pressed Al_2O_3 there was evidence of fracture in the contact area consisting of large pits (74c). With the flame sprayed coating there was considerable damage. From a microscopic examination of the surface it was concluded that the coating came off the

* Bonded aluminum oxide

surface and remained attached to the ball. The age in the center of Fig. 74d represents damage to the underlying surface.

Six of these material combinations were selected for 1000°F testing under the same conditions as previously listed. Those materials and the figures of the damage are listed in the previous table.

At 1000°F the M-2 tool steel flat (Fig. 59c) showed a shiny metallic portion at the center. It appeared as if some metal transfer had resulted, however, this was extremely difficult to determine within such a small contact area. There was clearly more damage than resulted at the lower temperatures; longer term tests are necessary to determine if serious damage would result at this temperature.

The K162B carbide and the Stellite Star J - Stellite 19 combination appeared to give essentially the same results at 1000°F as they did at the lower temperatures. (Figures 75a and 75b). No damage resulted; the surface merely had a polished appearance.

Both the cold pressed and the hot pressed Al_2O_3 showed fracture damage at 1000°F (Figures 74c and 74d). The damage was more severe in the case of the cold pressed than with the hot pressed Al_2O_3 . Because of these results, and the effective results with carbides and metals, further consideration was not given to ceramic materials.

A test was also run with the WC (K96) flame spray WC coating at 1000°F. It was apparent that the coating had worn through (Fig. 76a) or removed from the A-286 flat and had adhered to the ball specimen. Damage with this combination was severe.

Because of the promising results with the K162B carbide and the Stellite Star J - Stellite 19 these combinations were run at 1400°F. Photographs of the surfaces of the ball and flat are shown in Figure 77a for the Stellite and 77b for the carbide. No damage could be detected with either combination.

From these short term tests, it can be seen that under the conditions which simulate tilting pad pivots that M-2 tool steel performed without damage to 1000°F and the K162B carbide and the Stellite Star J - Stellite 19 combination performed satisfactorily to 1400°F. Since it was desired to select two or three materials, these seemed more than adequate to fulfill the requirements of most applications. Further attention was then directed to the effect of several shapes. This is described in the following section.

5. Effect of Shape

With the materials selected it was desired to know if the use of specimens with more conforming radii would significantly effect the damage. Test specimens of M-2 tool steel spherical sockets were manufactured with radii of .256 in., .375 in., and .750 in.; cylindrical sockets of .256 in., and .750 in., were also made. These were run with the .250 in. radius ball and 15# load. The motions imparted were the same as those used in the material screening tests.

a. Tests with .256 Radius Socket

A total of 5 tests were run with the .256 socket at 400°F and 3 tests were run at 1000°F. Two types of behavior resulted regardless of the temperature. In several tests no evidence of a contact mark could be detected by microscopic examination. In most of the tests, however, evidence of motion was detected as an irregular scar on the side of the socket. Photographs of the ball and socket are shown in Fig. 78, along with the micro photo of the contact area. Because of the darkened appearance it was concluded that the damage consisted of a built up oxide film. At 1000°F a small irregular contact area was also observed. Its appearance was metallic as if some metal transfer had taken place. Macro photos of two of the 1000°F tests are shown in Fig. 79. It should be mentioned, however, that it is very difficult to distinguish microscopically between metal and oxide at high temperatures. First of all, the damage area is very small and secondly there can be burnishing of the oxide film which reflects light to give a more metallic like luster. It was concluded, however, that increase in the amount of damage did take place at 1000°F.

At both 400°F and 1000°F more observable damage takes place with the .256 socket than with ball on flat. One can hypothesize a reason for this behavior. There is, of course, a very small clearance between the .250 radius ball and the .256 radius socket. Any slight misalignment or irregularity will raise the contact area from a ring at the center to an irregular pattern on the side of the socket. This will add a tangential force to the contact area which could increase microslip. The absolute value of yaw motion will be increased since the motion is further from the center of rotation. However, most important rocking motion may also take place about the edge of the bearing which could cause a dynamic load at the contact area and increase the amount of damage as already observed. It is also significant that the pressure is extremely low as shown in Fig. 80. Under these conditions, the dynamic load is more probable and the gross slippage greater. Also under these conditions the damaged material cannot be pushed out of the way and builds up in the contact area. Once this happens rocking motion can take place about the damaged or oxidized area.

It appears then that the closely conforming radius in a socket can lead to damage in short times. At 400°F the damage consists of built up oxide while at 1000°F metal transfer may be beginning because of the softening of the M-2 tool steel. Although this damage may result from misalignment there is no assurance of perfect alignment in a practical bearing system.

When the radius of the socket was increased to .375 and .750 the more characteristic ring pattern was obtained (Fig. 81). However, more oxide build up was also evident. This was more noticeable in subsequent tests shown in Fig. 82. In Figs. 82a and 82b are shown two tests with .375 radius socket at 400°F and 1000°F. In Figs. 82c and 82d are shown two tests with the .750 socket at 400°F and 1000°F. Apparently most of the built up material was oxide but there may have been metal transfer at 1000°F. The build up is larger than with the flat but less than that found for the .256 radius (Fig. 78).

Because of the damage at 1000°F, a .375 radius socket was run at 900°F.

Since tool steel softens at 1000°F, it was felt that this may have been the cause of some of the metal transfer. This test showed very little damage in comparison to the 1000°F tests. This result suggests that the tool steel should be limited to 900°F application.

A number of tests were also run with the cylindrical sockets. The results were essentially the same as that found for the spherical sockets. A photograph of the results with the .256 radius cylinder is shown in Fig. 83.

Although the amount of damage which resulted with all the sockets would probably not be sufficient to interfere with the pivot motion, there was more build up with the sockets than with the flat specimens. This may have been due to the fact that with the lower pressures the built up oxide could not be extruded from the contact area. The most damage was found with the .256 socket which tends to confirm the above findings. Thus it appears from these tests that the more open curvatures (radius .375 or greater) are less prone to damage, however, longer term tests would be necessary to confirm this conclusion.

XI. FORMING GAS AND AIR TESTS

In the previous tests an argon atmosphere was used. Even so there always appeared to be evidence of oxidation at higher temperatures in the contact area.

The source of this oxidation could be from the oxygen in the argon or from a leak in the system. In order to determine its effect on the surface damage a series of tests was run with forming gas (93 N₂, 7 H₂) which is a reducing atmosphere, particularly at high temperatures. The conditions of the tests were as follows:

<u>MATERIAL</u>	<u>TEMPERATURE</u>	<u>OTHER CONDITIONS</u>
Stellite J vs Stellite 19	500°F 900°F	Shape -- .250" radius ball vs. flat & .375" radius socket
Carbide (K162B)	500°F 900°F	Load -- 15 pounds Frequency -- 1000 cps
M-2 Tool Steel	500°F 900°F	Motion -- Pitch -- 1.5 mil/inch Roll -- 0.5 mil/inch Yaw -- 0.25 mil/inch Time -- 12 hours

In these tests forming gas was used throughout the rig that is, in the gas bearing, the load bellows, and in the atmosphere around the specimens. Copper coupons placed in the specimen chamber during the test run showed no evidence of oxidation even at 900°F; in fact surface brightening took place. Furthermore, there was no evidence of general oxidation of the specimens.

In general, no differences could be detected between the results in these tests and those run in argon. Photographs of the tool steel specimens at 500°F are shown in Figure 84a and b. Figure 84a shows the ball and flat specimen; Figure 84b shows the ball and the .375" radius socket. The damage can be compared with that in Figure 59b for argon. It consisted of the characteristic ring of dark (not identified) material in the slip region. A Talysurf trace over the ring showed that its height was insignificant. The damage was of the same order of

magnitude of the surface scratches. As would be expected the contact ring is larger for the .375 radius specimen. The results for the 900°F tests are shown in the following Figures:

<u>MATERIAL</u>	<u>GEOMETRY</u>	<u>FIGURE NUMBER</u>
M-2 Tool Steel	Ball vs Flat	85a
	Ball vs .375" Socket	85b
Stellite J vs Stellite 19	Ball vs Flat	86a
	Ball vs .375" Socket	86b
Carbide (K162B)	Ball vs Flat	87a
	Ball vs .375" Socket	87b

Although there are some variations in the appearance of the rings the damage is insignificant as indicated by the Talysurf traces. Essentially the same conclusions can be drawn from the tests at 500°F. In all of the tests there is no indication of damage, weight change, or dimensional change of the specimens.

These results are further evidence that this amount of motion is too small to cause appreciable surface damage regardless of the atmosphere. Forming gas is a reducing atmosphere particularly at high temperatures. Even so the dark damage rings appeared. The ring material was not identified but appeared to be essentially the same as those formed in argon. This ring may be oxide, however, this atmosphere is about as limiting to oxidation as could be prepared.

It should also be noted that even though the pressure increased from 100,000 psi for the .375" radius specimen to 210,000 psi for the flat specimen there was no change in the amount of damage. In other words, no effect of shape was detected.

A series of four twelve hour tests with tool steel was run in air under the same conditions as the forming gas tests. Tests were run with both the flat and the .375 radius socket. Photographs of the damage which resulted with the .375 inch radius sockets at 500°F and 900°F are shown in Figure 88a and b. The usual

dark ring is formed in the slip zone at both temperatures. Comparing Figure 88 with Figures 84b and 85b shows the effect of the two extremes of air environment. In air it can be seen that the general level of oxidation is greater and that there is a more complete ring of damage. However, other than this, one can distinguish little difference between the tests. In neither case was there any significant damage.

XII. LONG TERM TESTS

It became apparent that even under the most severe conditions damage would not occur with rolling motions if the correct material were used. These, however, were short term tests which would indicate damage from metal transfer and welding but not from wear or surface fatigue. For this longer term tests would be necessary.

Originally a number of 100 hour tests were planned, however, after several tests (see Table 7) it became obvious that the results at 100 hours appeared exactly the same as the 12 hour tests. As a result the 100 hour selection tests were eliminated and 2,000 hour tests were run.

Several shapes and materials were used, however, all the tests were run at 900°F with a .250 radius ball, 1000 cycles/second; and amplitude with 1.5 mil/inch pitch, 0.5 mil/inch roll and 0.25 mil/inch yaw. The load was 15 pounds. These were the standard test conditions which were used for these as well as most of the other tests in this program.

The long term tests were completed on December 8, 1967 after 1950 hours of operation. The results of all of the tests are given for each material in Tables 8 - 11. The results are given in terms of overall wear, change of weight of the test specimens, observed microscopic damage, results of Talysurf trace, and changes in the motions.

The overall wear was measured with a capacitance probe which measured the overall specimen height before and after the test. There was considerable variation in this reading which had little relationship with the overall damage. It appears that this measurement has little value.

The weight changes of the specimen are very small, indicating that negligible wear had taken place. In fact on most specimens a weight gain resulted undoubtedly from surface oxidation. Small weight losses were noted on the damaged specimens.

Table 8

LONG TERM TESTS

M-2 Tool Steel vs. A-286
 900F (1.5 - .5 - .25) motion
 1000 r/sec .25" radius ball specimen

Rig Time No. Hrs.	Socket Radius	Shape	Overall Wear	Weight Change		Damage		Tal.-surf Trace		Motions
				Ball	Flat	Ball	Flat	Ball	Flat	
6b 1950	"	Flat	+1.2 mil	+0.0009	-.0004	Large roughened area covered with oxide	Same	General increased roughening of the surface Max. Hills .0008" Min. Valleys .0004"	General increased roughening of the surface Max. Hills .0003" Min. Valleys .00075"	Continual decrease in motions which where re- adjusted. After 700 Hours it was not pos- sible to increase motion

Table 9

LONG TERM TESTS

M-2 Tool Steel - M-2 Tool Steel
900F (1.5 : .5 - .25) motion
1000 c/sec .25" radius ball specimen

Fig. Time No. Era.	Radius	Socket Shape	Overall Wear	Weight Change(gms)		Damage		Talyseurf Trace		Motions
				Ball	Flat	Ball	Flat	Ball	Flat	
4b*	1950	"	Flat	+2.52	-.0049	Same	Very large shiny roughened area metal transfer	General increased roughening of the surface. Max. Hills .0002" Min. Valleys .0001"	General roughening of surface. Max. Hills .0002" No Valleys	Continual adjustment of amplitude-loss of roll motion.
5a	1105	.750	Sphere	0	+ .0010	No visible damage	No visible damage	One bump on both specimens(height .000075")		No change in motion
6a	1105	.256	Sphere	-3.2 mil	+ .0020	Large built-up area of trans- ferred material	Built-up area of transferred material	General increased roughening of the surface. Max. Hills .0002" Min. Valleys .0003"	Material transferred to the flat. Build-up .0008"	No change in motion
4a	2000	.256	Cylinder	≤-4.0	+ .0007 + .0026	No damage	Isolated spots of transferred material	No damage	Very slight increase roughening Total = .0004"	No change in motion

* Overheated to 1200F for 5 hours.

Table 10

Star J - Stellite 19
 900F (1.5 - .5 - .25) motion
 1000 c/sec .25" radius ball specimen

Fig. No.	Time Hrs.	Socket Radius	Shape	Overall Wear	Weight Change		Damage	Talysurf Trace		Motions
					Ball	Flat		Ball	Flat	
1b	1950	.750	Sphere	≤-5.5	-.0070	-.0108	Large built-up transferred material	Large built-up transferred material	General roughening No Hills Max. Valleys .0005" General roughening Max. Hills .0003" Valleys .0001"	Motions increased occasionally
3b*	1950	.256	Sphere	+0.6	+0.0004	+0.0012	No damage	No damage	No surface change	No change
2b	1950	.256	Cylinder	≤-5.9	+0.0073	-.0092	No damage	No damage	No surface change	No change

* Overheated to 1200F for 5 hours.

Table 11

LONG TERM TEST

K162B - K162B
 900F (1.5 - .5 - .25) motion
 1000 c/sec .25" radius ball specimen

Fig. No.	Time Hrs.	Radius	Socket Shape	Overall Wear	Weight Change (gms)		Damage	Tallysurf Trace		Motions
					Ball	Flat		Ball	Flat	
5b*	1345	"	Flat	+1.05 mil	- .001	+ .0013	No damage	No damage	No surface change	No significant change
1a	2000	.750	Sphere	-12.2 mil	+ .0108	+ .0018	Material transfer at small circular area	Material transfer in small circular area at center	No change	No change
									One peak in contact area .00016"	One valley in contact area .0001"
3a	2000	.256	Socket	-4.1 mil	+ .0083	+ .0023	Small polished area	Small polished area - may be transferred	No surface change	No change - improvement in wave shape
2a	2000	.256	Cylinder	-.3 mil	+.0004	-	Material transferred and re-moved elliptical area	Material transferred and re-moved elliptical area	General surface roughening Max. Hills .00008" Min. Valleys .00030"	No significant change

* Drivers burned out 1345 hours.

The amount of surface damage which resulted was determined by microscopic inspection and by comparison of the Talysurf traces before and after the run. Generally the results fell into two classes. Either there was no surface damage and the area of contact showed only a contact spot, or there was surface damage which consisted of a general roughening of the surfaces. Where this took place maximum height of the hills and the depth of the valleys is noted. In no case did this damage exceed a height of 1 mil. There was no consistent pattern to the change. In several cases it was determined that some transfer had resulted, this is indicated by an arrow in the table noting the direction of transfer. However, this damage is on a microscale. On a macroscale the damage for all tests, except possibly the M-2, A286 combination, is small and probably would have little influence on the overall operation of the pivots. Macrophotos of the carbide and tool steel tests are shown in Figure 89.

Any changes in the motions were noted in the log books and adjustments made. A summary of the significant changes are noted in the table. In all cases these changes consisted of increase or decreases in the amplitude. It was found that where the motions changed (either increase or decrease in amplitude) damage was found upon disassembly and inspection. This was most apparent with the tool steel A286 combination where the motions continually changed and eventually it was not possible to increase them again. This was the test where the greatest damage was observed.

These results show essentially the same behavior as was found in the short term tests. No significant wear could be detected and the damage was microscopic when it existed at all. The most damage was found with the M-2-A286 combination shown in Table 8. This was included in the test program to see how much damage would result with a poor combination of materials and under high stress (ball-flat geometry). The damage consisted of a roughening of the surface with the transfer of material from the ball to the flat. Even here however the maximum peak to peak height was only 1.2 mil, although this was sufficient to interfere with the established motions. A Talysurf trace of the damaged area is shown in Figure 90. The other combination of materials gave much less damage (Tables 8 - 11). On the basis of these tests no material could be judged superior to the

others. This is understandable since they were selected as the best materials in the initial screening tests.

The damage which resulted was independent of the geometry as shown in the following table. (Damaged specimens are indicated with an X).

<u>MATERIAL</u>		<u>SOCKET GEOMETRY</u>		
		.750	.256	.256
	Flat	Sphere	Sphere	Cylinder
M-2 Tool Steel vs. M-2 Tool Steel	X		X	
M-2 Tool Steel vs. A286	X	Not Tested	Not Tested	Not Tested
Stellite Star J vs. Stellite 19	Not Tested	X		
K162B Carbide vs. K162B Carbide		X		X

It can be seen that some damage was detected with each shape regardless of the material. Thus, the socket geometry (at least within the range of geometries tried) does not appear to be a principal factor in determining whether damage occurs or not. This same behavior was encountered in the short time tests. There it was hypothesized that the difference in damage may result from the changes in the area of contact if small amounts of misalignment occur with shaped specimens.

In each case, surface oxidation was apparent on the specimens at the conclusion of the test. It was felt that this oxidation was due to the impurities in the argon.

The conclusions from these tests are that the selected materials are satisfactory for long term service under the conditions of these tests. No conclusion can be drawn as to the optimum shape, from these results.

XIII. LUBRICANT TESTS

Although the unlubricated surfaces were not severely damaged even after 2000 hours of operation it is desirable to know the extent of effectiveness of solid film lubricants. In order to answer this question 4 - 100 hour lubricant tests were run and compared with unlubricated tests run at the same times. The lubricants were applied to both surfaces of M-2 tool steel specimens. The lubricant test was run in conjunction with each lubricant test under the same conditions.

<u>Lubricant</u>	<u>Time</u>	<u>Temp.</u>	<u>Frequency</u>	<u>Load</u>	<u>Amplitude</u> P R Y	<u>Test</u> <u>Rig</u>	<u>Pivot</u> <u>Shape</u>	<u>Socket</u> <u>Shape</u>
Fused Fluoride	100 hrs.	500°F	1000 cps	15#	1.5,.5,2.5 $\frac{1}{16}$ in	6	.250 Rad.	.375 Rad.
Fused Fluoride	100 hrs.	900°F	1000 cps	15#	1.5,.5,2.5 $\frac{1}{16}$ in	5	.250 Rad.	.375 Rad.
MoS ₂ Silicate	100 hrs.	500°F	1000 cps	15#	1.5,.5,2.5 $\frac{1}{16}$ in	6	.250 Rad.	.375 Rad.
MoS ₂ Silicate	100 hrs.	900°F	1000 cps	15#	1.5,.5,2.5 $\frac{1}{16}$ in	5	.250 Rad.	.375 Rad.

The results of these tests were quite surprising in that in each test the lubricant remained on the surface in the contact area at the conclusion of the test (100 hours = 3.6×10^8 cycles). This is much longer life than would normally be expected from a solid film lubricant. Thus one must again conclude that the amount of slip is so small that it can do little damage or wear to the surface. Microphotos of the 500°F contact areas are shown in Figure 91. Macrophotos of the MoS₂ coatings are shown in Figure 92. These photographs show that the lubricant film is still retained in the contact area.

In the 900°F fluoride test separation occurred between the film and its base at the conclusion of the test. Since these coatings were experimental no particular significance is attached to its removal in this manner.

XIV. SPECIAL DESIGN TESTS

During the course of the investigation a number of specific pivot designs were evaluated in 100 hour tests. In the following sections the results of these tests are presented.

1. Tungsten Carbide vs. A286 Flame Sprayed with Tungsten Carbide-Conforming Radius

Drawings for these test specimens are shown in Figures 93 and 94. Essentially they consist of a .500 diameter tungsten carbide ball and a .500 diameter socket element made of A286 stainless steel sprayed with a tungsten carbide film. The ball and socket elements are lapped together to achieve a fully conforming geometry. A hole in the center of the specimen is to simulate the hole for hydrostatic jacking gas in the pivot. Five of these specimens in matched sets were supplied by NASA for evaluation.

In order to run these tests it was necessary to modify the test rig as shown in Figure 95. The essential difference is that the ball specimen is mounted in the spherical seat and the socket is held rigidly. The cleaning and operating procedures for these tests were the same as those used in the preceding tests. Six tests were run with these pivots (one set 003 was reused). The running conditions are given in Table 12. These are the same standard input conditions as used in previous tests. Two tests were started at 500° F (specimens 003 and 004) and run for 16 hours. The tests were then stopped and the surfaces examined. Rather severe surface damage had resulted. Originally it was planned to restart both of these specimens for an additional 100 hours; however, since the damage was so severe, it was decided to only restart only one of the specimens and to retain the other for examination. One set (003) was reassembled along with a new specimen set (002) and the additional 100 hours run. (117 1/4 hours were run to correspond to the shut off date for the 2000 hour test.) After 117 1/4 hours the surface damage became so severe and the motions so erratic, that the test was not restarted to complete 480 hours of testing as planned. Two additional comparative tests were run at room temperature for 117 1/4 hours.

The results of these tests are given in Table 13. Photographs of the surface at the conclusion of the tests are shown in Figures 96 through 101. Referring to Table 13 some generalizations can be made: In all tests the sockets lost weight. The overall wear was negligible probably within the accuracy of the measurements (h dimension is shown in Figure 95).

Rig No.	Spec. Set No.	Time Hrs.	Amplitude (peak to peak)			Load Lbs.	Temp °F	Freq. CPS	Atmosphere
			Pitch Mils/in	Roll Mils/in	Yaw Mils/in				
5	003	16	1.47	.53	.28	15	490	1000	Ar
6	004	16	1.41	.53	.28	15	500	1000	Ar
5	003	117-1/4	1.59	.53	.15	15	480	1000	Ar
6	002	117-1/4	1.47	.53	.28	15	490	1000	Ar
5	005	117-1/4	1.59	.70	.28	15	95	1000	Ar
6	001	117-1/4	1.47	.53	.23	15	95	1000	Ar

TABLE 12 TEST CONDITIONS

Rig No.	Spec. Set No.	Socket Weight		Ball Weight		Overall Wear Measurement h in.	Changes in Imposed Motion		Comments on Surface Damage
		Before gms	After gms	Before gms	After gms				
5	003	24.818	-	11.246	11.47	-.0001	Large increase (.6 mil) in motion	96	1) General roughening of the surface 2) Isolated spots of transferred material
6	004	24.795	24.794	11.129	-	-.0009	Slight decrease	97	1) General roughening of the surface 2) Isolated spots of transferred material
5	003	-	24.816	11.247	11.248	.0000	Slight decrease initially then constant	98	Material transferred over entire surface
6	002	24.964	24.963	10.888	10.888	+ .0001	Motions constant throughout test	99	Material transferred over entire surface
5	005	24.793	24.791	11.099	11.100	+ .0005	Slight decrease initially then large increase in amplitude (.5 mil) Roll motion not controllable	100	Material transferred in one area
6	001	24.856	24.855	11.020	11.022	+ .0005	Motions constant throughout test	101	Material transferred over 1/2 area of contact

TABLE 13 TEST RESULTS

Changes in motion were for the most part changes in amplitude. There was however no consistent pattern to the changes. Test specimens 005 gave variable motions throughout the test while its companion test 001 maintained constant motions.

The surface damage though obvious to the eye, did not involve large volumes of material. The damage was limited to isolated areas in the 16 hour test (Figures 96 and 97) and in the room temperature, 117 hour test (Figures 100 and 101). In the 500°F, 117 hour tests the damage was essentially the same as in the other tests except that it covered the whole surface (Figures 98 and 99).

Microscopically all the damaged areas appeared the same. Compare, for example, Figures 96c, 97c and 97d. It was very difficult to determine the exact nature of the damage with the microscope. Talysurf traces made by M. Swikert of NASA on specimen set 004 (Figures 102 and 103) showed that material was removed from the socket to a depth of .0003 in. and transferred to the ball. The amount of material removed from the socket is of the same order of magnitude as the sprayed carbide film thickness. All the results are consistent with the hypothesis that the film was removed by the fretting motion and adhered to the ball. The same result was found for the same combination of materials in the screening tests. Thus this appears to be a materials problem rather than a design problem.

2. Sapphire vs. WC (Conforming and Non-conforming Geometry)

Eight tests were run for 100 hours at 500°F using the standard conditions of operation previously outlined. The specific shapes used are shown in Table 14. Two tests were run with each shape. The radius of the balls were .250"; the radius of the non-conforming sockets was .375". The results of these tests are given in Table 14. In all cases there was damage to the specimens. For the non-conforming radii the damage was caused by the edge; for the conforming radii the damage consisted of isolated regions of minor surface roughening. In most cases the sapphire ball lost weight and the carbide gained weight. Small fracture pits were occasionally seen in the surface of the sapphire.





Specimen No.	Test R16	Shape	Ball			Socket			Damage
			Wt Change GMS	Max Peak Roughness (micro-inch)	Max Valley Roughness (micro-inch)	Wt Change GMS	Max Peak Roughness (micro-inch)	Max Valley Roughness (micro-inch)	
1	1	Non Conforming 	+ .0001	0	20	+ .0004	0	0	Sapphire worn by carbide edge. Carbide chipped at edge. Only partial contact on hole.
3	1		- .0021	20	5	- .0007	0	0	
2	1	Non Conforming 	- .0023	0	0	+ .0026	20	10	Sapphire ball chipped at edge. Groove worn in WC socket.
4	1		+ .0005	0	0	+ .0001	10	20	
A	2	Conforming 	- .0030	0	10	+ .0043	0	10	Random area of contact. Cloudy appearance makes the contact area on both specimens. Considerable wear debris. No gross damage. Some chips out of sapphire.
C	2		- .0045	50	10	+ .0005	10	10	
B	2	Conforming 	- .0038	1000	0	+ .0014	0	20	
D	2		- .0020	0	0	+ .0010	0	0	

TABLE 14

A photograph of the surface of the non-conforming radius before and after the test is shown in Figure 104. The ring shown in Figure 104b produced the wear debris shown on the socket. This wear debris caused the weight gain shown in Table 14. It was firmly attached to the socket and had to be scraped away. When it was removed the wear area was confined to a very small area on the edge of the tungsten carbide socket. When the hole was in the sapphire ball the results were essentially the same except the sapphire edge was chipped and the groove was worn in the tungsten carbide. In this test the contact area produced surface roughening of 10 to 20 microinches.

A photograph of a typical damaged surface for the conforming radii is shown in Figures 105 and 106. Figure 105 shows the test specimens before and after test. These damage areas are identical on the ball and socket. This type of damage was found on all specimens with the conforming radius. The damaged areas are shown at higher magnification in Figure 106. The damage was carefully inspected at higher magnifications and with a variety of light sources, however, no understanding could be obtained as to its exact nature. Talysurf traces indicated that there was build up and material removal from each surface. As with the previous configuration some surface chipping of the sapphire was noted. With the conforming radii tests some difficulty with the motions was experienced. Sudden changes in the amplitude took place without any shift in the wave form. These would be corrected when they occurred. This was not a consistent phenomenon, however, since it occurred only occasionally and in certain tests more than in others. It is easy to explain this effect; with damaged surfaces one would expect varying friction and thus varying amplitude. Even more likely is the possibility that the damaged area separated the surfaces sufficiently so that a rolling contact could result.

On a microscale the damage appeared severe, however, on a macroscale the damage was small. With these specimens the fracture pits on the sapphire would be sufficient cause for its rejection particularly since other materials are available. These were run and described in the following section.

SPECIMEN NO.	SPECIMEN	WEIGHT CHANGE GRAMS	ROUGHNESS CHANGE MICRO-IN.	MOTIONS CHANGE	SURFACE DAMAGE	FIG. NO.
113	Ball	-.0050	20 (30)*	Minor Adjustment in Roll	Isolated foggy appearing areas on both ball and socket. Matched areas on ball and socket	107
	Socket	-.0188	20 (40)*		Foggy areas appear to be minute metal transfer to both ball and socket	108
115	Ball	+.0273	0	Motion Increased at End of Test	Same as 113	110c
	Socket	+.0144	10			
111	Ball	+.0239	25	No Change	Same as 113	110a
	Socket	+.0144	60			
114	Ball	-.0052	0	No Change	Same as 113	110b
	Socket	-.0210	25 (50)*			

TABLE 15 CARBIDE VS. CARBIDE PIVOTS

3. Carbide and Tool Steel - BRU Conforming Geometry

Because of the difficulties with the sapphire tests a series of tests were run with the carbide-carbide and the tool steel-tool steel combination. The geometry was a .250" radius ball with a mated .250" socket. The specimens were lapped together. Each specimen had a center hole. Four tests were run with K162B carbide and four with M-2 tool steel hardened to 56Rc. The carbide specimens were of the same material and geometry as the pivots in the delivered BRU at NASA-Lewis. The following test conditions were used:

Load:	15 pounds
Temperature:	500 ^o F
Frequency:	1,000 cps
Motion:	Pitch 1.5 mil/inch
	Roll .5 mil/inch
	Yaw .25 mil/inch
Time:	100 hours
Shape:	Conforming radius 0.50 inch diameter

The results of these tests are given in Table 15 for the carbide and Table 16 for the tool steel.

The results of all the tests were similar. This is illustrated by the results of the 113 carbide test. The damage consisted visually of isolated foggy appearing areas (Figure 107). The contact areas on the both specimens were mirror images of each other. Two corresponding spots are shown in Figure 107. A microscopic examination of this spot indicated that it consisted of roughened surface (Figure 108) and wear debris. The rough appearance seemed to be due to metal transfer from one specimen to the other. A Talysurf trace across the surface of the damaged (Figure 109) area of the ball, confirmed the increased roughness. It should also be noted that the damage consists of build up on the ball as well as recesses. This damage was identical to that which was found in the previous tests of conforming radii. A number of Talysurf traces were made across the various damage areas. From this an average roughness change was recorded

for each set of test specimens. For the 113 test the surface roughness increased by 20 microinches. At one small spot, however, the roughness was larger. No significant changes in weight or in the motions were noted.

The results for the other carbide tests were essentially the same. Macrophotos of the ball and sockets of this identical tests are shown in Figure 110a, b, and c. It should be noted that the wear is sufficiently small and that the contact areas are relatively isolated.

The results for the tool steel tests are shown in Table 16. The type of damage was essentially the same as that for the carbide with several exceptions.

1. The contact area generally covered a larger portion of the specimen area (Figure 111).
2. In several tests the metal transfer was more severe at isolated spots (Figure 112a and 112b).
3. The surface roughness from damage was larger (See roughness change column, Table 16).
4. More difficulty was encountered in maintaining the motions during the test run. This was undoubtedly due to the increased damage.

In summary these results show that with the conforming pivot design, surface damage in the form of metal transfer occurs in a period of 100 hours. The carbides were damaged less than the tool steel; in both cases the damage was microscopic.

SPECIMEN NO.	SPECIMEN	WEIGHT CHANGE GRAMS	ROUGHNESS CHANGE MICRO-IN.	MOTIONS CHANGE	SURFACE DAMAGE	FIG. NO.
3	Ball	-.0046	+80	Motions Increased	Contact is primarily in three areas. Contact area appears roughened by minute metal transfer. Surfaces generally covered with wear debris.	112a
	Socket	-.0057	+60		Three small shiny areas of severe metal transfer.	112b
2	Ball	-.0350	+90	Several Large Increases in Pitch	Contact over nearly complete area. Surface is generally roughened by minute metal transfer.	
	Socket	-.0078	+80			
5	Ball	+.0665	0	No Change	Same as #2. General Roughening which appears to be metal transfer	111
	Socket	-.1154	30 μ			
4	Ball	-.0127	50	Minor Adjustments Lost Roll Motion	Same as #3. Contact concentrated in three small areas. Metal transfer more severe in these areas.	
	Socket	-.0272	75			

XV. 1000 HOUR BRU TEST

In order to determine the long term behavior of the conforming geometry, two of the previously run BRU carbide pivots were replaced in the test rig and run for an additional 1000 hours at 500°F under the standard operating conditions used in the 100 hour tests. The results of these tests are given in Table 17.

The surface damage was essentially the same as that found in the 100 hour test except that it completely covered the contact area rather than being confined to isolated contact spots. Macrophotos of the specimens are shown in Figure 113. Microphotographs of the ball and socket of the 115 test specimen are shown in Figure 114. It is seen that essentially the same form of damage results which has been found with all the conforming geometries; that is a general surface roughening and darkening of the contact area. Extensive microscopic examinations were made of the damaged area to establish the nature of the surface damage, however, this could not be resolved. Talysurf traces showed that there is "build-up" and material removal occurring in both the ball and socket elements. Darkening of the contact surfaces did not provide any significant information regarding the specific nature of the damage. Electron microscopy or diffraction may give some further insight, however, the techniques were not utilized.

From Table 17 it can be seen that the surface roughness has increased as a result of the 1000 hour tests. There were, however, no significant changes in the motions during the test in spite of this increased damage. A significant fact is that all of the test specimens lost weight during the run; an indication that wear had taken place. The total wear amounted to .0060 gram in the case of the 111 specimens and .0032 for the 115 specimens. This amount of wear is small, but if the .006 gram were uniformly removed from the specimens, a change in height of .0002" would result. In other words, the wear would amount to about .2 mil in 1000 hours. There was, however, no other substantiating evidence of this wear and the numerous Talysurf traces taken at the edges of the damaged areas (for example see Figure 114d) showed no change of height, only a surface roughening.

One further point is of interest. In Figure 114-d the line of contact formed by the edge of the hole in the ball can be seen. In these tests there were no signs of any damage at the edges of the hydrostatic gas feed holes.

In conclusion, the tests showed again that while conforming surface pivots suffer significantly more damage than non-conforming ones, the extent of damage after 1100 hours of operation is still small enough so that it did not affect the performance of the pivots in the test rigs. Based on MTI experience, this amount of damage would also have no significant effect in an actual pivoted pad gas bearing.

On the basis of the tests, therefore, we conclude that the conforming surface pivots that were tested will operate successfully in an otherwise properly designed pivoted pad gas bearing, at least for the order of one to several thousand hours.

There are, however, two reservations of an essentially statistical nature that should be noted for conforming pivots with a central hole for hydrostatic jacking gas. These are:

1. If a large chip were to come loose, it would tend to wedge between the conforming mating surfaces, with significant effect on clearance and freedom of motion of the pad.
2. Transfer of debris from the wear zones to the gas film through the hydrostatic gas feed hole.

Specimen Number	Specimen	Weight Change Grams 1000 Hours	Roughness Before 1000 Hour Test (micro-inches)	Roughness After 1000 Hour Test (micro-inches)	Motion Change	Test Rig	Damage	Fig. No.
111	Ball	-.0030	25	50 *	No Significant Change	#4	General Surface Roughening	113a
	Socket	-.0030	60	100				
115	Ball	-.0022	0	25	No Significant Change	#6	General Surface Roughening	113b 114
	Socket	-.0010	10	40				

* Roughness at one point

TABLE 17 RESULTS FOR 1000 HOUR BRU TEST Material: WC 500°F Load 15 lb. 1000 cps.

XVI PIVOT DESIGN

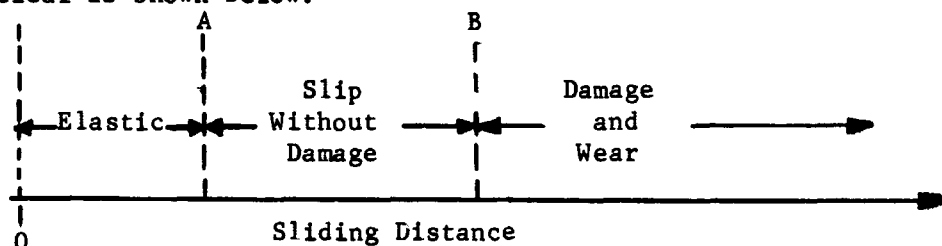
A properly designed pivot should operate for long periods of time without either wear or surface damage. The previous results have shown that this objective can be achieved. Tool steel and carbide pivots were operated with both the conforming and the non-conforming geometries for 1000 hours without measurable wear. Damage, however, was generally found with the most conforming geometries.

In the past, pivot designs have been somewhat arbitrary. Generally, every effort was made to keep the pressure in the contact zone to a minimum. MTI practice for unlubricated pivots has been to design for a stress of 120,000 psi with a radius ratio ($\frac{r_{\text{socket}}}{r_{\text{pivot}}}$) of 1.02 to 1.1. The size of the pivot is chosen to conform to these requirements. Thus higher loads will result in larger pivots. The results of these studies have indicated that these design guidelines are very conservative. First, the results have indicated that pivots may be operated at higher pressures. Secondly, the results have indicated that the radius ratio should be larger. Pivot damage (but no significant wear) was almost always found with the conforming radius and with the 1.02 radius ratio. The question then arises as to what limits should be placed upon these variables. The safest approach is to select design values which were actually run in the present test program.

The maximum running pressure in the 2000 hour test for the tool steel, ball-flat combination was 220,000 psi. Since the yield pressure of hardened and tempered tool steel is 300,000 to 400,000 psi (depending upon the tempering temperature), this value represents a reasonable design limit. Although the carbides were run at slightly higher pressures, there would be insufficient gain to justify a different pressure for each material.

In most of the tests, satisfactory operation was obtained with a radius ratio of 1.50 or higher. Surface damage was almost always found with a radius ratio of 1.02 or smaller. Thus, it seems logical to design with the 1.50 radius ratio as an acceptable value.

A third criterion may be applied to the design of pivots or any sliding contact. It is known that when two surfaces slide together the total distance of slip is critical as shown below.



If two points are in contact and motion is imposed, they can move together elastically for a short distance (0 - A). If motions are larger, actual microslip will occur; however, a certain amount of microslip is necessary before damage will occur (A to B). Damage and wear occur at microslips above point B. Unfortunately, numerical values can not be assigned to these transitions at the present time.

In this program a design has been suggested which would eliminate the microslip, that is, all the motion would be taken in the elastic region. Essentially, this approach calls for a rather complex geometry with high pressures in the slip region of contact. Although this approach could be used, the experimental work indicated that the simple ball-socket geometries would suffice. The computer program developed in Appendix D allows the microslip at any point in the contact region to be calculated. The correct criterion then is to design the pivot so that the maximum microslip is less than that required to produce damage. Although the amount of microslip necessary to produce damage was apparently not reached in the experimental program, it is still possible to select the maximum experimental microslip from the 2000 hour tests. This, of course, depends upon the friction coefficient and the shear traction of the pivot. If τ is chosen to be .20 where $\tau = \frac{\text{shear traction}}{\text{normal force}}$ then the following values of microslip will be obtained for tool steel surfaces:

LOAD POUNDS	MICROSLIP INCHES	
	$f = .35$	$f = .65$
15	$.245 \times 10^{-4}$	$.427 \times 10^{-4}$
30	$.389 \times 10^{-4}$	$.678 \times 10^{-4}$

It is difficult to know what coefficient of friction to use. A value of 0.65 can be accepted as at room temperature air value and 0.35 at 900°F. It could be higher in an oxygen-free environment or lower because of vibration. For the pivot design calculations used in this report, a value of 0.35 was selected, since the possibility of eliminating all oxygen from a system is rather remote.

The 15# test was run for 2000 hours without damage; the 30# test was run for 100 hours. Since sliding surface damage is not a function of time, either the 15# or the 30# value of microslip may be chosen. In view of the fact that the lower value of friction was chosen, it seems appropriate to select the microslip for the maximum load; that is, the value of $.389 \times 10^{-4}$ in.

Thus, the suggested approach is to design the pivots using a radius ratio of 1.5, a maximum pressure of 220,000 psi, and a limiting microslip of 4×10^{-5} in. In Figures 116 to 121 the microslip, pressure, radius of the contact region, and radius of the locked region are plotted as a function of pivot load for a radius ratio of 1.50. Three different pivot radii are selected to cover the probable range of loads; $r = .125, .250$, and $.375$. Curves are given for a friction coefficient of 0.35 and for both tool steel and tungsten carbide. The value of τ used was .20. This is somewhat greater than might be expected; however, as shown in Figure 115, $\tau = 0$ gives only a slightly lower value of microslip.

Figures 122 to 125 show the effect of changing the radius ratio to the extreme limits for the .250" radius ball. Here the design curves are given for the .250" ball vs the flat and the .300" socket radius. On each of these curves, the design limits of $.400 \times 10^{-4}$ in microslip and 220,000 psi pressure are drawn. This shows the load limit for each of the design shapes. In the following table, these limits are reproduced.

DESIGN LOAD LIMITS

Material	Radius of Pivot in	Radius of Socket in	Load Limit Pressure Criterion	Load Limit Slip Criterion	Figure Number
Tool Steel	.125	.1625	32# -	38#	116
Carbide	.125	.1625	8# -	30#	117
Tool Steel	.250	.375	120#	52# -	118
Carbide	.250	.375	33# -	41#	119
Tool Steel	.375	.5625	150#	66# -	120
Carbide	.375	.5625	94#	50# -	121
Tool Steel	.250	∞ (flat)	15# -	25#	122
Carbide	.250	∞ (flat)	3# -	23#	123
Tool Steel	.250	.300	>150#	75#	124
Carbide	.250	.300	>150#	60#	125

It can be seen that, in some cases, the pivots are load limited by the pressure criterion and, in some cases, by the microslip criterion. Since the conservative approach has been followed in the selection of these limits, it may again be used to select the lower of the loads as the design limit.

The main point of interest shown in this table is that these three simple pivot shapes and two materials can be used to the widest range of design variables which would be expected in small Brayton cycle machinery.

REFERENCES:

1. Midlin, R.D., "Compliance of Elastic Bodies in Contact, "Journal of Applied Mechanics, Vol. 16, pp. 259-268 (1949)
2. Johnson, K.L., "Recent Developments in the Theory of Elastic Contact Stresses: Their Significance in the Study of Surface Breakdown," Proceedings of the Conference on Lubrication and Wear, Institute of Mechanical Engineering, London, Paper No. 24
3. Burton, R.A., Tyler, J.C. and Ku, P.M., "Thermal Effects in Contact Fatigue Under Oscillatory Normal Load," Proc. 1963 USAF Aerospace Fluids and Lubricants Conference, San Antonio, Texas, p. 460, 1963
4. Tyler, J.C., Burton, R.A. and Ku, P.M., "Contact Fatigue Under Oscillatory Normal Load," ASLE Transactions, p.p. 255-269 (1963)
5. Burton, R.A. and Russel, J.A., "Lubricant Effects on Fatigue in a Stationary Concentrated Contact Under Vibrating Loading," ASME Paper No. 65-WA/CF-3, ASME Annual Meeting, Chicago, Illinois, November 1965
6. Klint, R.V. and Owens, R., "The Effect of Lubrication on the Damping of Cantilever Beams," ASLE Transactions, Vol. 3, No. 1, p. 149 (1960)
7. Frost, A., "The Determination of Pivot Characteristics," M.T.I. Report 65TMI, February 11, 1965
8. Mov, V.C., Chow, P.L. and Ling, F.F., "Microslip Between Contacting Paraboloids," Journal of Applied Mechanics, Vol. 34, Trans ASME, Vol. 89 Series E, p. 321, 1967
9. Lund, J.W., "Rotor Bearing Dynamics Design Technology - Part V: Computer Program Manual for Rotor Response and Stability," Technical Report AFAPL-TR-65-45, Part V, Air Force AeroPropulsion Laboratory, Wright Patterson Air Force Base.
10. Curwen, P.W., "Research and Development of High Performance Axial Flow Turbomachinery, Vol. 2 - Design of Gas Bearings, "NASA CR-801, (PWA - 2977, Vol. 2; M.T.I. 67TR9)
11. Bisson, E.E. and Anderson, W.D., "Advanced Bearing Technology," NASA SP-38 (1964)
12. Glaeser, W.A., "High Temperature Bearing Materials," Metals Engineering Quarterly, Vol. 7, No. 2, p. 53, May, 1967
13. Wilson, D.S., "Evaluation of Unconventional Lubricants at 1200 F in High Speed Rolling Contact Bearings," ASME Paper 61-LUBS-9 (1961)

14. Lewis, P., Murray, S.F., and Schwartz, A.A., "Current Status of Knowledge on Design Criteria for Bearings used in High Temperature Aircraft Electrical Accessories," WADD TR58-519 (1958)
15. Murray, S.F. and Lewis, P., "Evaluation of Rolling Contacts in the Range of 550F to 1000F." Apex Report 560. U.S. Dept. of Commerce (February 1958)
16. Philip, T.V., Nehrenberg, A.E., and Steven, G.A., "Study of the Metallurgical Properties that are Necessary for Satisfactory Bearing Performance and the Development of Improved Bearing Alloys for Service up to 1000°F. WADC TR57-343, Part II, May 1958
17. Bulletins, Haynes Stellite Company.
18. Murray, S.F., and Lewis, P., "Oscillating Roller Bearing Materials for Temperatures to 1200°F," General Electric Company, Report 58GL208 (1958)
19. Peterson, M.B., and Murray, S.F., "Investigation of Possible Bearing Materials and Lubricants Above 1000°F," Department of Commerce, Apex, Report 624, April 1959
20. Murray, S.F., and Peterson, M.B., "The Selection and Evaluation of Materials and Lubricant Films for Gas Lubricated Gyro Bearings," M.T.I. Report 64TR1 (NOBS 88615 (FBM)) January 1964
21. Peterson, M.B., Florek, J.J., and Murray, S.F., "Consideration of Lubricants for Temperatures Above 1000°F." ASLE Transactions, Volume 2, No. 2, May 1960, Pages 225-234
22. Sliney, Harold E., "Lubricating Properties of Some Bonded Fluoride and Oxide Coatings for Temperatures to 1500°F." NASA TN D-478, 1960
23. Devine, M.J., Lamson, E.R., and Bowen, J.H., Jr., "Inorganic Solid Film Lubricants," Journal of Chemistry and Engineering Data, Volume 6, No. 1, January 1961, Pages 79-82
24. Johnson, R.L., and Sliney, H.E., "Ceramic Surface Films for Lubrication of Temperatures to 2000°F," American Ceramic Society Bulletin, Volume 41, No. 8, August 1962, Pages 504-508
25. Peterson, M.B., and Johnson, R.L., "PbO and Other Metal Oxides as Solid Lubricants for Temperatures to 1000°F," Lubrication Engineering, Volume 13, No. 4, April 1957, Pages 203-207
26. Sliney, Harold E., "Lubricating Properties of Ceramic-Bonded Calcium Fluoride Coatings on Nickel-Base Alloys from 75° to 1900°F." NASA TN D-1190, 1962

27. Peterson, Marshall B. and Johnson, Robert L., "Friction Studies of Graphite and Mixtures of Graphite with Several Metallic Oxides and Salts at Temperatures to 1000 F." NASA TN 3657, 1965
28. Hopkins, V. and Gaddis, D.H., "Development of Solid Film Lubricants for Use in Space Environments," Proc. USAF Aerospace Fluids and Lubricants Conference, San Antonio, Texas, April 16-19, 1963, P.M. Ku Editor, p. 330.

APPENDIX A The Dynamic Coefficients for the Pad Fluid Film

For small motion of the journal, the dynamic forces imposed on the journal by the fluid film of a fixed pad bearing can be represented by a set of spring and damping coefficients. The journal is considered to have four degrees of freedom: two radial displacement components and two angular displacement components.

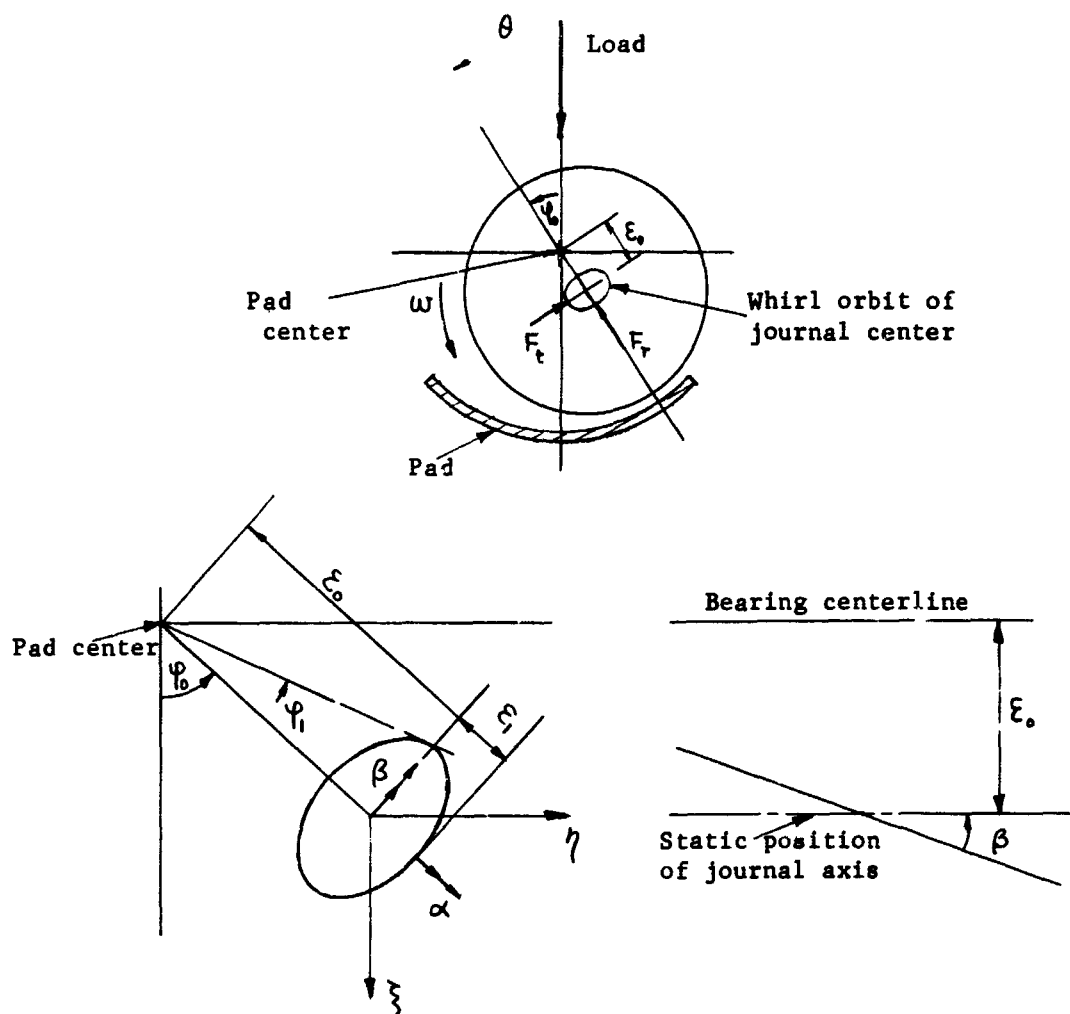


Figure A-1

The journal is operating with a static eccentricity ratio ϵ_0 and a corresponding attitude angle φ_0 . Under dynamic conditions the journal center whirls around the static equilibrium position with the displacements ϵ_1 and φ_1 measured from the equilibrium position. In addition, the journal axis is assumed to perform an angular oscillation with the angular displacements α and β .

The restoring forces and moments acting on the journal can be expressed by their first order Taylor's series expansion:

$$F_r = F_{r0} + \frac{\partial F_r}{\partial \epsilon} \epsilon_1 + \frac{\partial F_r}{\partial \epsilon \partial \varphi} \epsilon_0 \varphi_1 + \frac{\partial F_r}{\partial \dot{\epsilon}} \dot{\epsilon}_1 + \frac{\partial F_r}{\partial \epsilon \partial \dot{\varphi}} \epsilon_0 \dot{\varphi}_1$$

$$F_t = F_{t0} + \frac{\partial F_t}{\partial \epsilon} \epsilon_1 + \frac{\partial F_t}{\partial \epsilon \partial \varphi} \epsilon_0 \varphi_1 + \frac{\partial F_t}{\partial \dot{\epsilon}} \dot{\epsilon}_1 + \frac{\partial F_t}{\partial \epsilon \partial \dot{\varphi}} \epsilon_0 \dot{\varphi}_1$$

$$M_\alpha = \frac{\partial M_\alpha}{\partial \alpha} \alpha + \frac{\partial M_\alpha}{\partial \dot{\alpha}} \dot{\alpha} + \frac{\partial M_\alpha}{\partial \beta} \beta + \frac{\partial M_\alpha}{\partial \dot{\beta}} \dot{\beta}$$

$$M_\beta = \frac{\partial M_\beta}{\partial \alpha} \alpha + \frac{\partial M_\beta}{\partial \dot{\alpha}} \dot{\alpha} + \frac{\partial M_\beta}{\partial \beta} \beta + \frac{\partial M_\beta}{\partial \dot{\beta}} \dot{\beta}$$

The partial derivations represent the dynamic coefficients for the fluid film. They are obtained from a perturbation solution of Reynold's equation as described in the following.

For an incompressible lubricant, Reynold's equation can be written in dimensionless form as:

$$\frac{\partial}{\partial \theta} \left[h^3 \frac{\partial P}{\partial \theta} \right] + \frac{\partial}{\partial \zeta} \left[h^3 \frac{\partial P}{\partial \zeta} \right] = \frac{\partial h}{\partial \theta} + 2 \frac{\partial h}{\partial \tau} \quad (1)$$

where

$$P = \frac{\bar{P}}{6\mu W \left(\frac{R}{C}\right)^2}, \quad h = \frac{\bar{h}}{C}, \quad \zeta = \frac{\bar{Z}}{R}, \quad \tau = \omega t$$

assuming that the bearing is operating under isothermal conditions such that the viscosity of the lubricant is constant.

Set
$$\psi = \frac{3}{2} ph^2$$

and then Eq. (1) becomes

$$\frac{\partial^2 \psi}{\partial \theta^2} + \frac{\partial^2 \psi}{\partial \zeta^2} - \frac{3}{2} \left[\frac{1}{2} h^{-2} \left(\left(\frac{\partial h}{\partial \theta} \right)^2 + \left(\frac{\partial h}{\partial \zeta} \right)^2 \right) + h^{-1} \left(\frac{\partial^2 h}{\partial \theta^2} + \frac{\partial^2 h}{\partial \zeta^2} \right) \right] \psi = h^{-\frac{3}{2}} \left[\frac{\partial h}{\partial \theta} + 2 \frac{\partial h}{\partial \tau} \right] \quad (3)$$

The translatory motion of the journal is defined by the coordinates ϵ and φ and the corresponding velocity components $\dot{\epsilon}$ and $\dot{\varphi}$. Similarly, the angular motion is defined by the angular displacements α and β with velocity components $\dot{\alpha}$ and $\dot{\beta}$, as shown in Fig. 1. To make the first order perturbation set:

$$h = h_0 + \epsilon_1 \cos(\theta - \varphi_0) + \epsilon_0 \varphi_1 \sin(\theta - \varphi_0) - \zeta \alpha \sin(\theta - \varphi_0) + \zeta \beta \cos(\theta - \varphi_0) \quad (4)$$

$$\psi = \psi_0 + \epsilon_1 P_1 + \epsilon_0 \varphi_1 P_2 + \dot{\epsilon} P_3 + \epsilon_0 \dot{\varphi} P_4 + \alpha P_5 + \beta P_6 + \dot{\alpha} P_7 + \dot{\beta} P_8 \quad (5)$$

$$\text{where } h_0 = 1 + \epsilon_0 \cos(\theta - \varphi_0)$$

Hence:

$$h^{-\frac{3}{2}} = h_0^{-\frac{3}{2}} - \frac{3}{2} h_0^{-\frac{5}{2}} \left[\epsilon_1 \cos(\theta - \varphi_0) + \epsilon_0 \varphi_1 \sin(\theta - \varphi_0) - \zeta \alpha \sin(\theta - \varphi_0) + \zeta \beta \cos(\theta - \varphi_0) \right] \quad (6)$$

$$\begin{aligned} \frac{\psi}{h^{\frac{3}{2}}} = h_0^{-\frac{3}{2}} & \left\{ \psi_0 + \left[P_1 - \frac{3}{2} \frac{\cos(\theta - \varphi_0)}{h_0} \psi_0 \right] \epsilon_1 + \left[P_2 - \frac{3}{2} \frac{\sin(\theta - \varphi_0)}{h_0} \psi_0 \right] \epsilon_0 \varphi_1 + P_3 \dot{\epsilon} \right. \\ & \left. + P_4 \epsilon_0 \dot{\varphi} + \left[P_5 + \frac{3}{2} \frac{\zeta \sin(\theta - \varphi_0)}{h_0} \psi_0 \right] \alpha + \left[P_6 + \frac{3}{2} \frac{\zeta \cos(\theta - \varphi_0)}{h_0} \psi_0 \right] \beta + P_7 \dot{\alpha} + P_8 \dot{\beta} \right\} \quad (7) \end{aligned}$$

$$\frac{\partial h}{\partial \tau} = \dot{\epsilon} \cos(\theta - \varphi_0) + \epsilon_0 \dot{\varphi} \sin(\theta - \varphi_0) - \zeta \dot{\alpha} \sin(\theta - \varphi_0) + \zeta \dot{\beta} \cos(\theta - \varphi_0) \quad (8)$$

$$\frac{\partial h}{\partial \theta} = \frac{\partial h_0}{\partial \theta} - \epsilon_1 \sin(\theta - \varphi_0) + \epsilon_0 \varphi_1 \cos(\theta - \varphi_0) - \zeta \alpha \cos(\theta - \varphi_0) - \zeta \beta \sin(\theta - \varphi_0) \quad (9)$$

$$\frac{\partial h}{\partial \xi} = -\alpha \sin(\theta - \varphi_0) + \beta \cos(\theta - \varphi_0) \quad (10)$$

Substituting Eqs. (4), (5), (8), (9) and (10) into Eq. (3) and then collecting terms corresponding to ϵ_0 , ϵ_1 , $\epsilon_0 \psi_1$, $\dot{\epsilon}$, $\epsilon_0 \dot{\varphi}$, α , β , $\dot{\alpha}$ and $\dot{\beta}$ respectively, the general form of these result equations is:

$$\frac{\partial^2 \bar{\psi}_j}{\partial \theta^2} + \frac{\partial^2 \bar{\psi}_j}{\partial \xi^2} + A \bar{\psi}_j = B_j \quad (j = 0, 1, \dots, 8) \quad (11)$$

where

$$\bar{\psi}_0 = \psi_0$$

$$\bar{\psi}_1 = P_1$$

$$\bar{\psi}_2 = P_2, \quad \text{etc.}$$

$$A = -\frac{3}{2} \frac{1}{2} \left[\frac{\epsilon_0^2 \sin^2(\theta - \varphi_0)}{h_0^2} - \frac{\epsilon_0 \cos(\theta - \varphi_0)}{h_0} \right]$$

$$B_0 = -\frac{\epsilon_0 \sin(\theta - \varphi_0)}{h_0^{\frac{3}{2}}}$$

$$B_1 = \frac{3}{2} \left[-\frac{\cos(\theta - \varphi_0)}{h_0} + \frac{\epsilon_0 (1 + \epsilon_0 \cos^3(\theta - \varphi_0))}{h_0^3} \right] \psi_0 - \frac{\sin(\theta - \varphi_0)}{h_0^{\frac{5}{2}}} \left[1 - \frac{1}{2} \epsilon_0 \cos(\theta - \varphi_0) \right]$$

$$B_2 = -\frac{3}{2} \left[\frac{1}{h_0^2} + \frac{\epsilon_0 \cos(\theta - \varphi_0) + \epsilon_0^2}{h_0^3} \right] \sin(\theta - \varphi_0) \cdot \psi_0$$

$$+ 1 - \frac{1}{2} \epsilon_0 \cos(\theta - \varphi_0) \frac{\cos(\theta - \varphi_0)}{h_0^{\frac{5}{2}}} + \frac{3}{2} \frac{\epsilon_0}{h_0^{\frac{5}{2}}}$$

$$B_3 = \frac{2 \cos(\theta - \varphi_0)}{h_0^{\frac{3}{2}}}$$

$$B_4 = -\frac{2}{\epsilon_0} B_0$$

$$B_5 = -\zeta B_2$$

$$B_6 = \zeta B_1$$

$$B_7 = \frac{2}{\epsilon_0} \zeta B_0$$

$$B_8 = \zeta B_3$$

The pressures at both ends of the bearing and at the leading and trailing edges are ambient (i.e., = 0). At the bearing centerline there is symmetry. Thus, the boundary conditions become

$$\begin{aligned} \psi_0 = P_1 = \dots = P_8 = 0 \quad \text{at } \zeta = \xi, \theta = \theta_1 \text{ and } \theta = \theta_2 \\ \left\{ \begin{array}{l} P_5 = P_6 = P_7 = P_8 = 0 \\ \frac{\partial \psi_0}{\partial \zeta} = \frac{\partial P_1}{\partial \zeta} = \frac{\partial P_2}{\partial \zeta} = \frac{\partial P_3}{\partial \zeta} = \frac{\partial P_4}{\partial \zeta} \end{array} \right. \quad \text{at } \zeta = 0 \end{aligned} \quad (12)$$

the pressure distribution $\bar{\psi}_j$ can be solved by using a finite difference method as described later.

The components of load carrying capacity and the restoring moments in dimensionless form can be calculated from

$$F_r = -\frac{6\pi}{\xi} \int_0^\xi \int_{\theta_1}^{\theta_2} \cos(\theta - \varphi_0) \frac{\psi}{h^2} d\zeta d\theta \quad (13)$$

$$F_t = \frac{6\pi}{\xi} \int_0^\xi \int_{\theta_1}^{\theta_2} \sin(\theta - \varphi_0) \frac{\psi}{h^2} d\zeta d\theta$$

$$M_{\beta} = - \frac{3\pi}{2\xi^3} \int_0^{\xi} \int_{\theta_1}^{\theta_2} \zeta \cos(\theta - \varphi_0) \frac{\psi}{h_o^{\frac{3}{2}}} d\zeta d\theta \quad (14)$$

$$M_{\alpha} = \frac{3\pi}{2\xi^3} \int_0^{\xi} \int_{\theta_1}^{\theta_2} \zeta \sin(\theta - \varphi_0) \frac{\psi}{h_o^{\frac{3}{2}}} d\zeta d\theta$$

Substituting Eq. (7) into Eqs. (13) and (14) and then collecting terms in accordance with the first order Taylor's series expansion of restoring force and moment, the results are:

$$F_{ro} = - \frac{6\pi}{\xi} \int_0^{\xi} \int_{\theta_1}^{\theta_2} \cos(\theta - \varphi_0) \frac{\psi_o}{h_o^{\frac{3}{2}}} d\theta . d\zeta$$

$$\frac{\partial F_r}{\partial \epsilon} = - \frac{6\pi}{\xi} \int_0^{\xi} \int_{\theta_1}^{\theta_2} \left[P_1 - \frac{3}{2} \frac{\cos(\theta - \varphi_0)}{h_o} \psi_o \right] \frac{\cos(\theta - \varphi_0)}{h_o^{\frac{3}{2}}} d\theta . d\zeta$$

$$\frac{\partial F_r}{\epsilon_o \partial \varphi} = - \frac{6\pi}{\xi} \int_0^{\xi} \int_{\theta_1}^{\theta_2} \left[P_2 - \frac{3}{2} \frac{\sin(\theta - \varphi_0)}{h_o} \psi_o \right] \frac{\cos(\theta - \varphi_0)}{h_o^{\frac{3}{2}}} d\theta . d\zeta$$

$$\frac{\partial F_r}{\partial \epsilon} = - \frac{6\pi}{\xi} \int_0^{\xi} \int_{\theta_1}^{\theta_2} P_3 \frac{\cos(\theta - \varphi_1)}{h_o^{\frac{3}{2}}} d\theta d\zeta$$

$$\frac{\partial F_r}{\epsilon_o \partial \varphi} = - \frac{6\pi}{\xi} \int_0^{\xi} \int_{\theta_1}^{\theta_2} P_4 \frac{\cos(\theta - \varphi_0)}{h_o^{\frac{3}{2}}} d\theta . d\zeta$$

$$\frac{\partial M_{\beta}}{\partial \alpha} = - \frac{3}{2} \frac{\pi}{\xi^3} \int_0^{\xi} \int_{\theta_1}^{\theta_2} \left[P_5 + \frac{3}{2} \zeta \frac{\sin(\theta - \varphi_0)}{h_o} \psi_o \right] \frac{\zeta \cos(\theta - \varphi_0)}{h_o^{\frac{3}{2}}} d\theta . d\zeta$$

$$\frac{\partial M_B}{\partial \beta} = -\frac{3}{2} \frac{\pi}{\xi^3} \int_0^\xi \int_{\theta_1}^{\theta_2} \left[P_6 - \frac{3}{2} \xi \frac{\cos(\theta - \varphi_0)}{h_0} \psi_0 \right] \frac{\xi \cos(\theta - \varphi_0)}{h_0^{\frac{3}{2}}} d\theta d\xi$$

$$\frac{\partial M_B}{\partial \alpha} = -\frac{3}{2} \frac{\pi}{\xi^3} \int_0^\xi \int_{\theta_1}^{\theta_2} \frac{P_7}{h_0^{\frac{3}{2}}} \xi \cos(\theta - \varphi_0) d\theta d\xi$$

$$\frac{\partial M_B}{\partial \beta} = -\frac{3}{2} \frac{\pi}{\xi^3} \int_0^\xi \int_{\theta_1}^{\theta_2} \frac{P_8}{h_0^{\frac{3}{2}}} \xi \cos(\theta - \varphi_0) d\theta d\xi$$

and similarly for F_t and M_α .

The perturbed pressures ψ_0 , P_1, \dots, P_8 can be obtained from Eqs. (7) for given values of ψ_0 and ϵ_0 and for a specified bearing geometry (i.e., L/D , θ_1 and θ_2).

Under static equilibrium condition:

$$F_{ho} = -F_{ro} \sin \varphi_0 + F_{to} \cos \varphi_0 = 0.$$

$$S = \frac{1}{\sqrt{F_{ro}^2 + F_{to}^2}}$$

$$\varphi_0 = \tan^{-1} \left(\frac{F_{to}}{F_{ro}} \right)$$

The spring and damping coefficients along the radial and tangential directions are given as follows:

$$\frac{CK_{rr}}{W} = S \frac{\partial F_r}{\partial \epsilon}, \quad \frac{CK_{tr}}{W} = S \frac{\partial F_t}{\partial \epsilon}$$

$$\frac{CK_{rt}}{W} = S \frac{\partial F_r}{\partial \epsilon_0 \partial \varphi}, \quad \frac{CK_{tt}}{W} = S \frac{\partial F_t}{\partial \epsilon_0 \partial \varphi}$$

$$\frac{C\omega B}{W} \frac{rr}{r} = S \frac{\partial F}{\partial \dot{\epsilon}} \frac{r}{r}, \quad \frac{C\omega B}{W} \frac{tr}{r} = S \frac{\partial F}{\partial \dot{\epsilon}} \frac{t}{r}$$

$$\frac{C\omega B}{W} \frac{rt}{r} = S \frac{\partial F}{\partial \epsilon_0} \frac{r}{\partial \varphi}, \quad \frac{C\omega B}{W} \frac{tt}{r} = S \frac{\partial F}{\partial \epsilon_0} \frac{t}{\partial \varphi}$$

The spring and damping coefficients for angular motion along the radial and tangential directions are given as follows:

$$\frac{CM}{WL^2} \frac{rr}{r} = S \frac{\partial M}{\partial \beta} \frac{r}{r}, \quad \frac{CM}{WL^2} \frac{tr}{r} = S \frac{\partial M}{\partial \beta} \frac{t}{r}$$

$$\frac{CM}{WL^2} \frac{rt}{r} = S \frac{\partial M}{\partial \alpha} \frac{r}{\alpha}, \quad \frac{CM}{WL^2} \frac{tt}{r} = S \frac{\partial M}{\partial \alpha} \frac{t}{\alpha}$$

$$\frac{C\omega D}{WL^2} \frac{rr}{r} = S \frac{\partial D}{\partial \beta} \frac{r}{r}, \quad \frac{C\omega D}{WL^2} \frac{tr}{r} = S \frac{\partial D}{\partial \beta} \frac{t}{r}$$

$$\frac{C\omega D}{WL^2} \frac{rt}{r} = S \frac{\partial D}{\partial \alpha} \frac{r}{\alpha}, \quad \frac{C\omega D}{WL^2} \frac{tt}{r} = S \frac{\partial D}{\partial \alpha} \frac{t}{\alpha}$$

In performing a rotor response analysis it is more convenient to express the dynamic coefficients in a coordinate system whose orientation is independent of the static equilibrium position. This new system, the ξ - η system, has the ξ -axis parallel to the load direction and the η -axis is perpendicular to the load direction. The transformation equations from the ϵ_0 - φ_0 system to the ξ - η system are given by:

$$K_{\xi\xi} = K_{rr} \cos^2 \varphi_0 - K_{tt} \sin^2 \varphi_0 - (K_{rt} - K_{tr}) \cos \varphi_0 \sin \varphi_0$$

$$K_{\xi\eta} = K_{rt} \cos^2 \varphi_0 + K_{tr} \sin^2 \varphi_0 + (K_{rr} + K_{tt}) \cos \varphi_0 \sin \varphi_0$$

$$K_{\eta\xi} = K_{tr} \cos^2 \varphi_0 - K_{rt} \sin^2 \varphi_0 + (K_{rr} + K_{tt}) \cos \varphi_0 \sin \varphi_0$$

$$K_{\eta\eta} = -K_{tt} \cos^2 \varphi_0 + K_{rr} \sin^2 \varphi_0 + (K_{rt} - K_{tr}) \cos \varphi_0 \sin \varphi_0$$

$B_{\xi\xi}$, $B_{\xi\eta}$, $B_{\eta\xi}$ and $B_{\eta\eta}$ are analogous.

$$M_{\xi\xi} = M_{rr} \cos^2 \varphi_0 + M_{tt} \sin^2 \varphi_0 + (M_{rt} + M_{tr}) \cos \varphi_0 \sin \varphi_0$$

$$M_{\xi\eta} = -M_{rt} \cos^2 \varphi_0 + M_{tr} \sin^2 \varphi_0 + (M_{rr} - M_{tt}) \cos \varphi_0 \sin \varphi_0$$

$$M_{\eta\xi} = -M_{tr} \cos^2 \varphi_0 + M_{rt} \sin^2 \varphi_0 + (M_{rr} - M_{tt}) \cos \varphi_0 \sin \varphi_0$$

$$M_{\eta\eta} = M_{tt} \cos^2 \varphi_0 + M_{rr} \sin^2 \varphi_0 - (M_{rt} + M_{tr}) \cos \varphi_0 \sin \varphi_0$$

$D_{\xi\xi}$, $D_{\xi\eta}$, $D_{\eta\xi}$ and $D_{\eta\eta}$ are analogous

Finite Difference Equations

The pressure distribution equation is given as follows:

$$\frac{\partial^2 \Phi}{\partial \theta^2} + \frac{\partial^2 \Phi}{\partial \xi^2} + f_5(\theta) \cdot \Phi = f_6(\theta, \xi) \quad (15)$$

and then the corresponding finite difference equation is

$$\frac{1}{\Delta \xi^2} \Phi_{i+1,j} + \frac{1}{\Delta \xi^2} \Phi_{i-1,j} - 2 \left(\frac{1}{\Delta \xi^2} + \frac{1}{\Delta \xi^2} + f_{5,j} \right) \Phi_{i,j} + \frac{1}{\Delta \theta^2} \Phi_{i,j+1} + \frac{1}{\Delta \theta^2} \Phi_{i,j-1} = f_{6,i,j} \quad (16)$$

where the finite difference mesh is as follows:

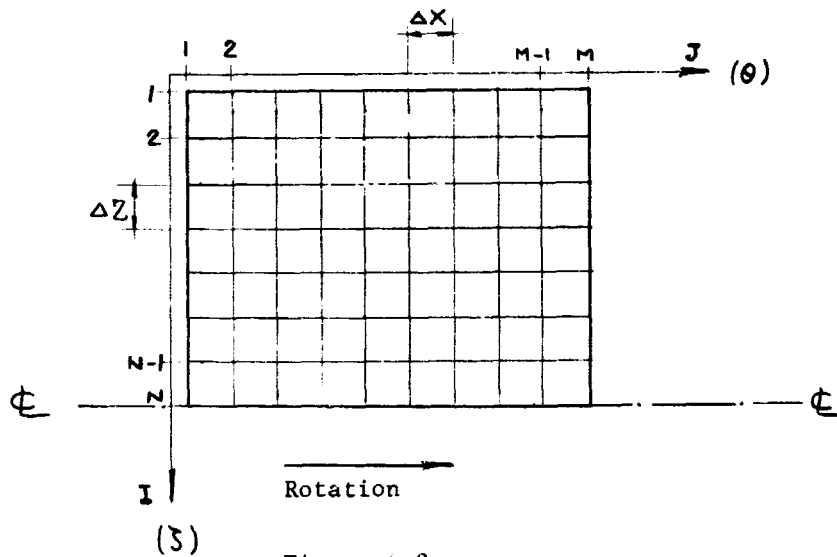


Figure A-2

The general form of the numerical approximation to Eq. (15) can also be represented in matrix notation as follows:

$$A_j \phi_j + B_j \phi_{j-1} + C_j \phi_{j+1} = F_j \quad (j = 1, 2, \dots, M-1, M) \quad (17)$$

where

M = number of columns

ϕ_j = vector of j th column of unknown ϕ

F_j = vector of j th column of right hand side of Eq. (17)

B_j and C_j are $N \times N$ diagonal matrices

A_j is $N \times N$ tridiagonal matrix

The solution of Eq. (17) can be obtained from searching for the influence coefficients between two successive ϕ - vectors and their relations can be written as

$$\phi_{j-1} = D_j \phi_j + E_j \quad (18)$$

Substituting Eq. (18) into Eq. (17), yields:

$$\Phi_j = (A_j + B_j D_j)^{-1} \left[-C_j \Phi_{j+1} - E_j E_j + F_j \right] \quad (19)$$

Comparing Eq. (19) with Eq. (18), the recurrence relationship for the matrices D_j and E_j are obtained as

$$D_{j+1} = -K_j C_j \quad (20)$$

$$E_{j+1} = K_j (-B_j E_j + F_j)$$

where

$$K_j = (A_j + B_j D_j)^{-1}. \quad (21)$$

Since Φ_1 is given equal to zero (from boundary conditions), then D_2 and E_2 are equal to zero by Eq. (18), K_2 is obtained from Eq. (21), and then D_3 and E_3 are determined from Eq. (20). Therefore, all values of Φ_j can be obtained from the boundary conditions for Φ and Eq. (18).

NOMENCLATURE FOR APPENDIX A

$B_{rr}, B_{rt}, B_{tr}, B_{tt}$	- Pad damping coefficients for translatory motion in the radial and tangential directions, lbs.sec/in.
$B_{\xi\xi}, B_{\xi\eta}, B_{\eta\xi}, B_{\eta\eta}$	- Pad damping coefficients for translatory motion in $\xi - \eta$ directions, lbs.sec/in.
C	- Radial bearing clearance, inch
D	- Journal diameter, inch
$D_{rr}, D_{rt}, D_{tr}, D_{tt}$	- Pad damping coefficients for rotational whirl in the radial and tangential directions, lbs.in.sec/radians.
$D_{\xi\xi}, D_{\xi\eta}, D_{\eta\xi}, D_{\eta\eta}$	- Pad damping coefficients for rotational whirl in $\xi - \eta$ directions, lbs.in sec/radians.
F_r, F_t	- Radial and tangential components of dimensionless pad forces.
F_{ro}, F_{to}, F_{ho}	- Static radial, tangential and horizontal components of dimensionless pad forces.
\bar{h}	- Radial film thickness, inch
h	- $= \bar{h}/C$, Dimensionless radial film thickness
h_o	- Dimensionless static radial film thickness
$K_{rr}, K_{rt}, K_{tr}, K_{tt}$	- Pad spring coefficients for translatory motion in the radial and tangential directions, lbs/in.
$K_{\xi\xi}, K_{\xi\eta}, K_{\eta\xi}, K_{\eta\eta}$	- Pad spring coefficients for translatory motion in $\xi - \eta$ directions, lbs/in.
L	- Journal length, inch
$M_{rr}, M_{rt}, M_{tr}, M_{tt}$	- Pad spring coefficients for rotational whirl in the radial and tangential directions, lbs.in/radians
$M_{\xi\xi}, M_{\xi\eta}, M_{\eta\xi}, M_{\eta\eta}$	- Pad spring coefficients for rotational whirl in $\xi - \eta$ directions, lbs.in/radians.
\bar{P}	- Film pressure, psia
P	- Dimensionless film pressure
P_1, P_2, \dots, P_8	- Dimensionless first order perturbed pressures
ψ	- $= Ph^2$, Dimensionless film pressure

Nomenclature (cont'd)

ψ_0	- Static dimensionless film pressure
R	- Journal radius, inch
S	- Pad Sommerfeld number
t	- Time, seconds.
Z	- Axial coordinate, inch
θ	- Circumferential angular coordinate, radians
ζ	- $= Z/R$, Dimensionless axial coordinate
μ	- Viscosity, lbs.sec/in ²
ω	- Angular speed of journal, rad/sec.
τ	- ωt , dimensionless time
ϵ_0	- Static eccentricity ratio
ϕ_0	- Static altitude angle, degrees
A, B	- Variable coefficients of differential equations for film pressure in Eq. (11).
ξ	- $= L/D$
i, j	- Finite difference axial and circumferential coordinates, see Fig. A-2.
m	- Number of circumferential subdivisions, see Fig. A-2
n	- Number of axial subdivisions, see Fig. A-2.
θ_1	- The leading angle of the pad, degrees, see Fig. A-1.
θ_2	- The trailing angle of the pad, degrees, see Fig. A-1.

APPENDIX B

Dynamic Coefficients for the Tilting Pad Journal Bearing

For a given steady-state operating condition of a tilting pad journal bearing, the eccentricity ratio and the attitude angle for each pad are known. Hence, the dynamic coefficients for each pad film are also known (See Appendix A). To get the dynamic coefficients of the complete tilting pad journal bearing, it is necessary to take into account the inertia and the tilting of each pad. Furthermore, when the pads are mounted on the flexibly supported pivots, the support flexibility must also be included in the calculation.

Consider a single pad which is free to tilt around an axial axis passing through the pivot point. This motion is called the pitch motion of the pad. Introducing a cartesian coordinate system (the ξ - η system) with the origins in the steady-state journal center position and with the ξ -axis passing through the pivot point, the motion of the pad center is parallel to the η_p , measured from the steady-state position of the pad center. Similarly, the pad has the radial motion ξ_p in the ξ -direction because of the flexible pivot support with stiffness K_p . With the 8 dynamic coefficients of the fluid film given as $K_{\xi\xi}$, $B_{\xi\xi}$, etc (see Appendix A), the forces acting on the journal with the amplitudes ξ and η become,

$$F_{\xi} = -Z_{\xi\xi} (\xi - \xi_p) - Z_{\xi\eta} (\eta - \eta_p) \quad (1)$$

$$F_{\eta} = -Z_{\eta\xi} (\xi - \xi_p) - Z_{\eta\eta} (\eta - \eta_p) \quad (2)$$

where

$$Z_{\xi\xi} = K_{\xi\xi} + i\omega b_{\xi\xi} \text{ etc.} \quad (3)$$

The equations of motion for the pad are:

$$\frac{I_p}{R^2} \ddot{\eta}_p = -F_{\eta} \quad (4)$$

$$M_p \ddot{\xi}_p = -F_{\xi} - K_p \xi_p \quad (5)$$

Let the journal be subjected to harmonic motion:

$$(\xi, \eta) e^{i\omega t}$$

Then from the Eqs. (4) and (5), obtain:

$$(\xi - \xi_p) = \alpha_{\xi\xi} \xi + \alpha_{\xi\eta} \eta \quad (6)$$

$$(\eta - \eta_p) = \alpha_{\eta\xi} \xi + \alpha_{\eta\eta} \eta \quad (7)$$

where:

$$\alpha_{\xi\xi} = \frac{(K_p - M_p \omega^2) (Z_{\eta\eta} - \frac{I_p}{R^2} \omega^2)}{A^*}$$

$$\alpha_{\xi\eta} = \frac{\frac{I_p}{R^2} \omega^2 \cdot Z_{\xi\eta}}{A^*}$$

$$\alpha_{\eta\xi} = - \frac{(K_p - M_p \omega^2) \cdot Z_{\eta\xi}}{A^*}$$

$$\alpha_{\eta\eta} = - \frac{\frac{I_p}{R^2} \omega^2 (Z_{\xi\xi} + K_p - M_p \omega^2)}{A^*}$$

$$\text{and } A^* = (Z_{\xi\xi} + K_p - M_p \omega^2) (Z_{\eta\eta} - \frac{I_p}{R^2} \omega^2) - Z_{\xi\eta} \cdot Z_{\eta\xi}$$

The dynamic coefficients for the tilting pad are related to the forces acting on the journal by:

$$F_\xi = - Z'_{\xi\xi} \xi - Z'_{\xi\eta} \eta \quad (8)$$

$$F_\eta = - Z'_{\eta\xi} \xi - Z'_{\eta\eta} \eta \quad (9)$$

By substituting Eqs. (6) and (7) into Eqs. (1) and (2), these dynamic coefficients become:

$$Z'_{\xi\xi} = \alpha_{\xi\xi} Z_{\xi\xi} + \alpha_{\eta\xi} Z_{\xi\eta} \quad (10)$$

$$Z'_{\xi\eta} = \alpha_{\xi\eta} Z_{\xi\xi} + \alpha_{\eta\eta} Z_{\xi\eta} \quad (11)$$

$$Z'_{\eta\xi} = \alpha_{\xi\xi} Z_{\eta\xi} + \alpha_{\eta\xi} Z_{\eta\eta} \quad (12)$$

$$Z'_{\eta\eta} = \alpha_{\xi\eta} Z_{\eta\xi} + \alpha_{\eta\eta} Z_{\eta\eta} \quad (13)$$

The x-y coordinate system for the bearing is employed with the origin in the steady-state journal center position and with the x-axis in the load direction (see Fig. B-1). The vibratory forces acting on the journal are

$$F_x = -Z_{xx}X - Z_{xy}Y \quad (14)$$

$$F_y = -Z_{yx}X - Z_{yy}Y \quad (15)$$

where

$$Z_{xx} = K_{xx} + i\omega B_{xx} \quad \text{etc.}$$

The coordinate transformations are:

$$\begin{Bmatrix} \xi \\ \eta \end{Bmatrix} = - \begin{Bmatrix} \cos\psi & \sin\psi \\ -\sin\psi & \cos\psi \end{Bmatrix} \begin{Bmatrix} X \\ Y \end{Bmatrix}$$

$$\begin{Bmatrix} F_x \\ F_y \end{Bmatrix} = - \begin{Bmatrix} \cos\psi & -\sin\psi \\ \sin\psi & \cos\psi \end{Bmatrix} \begin{Bmatrix} F_\xi \\ F_\eta \end{Bmatrix}$$

Substituting into Eqs. (8) and (9), the dynamic coefficients of the tilting pad in the x-y coordinate system become

$$K_{xx} = K'_{\xi\xi} \cos^2\psi + K'_{\eta\eta} \sin^2\psi - (K'_{\xi\eta} + K'_{\eta\xi}) \sin\psi \cos\psi$$

$$\omega B_{xx} = \omega B'_{\xi\xi} \cos^2\psi + \omega B'_{\eta\eta} \sin^2\psi - (\omega B'_{\xi\eta} + \omega B'_{\eta\xi}) \sin\psi \cos\psi$$

$$K_{xy} = K'_{\xi\eta} \cos^2\psi - K'_{\eta\xi} \sin^2\psi + (K'_{\xi\xi} - K'_{\eta\eta}) \sin\psi \cos\psi$$

$$\omega B_{xy} = \omega B'_{\xi\eta} \cos^2\psi - \omega B'_{\eta\xi} \sin^2\psi + (\omega B'_{\xi\xi} - \omega B'_{\eta\eta}) \sin\psi \cos\psi$$

$$K_{yx} = K'_{\eta\xi} \cos^2\psi - K'_{\xi\eta} \sin^2\psi + (K'_{\xi\xi} - K'_{\eta\eta}) \sin\psi \cos\psi$$

$$\omega B_{yx} = \omega B'_{\eta\xi} \cos^2 \psi - \omega B'_{\xi\eta} \sin^2 \psi + (\omega B'_{\xi\xi} - \omega B'_{\eta\eta}) \sin \psi \cos \psi$$

$$K_{yy} = K'_{yy} \cos^2 \psi + K'_{\xi\xi} \sin^2 \psi + (K'_{\xi\eta} + K'_{\eta\xi}) \sin \psi \cos \psi$$

$$\omega B_{yy} = \omega B'_{\eta\eta} \cos^2 \psi + \omega B'_{\xi\xi} \sin^2 \psi + (\omega B'_{\xi\eta} + \omega B'_{\eta\xi}) \sin \psi \cos \psi$$

where:

$$K'_{\xi\xi} = \text{Re} \left\{ Z'_{\xi\xi} \right\}$$

$$\omega B'_{\xi\xi} = \text{Im} \left\{ Z'_{\xi\xi} \right\} \quad \text{etc.}$$

A summation over all the pads making up the bearing gives the complete tilting pad bearing spring and damping coefficients. These coefficients can then be used directly in the rotor response calculations.

The Motion of the Pads

Once the amplitude response of the rotor is known, the corresponding pad motion can be computed by means of the dynamic coefficients for the pad film.

A single pad can not only perform a pitch motion with amplitude η_p and a radial motion with amplitude ξ_p as described above, but it is also free to rotate around any other axis passing through the pivot point. These additional degrees of freedom are defined by the roll angle γ_ξ around a tangential axis and the yaw angle γ_η around the pivot axis (the ξ -axis) see Fig.B-1. The corresponding mass moments of inertia for the pad are I_ξ and I_η and the corresponding dynamic moment coefficients for the fluid film are $M_{\xi\xi}$, $D_{\xi\xi}$ etc. (see Appendix A). The angular motion of the rotor is defined by the angular displacements θ_ξ and θ_η of the journal. Hence, the equations of motion for the pad become:

$$I_\xi \ddot{\gamma}_\xi = Q_{\xi\xi} (\theta_\xi - \gamma_\xi) + Q_{\xi\eta} (\theta_\eta - \gamma_\eta) \quad (18)$$

$$I_\eta \ddot{\gamma}_\eta = Q_{\eta\xi} (\theta_\xi - \gamma_\xi) + Q_{\eta\eta} (\theta_\eta - \gamma_\eta) \quad (19)$$

where

$$Q_{\xi\xi} = M_{\xi\xi} + i\omega D_{\xi\xi} \quad \text{etc.}$$

$$(\gamma_{\xi}, \gamma_{\eta}) = (\gamma_{\xi}, \gamma_{\eta}) e^{i\omega t}$$

Solving Eqs. (18) and (19) and get:

$$\gamma_{\xi} = \left[1 + \frac{I_{\xi}\omega^2(Q_{\eta\eta} - I_{\eta}\omega^2)}{B^*} \right] \theta_{\xi} - \frac{I_{\eta}\omega^2 Q_{\xi\eta}}{B^*} \theta_{\eta}$$

$$\gamma_{\eta} = - \frac{I_{\xi}\omega^2 Q_{\eta\xi}}{B^*} \theta_{\xi} + \left[1 + \frac{I_{\eta}\omega^2(Q_{\xi\xi} - I_{\xi}\omega^2)}{B^*} \right] \theta_{\eta}$$

where

$$B^* = (Q_{\xi\xi} - I_{\xi}\omega^2)(Q_{\eta\eta} - I_{\eta}\omega^2) - Q_{\xi\eta} Q_{\eta\xi}$$

Thus, the roll and yaw motions of the pad can be determined when the angular displacements of the rotor have been given. Similarly, the pitch motion η_p and the radial motion ξ_p can be calculated from Eqs. (6). Finally, the force transmitted through the pivots becomes,

$$F_p = - \xi_p K_p \quad (20)$$

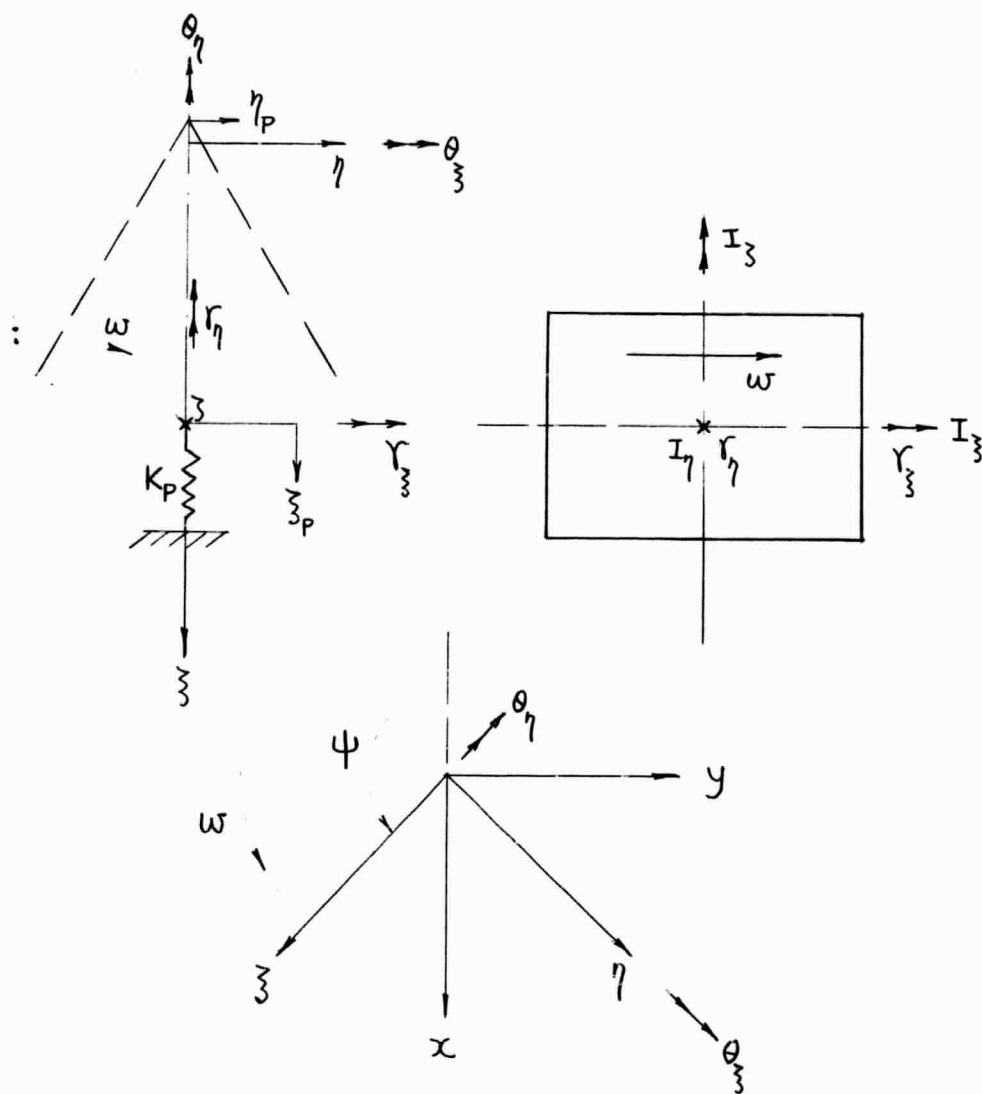


Figure B-1

NOMENCLATURE FOR APPENDIX B

$B_{\xi\xi}, B_{\xi\eta}, B_{\eta\xi}, B_{\eta\eta}$	Fixed pad damping coefficients for translatory motion, lbs.sec/in.
$B'_{\xi\xi}, B'_{\xi\eta}, B'_{\eta\xi}, B'_{\eta\eta}$	Tilting pad damping coefficients for translatory motion in ξ - η direction, lbs.sec/in.
$B_{xx}, B_{xy}, B_{yx}, B_{yy}$	Tilting pad damping coefficients for translatory motion in x-y direction, lb.sec/in.
$D_{\xi\xi}, D_{\xi\eta}, D_{\eta\xi}, D_{\eta\eta}$	Fixed pad damping coefficients for rotational motion, lb.in.sec/radians.
F_{ξ}, F_{η}	Fluid film force components in ξ - η direction, lbs.
F_x, F_y	Fluid film force components in x-y direction, lbs.
F_p	Transmitted force through the pivot, lbs.
$K_{\xi\xi}, K_{\xi\eta}, K_{\eta\xi}, K_{\eta\eta}$	Fixed pad spring coefficients for translatory motion, lbs/in.
$K'_{\xi\xi}, K'_{\xi\eta}, K'_{\eta\xi}, K'_{\eta\eta}$	Tilting pad spring coefficients for translatory motion in ξ - η direction, lbs/in.
$K_{xx}, K_{xy}, K_{yx}, K_{yy}$	Tilting pad spring coefficients for translatory motion in x-y direction, lbs/in.
K_p	Stiffness for the pivot support, lb/in.
$M_{\xi\xi}, M_{\xi\eta}, M_{\eta\xi}, M_{\eta\eta}$	Fixed pad spring coefficients for rotational motion, lbs.in/radians
M_p	Mass for the pivot support, lb.sec ² /in.
Q	$= M + i \omega D$
R	Journal radius, inches
x, y	Coordinates, see Fig. B-1, inches
Z	$= K + i \omega B$
I_{ζ}	Mass moment of inertia of pad around the axial axis, lb.in.sec ² .
I_{ξ}	Mass moment of inertia of pad around the tangential axis, lb.in.sec ² .
I_{η}	Mass moment of inertia of pad around the pivot axis, lb.in.sec ² .

NOMENCLATURE (cont'd)

γ_{ξ}	Angular displacement of pad around the tangential axis, radians
γ_{η}	Angular displacement of pad around the pivot axis, radians.
η_p	Coordinate for pad center motion, inches.
ξ_p	Radial motion for the pad, inches.
ξ, η	Coordinate, see Fig. B-1, inches.
ω	Angular speed of journal, rad/sec.
ψ	Angular position of pivot point, degrees.
$\theta_{\xi}, \theta_{\eta}$	Angular displacements of the journal, degrees
t	Time, seconds

APPENDIX C

Microslips Between Contacting Paraboloids

V. C. MOW¹
Graduate Assistant.

P. L. CHOW²
Graduate Assistant.

F. F. LING
Professor,
Mem. ASME

Department of Mechanics,
Rensselaer Polytechnic Institute,
Troy, N. Y.

Microslips Between Contacting Paraboloids

A generalization of a Hertz problem and that of a Mindlin problem were found for fourth-order paraboloids in contact. In particular, microslips and annulus of slip were sought. To this end an inverse method was devised. Moreover, an optimization procedure is described for finding the geometry for a given loading condition and set of material properties, within the family of paraboloids, which gives minimum slip. It has been shown in an example that the annulus of slip may be reduced by 60 percent while the maximum slip may be reduced by 90 percent.

Introduction

FRETING corrosion is a kind of damage which inflicts surfaces of contacting bodies when they experience oscillatory relative movements of low amplitude. Tomlinson, Thorpe, and Gough [1]³ found the threshold amplitude to be of the order of 10^{-8} cm. It is known that the amount of damage increases approximately in a linear fashion with increasing amplitude of relative movement and increasing load. More precisely, following Campbell [2], this kind of damage should be termed fretting inasmuch as there is no evidence of accompanying chemical action; for example, formation of paramagnetic or ferromagnetic iron oxides with steel surfaces and of accompanying abrasive action of the oxide particles or oxide films. Although not well understood, there has been increasing evidence of correlation between fretting and microslips; for example, a review by Johnson [3]. The theoretical and experimental bases of the work of Johnson and several others recently have their geneses in the work of Mindlin [4], Cattaneo [5], Mindlin, Mason, Osmer, and Deresiewicz [6].

The present investigation is characterized by: (a) A generalization of the Hertz problem, within the classical infinitesimal elasticity theory, for fourth-order paraboloids in contact; (b) a corresponding generalization of the Mindlin problem; and (c) the optimization of the shapes of the paraboloids for minimum microslips. Of course, the paraboloids refer to bodies with paraboloidal surfaces at the contact region, the shapes of the bodies far removed from the contact region being irrelevant within classical contact theory.

A Generalized Hertz Problem

Integral Equation Formulation

Under the classical Hertz assumptions, the contact problem of two elastic bodies is reducible to an equivalent punch problem; that is, the problem is reduced to that of finding the single-layer potential [7].

$$\Psi(x, y, z) = \int_{\Omega} \frac{p(x', y') dx' dy'}{[(x - x')^2 + (y - y')^2 + z^2]^{1/2}} \quad (1)$$

¹ Now Assistant Professor. Assoc. Mem. ASME.

² Now Assistant Professor, Mathematics Department.

³ Numbers in brackets designate References at end of paper.

Contributed by the Applied Mechanics Division for presentation at the Applied Mechanics Conference, Pasadena, Calif., June 28-29, 1967, of THE AMERICAN SOCIETY OF MECHANICAL ENGINEERS.

Discussion of this paper should be addressed to the Editorial Department, ASME, United Engineering Center, 345 East 47th Street, New York, N. Y. 10017, and will be accepted until one month after final publication of the paper itself in the JOURNAL OF APPLIED MECHANICS. Manuscript received by ASME Applied Mechanics Division, July 21, 1966; final draft, January 17, 1967. Paper No. 67-APM-12.

where (x, y, z) are the coordinates of a generic point in or on the surface of the contacting body, (x', y') are coordinates in the contact region Ω at which the normal pressure is p and z is perpendicular to the contact region, taken to be flat at $z = 0$. The potential is moreover subject to the boundary conditions

$$\Psi(x, y, 0) = \frac{2\pi}{\vartheta_1 + \vartheta_2} [\delta - F_1 - F_2] \quad \text{in } \Omega \quad (2)$$

and

$$\left. \frac{\partial \Psi}{\partial z} \right|_{z=0} = 0 \quad \text{outside } \Omega, \quad (3)$$

where $\vartheta_i = \frac{1 - \nu_i}{G_i}$ are material constants composed of ν_i , the Poisson's ratio, and G_i , the shear modulus, of the i th member of the contacting pair. δ is the normal closing-in of the bodies while $F_1(x, y)$ and $F_2(x, y)$ describe the surfaces of the contacting bodies in the neighborhood of the contact region. Equations (1) and (2) may be combined to give

$$\delta - F_1 - F_2 = \frac{\vartheta_1 + \vartheta_2}{2\pi} \int_{\Omega} \frac{p(x', y') dx' dy'}{[(x - x')^2 + (y - y')^2]^{1/2}} \quad (4)$$

Therefore, the pressure distribution over the contact region Ω is determined by the integral equation (4). Equation (2) can be used to determine the contact region; it is the locus of points at which

$$\delta - F_1 - F_2 = \text{const} \quad (5)$$

For this investigation the surfaces $z_1 = F_1(x, y)$ and $z_2 = F_2(x, y)$ have been assumed to be fourth-order polynomials:

$$F_1(x, y) = A_1 x^2 + A_2 y^2 + A_3 x^2 y^2 + A_4 x^4 + A_5 y^4 \quad (6)$$

and

$$F_2(x, y) = B_1 x^2 + B_2 y^2 + B_3 x^2 y^2 + B_4 x^4 + B_5 y^4, \quad (7)$$

where, for simplicity, the symmetry with respect to x and y has been introduced. It should be noted, however, that this restriction is not essential for a generalized Hertz analysis.

Within the classical contact theory, it is convenient to define the "apparent geometry" ϕ such that

$$\phi = F_1 + F_2 = b_1 x^2 + b_2 y^2 + b_3 x^2 y^2 + b_4 x^4 + b_5 y^4 \quad (8)$$

with $b_i = A_i + B_i$, $i = 1, 2, \dots, 5$.

The function ϕ satisfies the conditions

$$\phi(0, 0) = \phi_x(0, 0) = \phi_y(0, 0) = 0$$

By virtue of equation (8), the single-layer potential must then satisfy

$$\Psi(x, y, 0) = \frac{2\pi}{\partial_1 + \partial_2} (\delta - \phi) \quad \text{in } \Omega. \quad (9)$$

Further, the contact region Ω , in view of equation (5), is circumscribed by a closed fourth-order curve. Unfortunately, there are no known potential functions constructed in a fourth-order curvilinear coordinate system. In order that the subsequent shear problem may be solved in a manageable form and from which the microslip can be computed, it is desirable to find the normal pressure $p(x, y)$ in closed form. To this end, it is assumed that the contact region Ω is bounded by an ellipse. It will be seen that this assumption, together with the classical Hertz assumptions, in general, lead to unbounded pressures along the periphery of the contact region. This will be circumvented by generating the apparent geometry in a more restrictive manner.

Direct Formulation

Alternatively, the method of direct construction of the potential function [7] may be used:

Let ρ, μ, ν be the elliptical coordinates such that

$$\begin{aligned} e^2 x^2 &= a^2 \rho^2 \mu^2 \nu^2 \\ (1 - e^2) e^2 y^2 &= a^2 (\rho^2 - e^2) (\mu^2 - e^2) (e^2 - \nu^2) \\ (1 - e^2) z^2 &= a^2 (\rho^2 - 1) (1 - \mu^2) (1 - \nu^2), \end{aligned} \quad (10)$$

where

$$\begin{aligned} 0 &\leq \nu^2 \leq e^2 \\ e^2 &\leq \mu^2 \leq 1 \\ 1 &\leq \rho^2 < \infty \end{aligned} \quad (11)$$

and e is the eccentricity while a is the semimajor axis of the ellipse. The surface $\rho = \text{const}$ is an ellipsoid, given by $\frac{x^2}{a^2 \rho^2} +$

$\frac{y^2}{a^2 (\rho^2 - e^2)} + \frac{z^2}{a^2 (\rho^2 - 1)} - 1 = 0$. Hence, the limit of $\rho \rightarrow 1$ yields an elliptic disk for $z = 0$,

$$\frac{x^2}{a^2} + \frac{y^2}{a^2 (1 - e^2)} - 1 = 0, \quad (12)$$

which is suitable for describing the contact region Ω .

In the general elliptical coordinates, the harmonic functions are products of Lamé's functions, each of which depends on only one of the coordinates ρ, μ, ν .

Suppose $F(x, y, z)$ is a harmonic polynomial which is capable of representation in the form

$$F(x, y, z) = R(\rho)M(\mu)N(\nu), \quad (13)$$

where $R(\rho), M(\mu), N(\nu)$ are Lamé's functions. Then on the surface S_0 of the ellipsoid $\rho = \rho_0$, the function assumes the value

$$F(x, y, z)|_{\rho=\rho_0} = R(\rho_0)M(\mu)N(\nu), \quad (14)$$

where x, y, z must satisfy

$$\frac{x^2}{a^2 \rho_0^2} + \frac{y^2}{a^2 (\rho_0^2 - e^2)} + \frac{z^2}{a^2 (\rho_0^2 - 1)} - 1 = 0.$$

If equation (14) is of the given distribution over the surface S_0 , then the harmonic polynomial $F(x, y, z)$ is the solution to the internal Dirichlet problem.

The second solution, the solution to the external Dirichlet problem, which vanishes as $\rho \rightarrow \infty$ is

$$G(x, y, z) = \frac{\psi(\rho)}{\psi(\rho_0)} F(x, y, z), \quad (15)$$

where

$$\psi(\rho) = \int_{\rho}^{\infty} \frac{d\lambda}{\Delta(\lambda) R^2(\lambda)} \quad (16)$$

with

$$\Delta(\lambda) = [(\lambda^2 - e^2)(\lambda^2 - 1)]^{1/2}. \quad (17)$$

By considering the internal and external Dirichlet problems, the pressure distribution over S_0 may be constructed:

$$p(x, y, z)|_{S_0} = \frac{1}{4\pi a} \frac{F(x, y, z)|_{S_0}}{[(\rho_0^2 - \mu^2)(\rho_0^2 - \nu^2)]^{1/2} \psi^2(\rho_0) R^2(\rho_0)}. \quad (18)$$

For $\rho = 1$, the surface S_0 degenerates into an elliptic disk Ω , and equation (18) reduces to

$$p(x, y) = \frac{F(x, y, 0)}{2\pi a (1 - e^2)^{1/2} L^{1/2} R^2(1)} \quad \text{in } \Omega, \quad (19)$$

in which

$$b^2 = a^2 (1 - e^2)$$

and

$$L = \left(1 - \frac{x^2}{a^2} - \frac{y^2}{b^2}\right). \quad (20)$$

In the determination of pressure distribution $p(x, y)$ in the contact region Ω , the task is to seek a proper combination of harmonic polynomials of different order which will yield the correct boundary value specified by equation (9).

Solution

By the method of superposition, it is found that the required potential function for the external Dirichlet problem may be represented by

$$\begin{aligned} \Psi = & c_0 \omega_0 \frac{\psi_0(\rho)}{\psi_0(\rho_0)} + c_2^{(1)} \frac{\psi_2^{(1)}(\rho)}{\psi_2^{(1)}(\rho_0)} \omega_2^{(1)} + c_2^{(2)} \frac{\psi_2^{(2)}(\rho)}{\psi_2^{(2)}(\rho_0)} \omega_2^{(2)} \\ & + c_4^{(1)} \frac{\psi_4^{(1)}(\rho)}{\psi_4^{(1)}(\rho_0)} \omega_4^{(1)} + c_4^{(2)} \frac{\psi_4^{(2)}(\rho)}{\psi_4^{(2)}(\rho_0)} \omega_4^{(2)} \\ & + c_4^{(3)} \frac{\psi_4^{(3)}(\rho)}{\psi_4^{(3)}(\rho_0)} \omega_4^{(3)}. \end{aligned} \quad (21)$$

Referring to equation (19), the pressure intensity corresponding to the potential, equation (21), over the elliptic contact region is

$$p(x, y) = \frac{1}{2\pi a (1 - e^2)^{1/2} L^{1/2}} \left\{ \frac{c_0 \omega_0}{\psi_0(1) R_0^2(1)} + \frac{c_2^{(1)} \omega_2^{(1)}}{\psi_2^{(1)}(1) [R_2^{(1)}(1)]^2} + \dots + \frac{c_4^{(3)} \omega_4^{(3)}}{\psi_4^{(3)}(1) [R_4^{(3)}(1)]^2} \right\}_{\rho=1} \quad (22)$$

The harmonic functions $\omega_0, \omega_2^{(1)}, \dots, \omega_4^{(3)}$, are given in the Appendix. They are in the form of products of Lamé's function. In particular, these are ellipsoidal harmonics of first species and of zeroth, second, and fourth order. From the theory of Lamé's function, equation (21) evaluated at $\rho = 1$ represents a fourth-order polynomial which is symmetric in x and y .

Using the Cartesian form of $\omega_0, \omega_2^{(1)}, \omega_2^{(2)}, \dots, \omega_4^{(3)}$ (see Appendix), and combining equations (8), (9) and (21), the constants $c_0, c_2^{(1)}, \dots, c_4^{(3)}$ are uniquely determined in terms of the parameters of the apparent geometry. Hence, the pressure distribution over the contact region is found. However, this solution is singular at the periphery Ω_0 of the contact region unless the terms in $\{ \}$ in equation (22) contain the factor L .

Inverse Method

Clearly, the aforementioned statement is not always true for any apparent geometry. To avoid this difficulty, an inverse method is introduced as follows. Assume that the pressure dis-

tribution vanishes along Ω_0 , then factorization of L for terms in $\{ \}$ is permissible. The pressure distribution must now take the form

$$p(x, y) = L^{-1/2} \left(\alpha_1 + \alpha_2 \frac{x^2}{a^2} + \alpha_3 \frac{y^2}{b^2} \right) \quad (23)$$

where $\alpha_1, \alpha_2, \alpha_3$ are constants which can be determined.

Rather than prescribing the apparent geometry, one seeks the geometry for a specified pressure distribution. In so doing, the aforementioned Dirichlet problem is converted into a Neumann problem which is only determined within an additive constant. But in this case, this arbitrary constant may be determined by requiring the apparent geometry $\phi(x, y)$ to vanish when $x = y = 0$.

Expressing Lamé's function in Cartesian form, the intensity given by equation (22) may be written

$$\begin{aligned} p(x, y) = & \frac{L^{-1/2}}{2\pi b} \left\{ \frac{c_0}{K(e)} \right. \\ & + \frac{c_2^{(1)}}{(\sigma_1 - 1)^2 \psi_2^{(1)}(1)} \left(\frac{x^2}{a^2 \sigma_1} + \frac{y^2}{a^2 (\sigma_1 - e^2)} - 1 \right) \\ & + \frac{c_2^{(2)}}{(\sigma_2 - 1)^2 \psi_2^{(2)}(1)} \left(\frac{x^2}{a^2 \sigma_2} + \frac{y^2}{a^2 (\sigma_2 - e^2)} - 1 \right) \\ & + \frac{x^2}{a^2} \left[\frac{c_4^{(1)}}{(\gamma_2^{(1)} + \gamma_1^{(1)} + 1) \psi_4^{(1)}(1)} \frac{\gamma_1^{(1)}}{\gamma_2^{(1)}} \right. \\ & + \frac{c_4^{(2)}}{(\gamma_2^{(2)} + \gamma_1^{(2)} + 1) \psi_4^{(2)}(1)} \frac{\gamma_1^{(2)}}{\gamma_2^{(2)}} \\ & + \left. \frac{c_4^{(3)}}{(\gamma_2^{(3)} + \gamma_1^{(3)} + 1) \psi_4^{(3)}(1)} \frac{\gamma_1^{(3)}}{\gamma_2^{(3)}} \right] \\ & + \frac{y^2}{a^2} \left[\frac{c_4^{(1)}}{(\gamma_2^{(1)} + \gamma_1^{(1)} + 1) \psi_4^{(1)}(1)} \left(\frac{\gamma_1^{(1)} + 2e^2}{\gamma_2^{(1)} + \gamma_1^{(1)} e^2 + e^4} \right) \right. \\ & + \frac{c_4^{(2)}}{(\gamma_2^{(2)} + \gamma_1^{(2)} + 1) \psi_4^{(2)}(1)} \left(\frac{\gamma_1^{(2)} + 2e^2}{\gamma_2^{(2)} + \gamma_1^{(2)} e^2 + e^4} \right) \\ & + \left. \frac{c_4^{(3)}}{(\gamma_2^{(3)} + \gamma_1^{(3)} + 1) \psi_4^{(3)}(1)} \left(\frac{\gamma_1^{(3)} + 2e^2}{\gamma_2^{(3)} + \gamma_1^{(3)} e^2 + e^4} \right) \right] \\ & + \frac{x^4}{a^4} \left[\frac{c_4^{(1)}}{(\gamma_2^{(1)} + \gamma_1^{(1)} + 1) \psi_4^{(1)}(1) \gamma_2^{(1)}} \right. \\ & + \frac{c_4^{(2)}}{(\gamma_2^{(2)} + \gamma_1^{(2)} + 1) \psi_4^{(2)}(1) \gamma_2^{(2)}} \\ & + \left. \frac{c_4^{(3)}}{(\gamma_2^{(3)} + \gamma_1^{(3)} + 1) \psi_4^{(3)}(1) \gamma_2^{(3)}} \right] \\ & \times \frac{x^2 y^2}{a^4} \left[\frac{c_4^{(1)}}{(\gamma_2^{(1)} + \gamma_1^{(1)} + 1) \psi_4^{(1)}(1)} \left(\frac{2\gamma_2^{(1)} + \gamma_1^{(1)} e^2}{\gamma_2^{(1)} (\gamma_2^{(1)} + \gamma_1^{(1)} e^2 + e^4)} \right) \right. \\ & + \frac{c_4^{(2)}}{(\gamma_2^{(2)} + \gamma_1^{(2)} + 1) \psi_4^{(2)}(1)} \left(\frac{2\gamma_2^{(2)} + \gamma_1^{(2)} e^2}{\gamma_2^{(2)} (\gamma_2^{(2)} + \gamma_1^{(2)} e^2 + e^4)} \right) \\ & + \left. \frac{c_4^{(3)}}{(\gamma_2^{(3)} + \gamma_1^{(3)} + 1) \psi_4^{(3)}(1)} \left(\frac{2\gamma_2^{(3)} + \gamma_1^{(3)} e^2}{\gamma_2^{(3)} (\gamma_2^{(3)} + \gamma_1^{(3)} e^2 + e^4)} \right) \right] \\ & \times \frac{y^4}{a^4} \left[\frac{c_4^{(1)}}{(\gamma_2^{(1)} + \gamma_1^{(1)} + 1) \psi_4^{(1)}(1) (\gamma_2^{(1)} + \gamma_1^{(1)} e^2 + e^4)} \right. \\ & + \frac{c_4^{(2)}}{(\gamma_2^{(2)} + \gamma_1^{(2)} + 1) \psi_4^{(2)}(1) (\gamma_2^{(2)} + \gamma_1^{(2)} e^2 + e^4)} \\ & + \left. \frac{c_4^{(3)}}{(\gamma_2^{(3)} + \gamma_1^{(3)} + 1) \psi_4^{(3)}(1) (\gamma_2^{(3)} + \gamma_1^{(3)} e^2 + e^4)} \right] \\ & + \left[\frac{c_4^{(1)}}{(\gamma_2^{(1)} + \gamma_1^{(1)} + 1) \psi_4^{(1)}(1)} + \frac{c_4^{(2)}}{(\gamma_2^{(2)} + \gamma_1^{(2)} + 1) \psi_4^{(2)}(1)} \right. \\ & + \left. \frac{c_4^{(3)}}{(\gamma_2^{(3)} + \gamma_1^{(3)} + 1) \psi_4^{(3)}(1)} \right]. \quad (24) \end{aligned}$$

In order to determine the constants $c_0, c_2^{(1)}, \dots, c_4^{(3)}$, equate equation (23) to equation (24) and collect coefficients of like powers of x and y . This process yields

$$\begin{aligned} \frac{c_0}{K(e)} - \frac{c_2^{(1)}}{(\sigma_1 - 1)^2 \psi_2^{(1)}(1)} - \frac{c_2^{(2)}}{(\sigma_2 - 1)^2 \psi_2^{(2)}(1)} \\ + \frac{c_4^{(1)}}{(\gamma_2^{(1)} + \gamma_1^{(1)} + 1) \psi_4^{(1)}(1)} + \frac{c_4^{(2)}}{(\gamma_2^{(2)} + \gamma_1^{(2)} + 1) \psi_4^{(2)}(1)} \\ + \frac{c_4^{(3)}}{(\gamma_2^{(3)} + \gamma_1^{(3)} + 1) \psi_4^{(3)}(1)} = 2\pi b \alpha_1, \quad (25) \end{aligned}$$

$$\begin{aligned} \frac{c_2^{(1)}}{(\sigma_1 - 1)^2 \psi_2^{(1)}(1) \sigma_1} + \frac{c_2^{(2)}}{(\sigma_2 - 1)^2 \psi_2^{(2)}(1) \sigma_2} \\ + \frac{c_4^{(1)}}{(\gamma_2^{(1)} + \gamma_1^{(1)} + 1) \psi_4^{(1)}(1)} \frac{\gamma_1^{(1)}}{\gamma_2^{(1)}} \\ + \frac{c_4^{(2)}}{(\gamma_2^{(2)} + \gamma_1^{(2)} + 1) \psi_4^{(2)}(1)} \frac{\gamma_1^{(2)}}{\gamma_2^{(2)}} \\ + \frac{c_4^{(3)}}{(\gamma_2^{(3)} + \gamma_1^{(3)} + 1) \psi_4^{(3)}(1)} \frac{\gamma_1^{(3)}}{\gamma_2^{(3)}} = 2\pi b (\alpha_2 - \alpha_1). \quad (26) \end{aligned}$$

$$\begin{aligned} \frac{c_2^{(1)}}{(\sigma_1 - 1)^2 (\sigma_1 - e^2) \psi_2^{(1)}(1)} + \frac{c_2^{(2)}}{(\sigma_2 - 1)^2 (\sigma_2 - e^2) \psi_2^{(2)}(1)} \\ + \frac{c_4^{(1)}}{(\gamma_2^{(1)} + \gamma_1^{(1)} + 1) \psi_4^{(1)}(1)} \left(\frac{\gamma_1^{(1)} + 2e^2}{\gamma_2^{(1)} + \gamma_1^{(1)} e^2 + e^4} \right) \\ + \frac{c_4^{(2)}}{(\gamma_2^{(2)} + \gamma_1^{(2)} + 1) \psi_4^{(2)}(1)} \left(\frac{\gamma_1^{(2)} + 2e^2}{\gamma_2^{(2)} + \gamma_1^{(2)} e^2 + e^4} \right) \\ + \frac{c_4^{(3)}}{(\gamma_2^{(3)} + \gamma_1^{(3)} + 1) \psi_4^{(3)}(1)} \left(\frac{\gamma_1^{(3)} + 2e^2}{\gamma_2^{(3)} + \gamma_1^{(3)} e^2 + e^4} \right) \\ = 2\pi b (\alpha_3 - \alpha_1) / (1 - e^2). \quad (27) \end{aligned}$$

$$\begin{aligned} \frac{c_4^{(1)}}{(\gamma_2^{(1)} + \gamma_1^{(1)} + 1) \psi_4^{(1)}(1) \gamma_2^{(1)}} + \frac{c_4^{(2)}}{(\gamma_2^{(2)} + \gamma_1^{(2)} + 1) \psi_4^{(2)}(1) \gamma_2^{(2)}} \\ + \frac{c_4^{(3)}}{(\gamma_2^{(3)} + \gamma_1^{(3)} + 1) \psi_4^{(3)}(1) \gamma_2^{(3)}} = -2\pi b \alpha_2. \quad (28) \end{aligned}$$

$$\begin{aligned} \frac{c_4^{(1)}}{(\gamma_2^{(1)} + \gamma_1^{(1)} + 1) \psi_4^{(1)}(1)} \left(\frac{2\gamma_2^{(1)} + \gamma_1^{(1)} e^2}{\gamma_2^{(1)} (\gamma_2^{(1)} + \gamma_1^{(1)} e^2 + e^4)} \right) \\ + \frac{c_4^{(2)}}{(\gamma_2^{(2)} + \gamma_1^{(2)} + 1) \psi_4^{(2)}(1)} \left(\frac{2\gamma_2^{(2)} + \gamma_1^{(2)} e^2}{\gamma_2^{(2)} (\gamma_2^{(2)} + \gamma_1^{(2)} e^2 + e^4)} \right) \\ + \frac{c_4^{(3)}}{(\gamma_2^{(3)} + \gamma_1^{(3)} + 1) \psi_4^{(3)}(1)} \left(\frac{2\gamma_2^{(3)} + \gamma_1^{(3)} e^2}{\gamma_2^{(3)} (\gamma_2^{(3)} + \gamma_1^{(3)} e^2 + e^4)} \right) \\ = -2\pi b (\alpha_2 + \alpha_3) / (1 - e^2). \quad (29) \end{aligned}$$

and

$$\begin{aligned} \frac{c_4^{(1)}}{(\gamma_2^{(1)} + \gamma_1^{(1)} + 1) \psi_4^{(1)}(1) (\gamma_2^{(1)} + \gamma_1^{(1)} e^2 + e^4)} \\ + \frac{c_4^{(2)}}{(\gamma_2^{(2)} + \gamma_1^{(2)} + 1) \psi_4^{(2)}(1) (\gamma_2^{(2)} + \gamma_1^{(2)} e^2 + e^4)} \\ + \frac{c_4^{(3)}}{(\gamma_2^{(3)} + \gamma_1^{(3)} + 1) \psi_4^{(3)}(1) (\gamma_2^{(3)} + \gamma_1^{(3)} e^2 + e^4)} \\ = -2\pi b \alpha_3 / (1 - e^2)^2. \quad (30) \end{aligned}$$

From equations (25) to (30), the constants $c_0, c_2^{(1)}, c_2^{(2)}, \dots, c_4^{(3)}$ may be solved uniquely in terms of the parameters α_1, α_2 , and α_3 , provided that the quantities a, e , and δ are given.

Auxiliary Conditions

Actually, these quantities have yet to be determined through three additional equations. For this purpose, the following auxiliary conditions are recalled:

Equation of equilibrium,

$$Q = \int_{\Omega} p(x, y) dx dy, \quad (31)$$

where Q is the load applied to the contacting bodies.

The displacement,

$$w(0, 0, 0) = \delta; \quad (32)$$

and the condition,

$$\phi(0, 0) = 0. \quad (33)$$

For the pressure distribution given by equation (23), the "closing-in" may be computed in terms of parameters α_1 , α_2 , and α_3 .

$$\begin{aligned} \delta = w(0, 0, 0) &= \frac{\partial_1 + \partial_2}{2\pi} \int_{\Omega} \frac{p(x, y)}{(x^2 + y^2)^{1/2}} dx dy \\ &= \frac{\partial_1 + \partial_2}{2\pi} \int_{\Omega} \frac{L^{1/2} \left(\alpha_1 + \frac{\alpha_2}{a^2} x^2 + \frac{\alpha_3}{b^2} y^2 \right)}{(x^2 + y^2)^{1/2}} dx dy \end{aligned} \quad (34)$$

Let $x = ar \cos \phi$ and $y = br \sin \phi$, then $J = abr$, $L^{1/2} = (1 - r^2)^{1/2}$ and $(x^2 + y^2) = r(a^2 \cos^2 \phi + b^2 \sin^2 \phi)$. Using the above, equation (34) becomes

$$\begin{aligned} \delta &= \frac{\partial_1 + \partial_2}{2\pi} \left\{ \alpha_1 \int_0^{2\pi} \int_0^1 \frac{(1 - r^2)^{1/2} ab dr d\phi}{(a^2 \cos^2 \phi + b^2 \sin^2 \phi)^{1/2}} \right. \\ &\quad + \frac{\alpha_2}{a^2} \int_0^{2\pi} \int_0^1 \frac{(1 - r^2)^{1/2} a^2 r^2 \cos^2 \phi ab dr d\phi}{(a^2 \cos^2 \phi + b^2 \sin^2 \phi)^{1/2}} \\ &\quad \left. + \frac{\alpha_3}{b^2} \int_0^{2\pi} \int_0^1 \frac{(1 - r^2)^{1/2} ab^3 r^2 \sin^2 \phi dr d\phi}{(a^2 \cos^2 \phi + b^2 \sin^2 \phi)^{1/2}} \right\} \end{aligned} \quad (35)$$

If $a > b$, the eccentricity is defined as

$$e^2 = \frac{a^2 - b^2}{a^2}.$$

Then equation (35) yields

$$\delta = \frac{\partial_1 + \partial_2}{2} b \left\{ \alpha_1 K(e) + \frac{\alpha_2}{4} [K(e) - D(e)] + \frac{\alpha_3}{4} D(e) \right\}, \quad (36)$$

in which the elliptic integral $K(e) = F\left(\frac{\pi}{2}, e\right)$ and $D(e) = \frac{K(e) - E(e)}{e^2}$, $F(\varphi, e)$ is the Legendre standard form of the first kind, $E(e) = E\left(\frac{\pi}{2}, e\right)$ and $E(\varphi, e)$ is the Legendre standard form of the second kind.

The equation of equilibrium can also be integrated to give

$$Q = 2\pi ab \left(\frac{\alpha_1}{3} + \frac{\alpha_2}{15} + \frac{\alpha_3}{15} \right). \quad (37)$$

Theoretically, the nine equations, equations (25) through (30), together with equations (33), (36), and (37), can be solved simultaneously for nine unknowns c_0 , $c_2^{(1)}$, \dots , $c_4^{(3)}$ and a , e , δ . The task of solving the previous nine transcendental equations is, however, simplified by prescribing the eccentricity e . The inverse method will proceed in the following manner. Let α_1 , α_2 , α_3 and e be given. From equations (36) and (37), the semimajor axis a and the closing-in δ can be determined. Then by solving equations (25) through (30), the numerical values of c_0 , $c_2^{(1)}$, \dots , $c_4^{(3)}$ may be computed. Then, determination of single-layer potential, equation (21), follows. Finally, in view of equation (9), one finds the apparent geometry

$$\phi(x, y) = \delta - \frac{\partial_1 + \partial_2}{2\pi} \Psi(x, y, 0) \quad \text{in } \Omega, \quad (38)$$

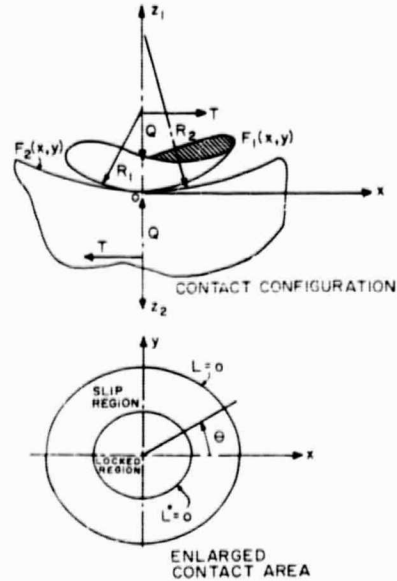


Fig. 1 Schematic diagram of the contact configuration and contact area

which, in general, does not satisfy equation (33). But with an arbitrary additive constant in the potential $\Psi(x, y)$ at one's disposal, equation (33) can be enforced. Thus a class of compatible geometry is generated. Obviously, there are infinitely many ways to decompose $\phi(x, y)$ into $F_1(x, y)$ and $F_2(x, y)$. However, to make the solution meaningful, one must select according to the following general principles: (1) Both bodies must be convex in the horizontal cross section; (2) the nose of each must be "blunt;" and (3) for design purposes, the selection can be guided by practical considerations.

Points 1 and 2 were used to safeguard against physical inconsistencies in the subsequent numerical example. To simplify the analysis of the subsequent shear problem, it will further be assumed that the pressure distribution takes the particular form

$$p(x, y) = \alpha_1 L^{1/2} + \alpha_2 L^{3/2} \quad (39)$$

where the pressure is constant along any homothetic ellipse.

In the generalized Hertz problem, under the same assumptions, the apparent geometry need not be restricted to fourth-order polynomials. The previous analysis may be extended to apparent geometry of higher-order polynomials by constructing the potential function of Lamé's products of higher order.

A Generalized Mindlin Problem

Formulation

Consider a force T , tangent to the contact plane and acting on the contacting body in the x -direction, superimposed on the normal force problem. The contact area is an ellipse, $L = 0$, as indicated previously. Mindlin [4] has shown that if slip is not permitted between the bodies, then the shearing stress generated would become infinite on the periphery of the contact region. Thus slip must occur on physical grounds and it progresses from the periphery to a homothetic ellipse in the interior of the contact region. Let this ellipse be denoted by $L^* = 1 - \left(\frac{x}{a\xi}\right)^2 - \left(\frac{y}{b\xi}\right)^2 = 0$ where $0 < \xi < 1$. The region interior to L^* is the locked region, see Fig. 1. Let Ω_1 and Ω_2 denote the locked and slip region, respectively.

It is assumed that the shearing stress in the contact region

cannot exceed the frictional force between the bodies. Hence, it must be no greater than $-\mu p(x, y)$ where μ is the coefficient of friction and $p(x, y)$ is the pressure intensity found from the generalized Hertz problem. The appropriate boundary conditions for the shear problem are:

$$\left. \begin{aligned} u'(x, y, 0) &= \frac{\delta_x}{2} = \text{const} \\ v'(x, y, 0) &= 0 \end{aligned} \right\} \quad \text{in } \Omega_1, \quad (40)$$

$$\left. \begin{aligned} \tau_{xz}'(x, y, 0) &= -\mu p(x, y) \\ \tau_{yz}'(x, y, 0) &= 0 \end{aligned} \right\} \quad \text{in } \Omega_2, \quad (41)$$

and

$$\sigma_{zz}'(x, y, 0) = \frac{\partial w'}{\partial z}(x, y, 0) = 0 \quad \text{in } \Omega = \Omega_1 + \Omega_2, \quad (42)$$

in which (u', v', w') are the displacement components in the (x, y, z) -directions emanating from the shear problem, δ_x is the rigid-body displacement in the tangential direction, and $(\tau_{xz}', \tau_{yz}', \sigma_{zz}')$ are the shear and normal stresses emanating from the shear problem. Further, the stresses on the surface outside the contact region must all vanish; i.e.,

$$\tau_{xz}' = \tau_{yz}' = \sigma_{zz}' = 0. \quad (43)$$

The elasticity problem with the previous boundary conditions is equivalent to the problem of prescribing

$$t(x', y') = -\tau_{xz}' = \begin{cases} \mu p(x', y') & \text{in } \Omega_2 \\ \mu p(x', y') - \beta_1 L'^{1/2} - \beta_2 L'^{1/2} & \text{in } \Omega_1 \end{cases} \quad (44)$$

and

$$\tau_{yz}' = \sigma_{zz}' = 0 \quad \text{in } \Omega = \Omega_1 + \Omega_2$$

Equations (44) may be considered the superposition of two problems, the boundary conditions of which are $\tau_{yz}' = \sigma_{zz}' = 0$ in Ω ,

$$t(x', y') = -\tau_{xz}' = \mu p(x', y') \quad \text{in } \Omega = \Omega_1 + \Omega_2 \quad (45)$$

and

$$t(x', y') = -\tau_{xz}' = -\beta_1 L'^{1/2} - \beta_2 L'^{1/2} \quad \text{in } \Omega_1. \quad (46)$$

Solution

Using the fundamental solution from the problem of a concentrated shear force on an elastic half space as the kernel, and integrating it with equations (45) and (46), the boundary conditions (41), (42), and (43) are automatically satisfied. The displacements on the surface in the required loading are:

$$2\pi G u'(x, y, 0) = \int_0^{2\pi} \Theta(x, y, \lambda) d\lambda - \nu \times \int_0^{2\pi} \Theta(x, y, \lambda) \sin^2 \lambda d\lambda, \quad (47)$$

$$2\pi G v'(x, y, 0) = \nu \int_0^{2\pi} \Theta(x, y, \lambda) \sin \lambda \cos \lambda d\lambda, \quad (48)$$

$$2\pi G w'(x, y, 0) = \nu \int_0^{2\pi} \Theta(x, y, \lambda) \cos \lambda d\lambda, \quad (49)$$

$$\Theta = \int_0^{\rho(\lambda)} t(x', y') d\rho. \quad (50)$$

Finally, the unknown quantities ζ , β_1 , and β_2 are determined such that boundary conditions (40) are satisfied.

Let $t(x, y) = \kappa_1 L'^{1/2} + \kappa_2 L'^{1/2}$ represent equations (45) and (46) in their respective regions; i.e.,

$$\kappa_1 = \mu\alpha_1, \quad \kappa_2 = \mu\alpha_2, \quad L = 1 - \frac{x^2}{a^2} - \frac{y^2}{b^2} \quad \text{in } \Omega \quad (51)$$

and

$$\kappa_1 = -\beta_1, \quad \kappa_2 = -\beta_2, \quad L = 1 - \left(\frac{x}{a\zeta}\right)^2 - \left(\frac{y}{b\zeta}\right)^2 \quad \text{in } \Omega_1. \quad (52)$$

Using the transformations

$$x' - x = \rho \cos \theta; \quad y' - y = \rho \sin \theta, \quad (53)$$

where x, y represent coordinates for interior points of Ω_1 . Equation (50) may be reduced to

$$\Theta = \frac{\kappa_1 \pi}{4} \left(\frac{L}{\sqrt{\Phi_2}} + \frac{\Phi_1^2}{\Phi_2^{3/2}} \right) + \frac{3\kappa_2 \pi}{16} \left(L + \frac{\Phi_1^2}{\Phi_2} \right) \frac{1}{\sqrt{\Phi_2}} \quad (54)$$

where

$$\Phi_1 = \frac{x \cos \lambda}{a^2} + \frac{y \sin \lambda}{b^2}, \quad \Phi_2 = \frac{\cos^2 \lambda}{a^2} + \frac{\sin^2 \lambda}{b^2}$$

The dot over the equality sign denotes the fact that the remaining terms of equation (54) do not contribute to the integrals (47), (48), and (49). For the previous loading, the displacement in the y -direction is (for $a > b$)

$$2\pi G v' = \nu \pi (2\kappa_1 + 3\kappa_2) \frac{b}{a^2 e^4} [(2 - e^2)K(e) - 2E(e)]xy - \nu \pi \kappa_2 \frac{b}{a^2 e^6} [(8 - 5e^2)K(e) - (8 - e^2)E(e)]x^2y - \nu \pi \kappa_2 \frac{b}{a^2 e^4} \left[-(8 - 3e^2)K(e) + \frac{(8 - 7e^2)}{1 - e^2} E(e) \right]xy^2. \quad (55)$$

where $K(e)$ and $E(e)$ are complete elliptic integrals of first and second kind. Hence, for the loading defined by equations (51) and (52) and the satisfaction of conditions, equation (40), two relations for the unknowns ζ , β_1 , β_2 are found:

$$\mu(2\alpha_1 + 3\alpha_2) - \frac{1}{\zeta} (2\beta_1 + 3\beta_2) = 0 \quad (56)$$

and

$$\mu\alpha_2 - \frac{\beta_2}{\zeta^3} = 0. \quad (57)$$

The third equation is obtained from the equilibrium condition; i.e.,

$$T = \int_{\Omega} t(x, y) dx dy = \mu \int_{\Omega} p(x, y) dx dy - \int_{\Omega_1} [\beta_1 L'^{1/2} + \beta_2 L'^{1/2}] dx dy = \mu Q - \left(\frac{2}{3} \beta_1 + \frac{2}{5} \beta_2 \right) \pi a b \zeta^2. \quad (58)$$

Therefore, ζ , β_1 , β_2 are completely determined if α_1 , α_2 , Q , T , and μ are prescribed. Under the conditions (56) and (57), the displacement in the x -direction for the loaded region ($a > b$) is found to be

$$2\pi G u' = bc\chi(e) \quad \text{in } \Omega_1 \quad (59)$$

where

$$c = \mu \left(\alpha_1 + \frac{3}{4} \alpha_2 \right) - \left(\beta_1 + \frac{3}{4} \beta_2 \right) \zeta \quad (60)$$

and

$$\chi(e) = K(e) - \frac{\nu}{e^2} [E(e) - (1 - e^2)K(e)] \quad a > b \quad (61)$$

The function $\chi(e)$, multiplied by $\frac{\pi}{2}$, is $2\mu_1 a \delta_z' / \rho_z$ as given in Fig. 4 of reference [4].

The displacements in the annulus of slip have been evaluated. Those portions of the displacements which correspond to the loading defined by equation (45) are integrated analytically while those which correspond to the loading defined by equation (46) can be integrated numerically. The expressions for the analytic portions are:

$$\begin{aligned} 2\pi G u_1' = & U_1(e)L + U_2(e)\frac{x^2}{a^2} + U_3(e)\frac{y^2}{b^2} + U_4(e)L^2 \\ & + U_5(e)L\frac{x^2}{a^2} + U_6(e)L\frac{y^2}{b^2} + U_7(e)L\frac{x^4}{a^4} \\ & + U_8(e)\frac{x^2}{a^2}\frac{y^2}{b^2} + U_9(e)\frac{y^4}{b^4}, \quad (62) \end{aligned}$$

where

$$L = 1 - \frac{x^2}{a^2} - \frac{y^2}{b^2}.$$

$$\frac{U_1(e)}{\mu\alpha_1\pi b} = (1 - \nu)K(e) + \nu D(e),$$

$$\frac{U_2(e)}{\mu\alpha_1\pi b} = K(e) - D(e) + \frac{\nu(1 - e^2)}{e^2} [K(e) - 2D(e)],$$

$$\frac{U_3(e)}{\mu\alpha_1\pi b} = D(e) - \frac{\nu}{e} [K(e) - (2 - e^2)D(e)],$$

$$\frac{U_4(e)}{\mu\alpha_2 3\pi b/2} = \frac{(1 - \nu)K(e)}{2} + \frac{\nu}{2} D(e),$$

$$\frac{U_5(e)}{\mu\alpha_2 3\pi b/2} = K(e) - D(e) + \frac{\nu(1 - e^2)}{e^2} [K(e) - 2D(e)],$$

$$\frac{U_6(e)}{\mu\alpha_2 3\pi b/2} = D(e) - \frac{\nu}{e} [K(e) - (2 - e^2)D(e)],$$

$$\begin{aligned} \frac{U_7(e)}{\mu\alpha_2 3\pi b/2} = & \frac{1}{6} [K(e) + E(e) - D(e)] \\ & - \frac{(1 - e^2)}{6e^2} [K(e) - (2 - e^2)D(e)] \\ & + \nu \left\{ \frac{(1 - e^2)^2}{e^6} \left[\frac{(8 - 3e^2)}{6} K(e) - \frac{(8 - 7e^2)}{6(1 - e^2)} E(e) \right] \right\}, \end{aligned}$$

$$\begin{aligned} \frac{U_8(e)}{\mu\alpha_2 3\pi b/2} = & \frac{1}{e^2} [K(e) - (2 - e^2)D(e)] \\ & + \frac{\nu(1 - e^2)}{e^4} [4K(e) - (8 - e^2)D(e)], \end{aligned}$$

$$\begin{aligned} \frac{U_9(e)}{\mu\alpha_2 3\pi b/2} = & \frac{1}{6e^2(1 - e^2)} [2e^2 E(e) - (1 + e^2)K(e) + 2D(e)] \\ & - \frac{\nu}{6e^2} [(7 + e^2)K(e) - (3 + 2e^2)E(e) - 8D(e)] \end{aligned}$$

and

$$2\pi G v_1' = \nu\pi\mu(2\alpha_1 + 3\alpha_2) \frac{b^2}{a} V_1(e) \frac{xy}{ab} \quad (63)$$

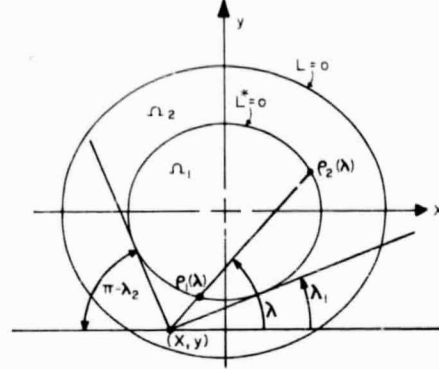


Fig. 2 Working diagram of the contact region showing parameters used in equations (64), (65), and (66)

$$- \nu\pi\mu\alpha_2 \frac{b^2}{a} V_2(e) \frac{x^3}{a^3} \frac{y}{b} - \nu\pi\mu\alpha_2 \frac{b^2}{a} V_3(e) \frac{x}{a} \frac{y^3}{b^3}, \quad (63) \quad (Cont.)$$

where

$$V_1(e) = \frac{1}{e^4} [(2 - e^2)K(e) - 2E(e)]$$

$$V_2(e) = \frac{1}{e^6} [(8 - 5e^2)K(e) - (8 - e^2)E(e)]$$

and

$$V_3(e) = \frac{(1 - e^2)}{e^4} \left[-(8 - 3e^2)K(e) + \frac{(8 - 7e^2)}{(1 - e^2)} E(e) \right]$$

For the loading defined by equation (46), the integrals for the displacements (in the annulus of slip) are:

$$2\pi G u_2' = \int_{\lambda_1}^{\lambda_2} \Theta(x, y, \lambda) d\lambda - \nu \int_{\lambda_1}^{\lambda_2} \Theta(x, y, \lambda) \sin^2 \lambda d\lambda, \quad (64)$$

$$2\pi G v_2' = \nu \int_{\lambda_1}^{\lambda_2} \Theta(x, y, \lambda) \sin \lambda \cos \lambda d\lambda, \quad (65)$$

where now

$$\Theta(x, y, \lambda) = \int_{\rho_1(\lambda)}^{\rho_2(\lambda)} t(x', y') d\rho \quad (66)$$

The limits of the integrals are defined in Fig. 2. These are integrated numerically. With these numerical results, the displacement in the slip region are:

$$u' = u_1' + u_2' \quad (67)$$

and

$$v' = v_1' + v_2' \quad (68)$$

Microslips

Numerical results are obtained for bodies of the same material constants, $G = 11.5 \times 10^6$ psi, and $\nu = 1/3$; the normal force $Q = 30$ lb, and the ratio of the shearing force to those of normal force $\tau = T/Q$ are taken at convenient values. The coefficient of friction is taken to be 0.35.

The quantity ζ defines the annulus of slip. Fig. 3 shows that ζ depends on the ratio α_2/α_1 . Further numerical results show that ζ does not depend on the magnitude of the Hertzian pressure, α_1 . For $\alpha_2/\alpha_1 = -1$, the slip region is minimized for nonadhering bodies in contact. For this case, the slip area of the fourth-order theory is less than 40 percent of the second-order theory.

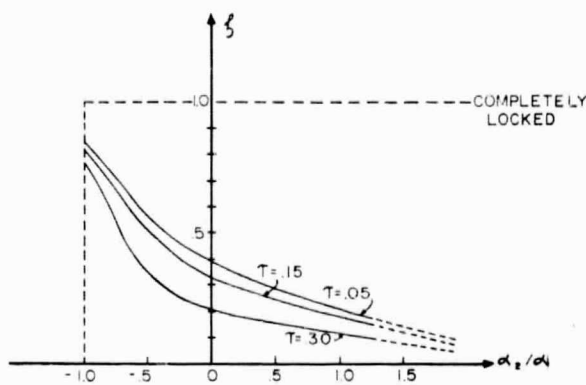


Fig. 3 Plot of ζ versus the ratio α_2/α_1 .
 $\tau = T/Q$, $\nu = 1/3$, $G = 11.5 \times 10^6$ psi, $\phi = 30$ lb, $\mu = 0.35$

The slip in the x -direction is defined by:

$$s = \delta_x - u'$$

Fig. 4 shows the slip for a typical case of close-fitting ball-and-socket configuration. The slip increases monotonically from $L^* = 0$ to $L = 0$. Shown in Fig. 4 is the slip at the periphery of the contact region $L = 0$. The maximum of this slip occurs at 90 deg from the direction of shear. Further, the slip is symmetric with respect to x and y -axes. It is seen that the slip for the fourth-order theory, for the case of $\alpha_2/\alpha_1 = -1$, is less than 10 percent of the second-order theory.

Similarly, the displacement in the y -direction is also computed. It is found that this is antisymmetric with respect to the x and y -axes, being positive in the first quadrant. The magnitude of this component of displacement is less than one percent of those in the x -direction.

For the cases shown in Fig. 4, the apparent geometry for the second-order theory in the neighborhood of contact region is

$$\phi = x^2 + y^2$$

The corresponding apparent geometry in the neighborhood of the contact region from the fourth-order theory is

$$\phi = x^2 + y^2 - 2.875 \times 10^3(x^2 + y^2)^2$$

Also, Table 1 shows a comparison of several parameters between the Hertz-Mindlin theory and the generalized Hertz-Mindlin theory.

Table 1 Comparison of the Hertz-Mindlin and the generalized Hertz-Mindlin theories

	Hertz-Mindlin	Generalized Hertz-Mindlin
$2\pi G\delta_x$ (lb/in.)	43.3×10^2	4.25×10^2
α_1 (lb/in. ²)	1.92×10^5	3.68×10^4
α_2 (lb/in. ²)	0	-3.68×10^4
ζ	0.3056	0.8074
β_1 (lb/in. ²)	0.205×10^5	0.497×10^4
β_2 (lb/in. ²)	0	-0.677×10^4
a (in.)	0.864×10^{-2}	1.563×10^{-2}
e	0.05234	0.100
S_{max} (in.)	3.1419×10^{-5}	0.1604×10^{-5}

It is seen that the fourth-order theory provides a means of controlling the size of slip region and the magnitude of slip. Hence, an effective way is found to reduce one of the causes of fretting by making the nose of the contacting bodies conform to the apparent geometry generated by the fourth-order theory.

Acknowledgment

The authors wish to acknowledge the support of the National Aeronautics and Space Administration under contract Nas 3-7629

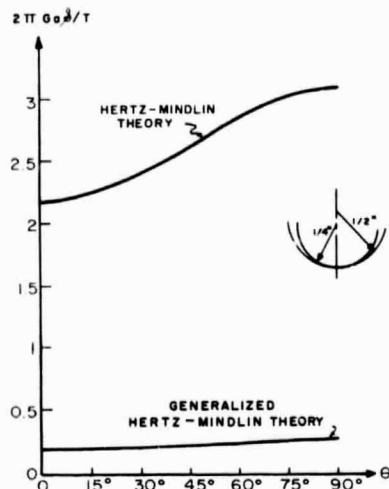


Fig. 4 Plot of slip S on the periphery of the contact region versus angular position θ for $\tau = 0.2$, and $\alpha_2/\alpha_1 = -1$

with Mechanical Technology Incorporated for whom one of us (F. F. Ling) is a consultant.

References

- Tomlinson, G. A., Thorpe, P. L., and Gough, H., "Investigation of Fretting Corrosion of Closely Fitting Surfaces," *Proceedings of the Institution of Mechanical Engineers*, Vol. 141, 1939, p. 223.
- Campbell, W. E., "The Current Status of Fretting Corrosion," *American Society of Testing Materials*, Special Technical Publication No. 144, 1952.
- Johnson, K. L., "Recent Developments in the Theory of Elastic Contact Stresses: Their Significance in the Study of Surface Breakdown," *Proceedings of the Conference on Lubrication and Wear*, Institution of Mechanical Engineers, London, 1957, p. 620.
- Mindlin, R. D., "Compliance of Elastic Bodies in Contact," *JOURNAL OF APPLIED MECHANICS*, Vol. 16, TRANS. ASME, Vol. 71, 1949, pp. 259-268.
- Cattaneo, C., "Sul contatto di due corpi elastici: distribuzione locale degli sforzi," *Accademia dei Lincei, Rendiconti*, June 27, 1939, p. 342.
- Mindlin, R. D., Mason, W. P., Osmer, T. F., and Deresiewicz, H., "Effect of an Oscillating Tangential Force on the Contact Surfaces of Elastic Spheres," *Proceedings of the First U.S. National Congress of Applied Mechanics*, 1951, p. 203.
- Lur'e, A. I., *Three-Dimensional Problems of the Theory of Elasticity*, Interscience, New York, 1964.

APPENDIX

The elliptic harmonics of the internal Dirichlet problem are:

$$\omega_0 = 1$$

$$\omega_{2(i)} = \frac{x^2}{a^2\sigma_i} + \frac{y^2}{a^2(\sigma_i - e^2)} + \frac{z^2}{a^2(\sigma_i - 1)} - 1 \quad i = 1, 2$$

$$\omega_{4(i)} = \left(\frac{x^2}{\theta_1^{(i)}} + \frac{y^2}{\theta_1^{(i)} - e^2} + \frac{z^2}{\theta_1^{(i)} - 1} - 1 \right) \times \left(\frac{x^2}{\theta_2^{(i)}} + \frac{y^2}{\theta_2^{(i)} - e^2} + \frac{z^2}{\theta_2^{(i)} - 1} - 1 \right), \quad i = 1, 2, 3$$

where

$$\sigma_{1,2} = \frac{1}{3} [(1 + e^2) \pm (1 - e^2 + e^4)^{1/2}]$$

$$\theta_1^{(i)} + \theta_2^{(i)} = -\gamma_1^{(i)}$$

$$\theta_1^{(i)}\theta_2^{(i)} = \gamma_2^{(i)}$$

$$\gamma_1^{(i)} = (1 + e^2)(p_i - 16)/14$$

$$\gamma_2^{(i)} = -e^2(p_i - 16)/7p_i$$

and

p_i are the roots of the cubic equation

$$p^3 - 20p^2 + p \left[64 + \frac{208e^2}{(1+e^2)^2} \right] - \frac{640e^2}{(1+e^2)^2} = 0, \quad 0 \leq e \leq 1.$$

The elliptic harmonics of the external Dirichlet problem are:

$$\omega_{0\text{ext}} = \int_p^\infty \frac{d\lambda}{\Delta(\lambda)}, \quad \Delta(\lambda) = [(\lambda^2 - e^2)(\lambda^2 - 1)]^{1/2}$$

$$\omega_{2\text{ext}}^{(i)} = \left\{ \int_p^\infty \frac{d\lambda}{\Delta(\lambda)(\sigma_i - \lambda^2)^2} \right\} \omega_2^{(i)}$$

and

$$\omega_{4\text{ext}}^{(i)} = \left\{ \int_p^\infty \frac{d\lambda}{\Delta(\lambda)(\lambda^4 + \gamma_1^{(i)}\lambda^2 + \gamma_2^{(i)})^2} \right\} \omega_4^{(i)}$$

Further, note that

$$\omega_0|_{\rho=1} = \int_1^\infty \frac{d\lambda}{\Delta(\lambda)} = K(e)$$

where

$K(e)$ is the complete Legendre elliptic integral of the first kind.

APPENDIX D

Computer Program for Determining Microslip

APPENDIX E

```

C. MAIN PROGRAM FOR BALL - SOCKET DESIGN CURVES
  DIMENSION AO1(100),AO2(100),X(6),C(6,7),C(2,6),EC(6),Q(10),
  1 TAU(10)
102 FORMAT (6F10.1)
103 FORMAT (6E10.2)
111 FORMAT ('C'7X'A'13X'B'12X'CEL'11X'PMAX'10X'SMAX'12X'UL'12X'RAD'12X
  1'A1'13X'AO2')
112 FORMAT (9E14.4)
116 FORMAT ('1 LOAD IN POUNDS = ',F10.1)
202 FORMAT (5I5,5X,2E10.1)
  US=0.
  UL=0.
  E = .CS
  ES = .C025
  EK = 1.57187
  CALL SETUP (D,C)
  READ (1,202) NC,NA1,NA2,MS,NT,AMIN,AMAX
  READ (1,102) (Q(I),I=1,NQ)
  READ (1,103) (AO1(I),I=1,NA1)
  READ (1,102) (AO2(I),I=1,NA2)
  IF (MS) 414,414,415
415 READ (1,102) U,PR
  READ (1,102) (TAU(I),I=1,MS)
414 DO 21 IA2=1,NA2
  DO 21 IQ=1,NQ
  WRITE (3,116) Q(IQ).
  WRITE (3,111)
  DO 21 MT=1,MS
  IF (MS) 410,410,411
411 CALL BETA (AO1,AO2,TAU,U,MT,810,820,GAM,IA2)
410 DO 21 IA1=1,NA1
  A1=AO1(IA1)
400 A2=AO2(IA2) *A1
  AB=Q(IQ)/(6.2832*(A1/3. -A2/5.))
  Y=SQRT(1.-ES)
  AA2=AB/Y
  AA=SQRT(AA2)
  BA=SQRT(AB*Y)
  Y=6.2832*BA
  D(1,7)=Y*(A1-A2)
  D(2,7)=Y*(2.*A2 - A1)
  D(3,7)=D(2,7)/(1.-ES)
  D(4,7)= -Y*A2
  D(5,7) = 2.*D(4,7)/(1.-ES)
  D(6,7)=D(4,7)/(1.-ES)**2
  D(1,7) = D(1,7)/D(1,1)
  DO 8 I=2,6
  L1=I-1
  SUM=0.
  DO 9 K=1,L1
  9 SUM=SUM+D(I,K)*D(K,7)
  8 D(I,7) =(D(I,7) -SUM)/D(I,1)
  X(6)=D(6,7)

```

```

DO 10 I=1,5
  L2=(7-I)
  SUM=0.
  L3=6-I
  DO 11 K=L2,6
11  SUM=SUM & D(L3,K)*X(K)
10  X(L3) = D(L3,7) -SUM
  DO 19 I=1,2
    EC(I)=0.
    DO 19 J=2,6
19  EC(I)=C(I,J)*X(J) & EC(I)
    EC(1)=EC(1)/AA2 *(-1.)
    EC(2)=EC(2)/AA2**2 *(-1.)
    IF (N1) 502,502,500
500 IF (EC(1)- AMIN) 21,501,501
501 IF (EC(1)- AMAX) 502,502,21
502 IF (MS) 412,412,413
413 CALL SLIP      (A1,A2,B10,B20,GAM,AB,US,UL,U,PR)
412 DEL = .5* BA*EK      *(A1-3.*A2/4.)
    I=IA2
    PMAX = A1*SQRT(-A02(I)/3.) &  A2 *SQRT((-A02(I)/3.)*3)
    WRITE (3,112) EC(1),EC(2),DEL,PMAX,US,UL,AA,A1,A02(I)
21  CONTINUE
    STOP
    END

```

```

SUBROUTINE BETA (A01,A02,TAU,U,MT,B1, B2, GAM,IA2)
DIMENSION A01(100),A02(100),TAU(10)
TOL=.005
C=.02
GAM = .8
FT=U - TAU(MT)
FS=FT
A1 = 1./(1./3. - A02(IA2)/5.)
A2 = A02(IA2) *A1
G=U*A2
H=U*(2.*A1 & 3.*A2)
L=0
1 IF (GAM) 8,399,399
399 B2 = G*GAM**3
    B1 = (GAM*H - 3.*B2)/2.
    FC = (5.*B1 & 3.*B2)*GAM**2
    IF (FC) 4,4,400
400 IF (ABS((FC-FT)/FT)- TOL) 8,8,2
    2 IF (FC-FT) 3,8,7
    3 IF (B1) 5,5,4
    4 IF (L) 402,402,401
401 C=C/3.
    L=C
402 GAM = GAM & C
    GO TO 1
    5 IF (FC-FS) 7,7,6
    6 FS=FC
    GO TO 4
    7 FS=FC
    IF (L) 404,403,404
403 L=1
    C=C/3.
404 GAM = GAM-C
    GO TO 1
    8 RETURN
END

```

```
SUBROUTINE SETUP (D,C)
DIMENSION C(6,7),C(2,6)
D(1,1) = 0.63613E00
D(1,2) = -0.40005E01
D(1,3) = -0.26670E01
D(1,4) = 0.36485E01
D(1,5) = 0.60918E00
D(1,6) = 0.91216E00
C(2,2) = 0.38149E01
D(2,3) = 0.35604E03
D(2,4) = -0.19474E04
D(2,5) = -0.50588E00
D(2,6) = -0.12229E03
D(3,3) = -0.27196E04
D(3,4) = -0.54734E01
C(3,5) = 0.31170E-05
D(3,6) = -0.34202E00
C(4,4) = 0.29718E07
D(4,5) = 0.56770E-06
D(4,6) = 0.18285E-03
D(5,5) = 0.13521E02
D(5,6) = 0.24161E03
D(6,6) = -0.10896E04
C(1,2) = 0.14991E01
C(1,3) = 0.80058E03
C(1,4) = -0.32010E04
C(1,5) = -0.49801E01
C(1,6) = -0.80402E03
C(2,2) = 0.0
C(2,3) = 0.0
C(2,4) = 0.12804E07
C(2,5) = 0.43535E01
C(2,6) = .93647E03
RETURN
END
```

```

SUBROUTINE SLIP (A1,A2,B10,B20,GAM,AB,US,UL,COF,PR)
DL = .02
CF = (A1/3. -A2/5.)
B1 = B10*CF
B2 = B20*CF
AA2 = AD
AA = SQRT(AA2)
BA2 = AB
BA=AA
CC=3.14159*BA*COF
C= COF*(A1*.75*A2) - GAM*(B1*.75*B2)
U3= .786 - PR*.591
U7= .295 -PR*.236
UL = BA*C*(9.87 - PR*4.93)
DR = AA*GAM/10.
TH = 4.7124
S = SIN(TH)
C = COS(TH)
X = -AA *C
X2 = X**2
Y = -BA *S
Y2 = Y**2
AS = AA2*GAM**2
BS = BA2*GAM**2
Z = ABS(BS*X2 & AS*Y2 - AS*BS)
Z=SQRT(Z)
TANI = Z/AS
TANN =-Z/AS
XLI = ATAN(TANI)
XLN = ATAN(TANN)
403 XLN = XLN & 3.14159
1 TL = TANI
Z = ((X*BS & Y*AS*TL)/(BS & AS*TL**2))**2
R11 = SQRT(Z*(1. & TL**2))
XL1 = XLI & .00875
S1 = SIN(XL1)
C1 = COS(XL1)
UF1 = PR*S1**2 - 1.
K = ABS(1.-(R11*C1-X)**2/AS - (R11*S1-Y)**2/BS)
R=SQRT(R)
R = B1*R & B2*R**3
W1 = UF1 * R
TL = S1/C1
ZB = X*BS & Y*AS*TL
ZA = BS & AS*TL**2
ZR = ABS(ZB**2 - ZA*(AS*Y2&BS*X2-AS*BS))
ZR=SQRT(ZR)
Z1 = (ZB- ZR)/ZA
Z2 = (ZB&ZR)/ZA
TL2 = TL**2
R21 = ABS(Z1**2*(1.&TL2))
R21=SQRT(R21)
R22 = ABS(Z2**2*(1.&TL2))
R22=SQRT(R22)

```

```

U = W1*(R22-R21)*DL/4.
R11 = R21
R12 = R22
NL = ABS((XLN-XL1)/DL)
DO 9 I=1,NL
XL2 = XL1+DL
W1 = 0.
W2 = 0.
S2 = SIN(XL2)
C2 = COS(XL2)
UF2 = PR*S2**2-1.
IF (ABS(S2)-.999) 12,12,11
11 TL = C2/S2
   TL2 = TL**2
   ZB = BS*X*TL & Y*AS
   ZA = BS*TL2 & AS
   GO TO 13
12 TL = S2/C2
   TL2 = TL**2
   ZB = X*BS & Y*AS*TL
   ZA = BS & AS*TL2
13 ZR = ABS(ZB**2 - ZA*(AS*Y2+BS*X2-AS*BS))
   ZR=SQRT(ZR)
   Z1 = (ZB- ZR)/ZA
   Z2 = (ZB+ZR)/ZA
   R21 = ABS(Z1**2*(1.6*TL2))
   R21=SQRT(R21)
   R22 = ABS(Z2**2*(1.6*TL2))
   R22=SQRT(R22)
   IF (ZB) 408,409,409
408 TEMP = R21
   R21 = R22
   R22 = TEMP
409 IF (R21-R11) 2,4,3
   2 XL = R11-R21
   R = ABS(1.-(R11*C2-X)**2/AS-(R11*S2-Y)**2/BS)
   R=SQRT(R)
   R = B1*R & B2*R**3
   W2 = UF2*R
   U = U+W2*XL*DL/4.
   R1 = R21+XL
   GO TO 4
   3 XL = R21-R11
   R = ABS(1.-(R21*C1-X)**2/AS - (R21*S1-Y)**2/BS)
   R=SQRT(R)
   R = B1*R & B2*R**3
   W1 = UF1*R
   U = U+W1*XL*DL/4.
   R1 = R11+XL
   4 IF(R12-R22) 5,5,6
   5 NR = (R12-R1)/CR
   GO TO 406
   6 NR = (R22-R1)/DR
406 IF (NR) 407,407,7
   7 DO 8 I=1,NR

```

```

R1 = R1 & DR
R = ABS(1.-(R1*C1-X)**2/AS - (R1*S1-Y)**2/BS)
R=SQRT(R)
R = B1*R & B2*R**3
W3 = UF1*R
R = ABS(1.-(R1*C2-X)**2/AS - (R1*S2-Y)**2/BS)
R=SQRT(R)
R = B1*R & B2*R**3
W4 = UF2*R
U = U & DR*DL*((W1*W2)           & (W3*W4)   1/4.
W1=W3
8 W2=W4
407 U = U & DL*           (W1*(R12-R1) & W2*(R22-R1))/3.
C1=C2
S1=S2
R11=R21
R12=R22
UF1=UF2
9 XL1=XL2
DLL = XLN -XL1
SN = SIN(XLN)
IF (SN - .999) 15,15,14
14 TL = CCS(XLN)/SN
Z = ((BS*X*TL & Y*AS)/(BS*TL**2 & AS))**2
GO TO 16
15 TL = SN/COS(XLN)
Z = ((X*BS & Y*AS*TL)/(BS & AS*TL**2))**2
16 R21 = ABS(Z*(1.&TL**2))
R21=SQRT(R21)
R = ABS(1.-(R21*C1-X)**2/AS - (R21*S1-Y)**2/BS)
R=SQRT(R)
R = B1*R & B2*R**3
W1 = UF1*R
U = (U & W1*(R12-R11)   *DL)   *(2.)
YR=Y2/BA2
UP1 = YR*U3
UP2 = YR**2*U7
UP = CC*(A1*UP1*1.5*A2*UP2)   *2.
US=UL-U-UP
RETURN
END

```


APPENDIX E : Detailed Analysis of Main Test Rig Components

Gas Bearing

The dynamic specimen is mounted in the male portion of a hemi-spherical hydrostatic gas bearing in order to achieve the necessary degrees of freedom of motions. In actuality the bearing configuration is less than a hemisphere in order to provide a shaft connection at the pole and to control the vertical axis component of lift.

Because of the positioning accuracy required the maximum achievable radial stiffness is needed but without excessive vertical lift capacity which would necessitate providing a high holding down load.

After rough sizing, the gas bearing was analyzed using MTI computer program PN 0256 "Hybrid Spherical Bearing". A graphical presentation of the non-dimensional results are given on Figures 21 through 23 for certain geometrical configurations. From these results the following performance was calculated.

Summary of Symbols and Data used in Calculations

$$R_s = .8125" = \text{Radius of Sphere}$$

$$C = .0003" = \text{Radial Clearance}$$

$$p_s = 114.7 \text{ psia} = \text{Supply Pressure}$$

$$p_a = 14.7 \text{ psia} = \text{Ambient Pressure}$$

$$V = 7.8 = \frac{p_s}{p_a} = \text{Absolute Pressure Ratio}$$

$$\mu = .25 \times 10^{-8} \text{ Reyns} = \text{Nitrogen Viscosity at Room Temperature}$$

$$T = 530^\circ R = \text{Inlet Temperature}$$

$$QT = 1.35 \times 10^8 \text{ in}^2/\text{sec}^2$$

$$N = 18 = \text{Number of Orifices}$$

$$d = .025" = \text{Feeder Hole Diameter}$$

$$a = .010" = \text{Orifice Radius}$$

$$\delta = \frac{a^2}{dC} = \text{Inherent Compensation Factor}$$

$$\epsilon = \text{Eccentricity Ratio}$$

$$\Lambda_{so} = \frac{6\mu Na^2 \sqrt{QT}}{p_s C^3 \sqrt{1+\delta}} = \text{Non Dimensional Bearing Number}$$

$$\bar{W}_A = \frac{W_A}{\pi p_a R_s^2} = \text{Non Dimensional Load}$$

$$\bar{S}_R = \frac{C^3 R_s^2}{\pi p_a} = \text{Non Dimensional Stiffness}$$

$$\bar{Q} = \frac{Q 12\mu QT}{\pi p_a^2 C^3} = \text{Non Dimensional Flow}$$

Detailed Evaluation of Gas Bearing Performance at Room Temperature and Zero Eccentricity

$$\Lambda_{so} = \frac{6 \times .25 \times 10^{-8} \times 18 \times .010^2 \times 1.162 \times 10^4}{114.7 \times .0003^3 \times 13.3}$$

$$= 7.64$$

Determination of Radial Stiffness.

From Figure E-1 at $\Lambda_{so} = 7.64$, $\bar{S}_s = 2.95$

$$\therefore S_R = \frac{2.95 \times \pi \times .8125^2 \times 14.7}{.0003}$$

$$= 300,000 \text{ lb/in}$$

Determination of Axial Load.

From Figure E-2 at $\Lambda_{so} = 7.64$, $\bar{W}_A = 1.64$

$$\therefore W_A = 1.64 \pi \times .8125^2 \times 14.7$$

$$= 50 \text{ lbs.}$$

Determination of Gas Flow

From Figure E-3 at $\Lambda_{so} = 7.64$, $\bar{Q} = 260$

$$\therefore Q = \frac{260 \pi \times 14.7^2 \times .0003^3}{12 \times .25 \times 10^{-8} \times 1.35 \times 10^8}$$

$$= 11.7 \times 10^{-7} \text{ lbsec/in}$$

or $Q = .34 \text{ scfm}$

Results of Gas Bearing Evaluations at 1400°F and Zero Eccentricity

Assuming nitrogen

$$T = 1860^\circ R$$

$$Q = 2.555 \times 10^5 \text{ in}^2/\text{sec}^2 \text{ } ^\circ R$$

$$QT = 4.75 \times 10^8 \text{ in}^2/\text{sec}^2$$

$$\mu = .58 \times 10^{-8} \text{ Reyns.}$$

Then from previous equations and curves

$$\Lambda_{so} = \underline{33.2}$$

Radial stiffness at $\bar{S}_R = 3.4$

$$S_R = \underline{346,000} \text{ lb/in}$$

Axial load capacity at $\bar{W}_A = 1.8$

$$W_A = \underline{55} \text{ lbs}$$

Gas Flow at $\bar{Q} = 300$

$$A = 1.66 \times 10^{-7} \text{ lbsec/in}$$

$$= \underline{.048} \text{ scfm}$$

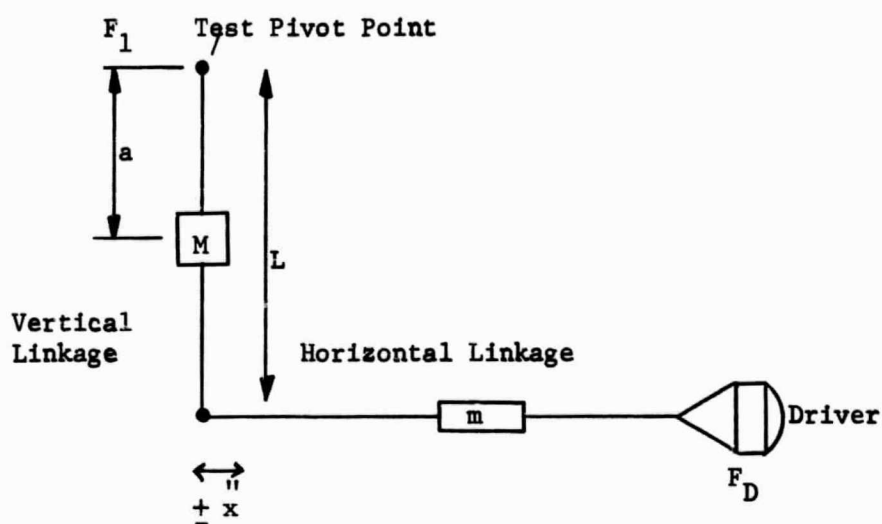
Driver Performance

The electromagnetic drive was selected for the final designs based on the evaluation discussed earlier in the report.

A critical aspect of the evaluation was to establish the maximum power to weight ratio in the drive system.

To achieve this a light weight linkage system was designed and analyzed to determine its force and load characteristics relative to the drive unit and bearing capability.

Detailed Analysis of Mechanical Linkage



where x is linear acceleration

Forces in System

$$F = F_D - m \ddot{x}$$

$$F = F_1 + \frac{a}{L} \ddot{x} M$$

$$FL = \frac{a}{L} \ddot{x} M a$$

$$\text{or } F = \frac{a^2}{L^2} \ddot{x} M$$

$$\therefore F_1 = \frac{a^2}{L^2} \ddot{x} M - \frac{a}{L} \ddot{x} M$$

$$F_1 = \ddot{x} M \left[\frac{a^2}{L^2} - \frac{a}{L} \right]$$

and

$$F_D = \ddot{x} M \left[\frac{a^2}{L^2} - \frac{a}{L} \right] + m \ddot{x}$$

at $\omega = 1000$ cps and displacement $\delta = \pm .0015$ inches/inch

$$\begin{aligned}\ddot{x} &= \pm \delta L \omega^2 \cos\theta \\ &= \pm .0015 \times 1.75 \omega^2 \cos\theta\end{aligned}$$

For very small displacements $\cos\theta \approx 1$

$$\begin{aligned}\text{Then } \omega^2 &= (2 \pi 1000)^2 \\ &= 39.5 \times 10^6 \text{ (rad/sec)}^2 \\ \therefore \ddot{x} &= 103.4 \times 10^3 \text{ in/sec}^2 \text{ or } \underline{270 \text{ g}}\end{aligned}$$

Equivalent Weight to be Driven by Electromagnetic Drive

Calculated weight of all components on the horizontal section of linkage is:
.010 lbs.

Equivalent weight of vertical linkage and gas bearing related to horizontal axis is as follows:

$$\sum W a^2 = .027 \text{ lb in}^2$$

Calculated $W = .155 \text{ lbs.}$

$$a^2 = .175 \text{ in}^2$$

and $a = .419 \text{ in.}$

$$\begin{aligned}\text{Equivalent weight on lower axis} &= \frac{\sum W a^2}{L^2} \\ &= \frac{.027}{1.75^2} = \underline{.0089 \text{ lbs}}\end{aligned}$$

\therefore Total equivalent weight on lower horizontal axis

$$= .010 + .0089 = .0189 \text{ lbs}$$

or 0.3 ozs.

This ignores minor frictional losses and deflection forces due to linkages for other axes of motion.

The simulated loading tests on the 75 watt Universal Driver is given on Figure E-4. Superimposing the 0.3 ozs. loading onto the graphs indicates that achieving this performance is quite feasible.

If necessary, double drivers can be utilized to increase the power input for any motion.

Further, the power demand can be reduced by establishing a resonant drive system as discussed in a preceeding section.

Reaction Forces on Hemi-Spherical Gas Bearing

$$F_1 = x M \left[\frac{a^2}{L^2} - \frac{a}{L} \right]$$

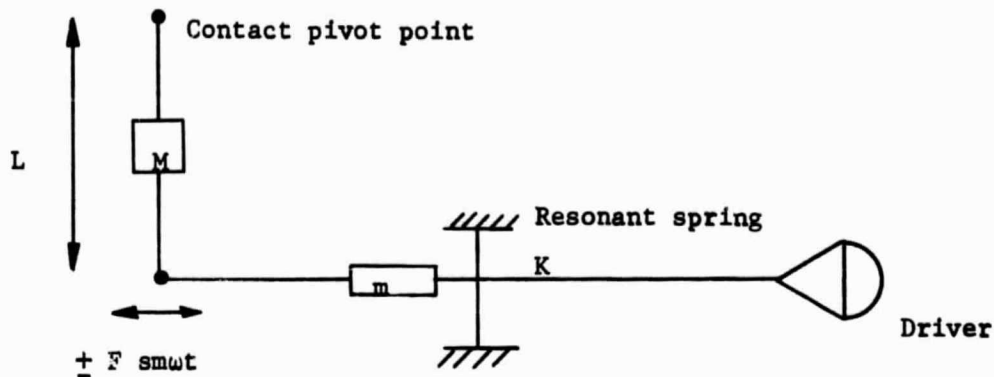
$$F_1 = 103.4 \times 10^3 \times \frac{.155}{386} \left[\frac{.175}{1.75^2} - \frac{.419}{1.75} \right]$$

$$F_1 = - \underline{7.62} \text{ lbs at } 1000 \text{ cps.}$$

If the radial stiffness of the gas bearing is 300,000 lb/in at room temperature then the deflection at zero eccentricity will be .00025". This can be reduced by higher gas bearing supply pressure or increased eccentricity in the gas bearing.

Detailed Analysis of Resonance

In the analysis the following symbols were used



I = Polar moment of inertia, in lb sec^2

ω = Driving frequency, rads/sec

ω_n = Natural frequency, rads/sec

$\beta = \frac{\omega}{\omega_n}$

F_o = Driving force, rads/sec

L = Moment arm of driving force, inches

K = Spring constant of system, lbs/in

C = Damping coefficient in lb. sec/rad.

C_e = Equivalent viscous damping coefficient

C_c = Critical damping coefficient

θ_o = Amplitude of torsional oscillation, radians

f_r = Friction torque = .27 lbins.

δ = Half amplitude of motion, inches

Determination of Spring Stiffness

From "Mechanical Vibration" by W. T. Thompson, Prentiss Hall Inc.

$$\theta_o = \frac{\frac{F_o L}{KL^2}}{\sqrt{\left[1 - \frac{I \omega^2}{KL^2}\right]^2 + \left(\frac{C\omega}{KL^2}\right)^2}}$$

If the damping coefficient is 0 then θ_o is infinite when $\frac{I\omega^2}{KL^2} = 1$

$$\text{or } \omega_n = \frac{\sqrt{KL^2}}{I}$$

For a magnification factor 2, $\frac{\omega}{\omega_n}$ should be approximately .75

$$\text{or } \omega_n = \frac{\omega}{.75} = \frac{1000}{.75} \times 2\pi = 8360 \text{ rad/sec}$$

The required spring characteristics are as follows:

$$\text{For } I \text{ of system} = \frac{.1007}{g} \text{ inlbsec}^2$$

and taking $L = 1.69$ in

$$\text{Then the required stiffness } K = \frac{\omega_n^2 I}{L^2} = \frac{8360^2}{(1.69)^2} \times \frac{.1007}{386} = 6370 \text{ in/in}$$

Damping Present in System

From "Mechanical Vibrations" by Bernard Morrill. The Ronald Press Co. 1957 p. 87.

$$C_e = \frac{4f_r KL^2}{\omega} \sqrt{\frac{(1 - \beta^2)}{\pi^2 (F_o L)^2 - 4^2 (f_r)^2}}$$

$$C_e = \frac{1.37}{28.2 F_o^2 - 1.165}$$

Taking a value of $F_o = 3$ lbs.

Then $C_e = .086 \text{ inlbsec/rad}$

$$C_c = 2\sqrt{K_L^2 I}$$

$$= 2\sqrt{6370 (1.69)^2 \cdot \frac{.1007}{386}}$$

$$C_c = 4.34 \text{ inlbsec/rad}$$

$$\zeta_e \text{ the damping ratio} = \frac{.086}{4.34} = \underline{.02}$$

It can be concluded that it is quite practical to design the system to operate near resonance with a suitably designed spring in the system. Also that the system is very lightly damped even under the most severe friction condition at the pivot point.

Analysis of Sealing Labyrinth

In order to achieve the test gas environment around the specimens, minimize the test gas flow and prevent back flow of contaminating external gases, a staggered type radial labyrinth seal was designed for sealing purposes at the interface between the upper specimen holder and lower dynamic specimen holder.

The design was based on achieving the maximum number of stages in the available space and assuming argon as the gas.

Detailed Analysis

The analysis was based on theoretical and test data presented in "The Flow of Air Through Radial Labyrinth Glands" by W.J. Kearton, Proceeding of the Institute of Mechanical Engineers, 1955, Vol. 139 No. 30. The case for pressure drops in each construction less than critical was used.

List of symbols and Equations

$r = .29'' = \text{radius of innermost constriction}$

$C = .005'' = \text{clearance}$

$A_1 = 2\pi rC \text{ sq.ins} = \text{area through first constriction}$

$n = 9 = \text{total number of constrictions}$

$a = .0125''$ = radial distance between two adjacent constrictions

$p_o = 15.2$ psia = pressure at inlet to seal

$p_n = 14.7$ psia = pressure at exit from seal

$T_o = 1860^\circ R$ = absolute temperature

$R = 466$ inlb/lb $^\circ R$ = gas constant for argon

$c_1 = .75$ = coefficient of discharge

$F = 1$ = function of pressure ratio in a single constriction

$$\phi_n = n - \left\{ \frac{2 a n (n-1)}{2r+a(2n-1)} \right\} = \text{area function for outward flow}$$

$$W_m = A_1 c_1 \left\{ \frac{F g (p_o^2 - p_n^2)}{R T_o \phi_n} \right\}^{1/2} = \text{mass flow through seal} \quad \text{lb/sec}$$

On the basis of 0.5 psi pressure drop across the complete seal the following flow can be established:

$$\phi_n = 9 - \left\{ \frac{2 \times .0125 \times 9 (8)}{.58 + .0125(18-1)} \right\}$$

$$\therefore \phi_n = 6.73$$

$$A_1 = 2\pi \times .29 \times .005 = .0091 \text{ sqins.}$$

Mass Flow Through Seal

$$W_m = .0091 \times .75 \left\{ \frac{1 \times 386 (15.2^2 - 14.7^2)}{466 \times 1860 \times 6.73} \right\}^{1/2}$$

$$= .000215 \text{ lbs/sec}$$

$$W_m = .129 \text{ scfm at } 1400^\circ F$$

$$W_m = .24 \text{ scfm at room temperature}$$

In order to reduce the flow of argon below these values the clearance can probably be reduced based on operating experience and also the pressure drop across the seal reduced further.

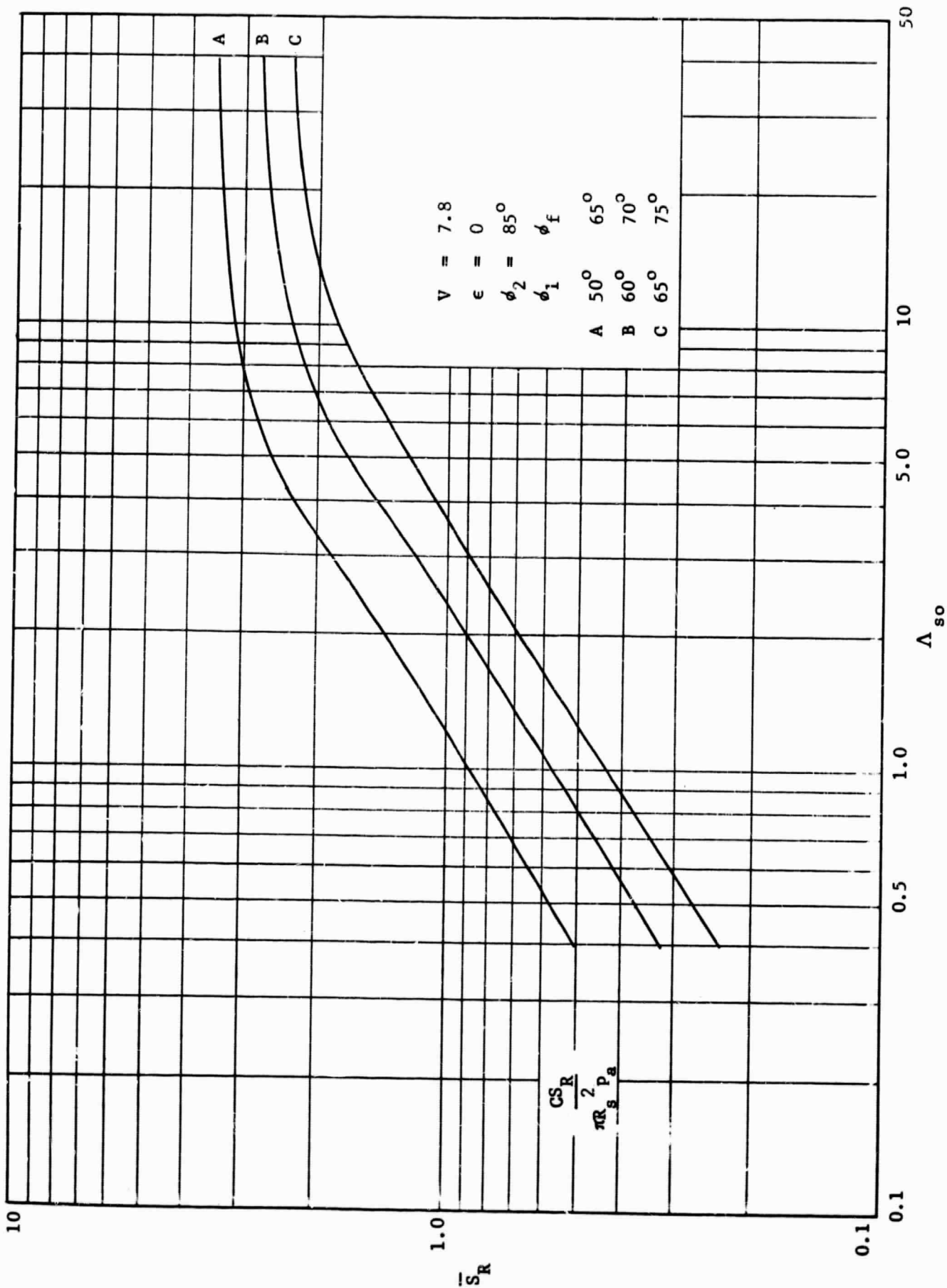


Fig. E-1 Dimensionless Stiffness for Hemispherical Gas Bearing

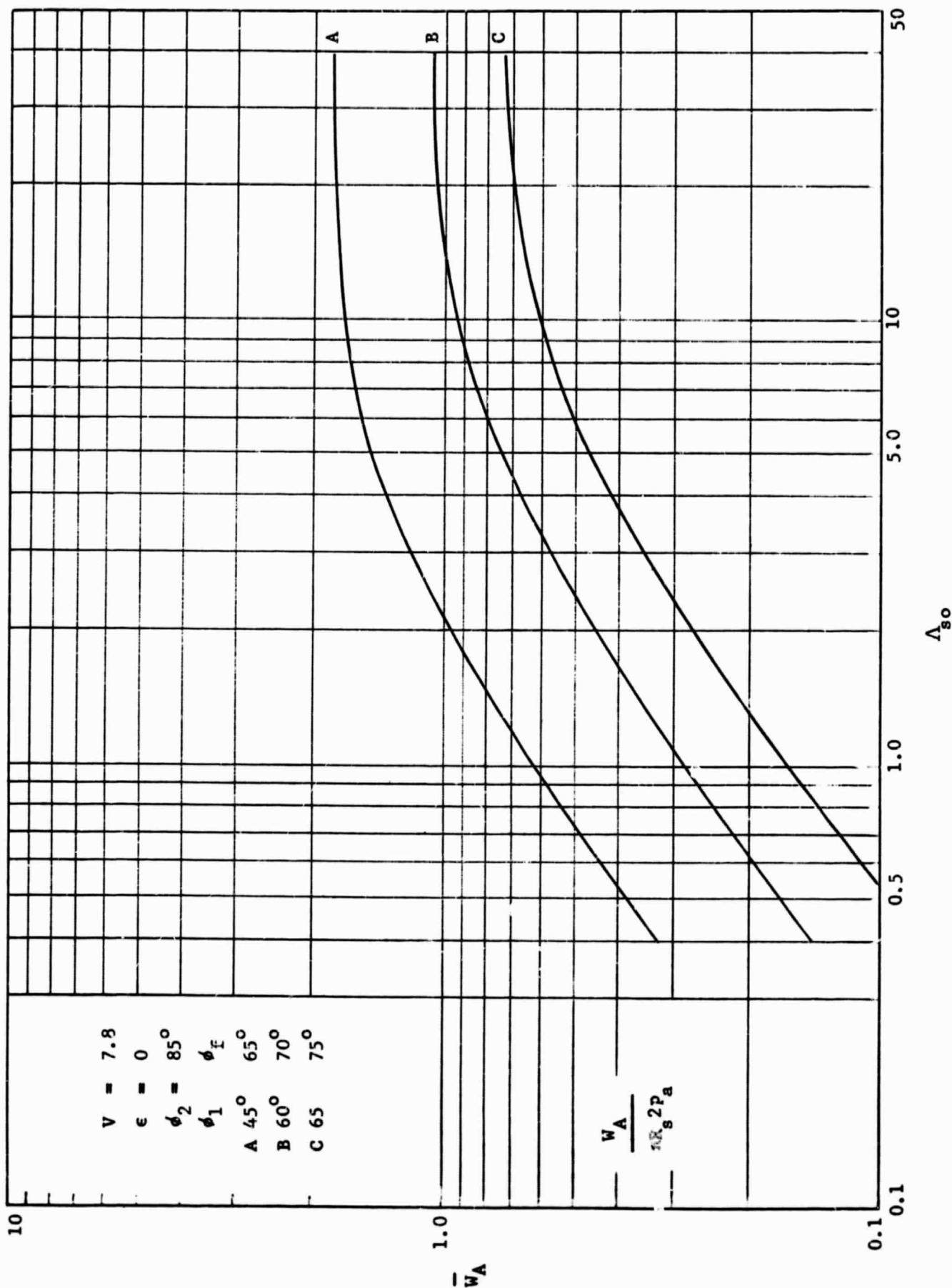


Fig. E-2 Dimensionless Axial Load for Hemispherical Gas Bearing

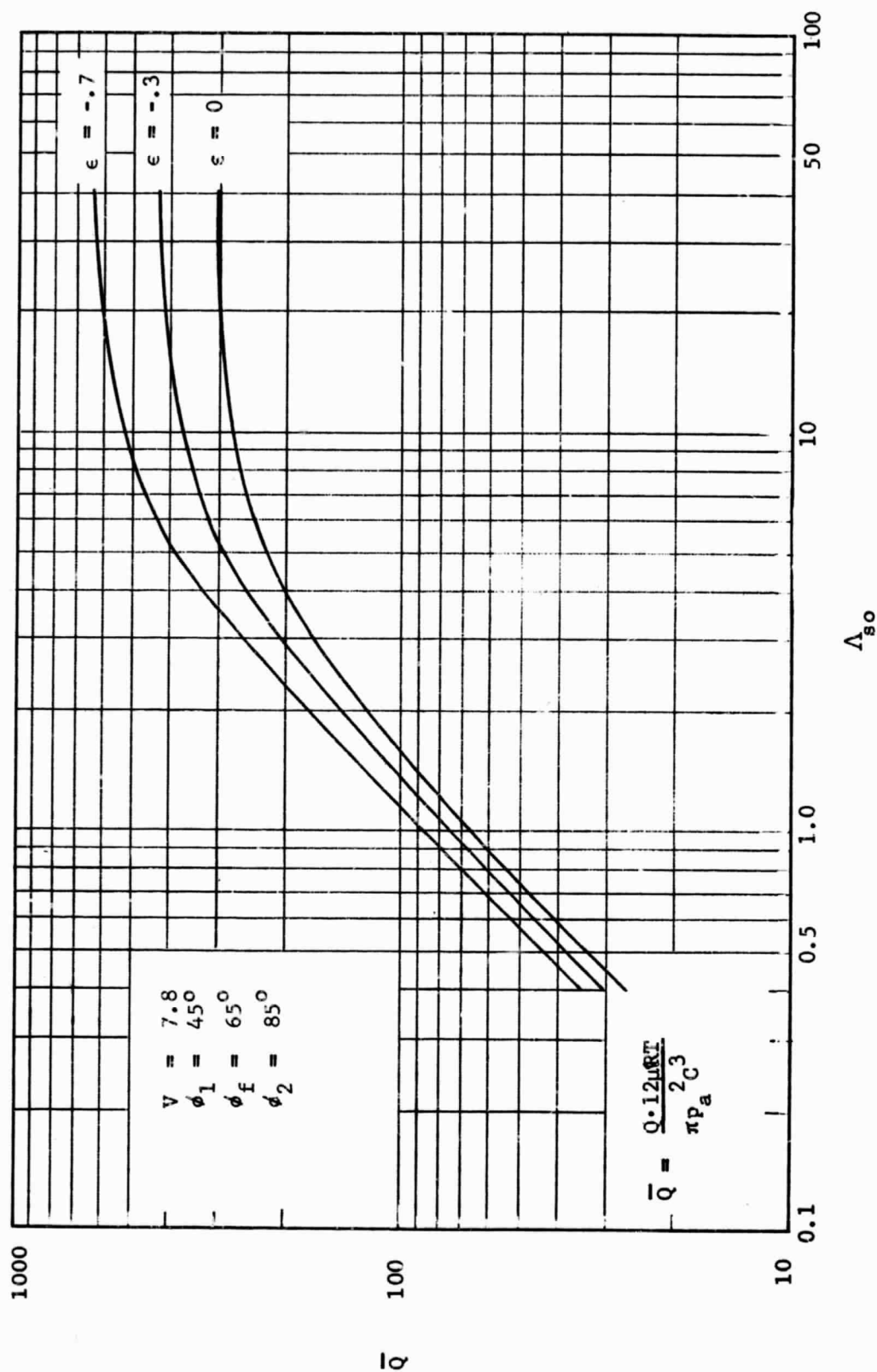


Fig.E-3 Dimensionless Flow for Hemispherical Gas Bearing

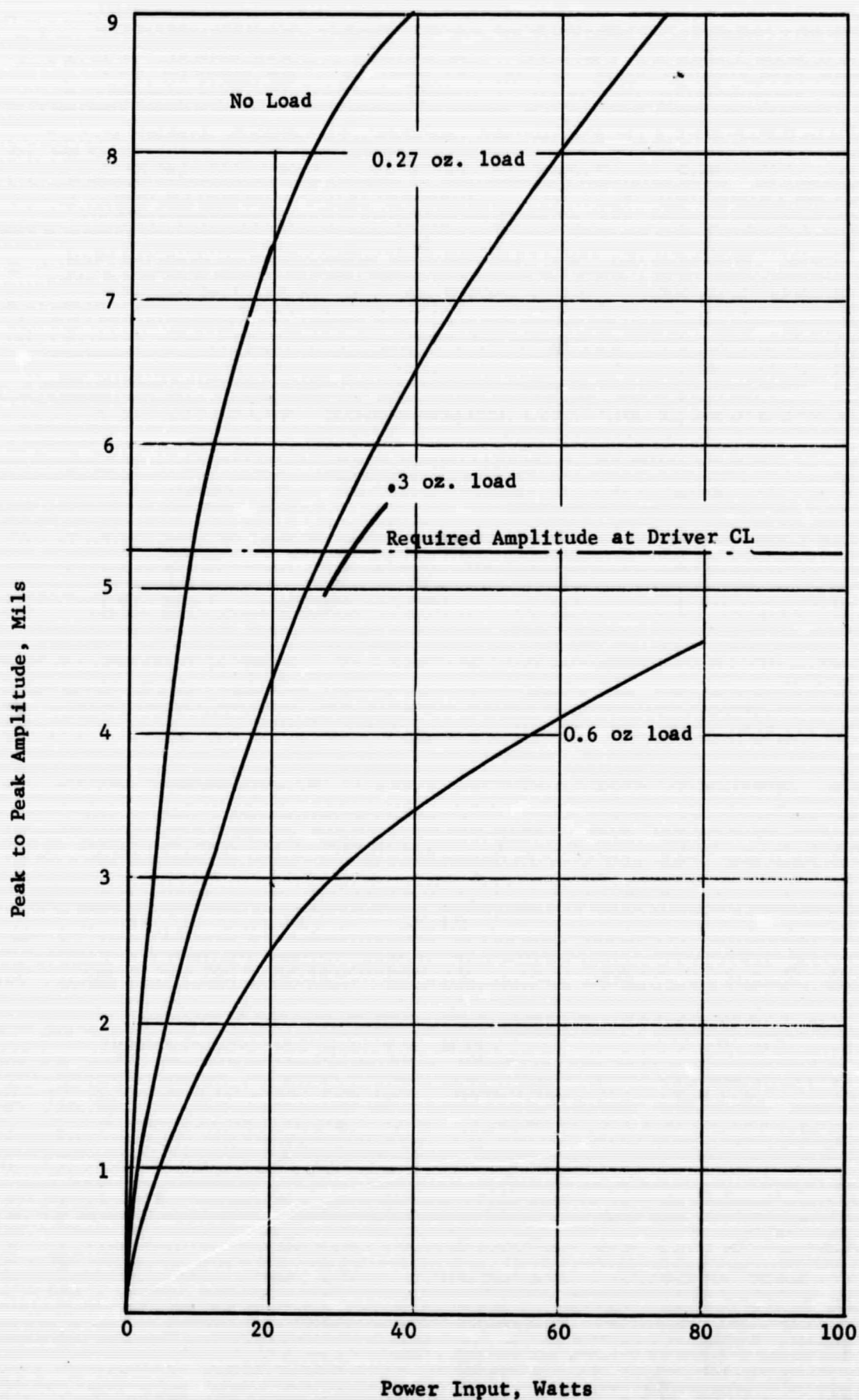


Fig. E-4 Simulated Driver Tests at 1000 cps. 75 watt Universal Model with Various Added Weights

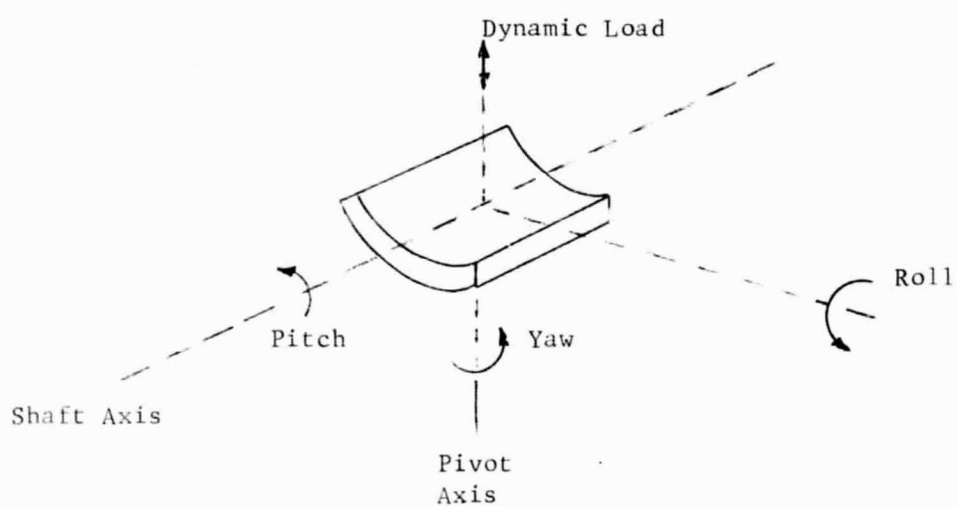


Fig. 1 Pad Motions

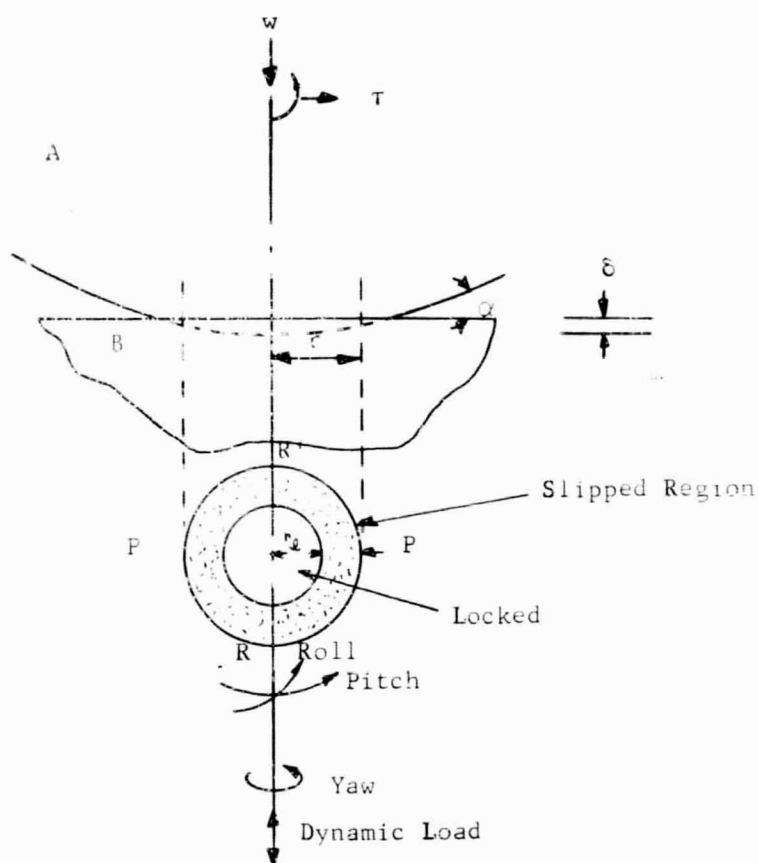


Fig. 2 Ball-Plate Configuration

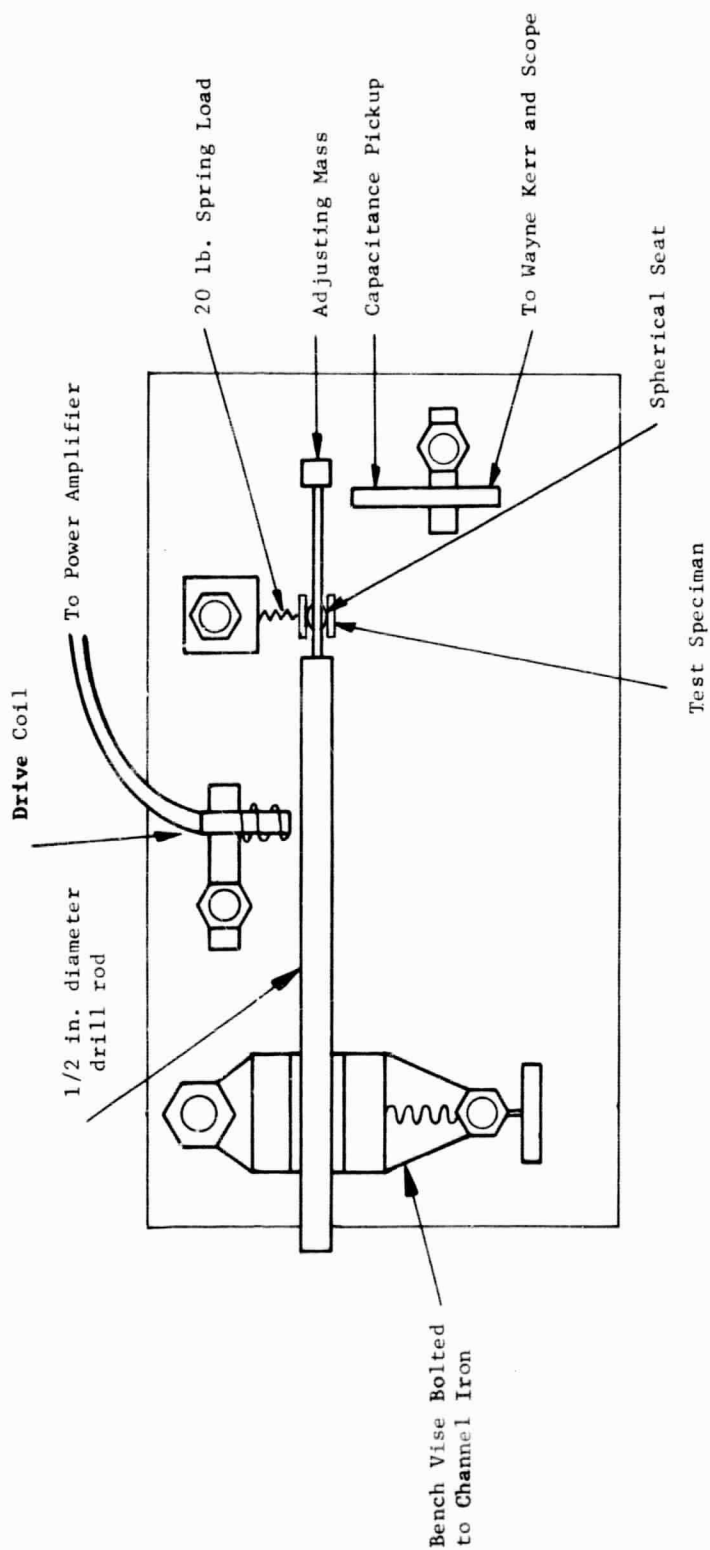


Fig. 3 MTI Basic Fretting Test Rig

MTI-2541

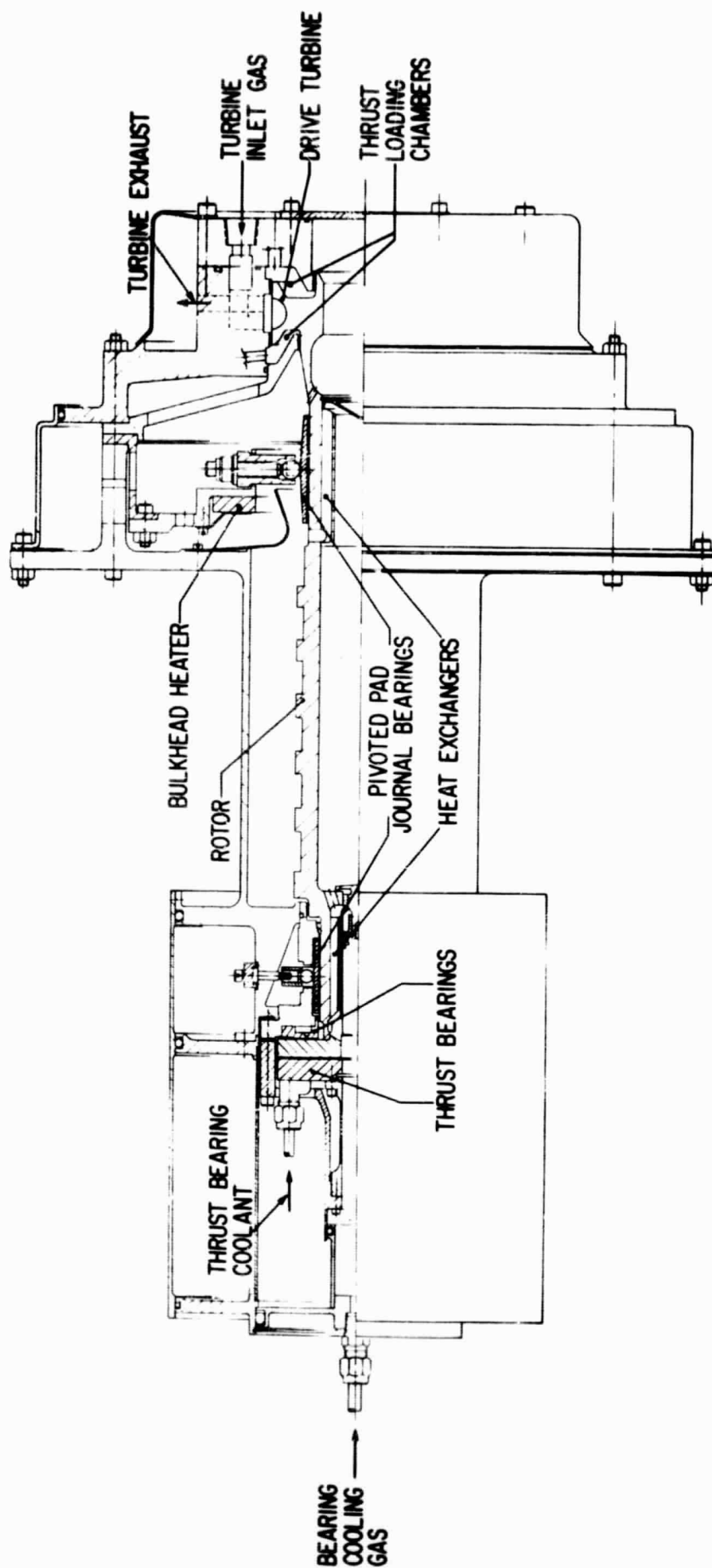


Fig. 4 Cross-Section View of Rotor-Bearing System Simulator

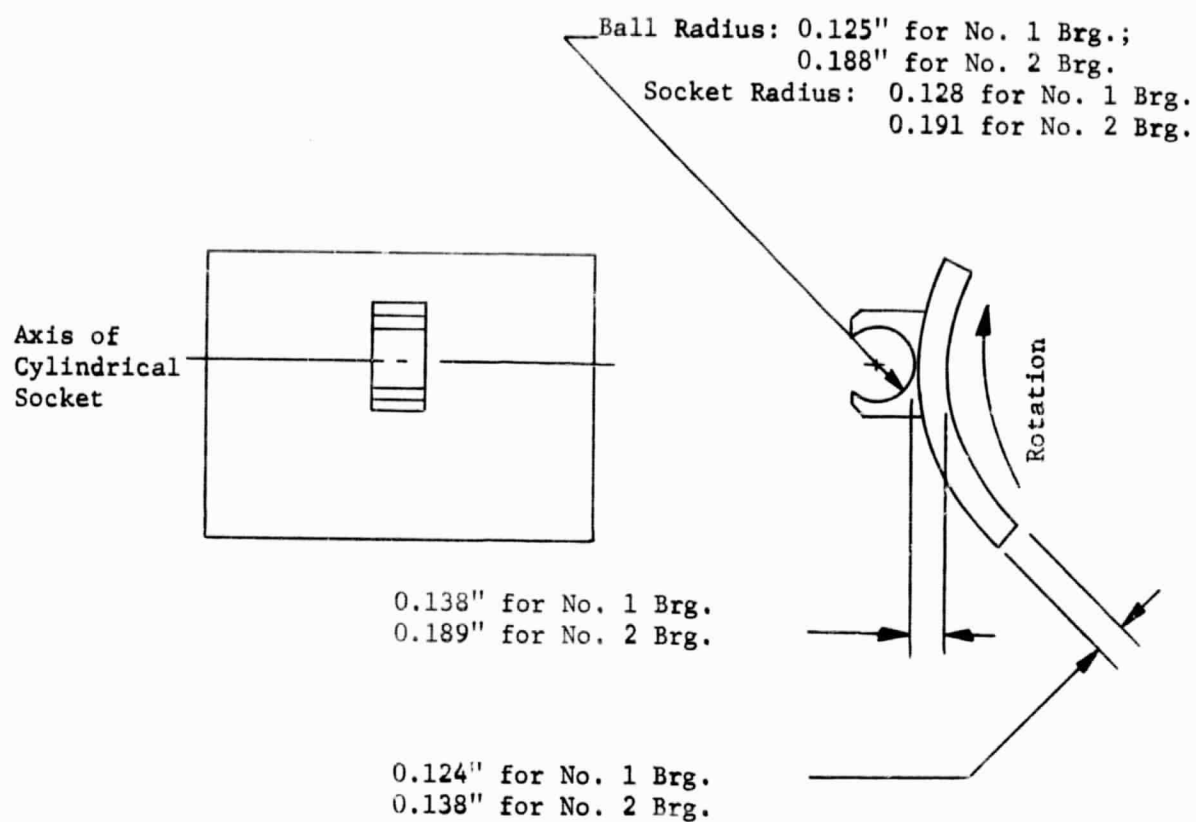
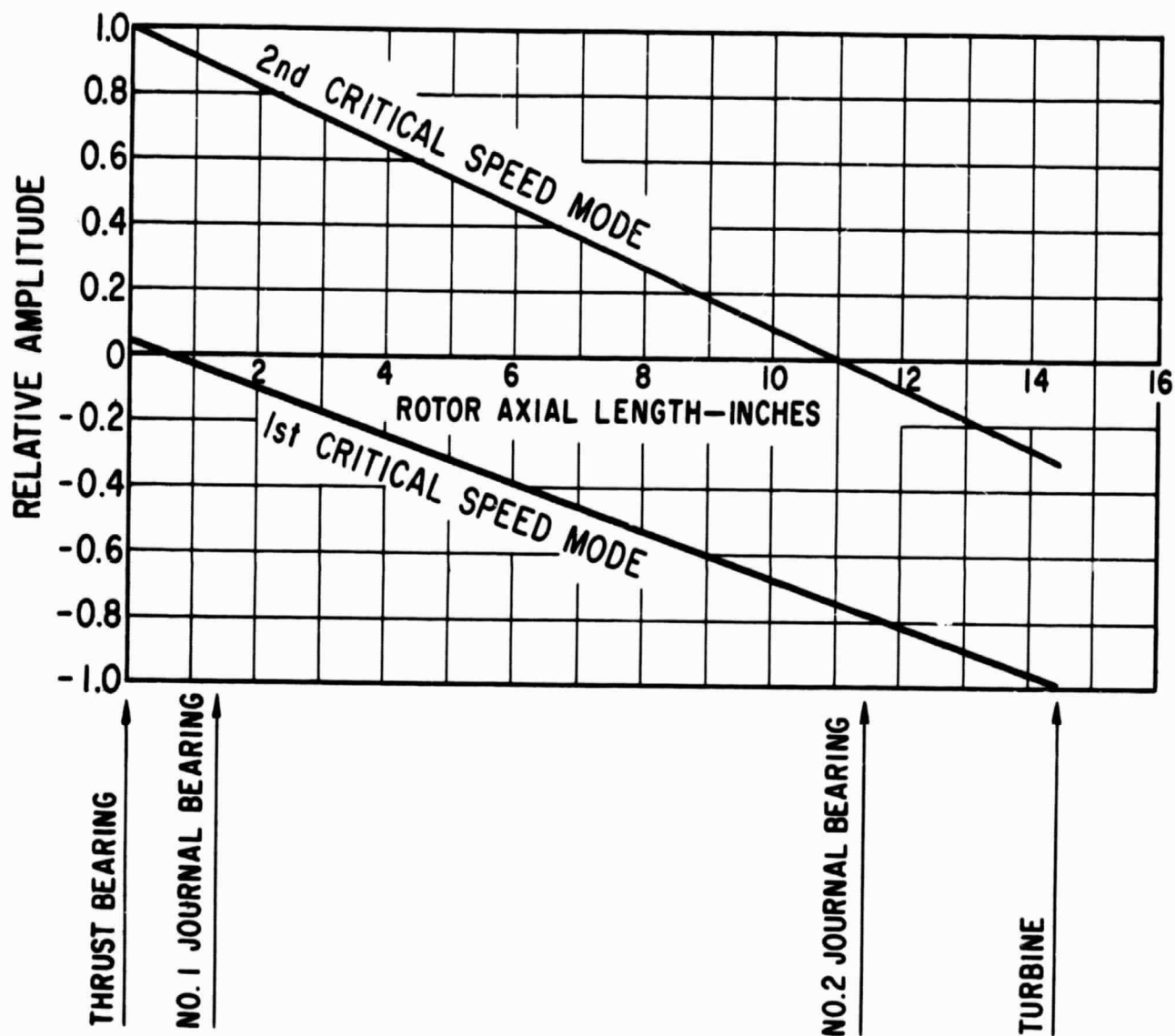


Fig. 5 Schematic of Pad and Pivot



JOURNAL BEARING

GAS FILM STIFFNESS (LB/IN.)

SUPPORT STIFFNESS (LB/IN.)

NO. 1

17,500

52,900

NO. 2

46,000

72,000

Fig. 6 Calculated Mode Shapes for the Two Rigid-Body Critical Speeds of the Final Rotor-Bearing System Design

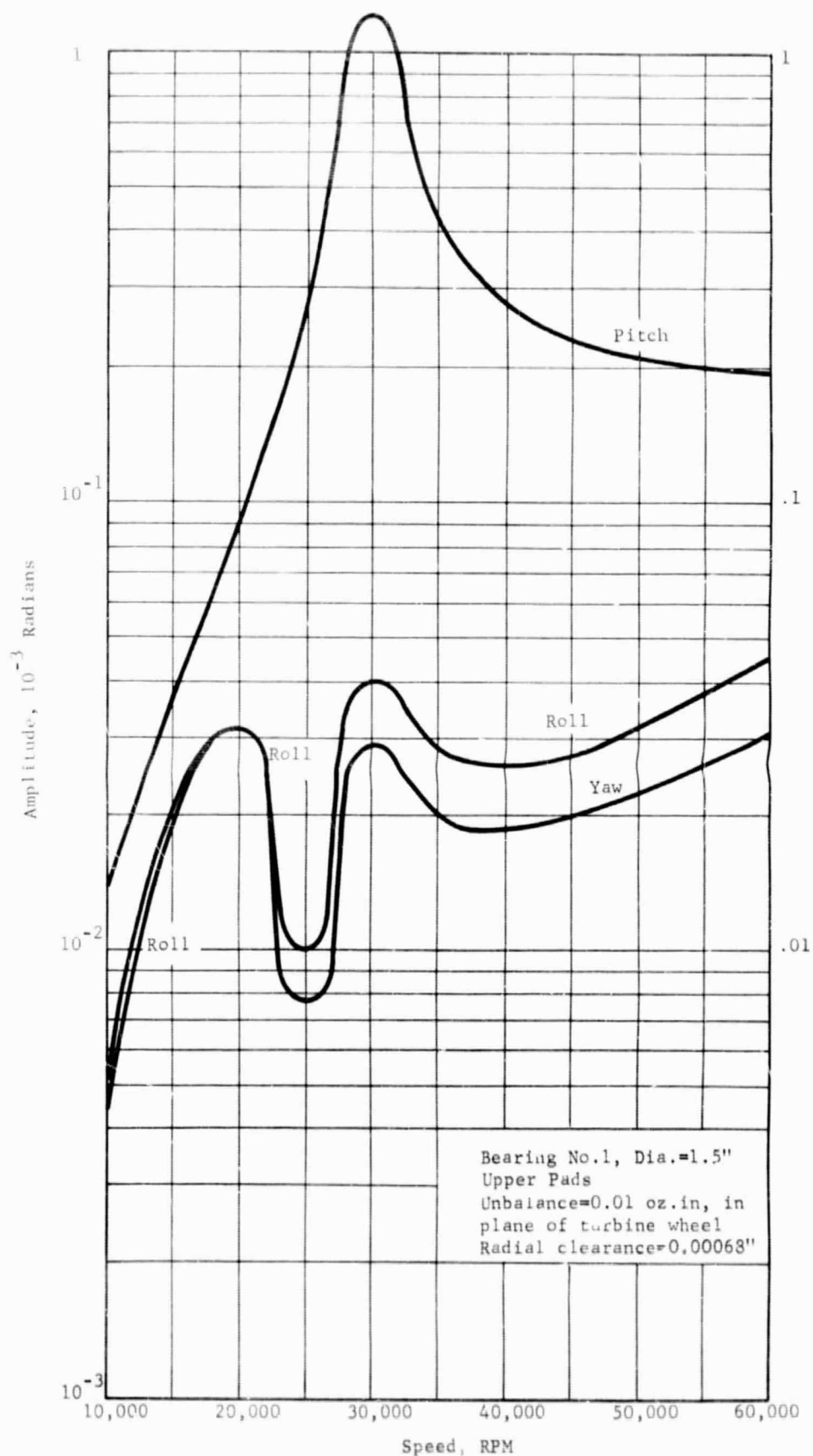


Fig. 7 Calculated Amplitudes of Pad Motion

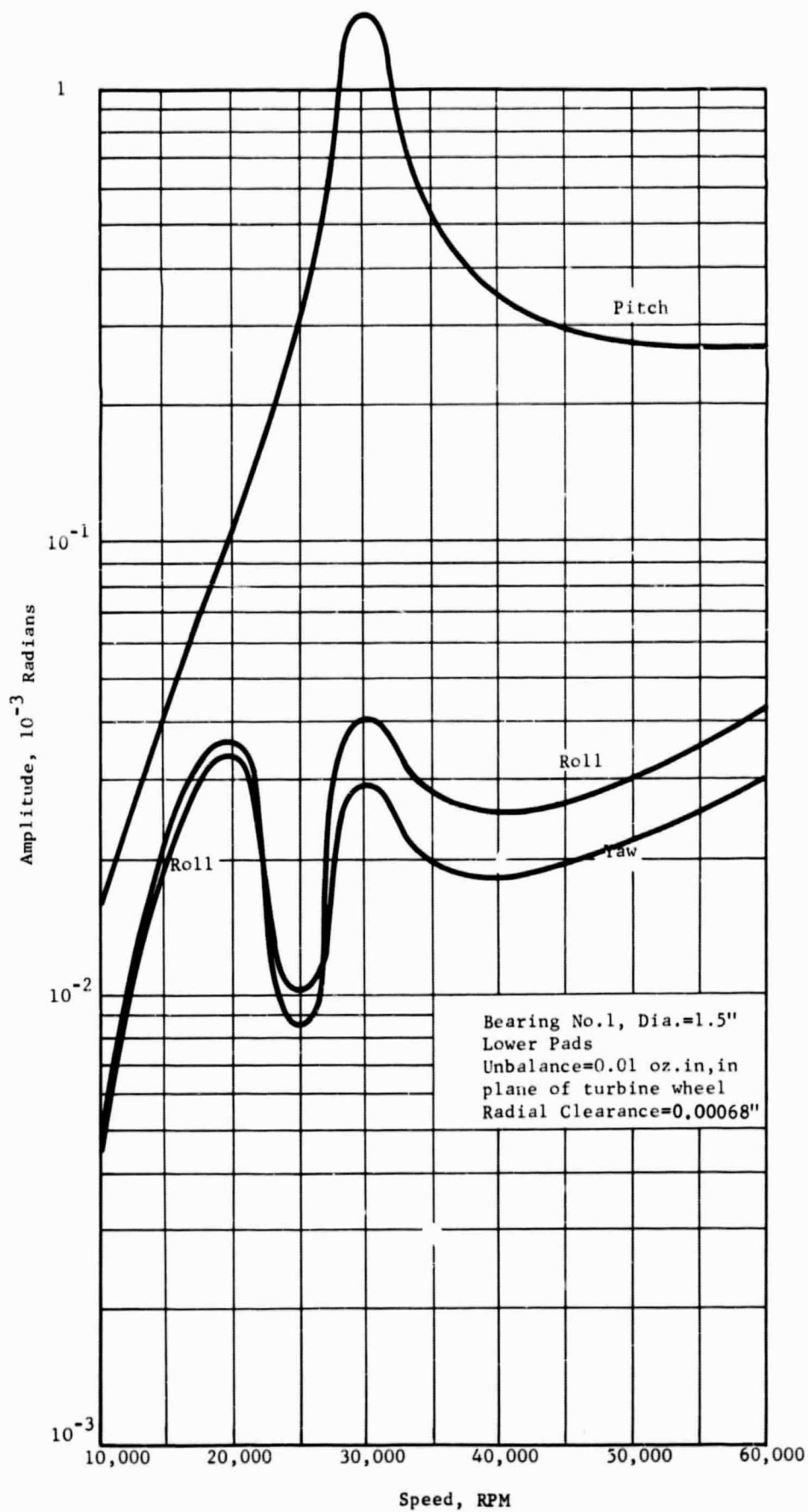


Fig. 8 Calculated Amplitudes of Pad Motion

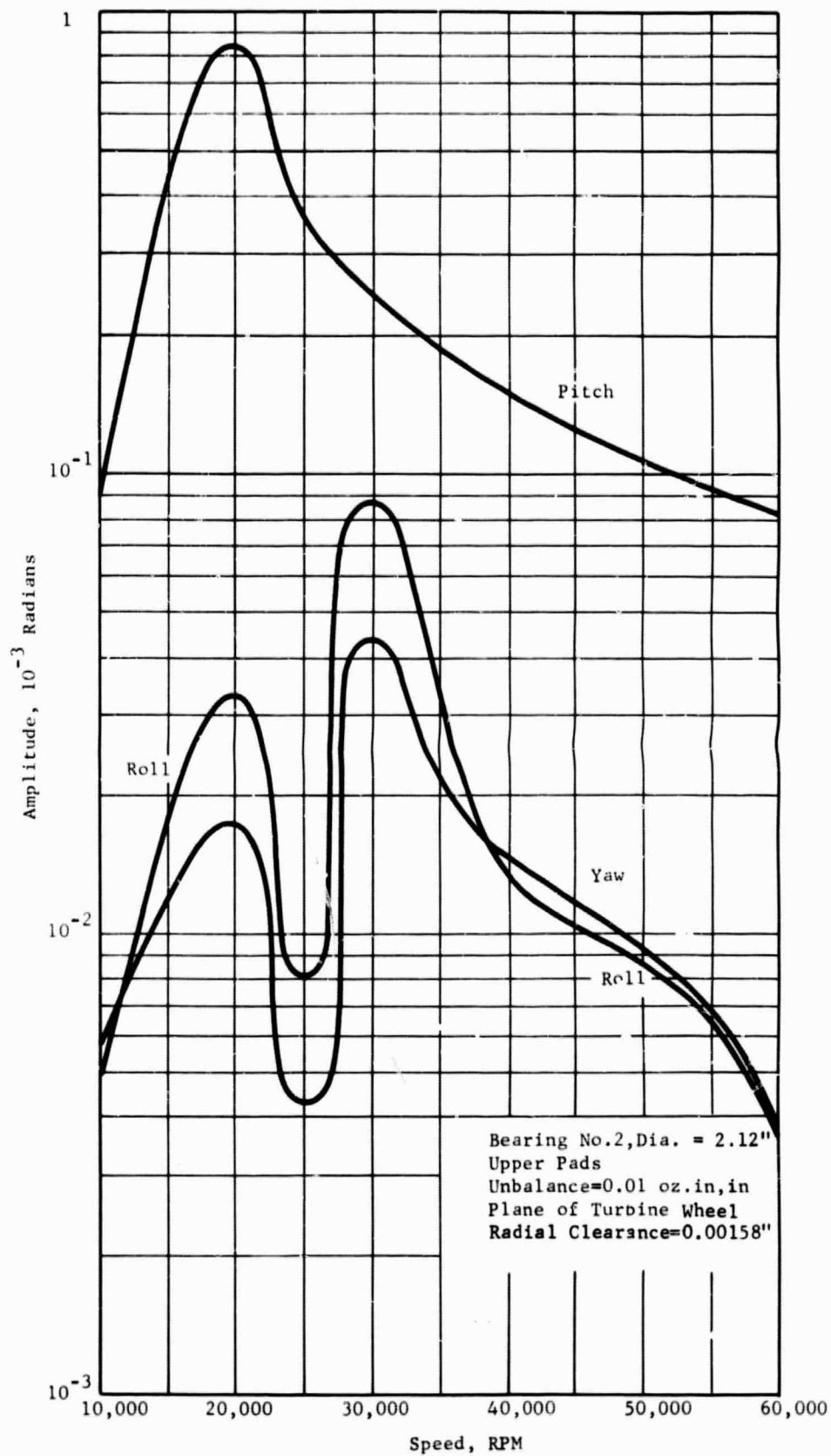


Fig. 9 Calculated Amplitudes of Pad Motion

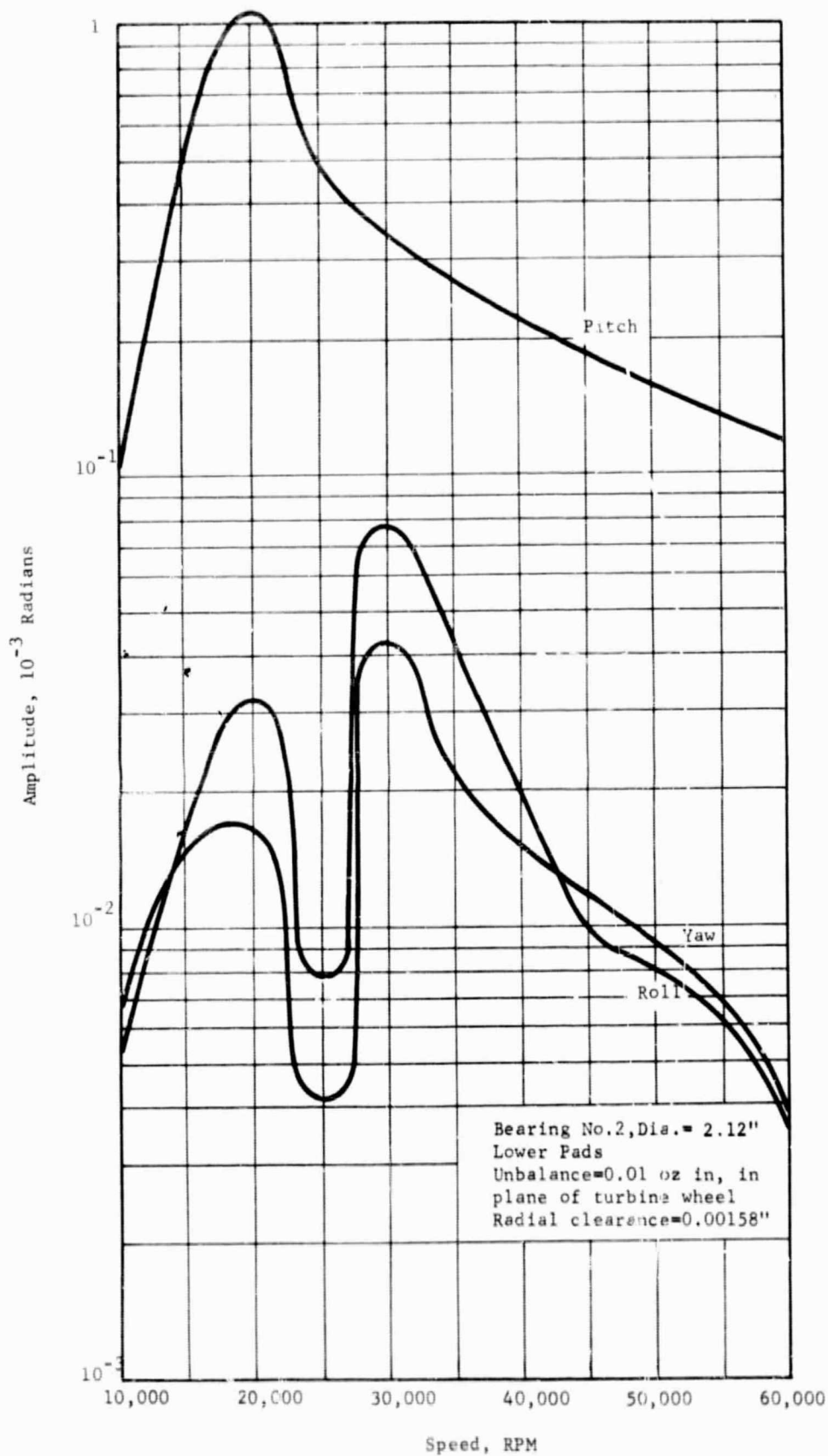


Fig. 10 Calculated Amplitudes of Pad Motion

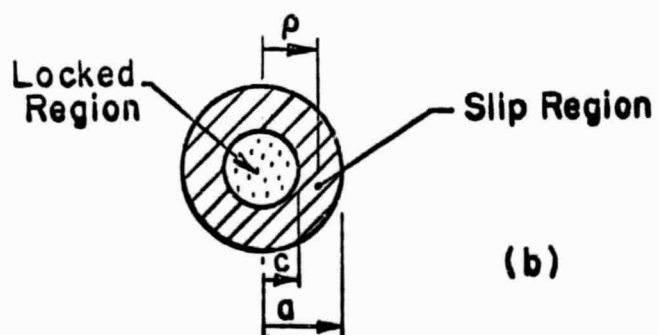
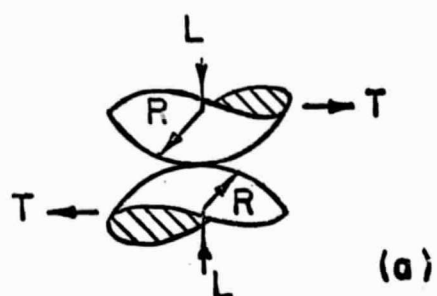


Fig. 11 Schematic Diagram Showing (a) Balls in Contact, (b) Contact Area

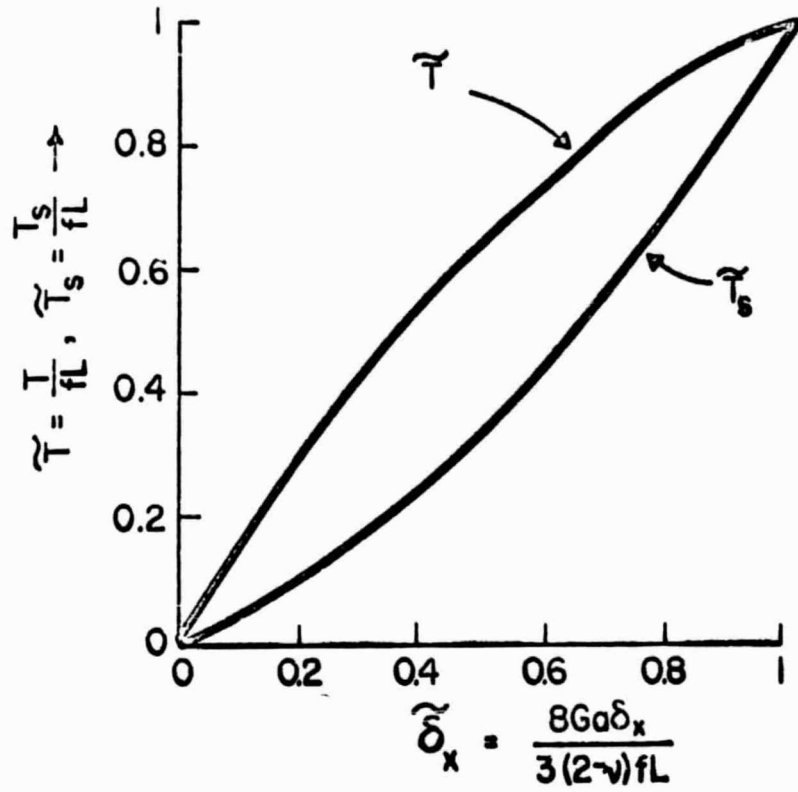
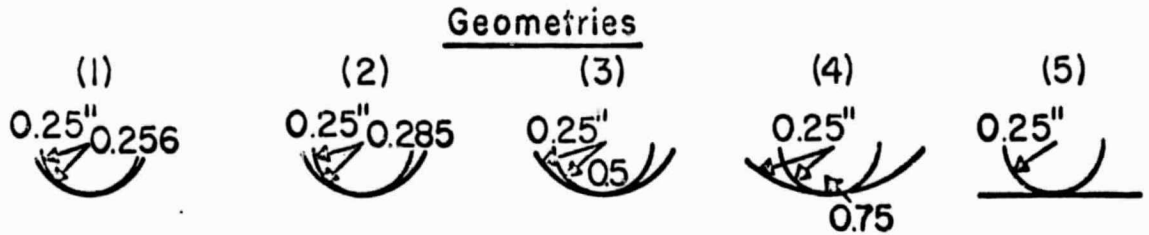


Fig. 12 Curves Showing Shear Traction and that Portion Expanded for Slippage as a Function of Rigid Body Displacement.



Equivalent Geometries - (Within Contact Theory)

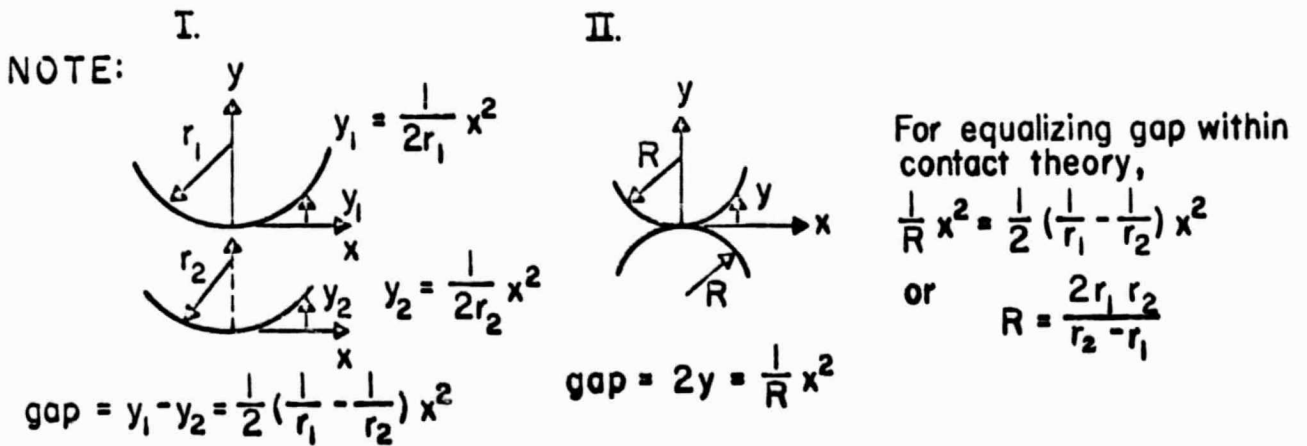


Fig. 13 Five Selected Geometries

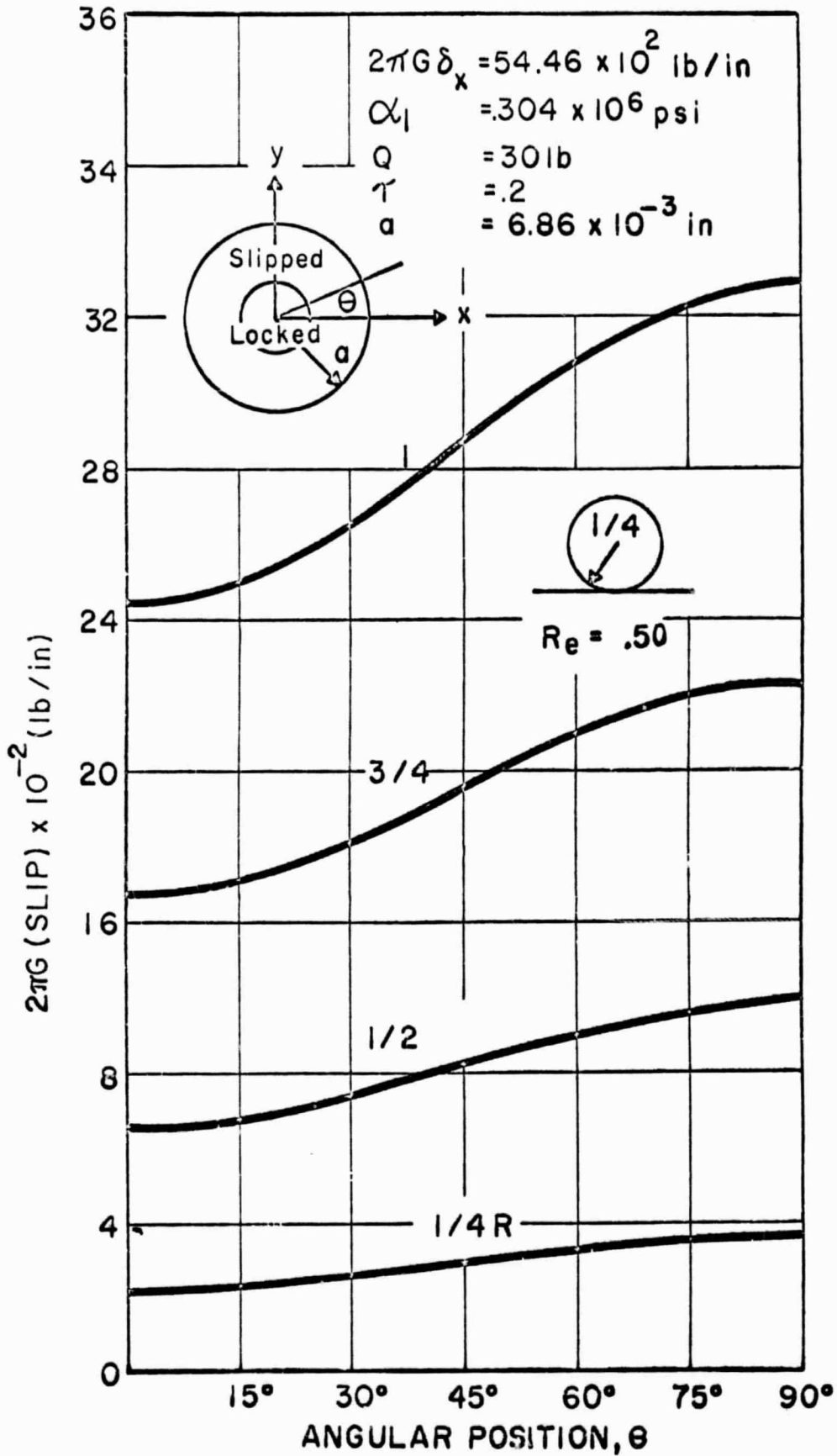


Fig. 14 Distribution of Microslip Within Classical Theory for $R_e = .50 \text{ in.}$

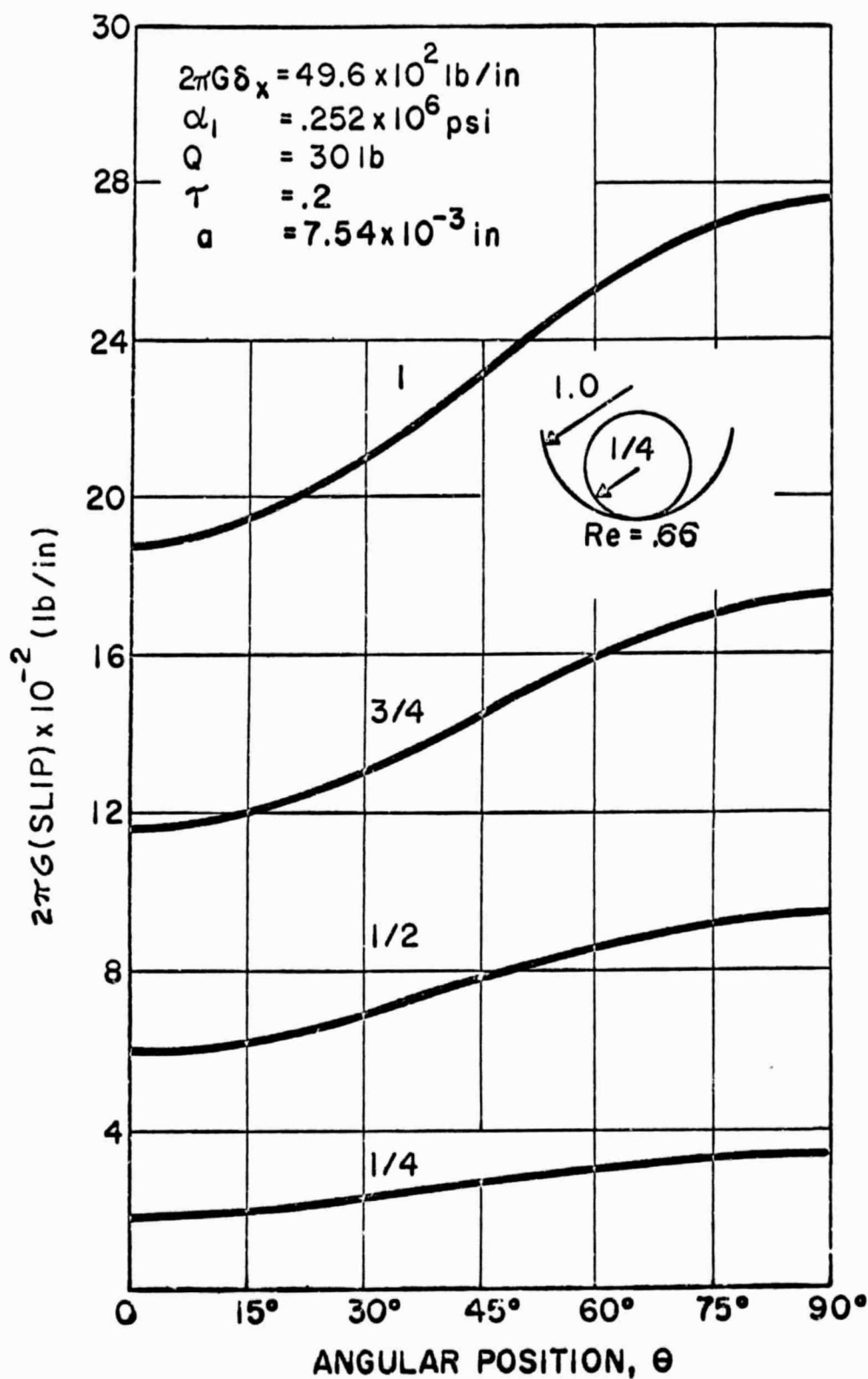


Fig. 15 Distribution of Microslip Within Classical Theory for $R_e = .66 \text{ in.}$

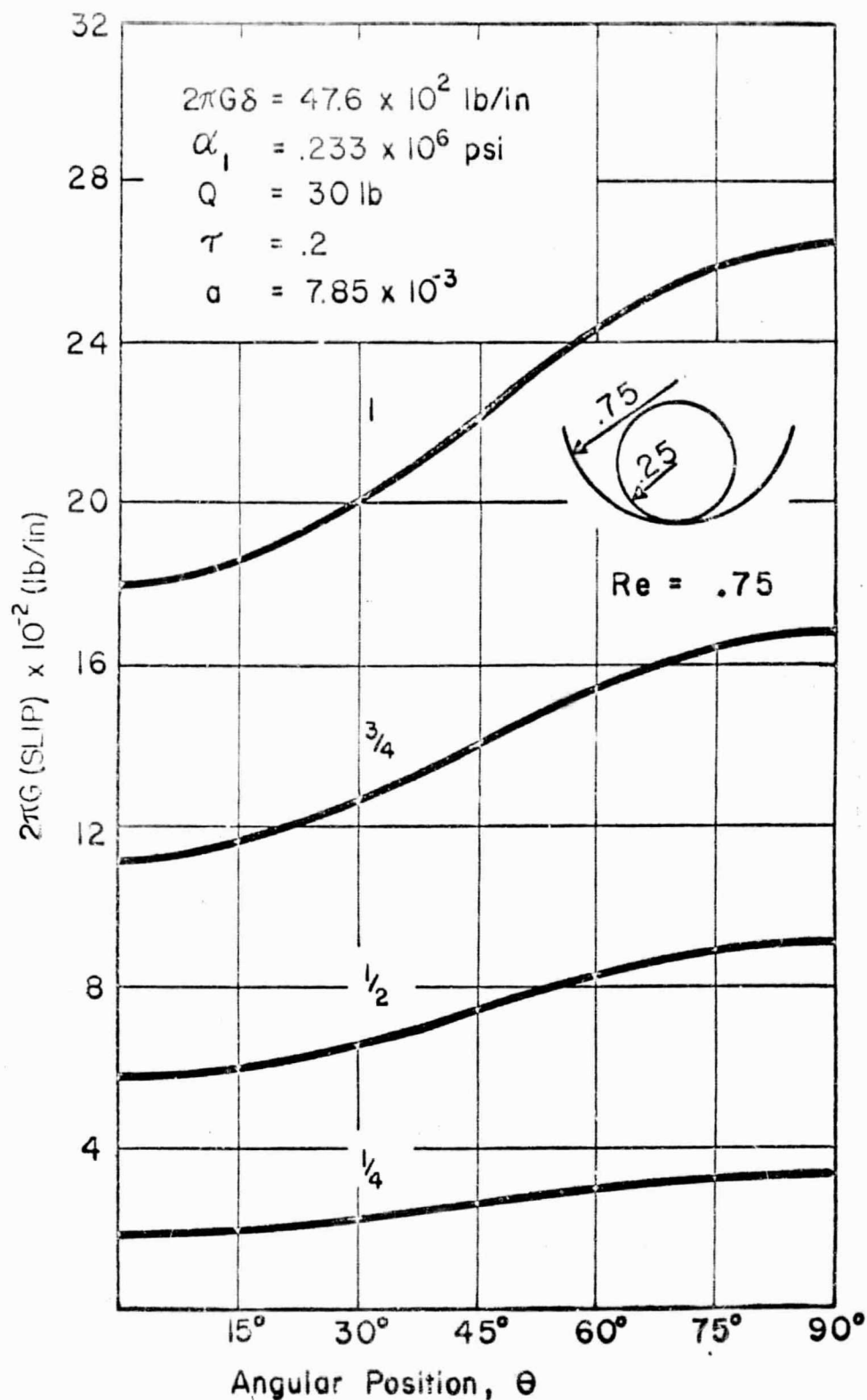


Fig. 16 Distribution of Microslip Within Classical Theory for $R_e = .75 \text{ in.}$

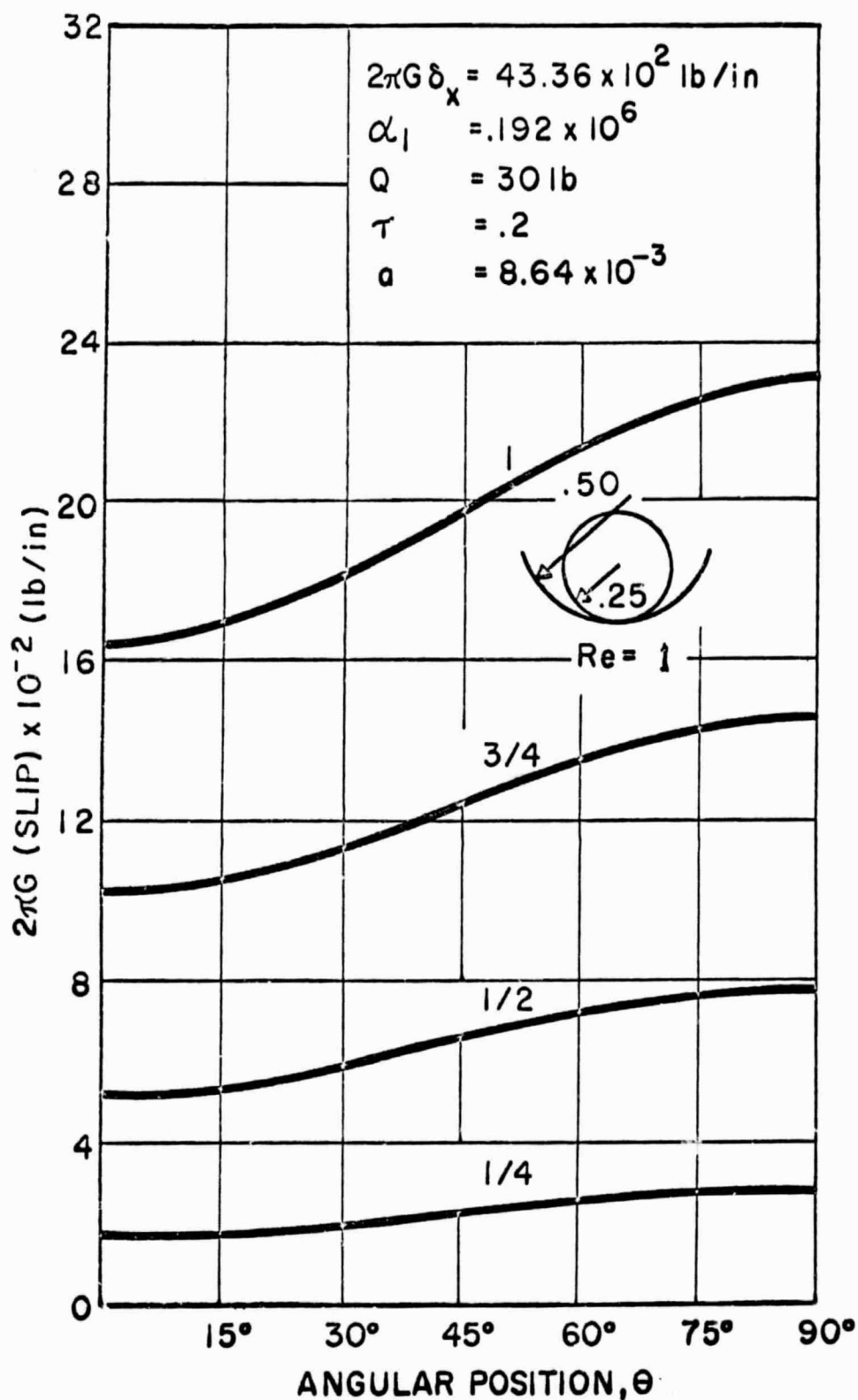


Fig. 17 Distribution of Microslip Within Classical Theory for $R_e = 1.0$ in.

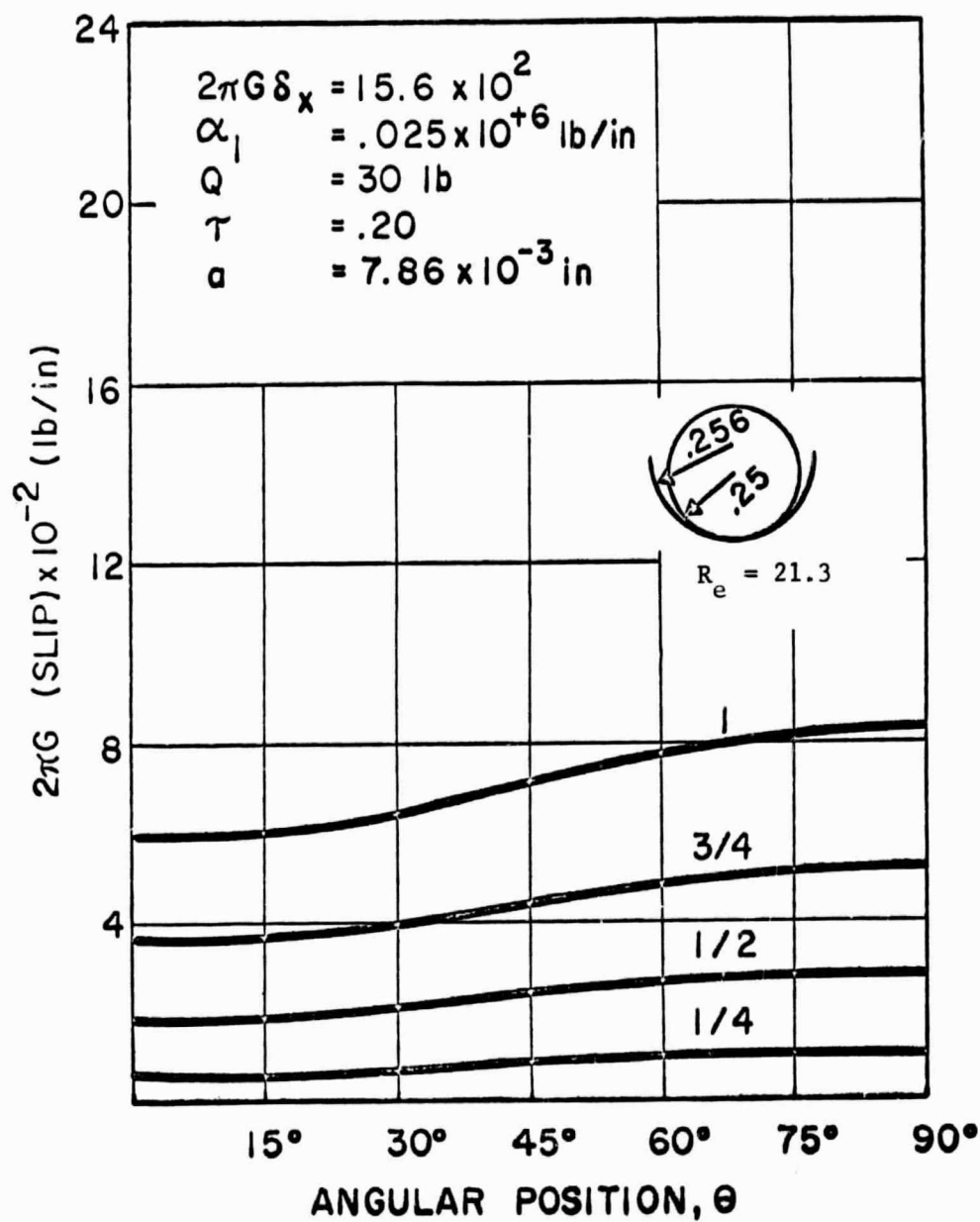


Fig. 18 Distribution of Microslip Within Classical Theory for $R_e = 21.3$ in.

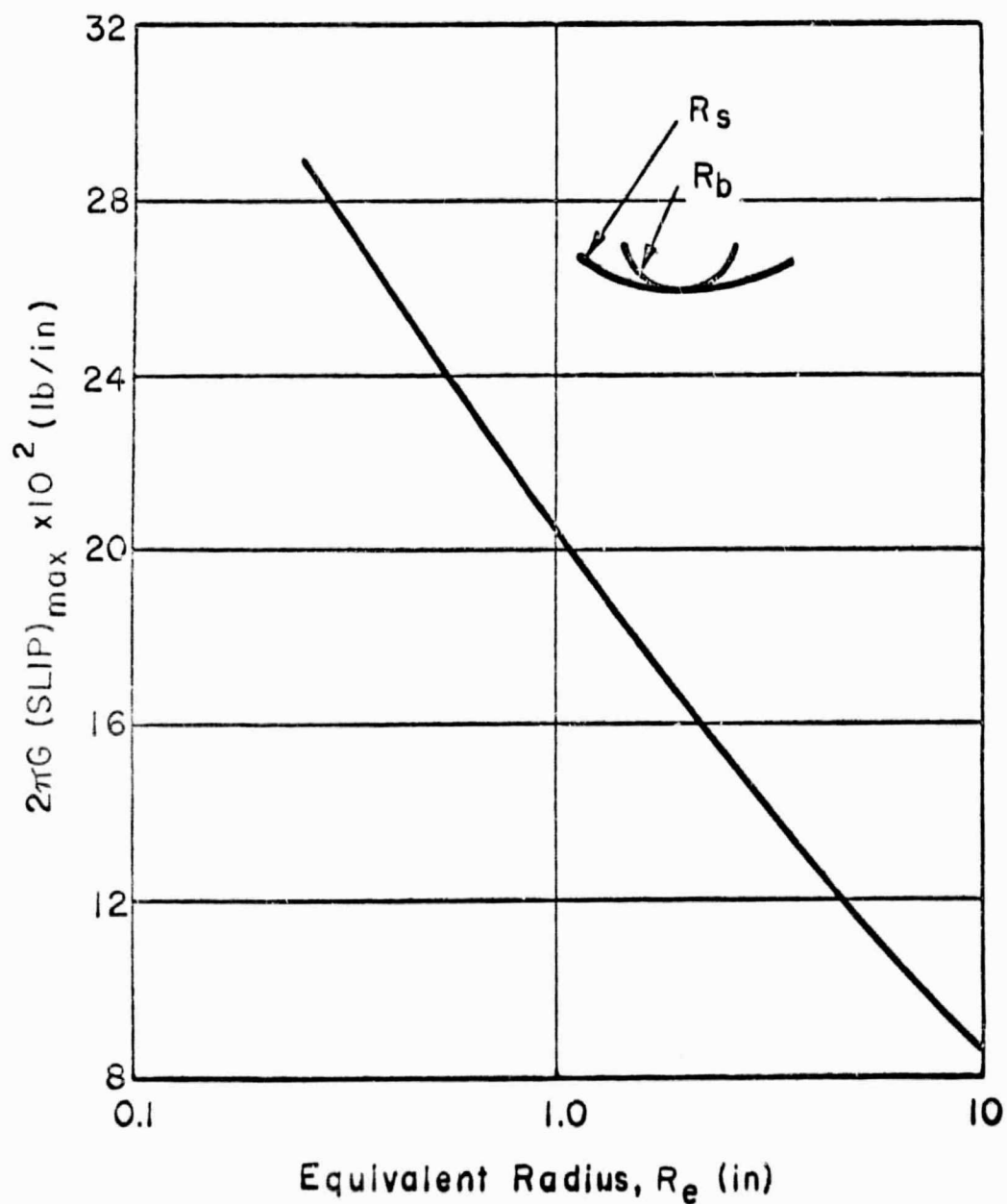


Fig. 19 Maximum Microslip as a Function of Equivalent Radius

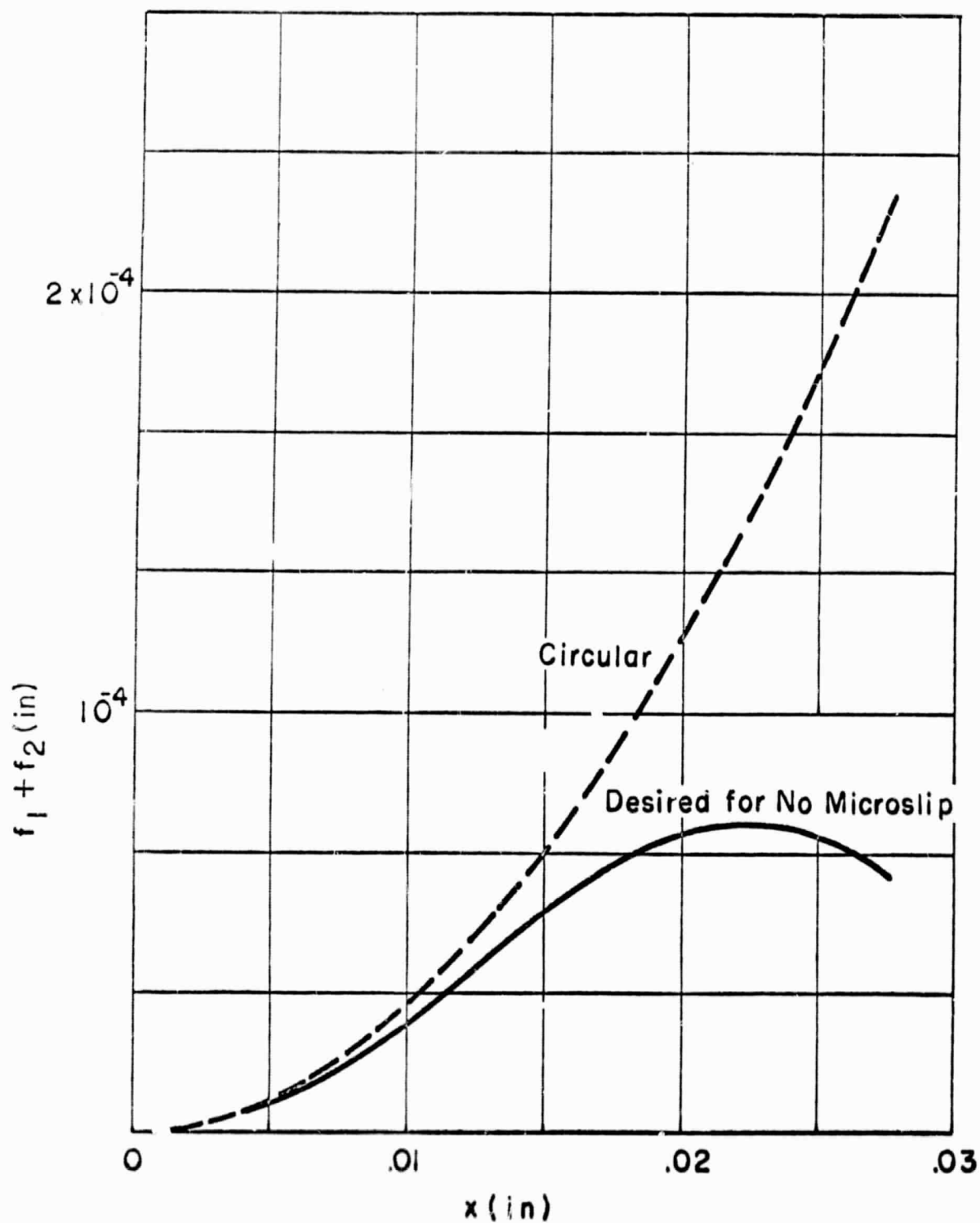


Fig. 20 Theoretical Pivot Shape for Zero Microslip.

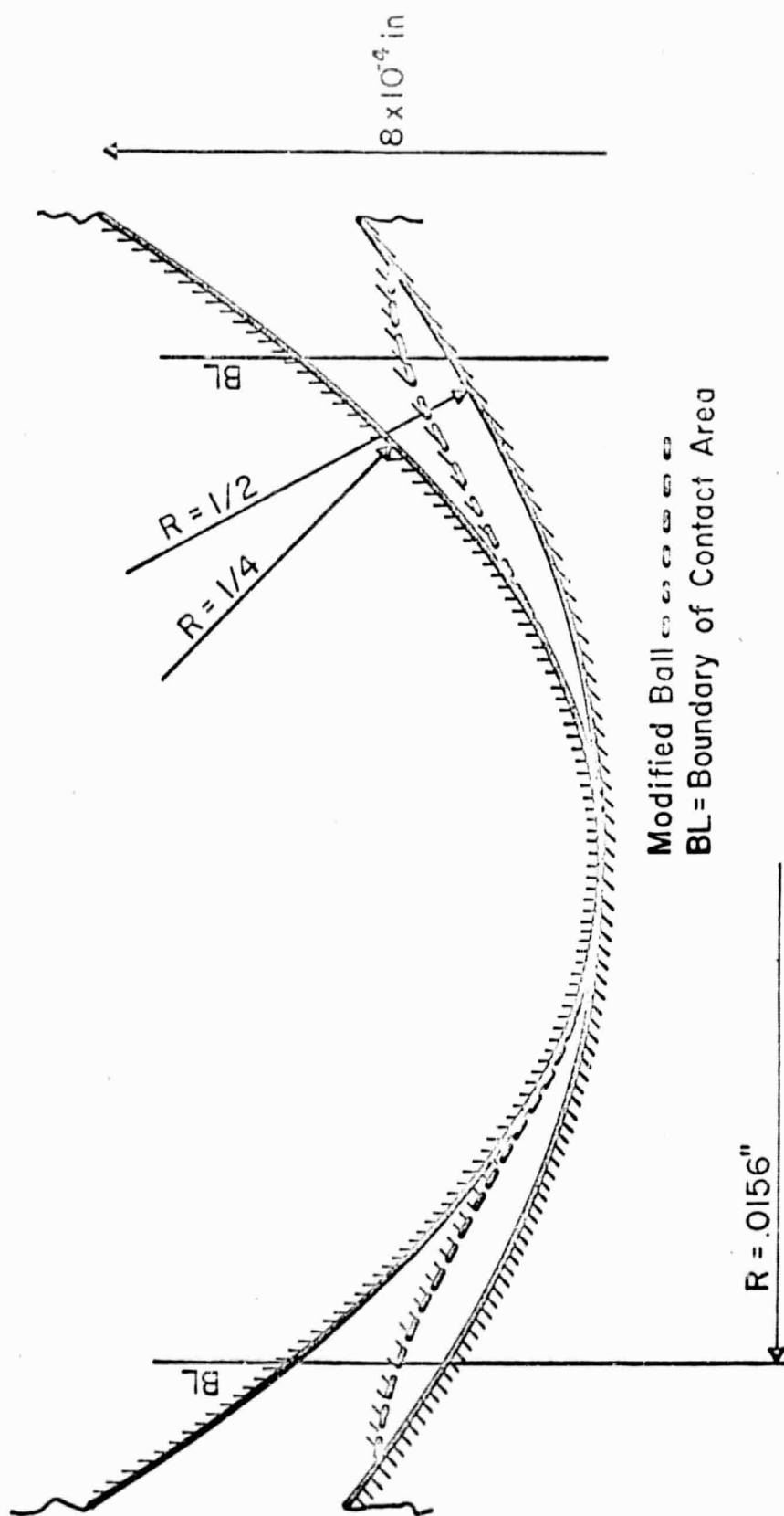


Fig. 21 Typical Cross-section View of Ball and Socket.

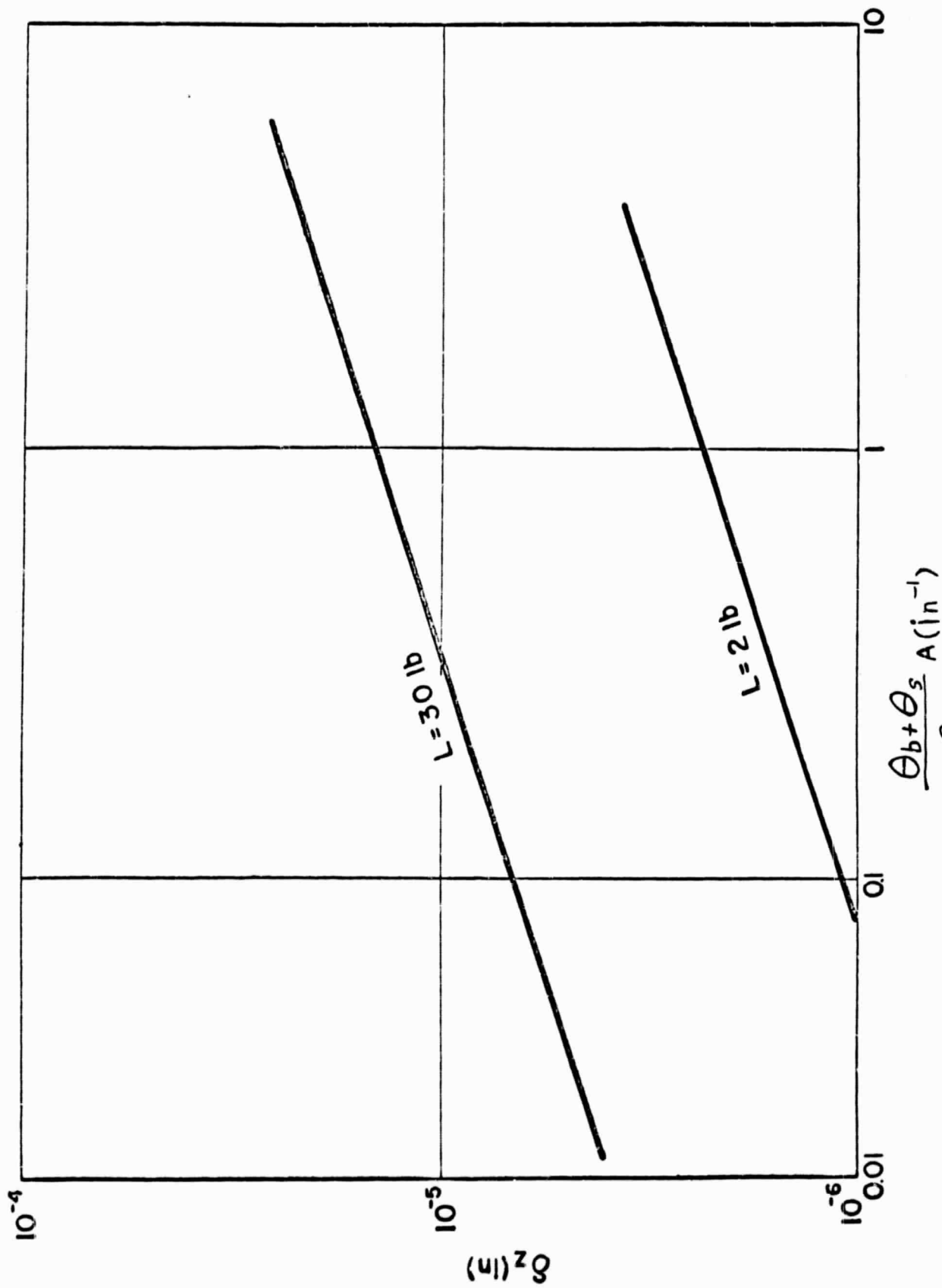


Fig. 22 Normal Approach vs. the Parameter $\frac{\theta_b + \theta_s}{2\pi} A$.

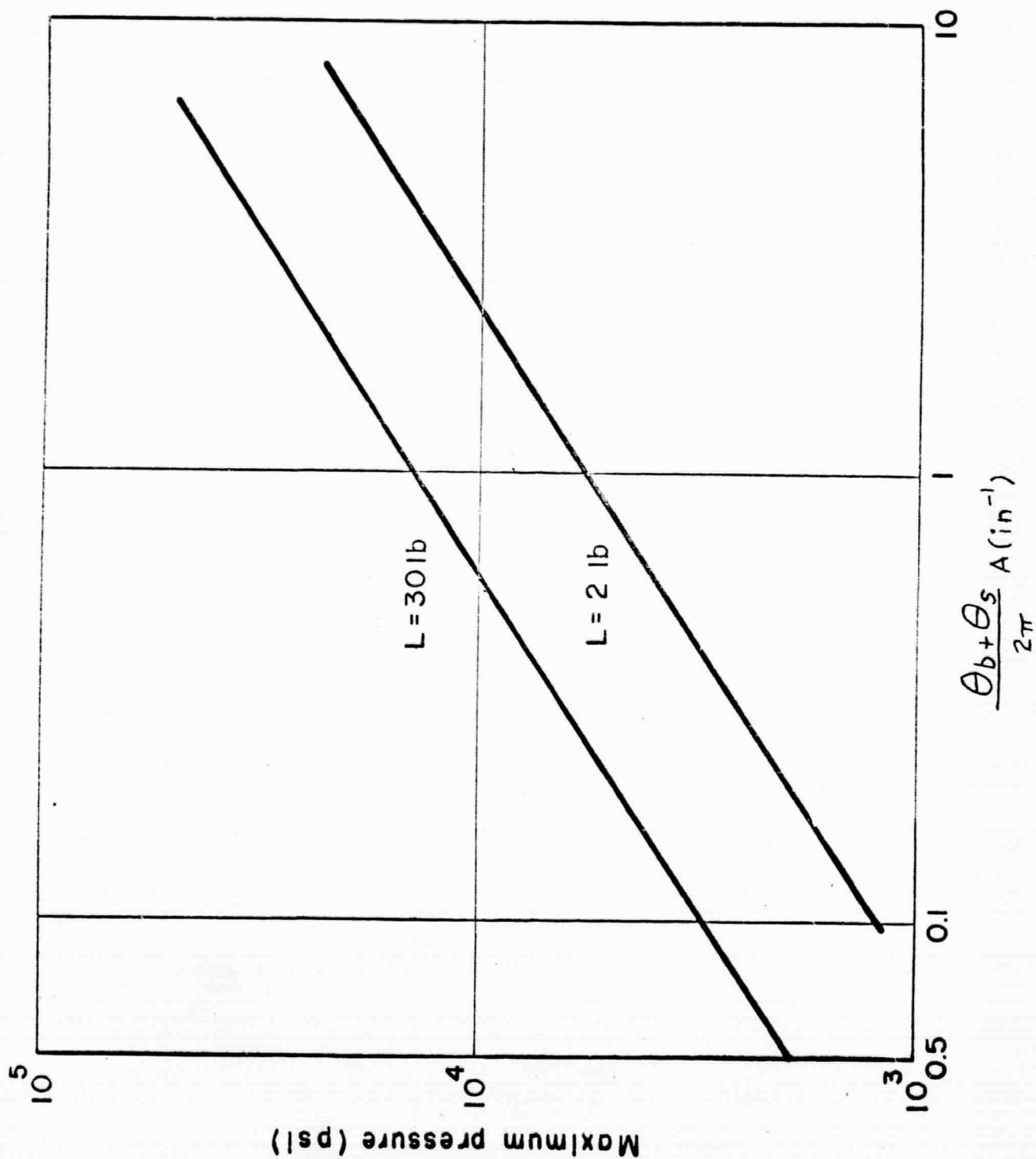


Fig. 23 Maximum Pressure vs. the Parameter $\frac{\theta_b + \theta_s}{2\pi} A$.

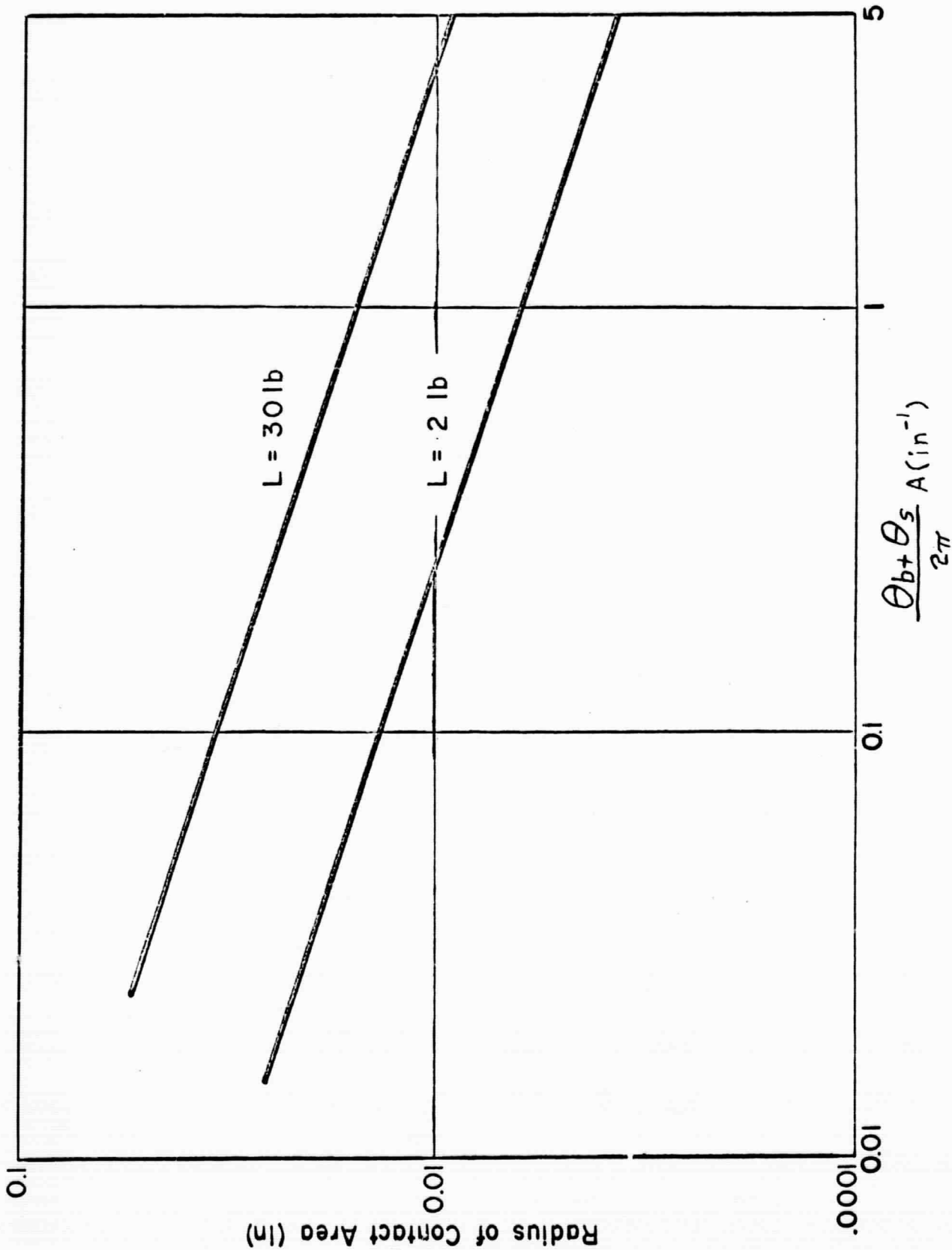


Fig. 24 Radius of Contact Area vs. the Parameter $\frac{\theta_b + \theta_s}{2\pi} A$.

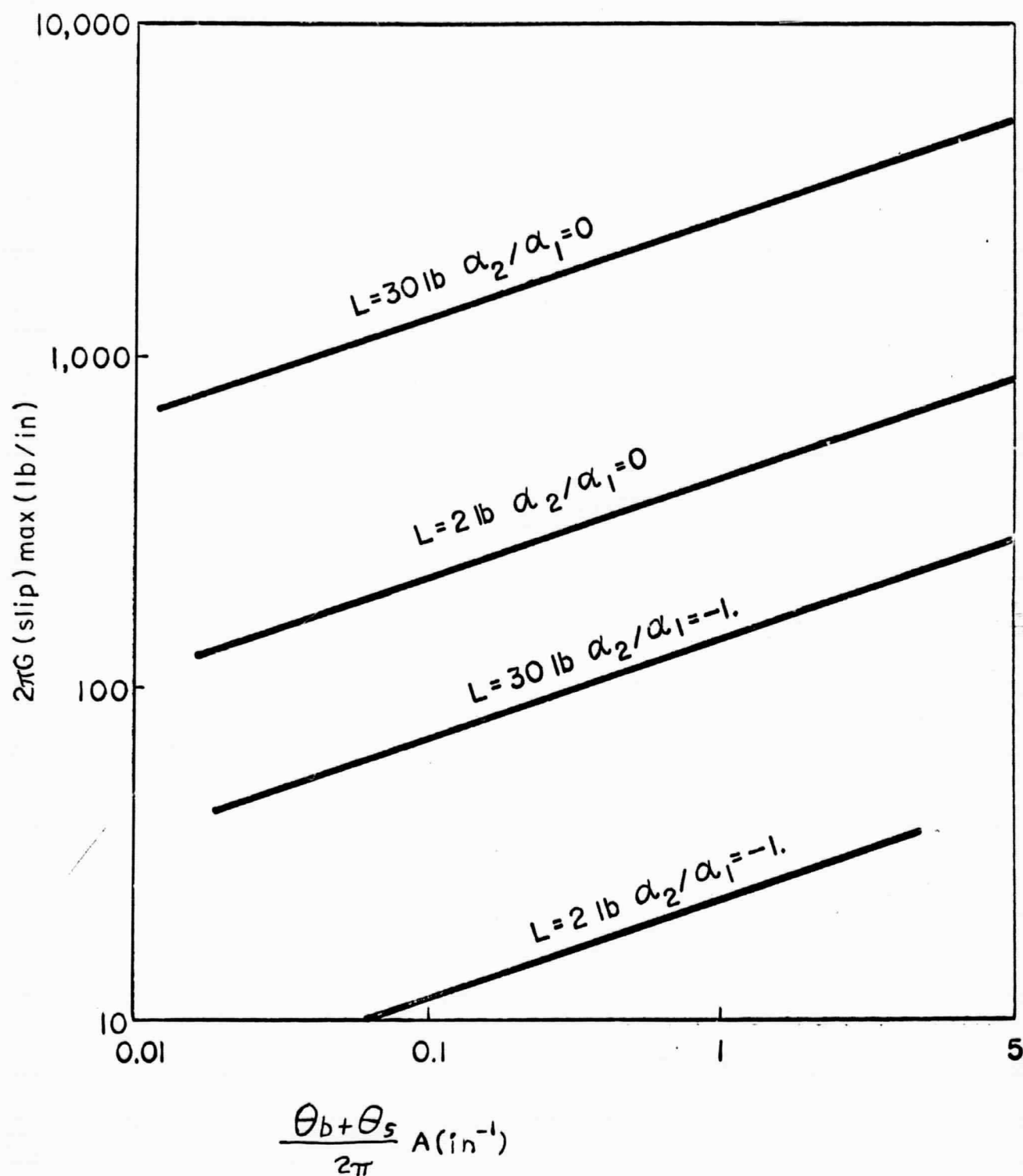


Fig. 25 Maximum Microslip vs. the Parameter $\frac{\theta_b + \theta_s}{2\pi} A$.

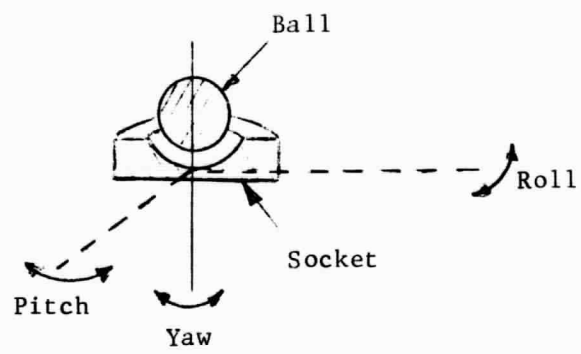


Fig. 26 Motions Desired

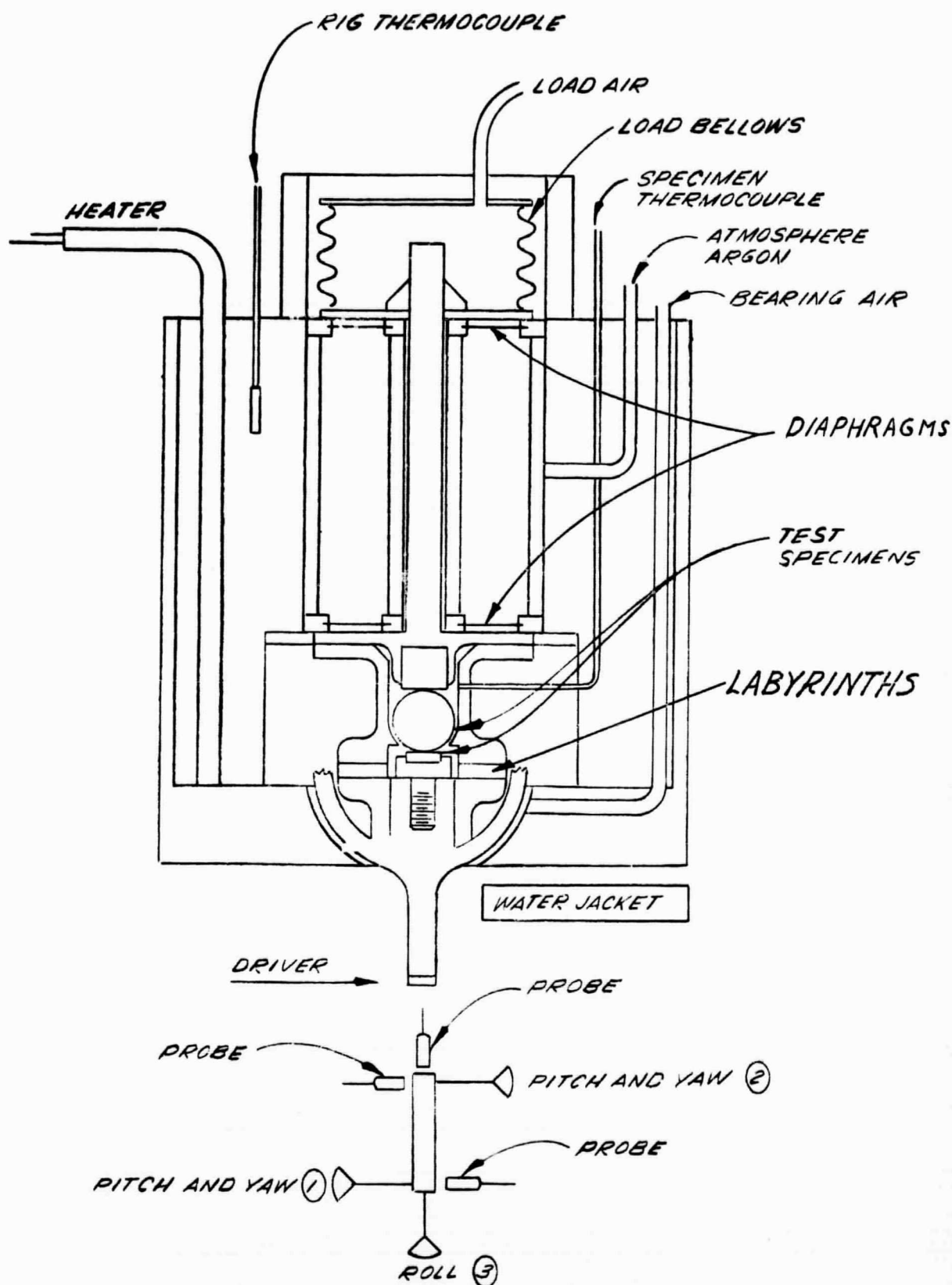


Fig. 27 Schematic of Test Rig

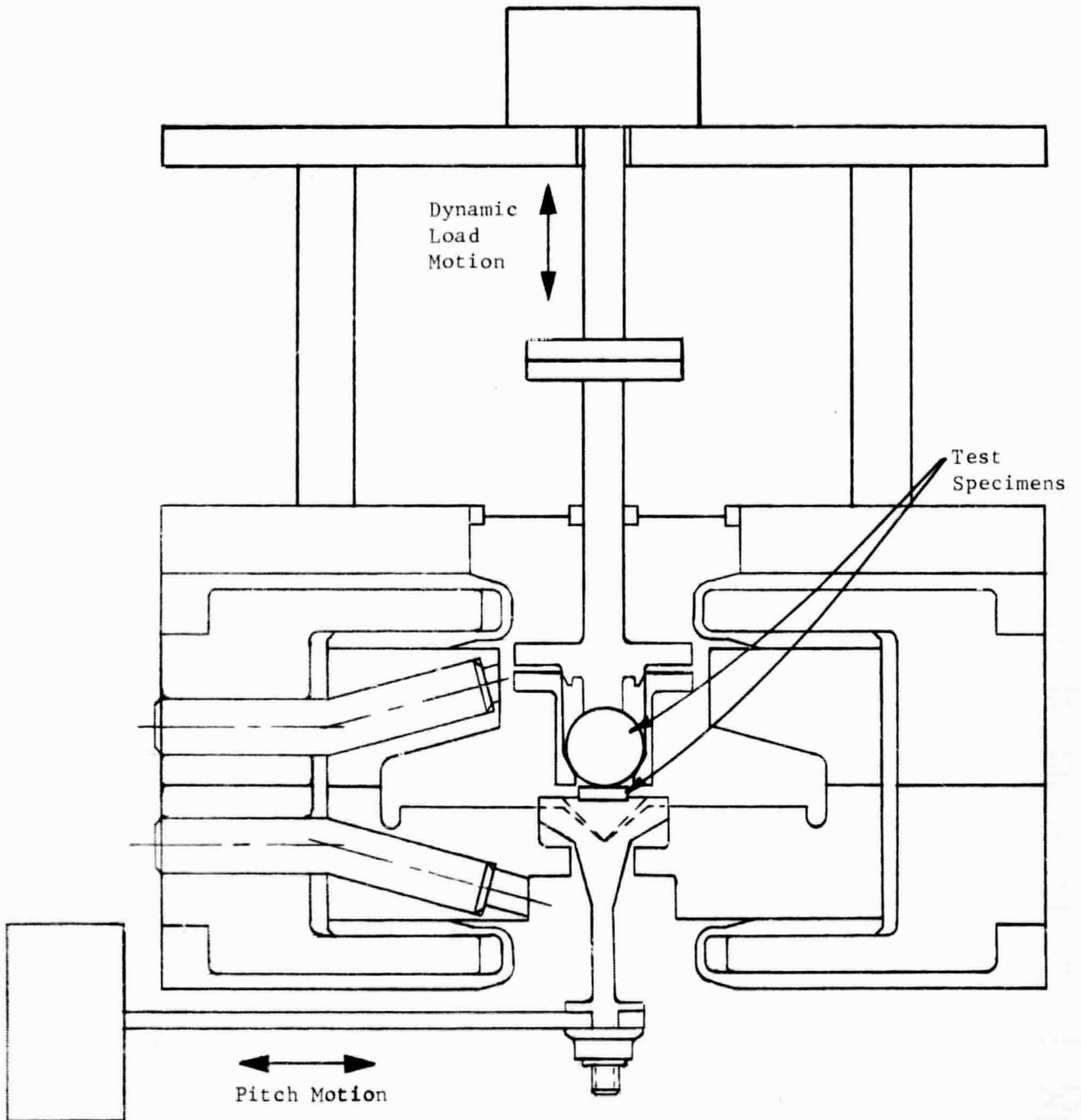


Fig. 28 Dynamic Load Test Rig

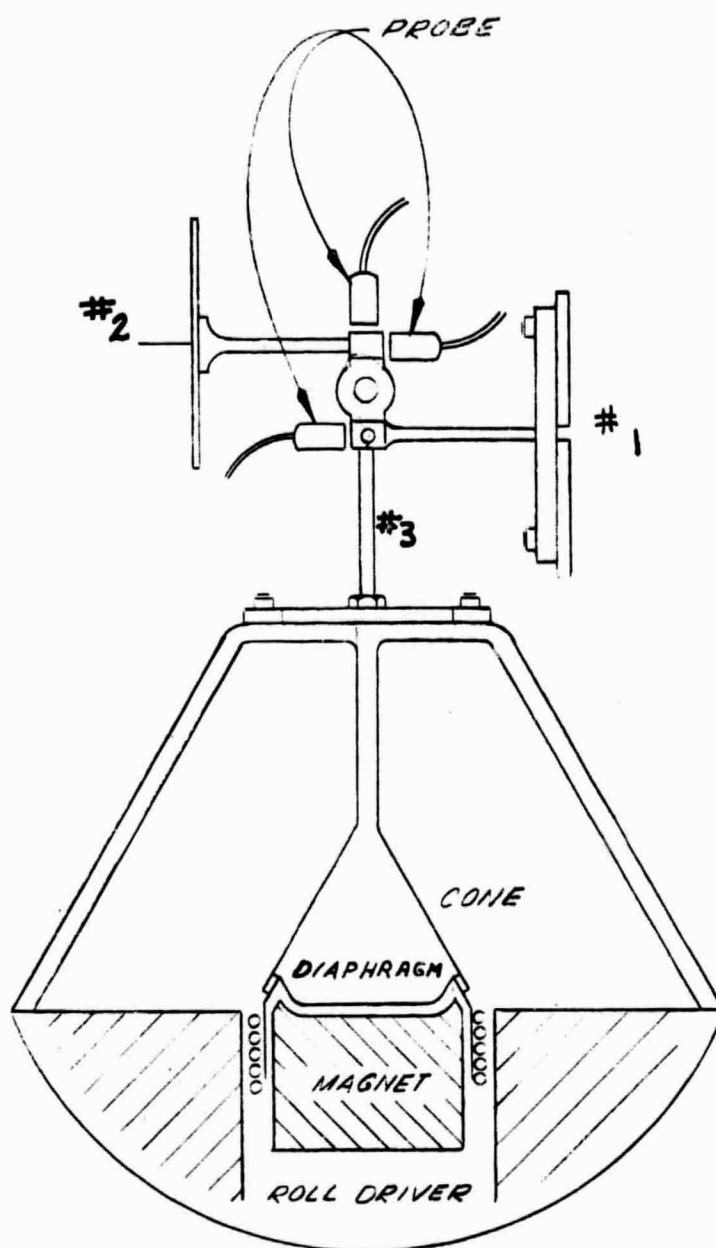


Fig. 29 Sketch of the Driver System

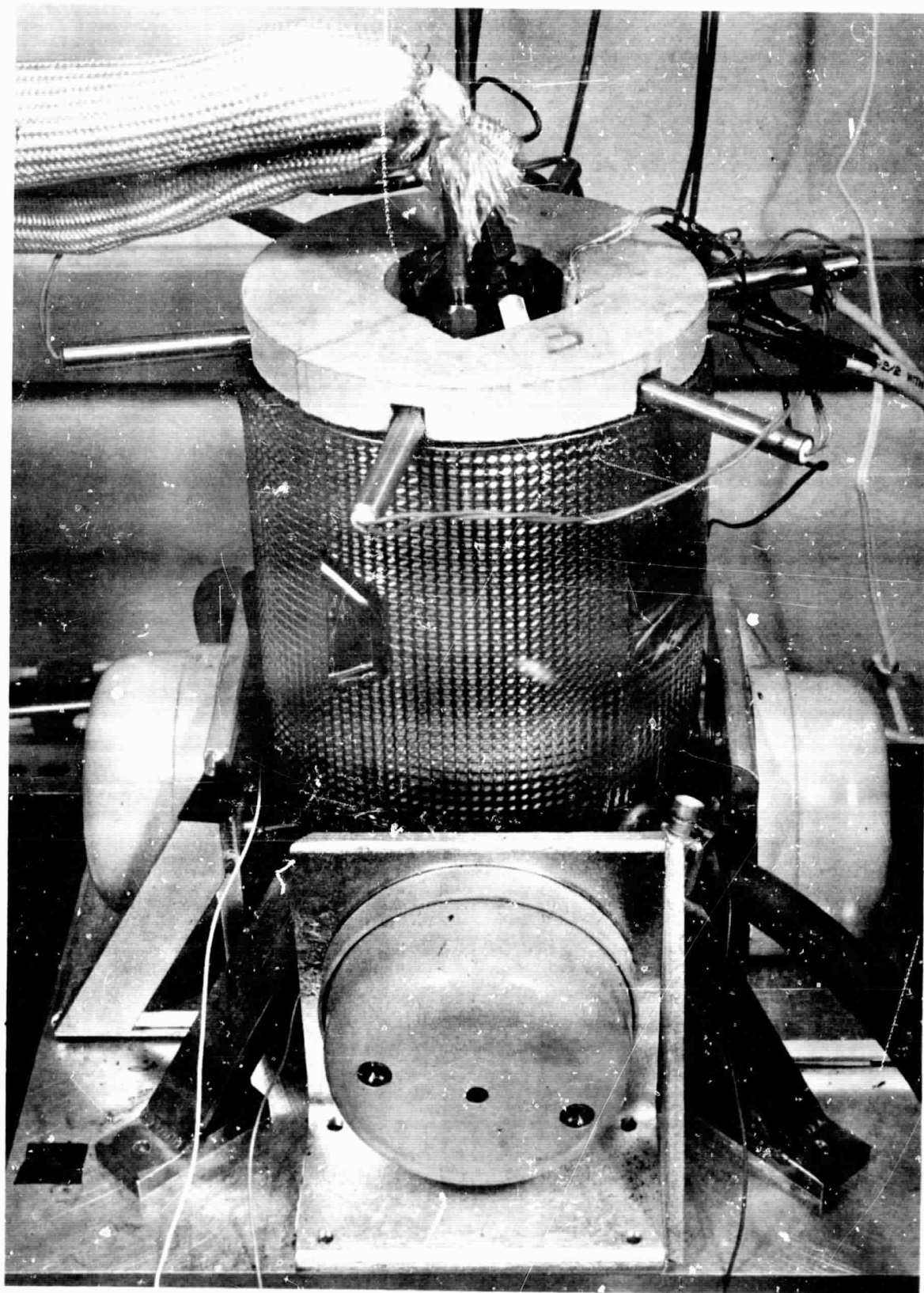


Fig. 30 Photograph of Test Rig Showing Driver Position

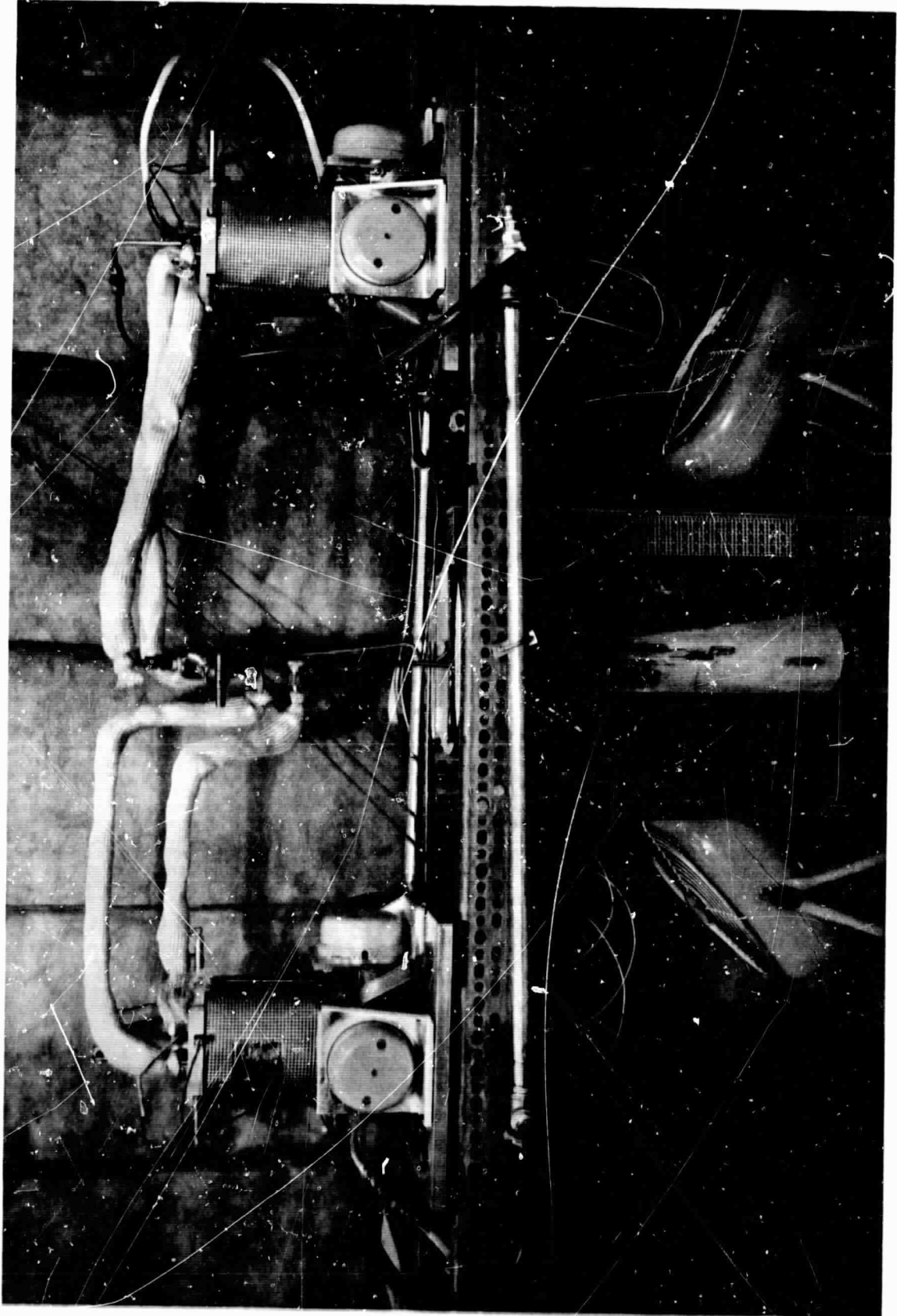


Fig. 31 Photograph of the Two Rig System

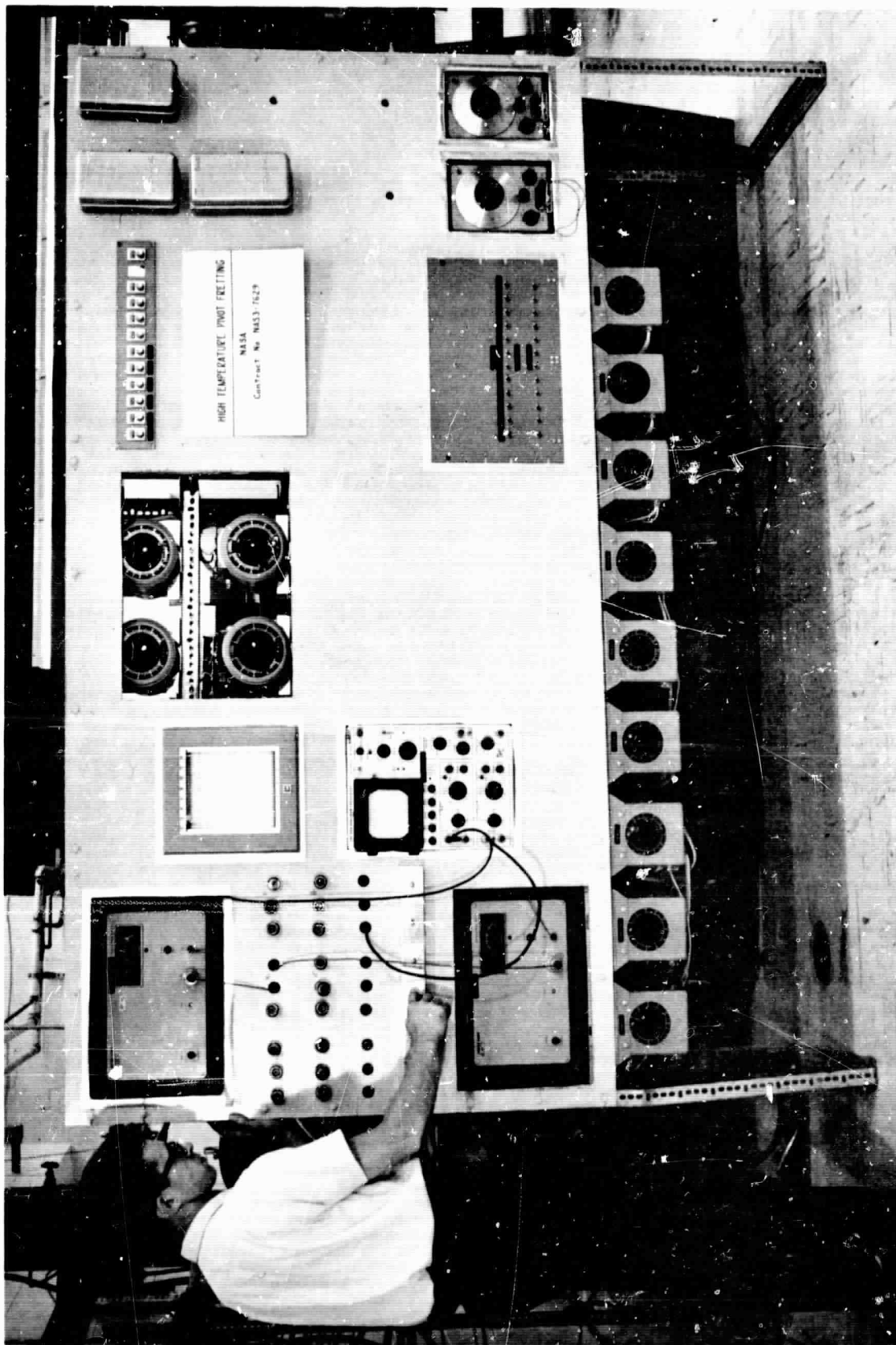


Fig. 32 Photograph of the Test Panel



a) Socket



b) Flat

Fig. 33 Photograph of Specimens Prior to Test

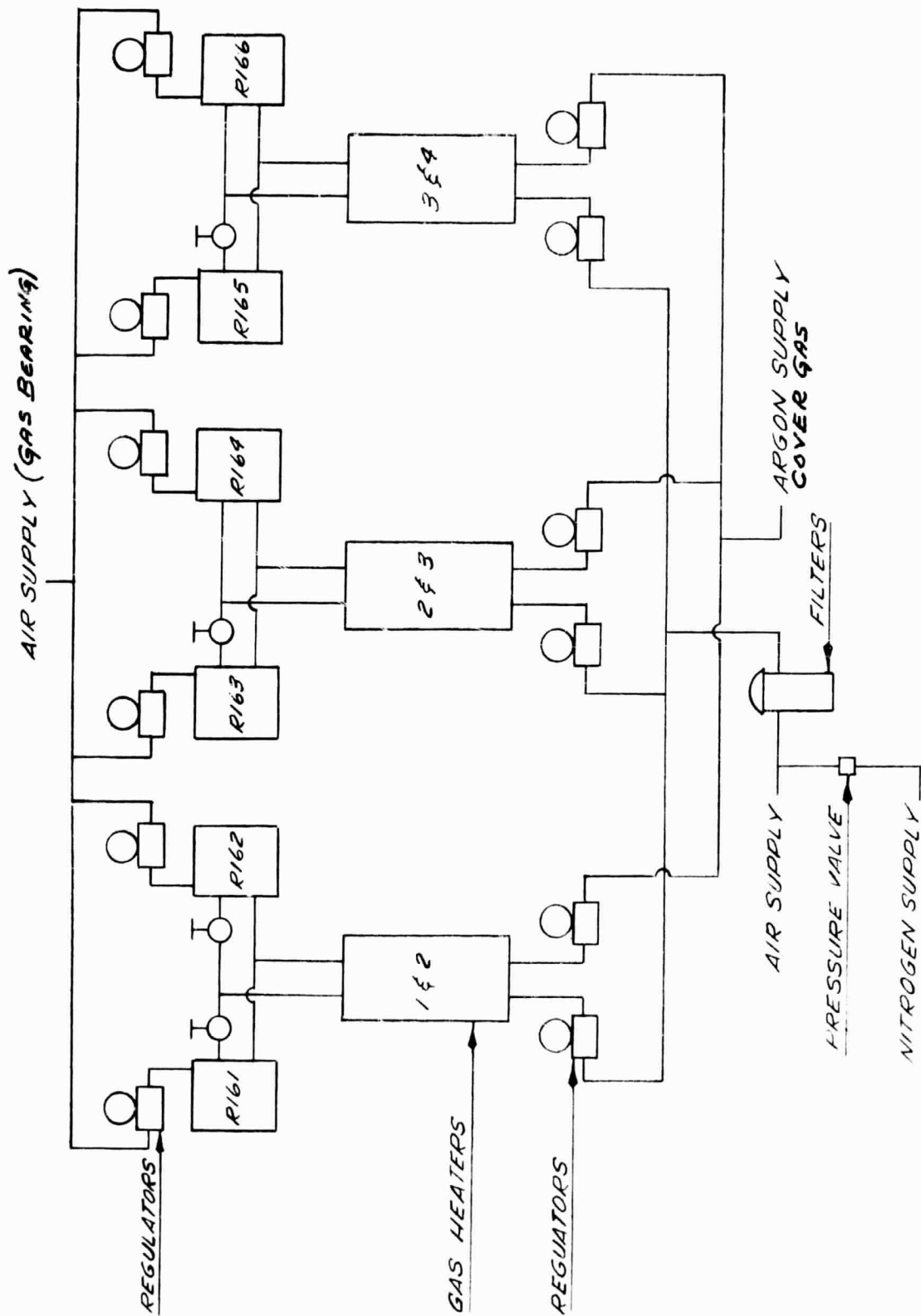


Fig. 34 Diagram of the Gas System

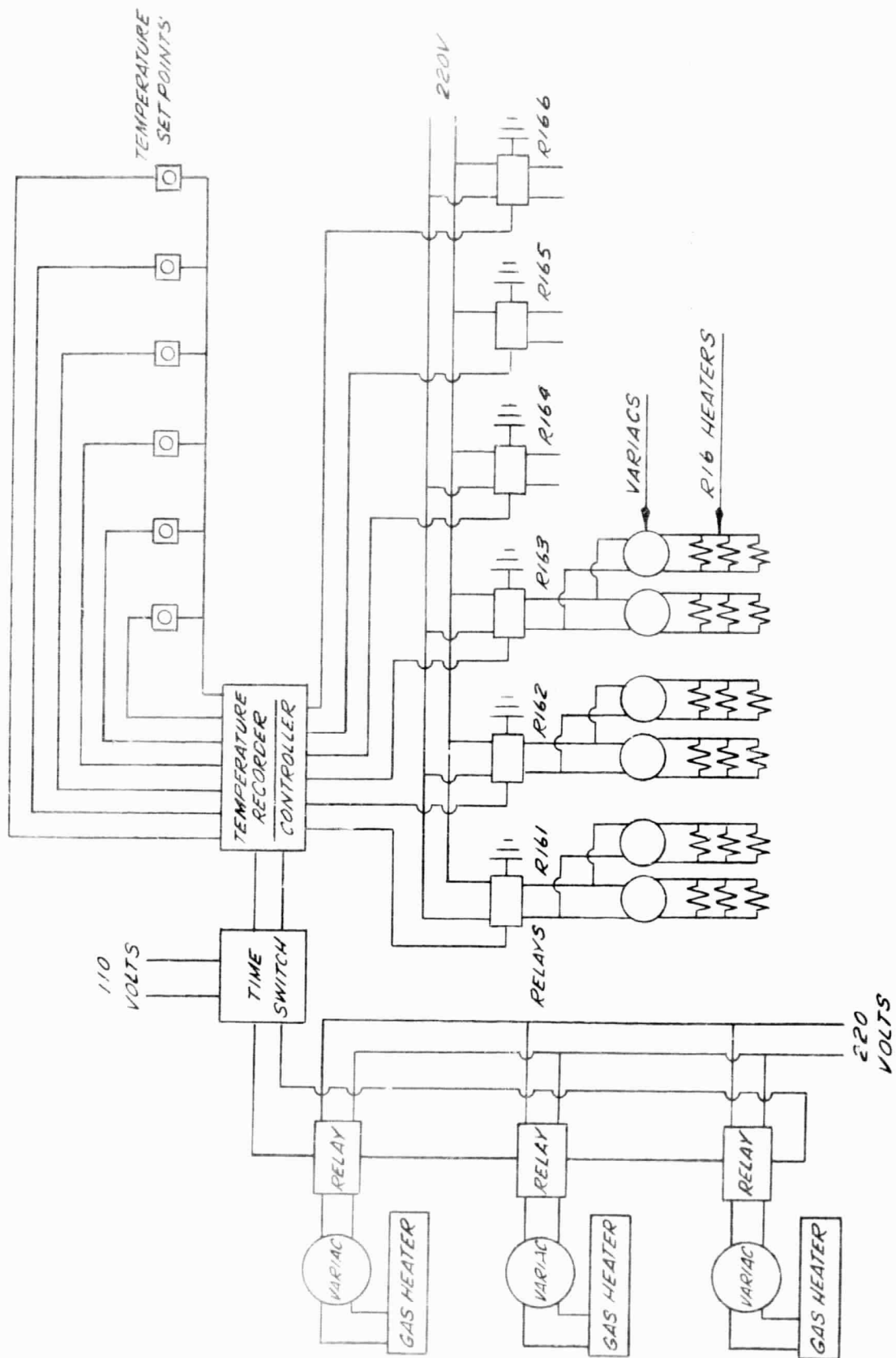


Fig. 35 Diagram of the Heating System

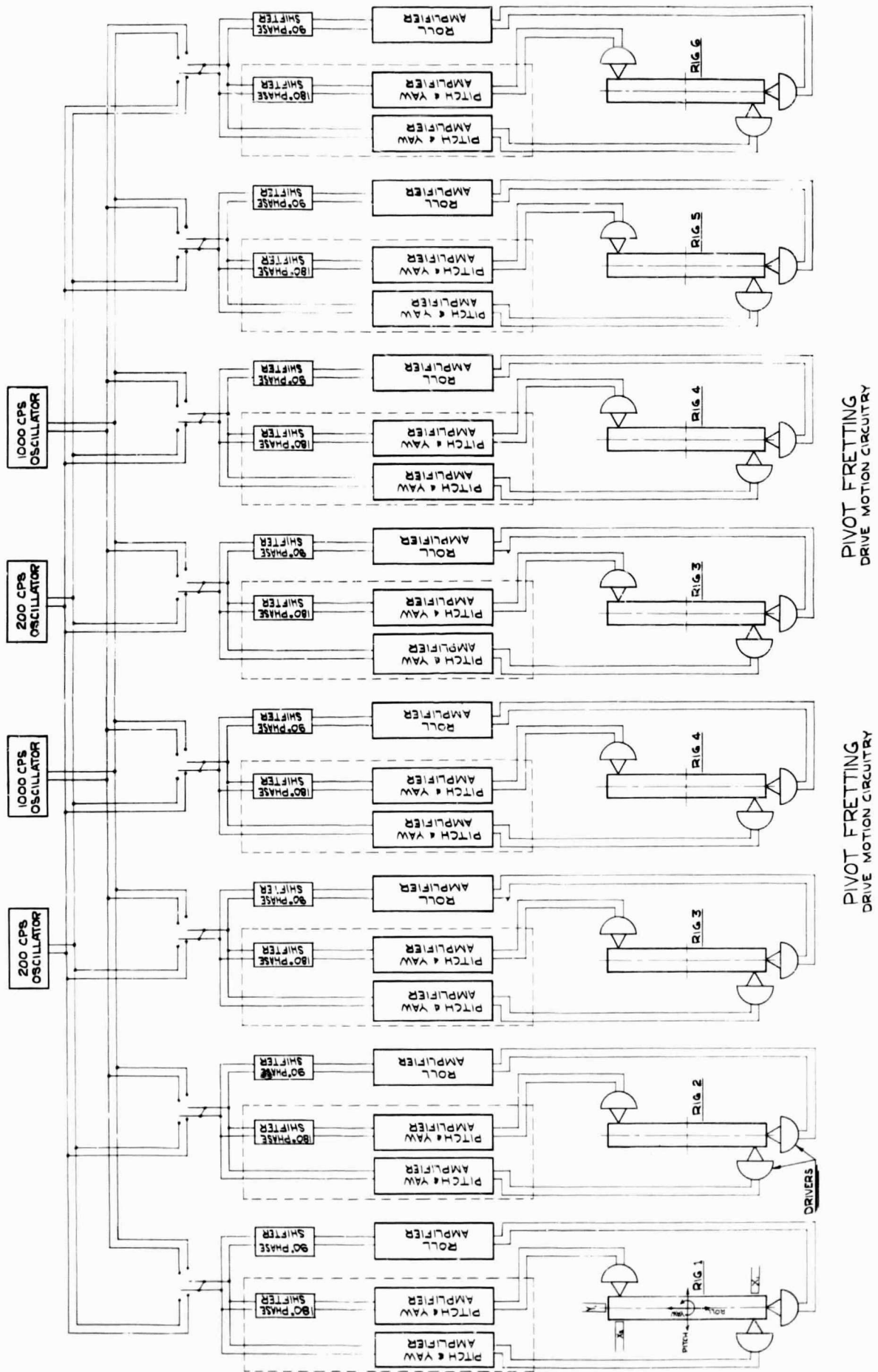
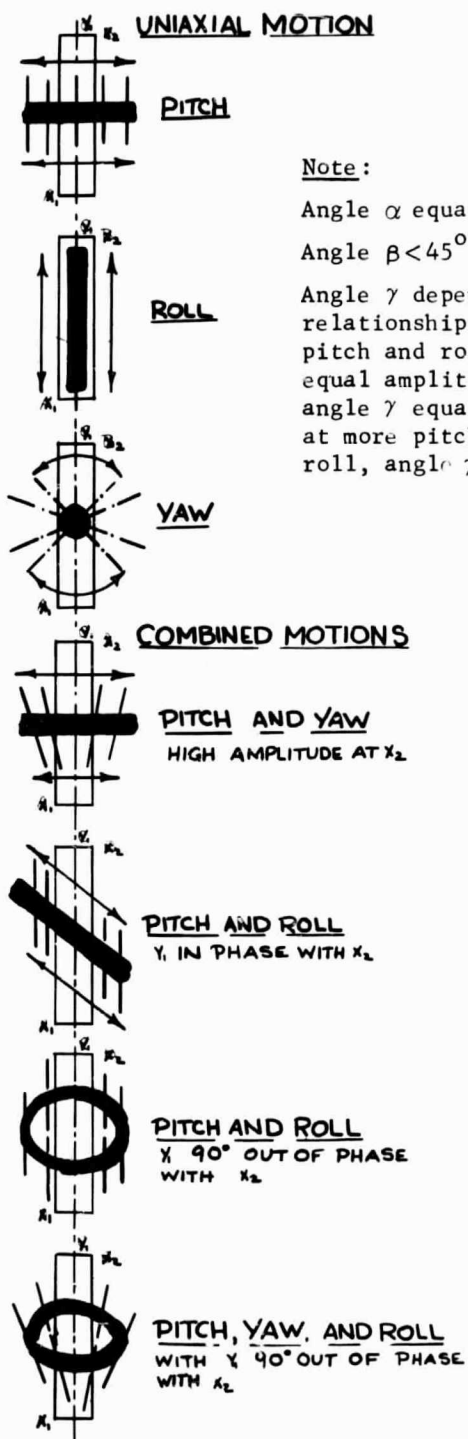


Fig. 36 Diagram of the Motion Detection System



Note:
Angle α equals 45°
Angle $\beta < 45^\circ$
Angle γ depends on relationship between pitch and roll; at equal amplitudes, angle γ equals 45° .
at more pitch than roll, angle $\gamma > 45^\circ$.

TYPICAL OSCILLOSCOPE PATTERNS

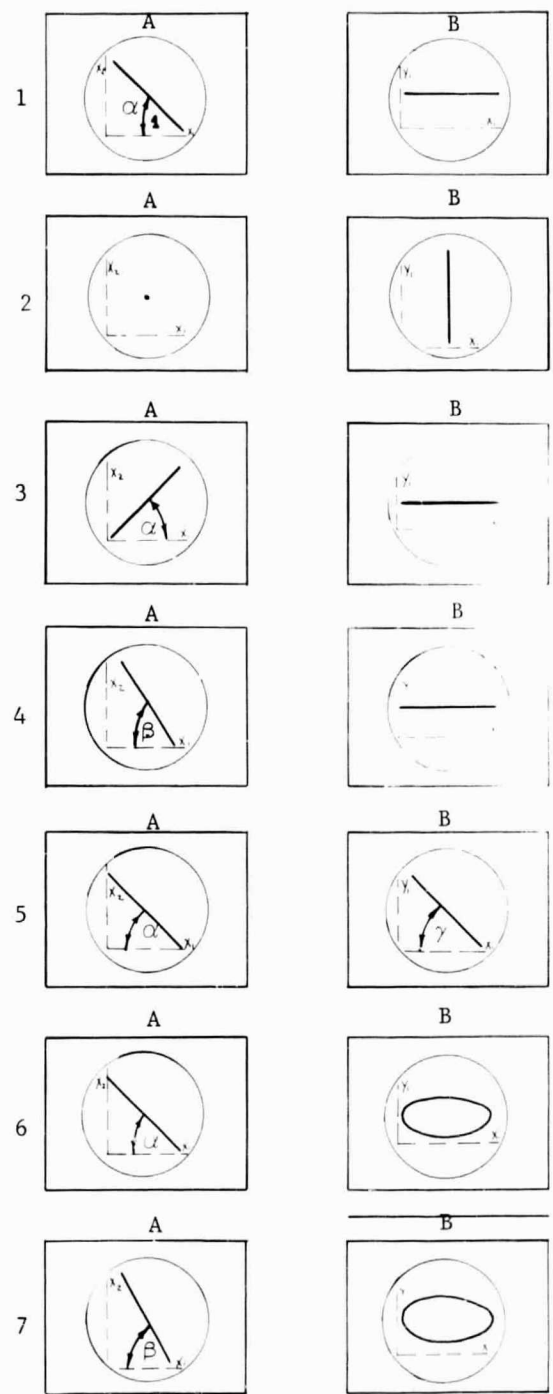


Fig. 37 Sketch of Oscilloscope Patterns

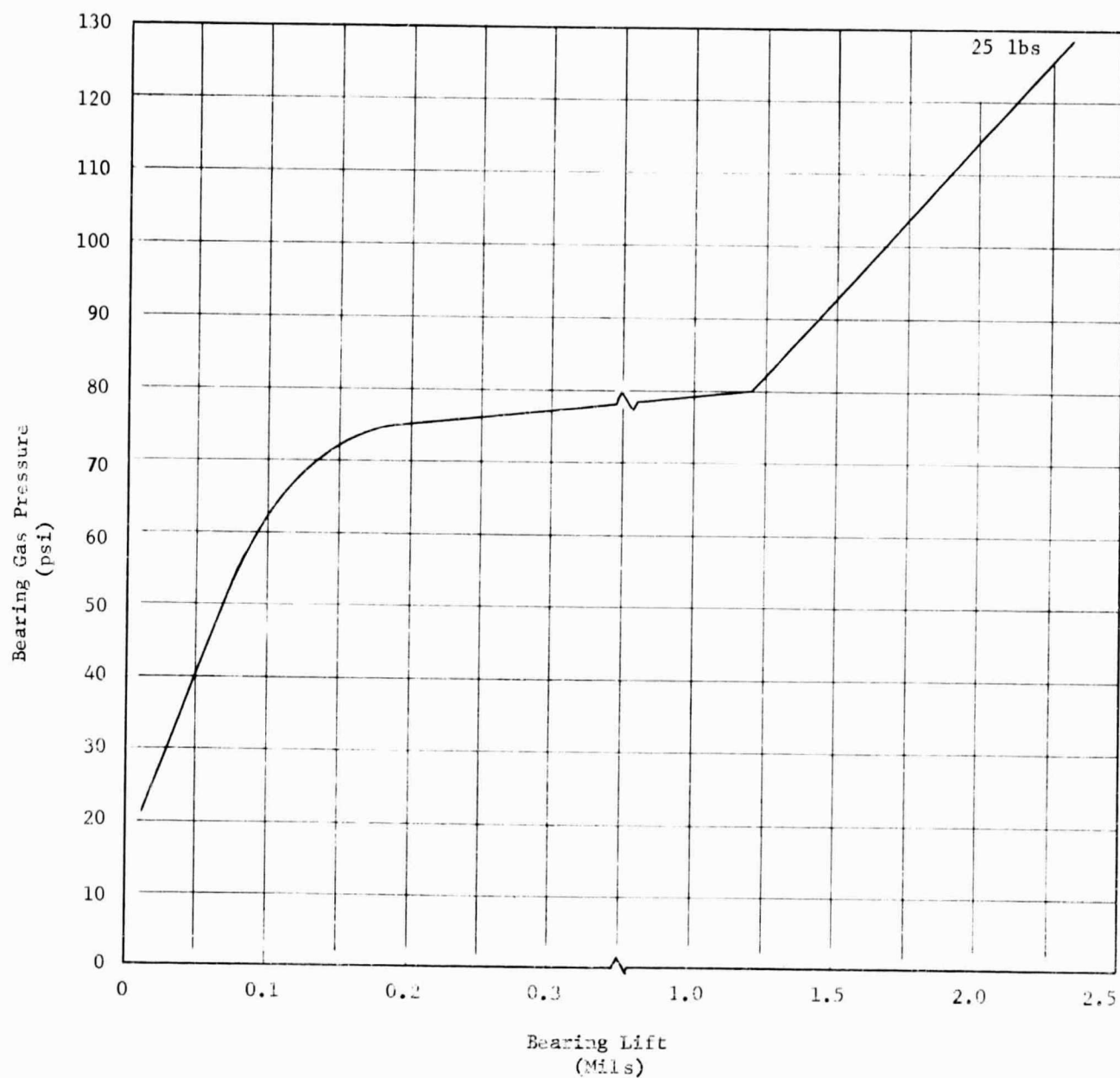


Fig. 38 Effect of Bearing Pressure on Lift for the Spherical Seat (Rig #1)

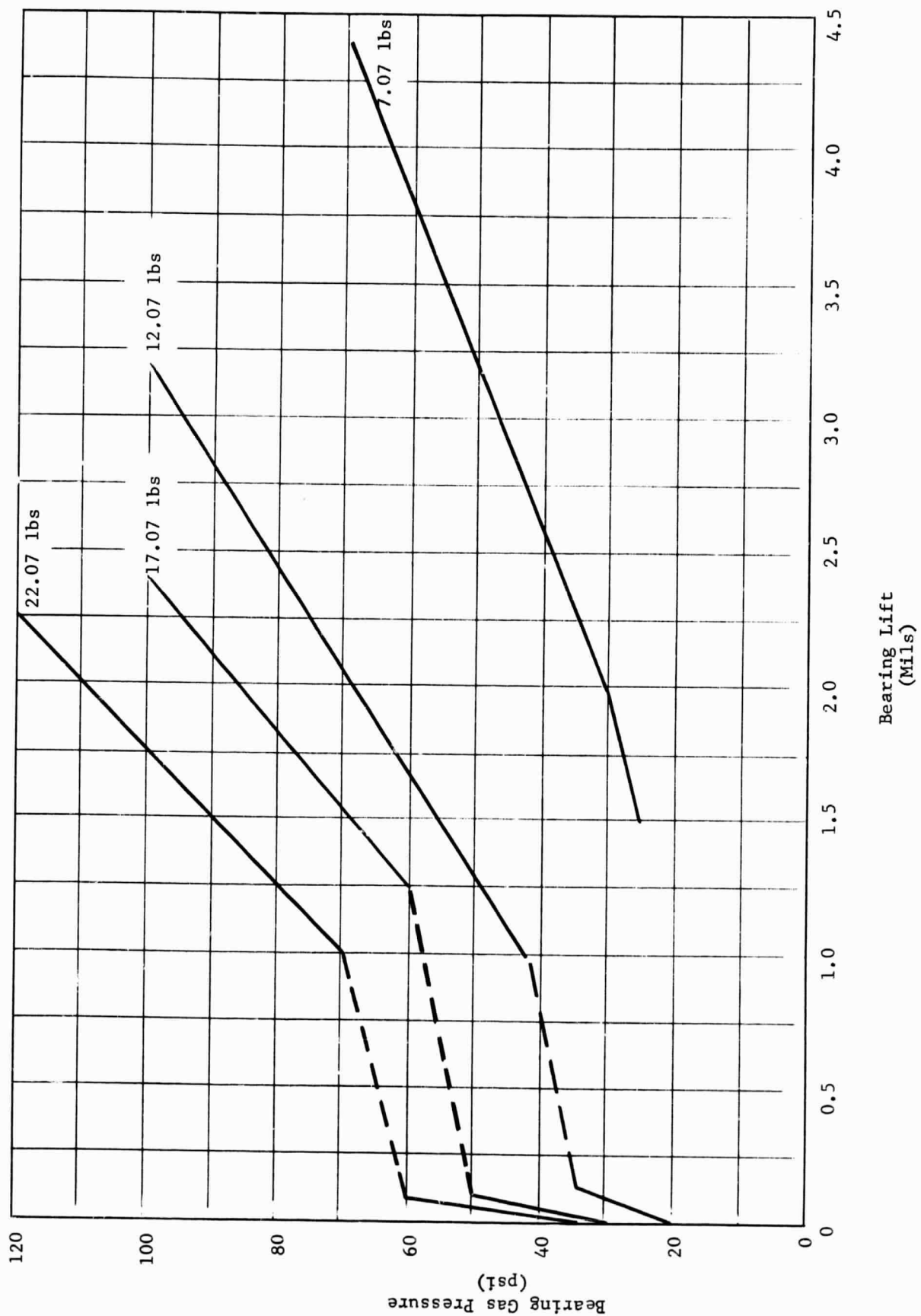


Fig. 39 Effect of Gas Pressure on Bearing Lift for the Spherical Seat (Rig #1)

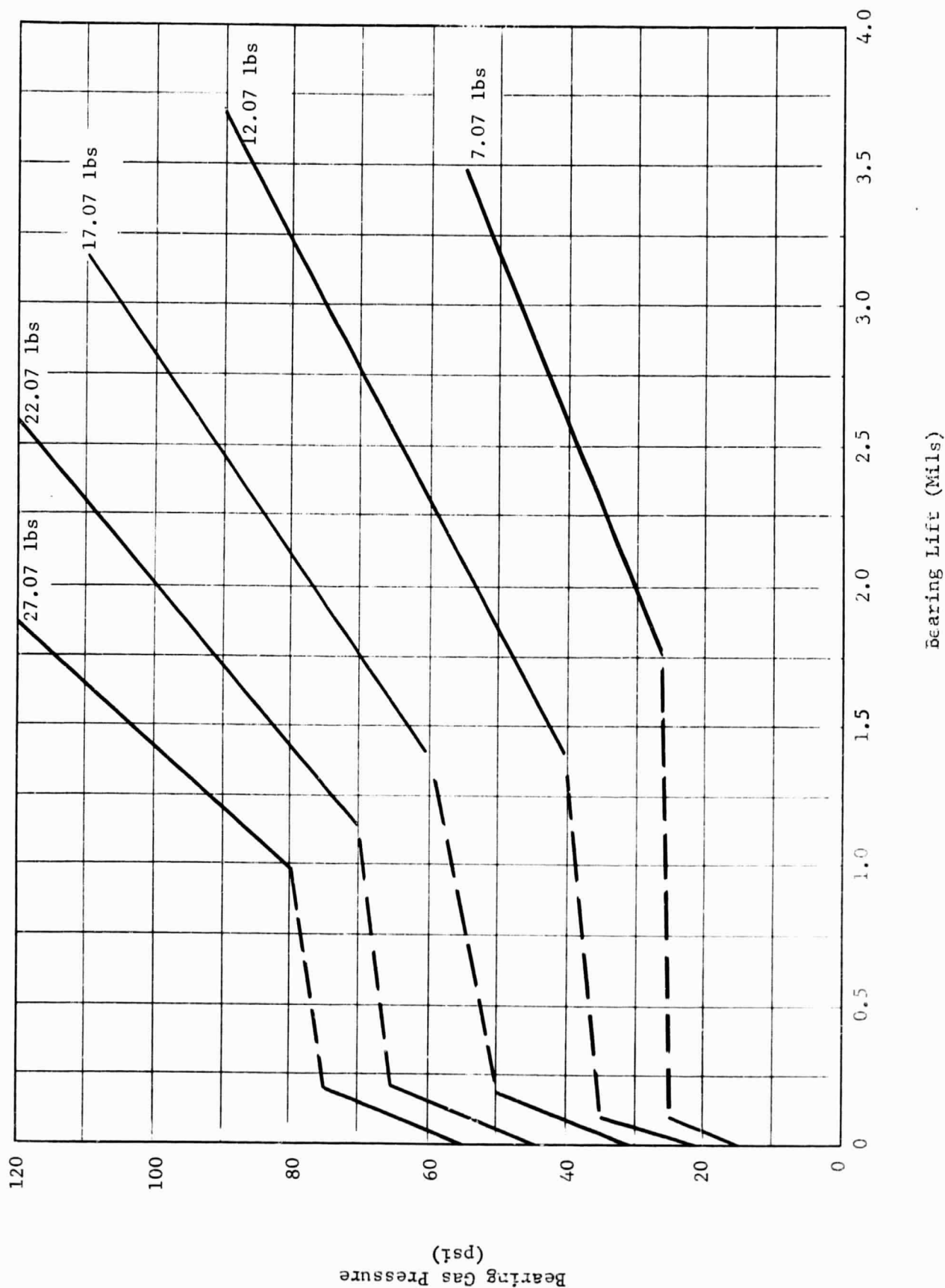


Fig. 40 Effect of Gas Pressure on the Bearing Lift for the Spherical Seat (Rig #2)

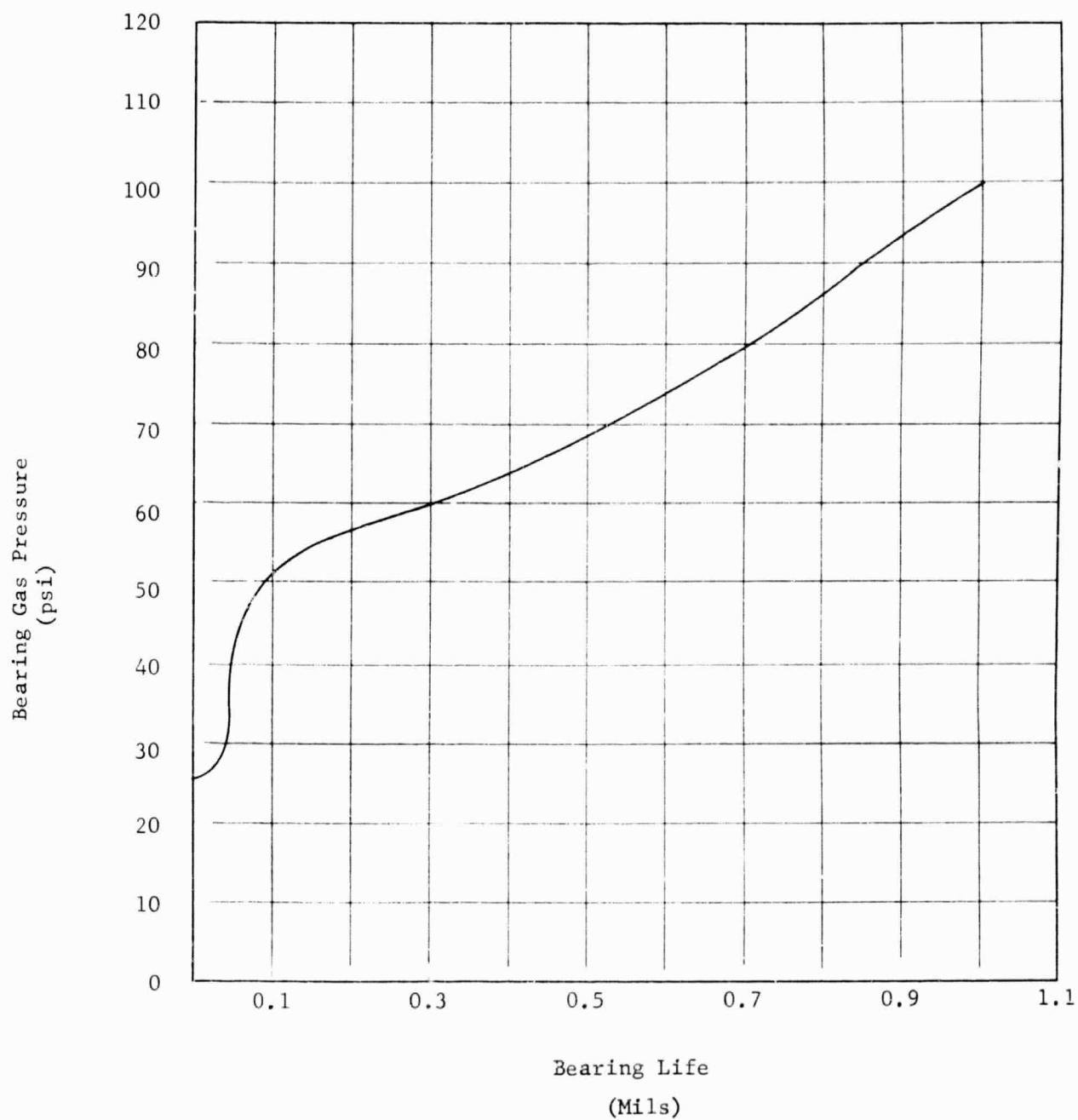


Fig. 41 Effect of Bearing Pressure on Lift of the Spherical Seal (Rig #3)

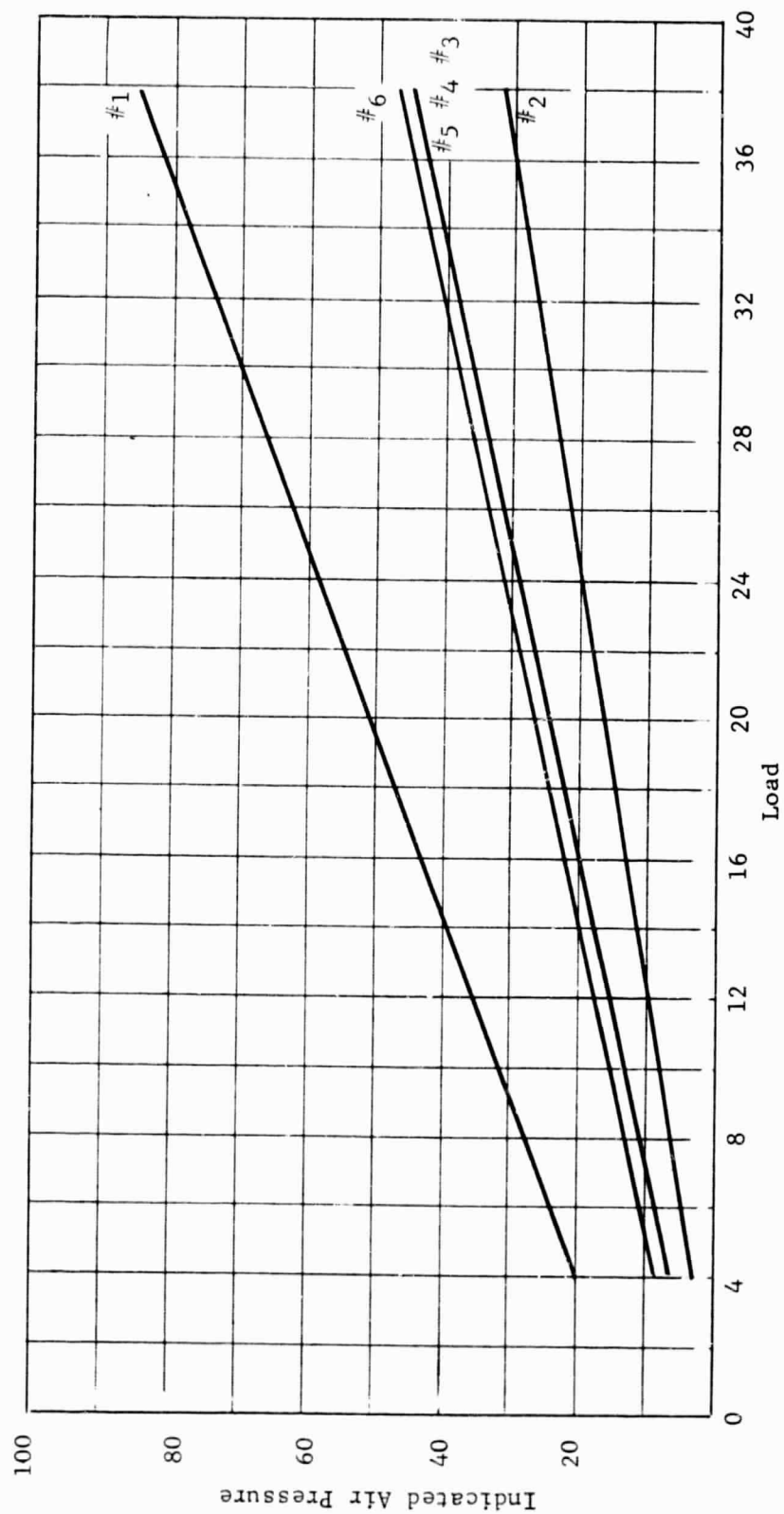


Fig. 42 Indicated Air Pressure (psi) Load (Pounds)

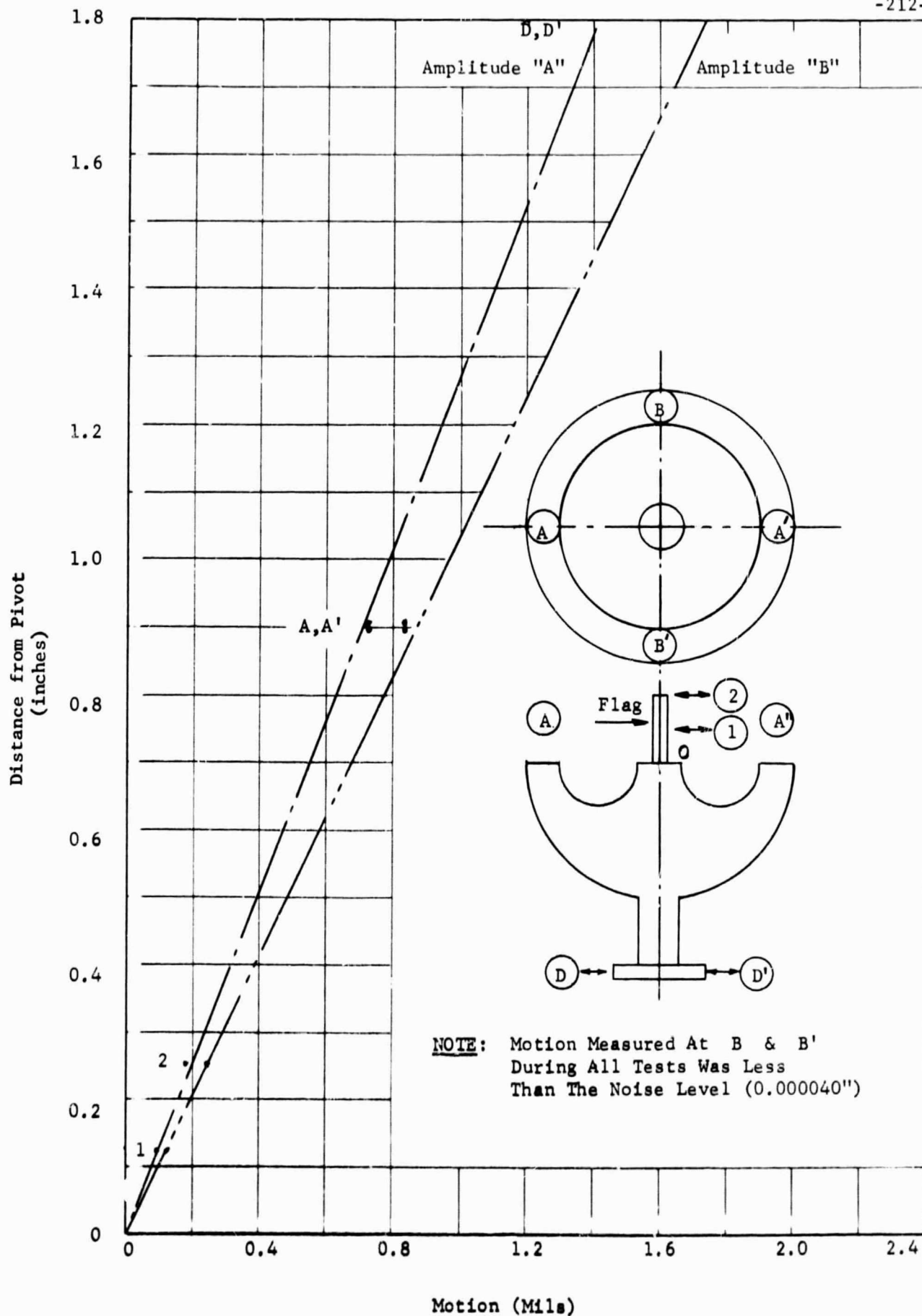


Fig. 43 Motion Relationships on Pitch

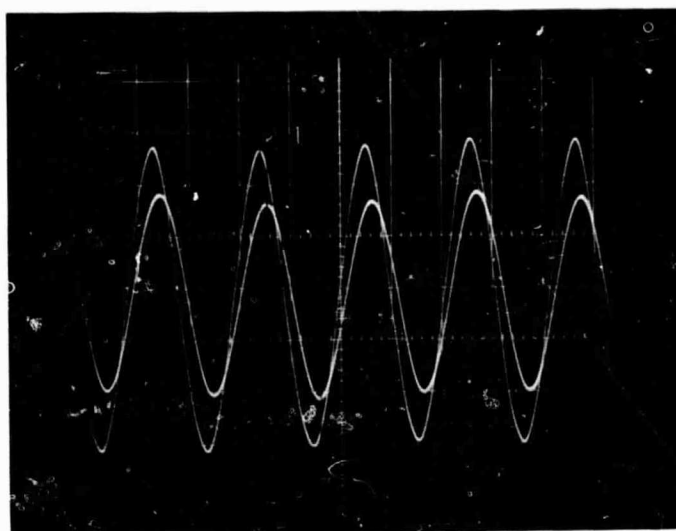


Fig. 44 Photograph of the Oscilloscope Traces of
the Pitch Motion, Calibration .5 mil/cm.

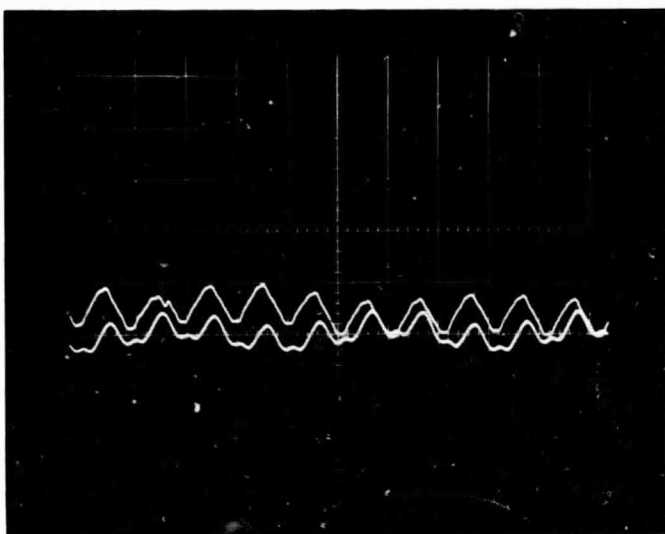


Fig. 45 Photograph of the Oscilloscope Traces
of Yaw Motions 1000 cps.

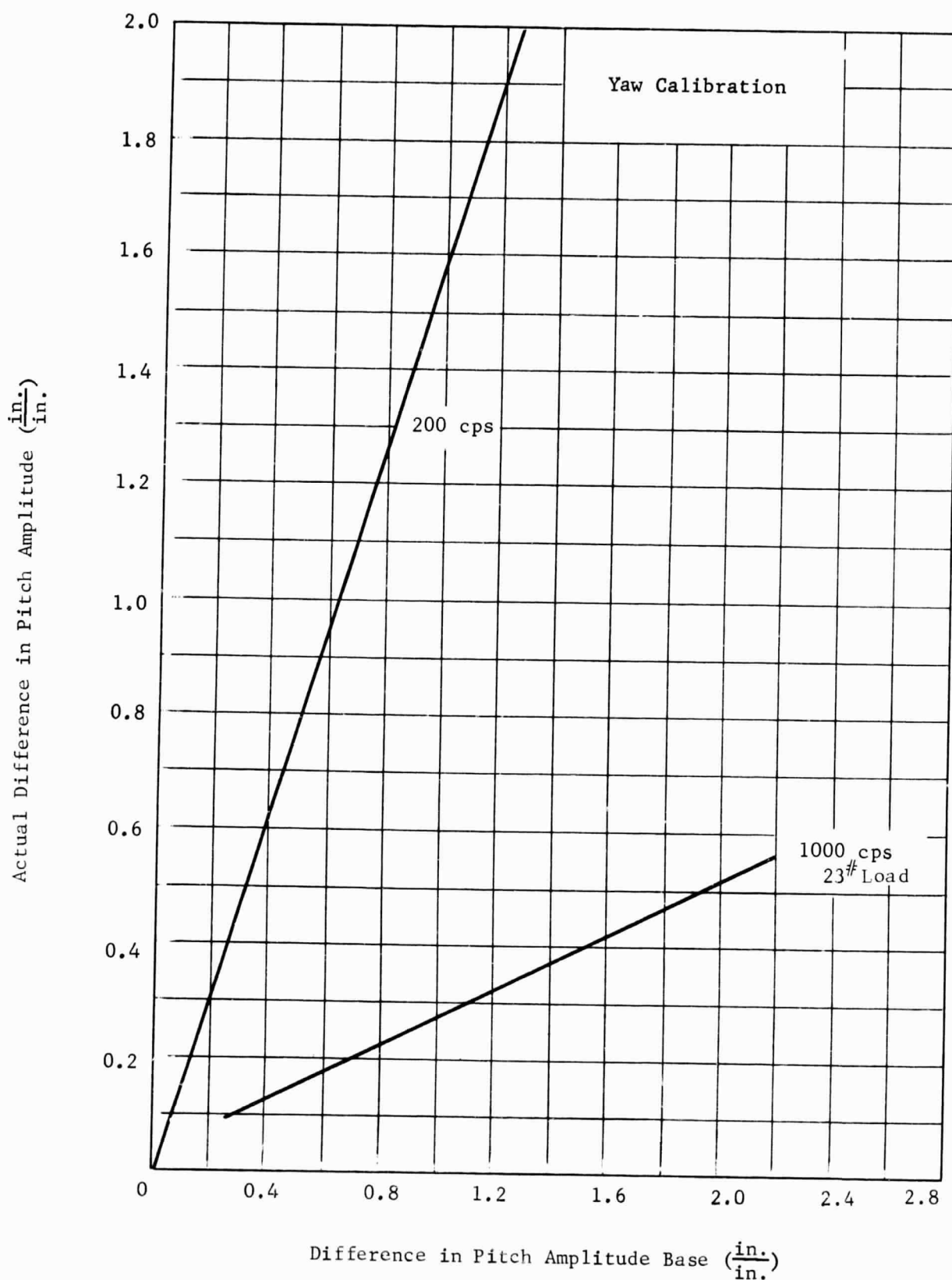


Fig. 46 Effect of Difference in Pitch Amplitude on the Yaw at 1 inch radius

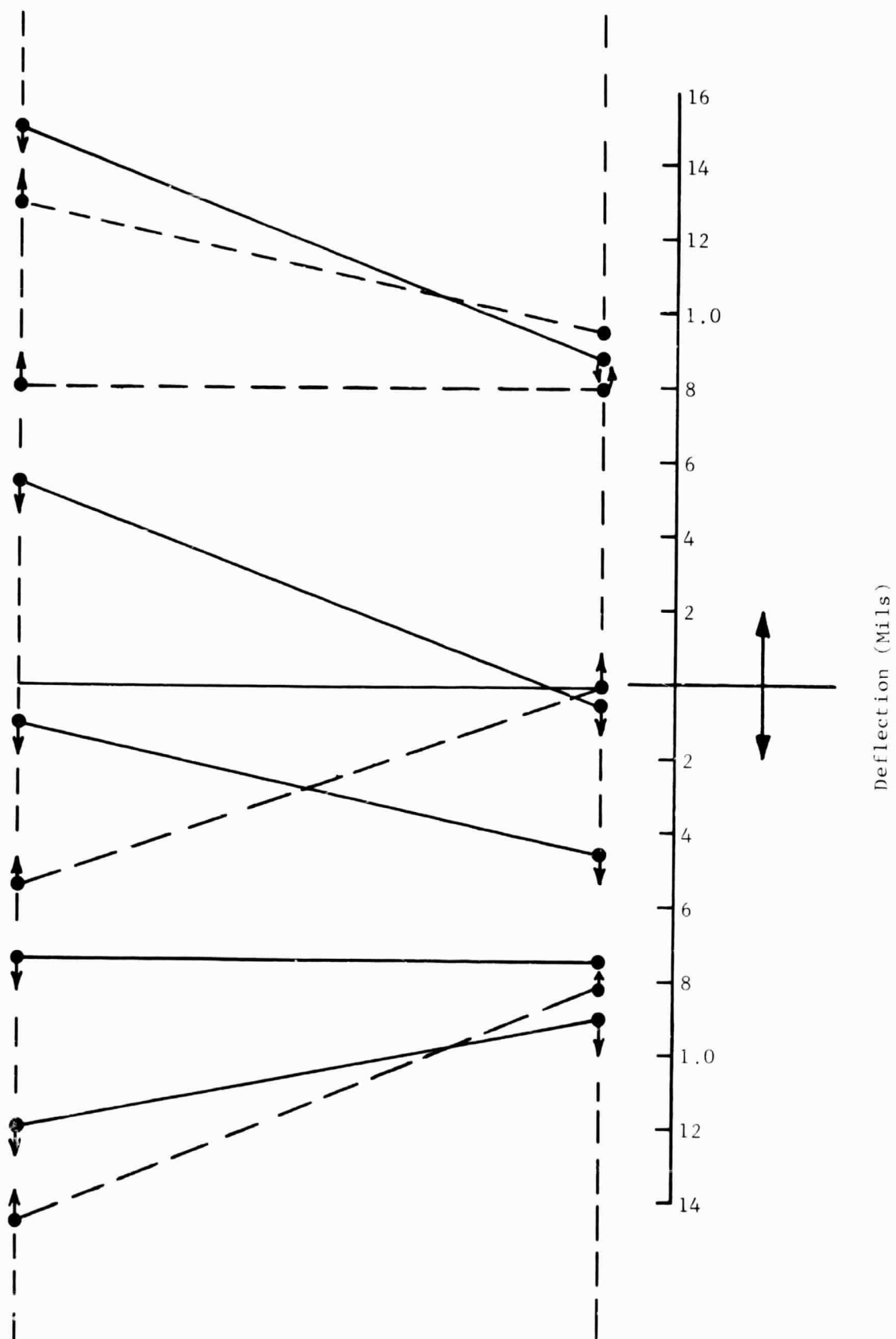


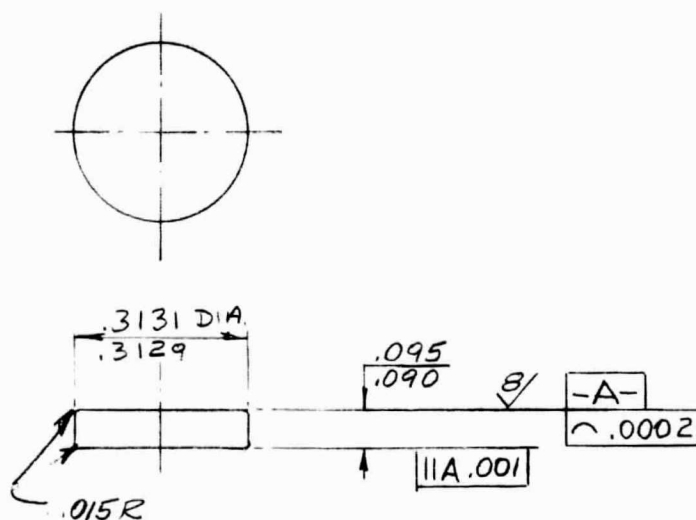
Fig. 47 Diagram of the Pendulum - Plate Motions

MECHANICAL TECHNOLOGY INCORPORATED

163-A-66
SHEET OF

TITLE

TEST SPECIMEN
(PIVOT TEST APPARATUS)



UNLESS OTHERWISE SPECIFIED USE	STANDARD PRACTICES	STUFF 63V	TOLERANCES		
			DECIMALS	FRACTIONS	ANGLES
			± .005	+ -	+ -
APPROVED H. JONES 9/7/67		REV. NO.	163-A-66		
CHECKED		SCALE NONE			
DRAWN M. SWEDSKY 9/7/67		SHEET	OF		

Fig. 48 Drawing of Flat Test Specimen

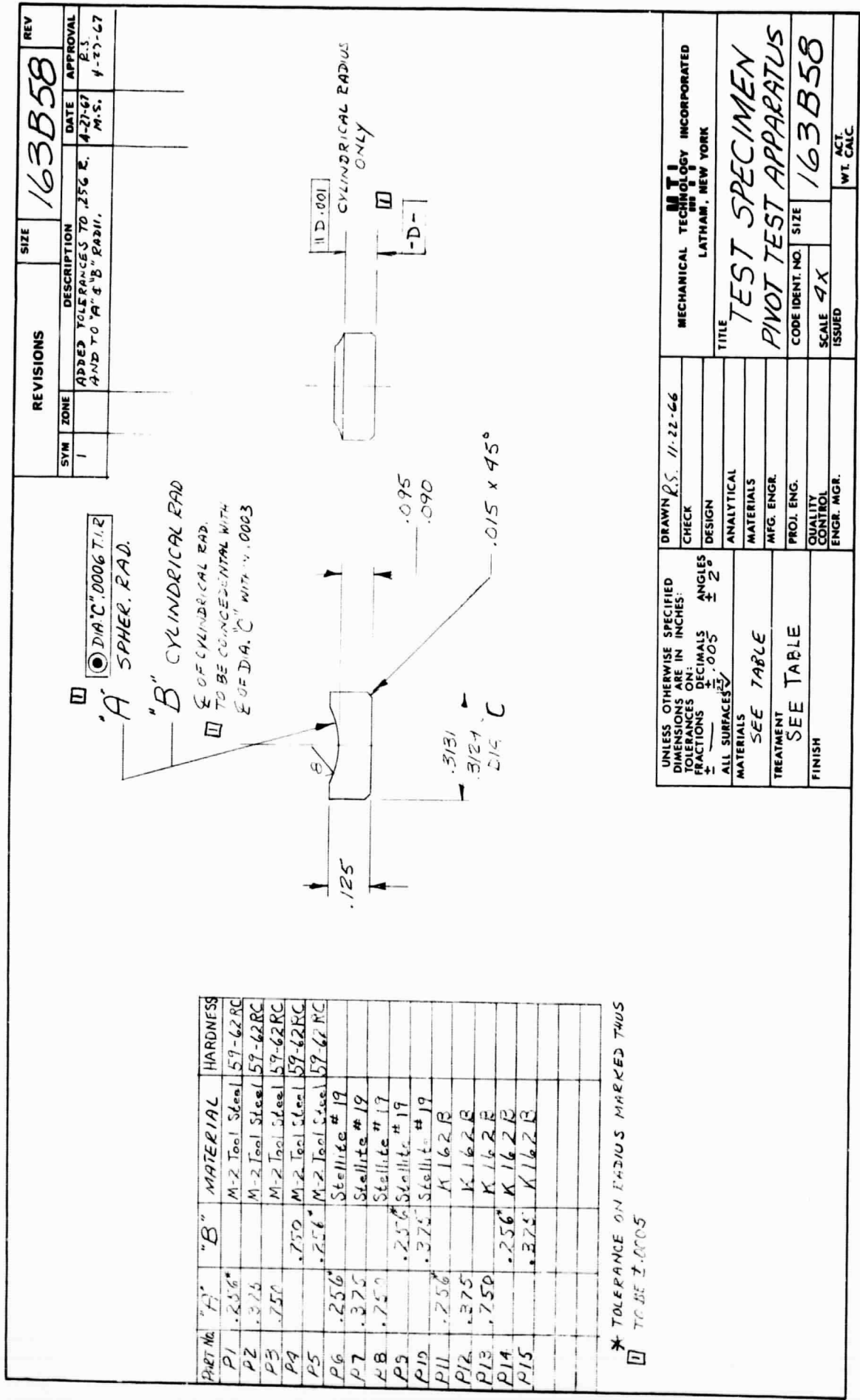
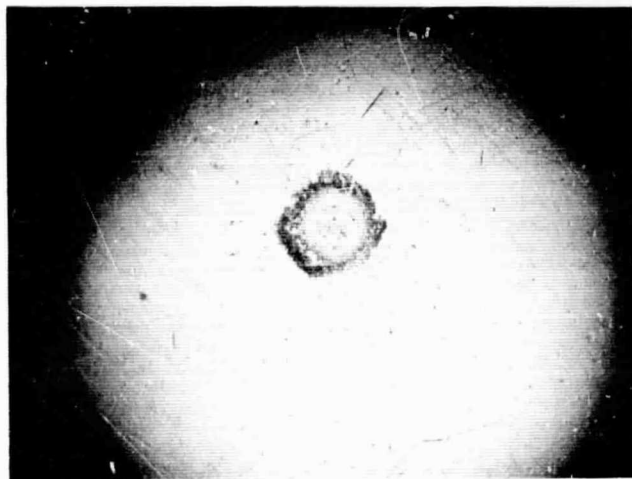
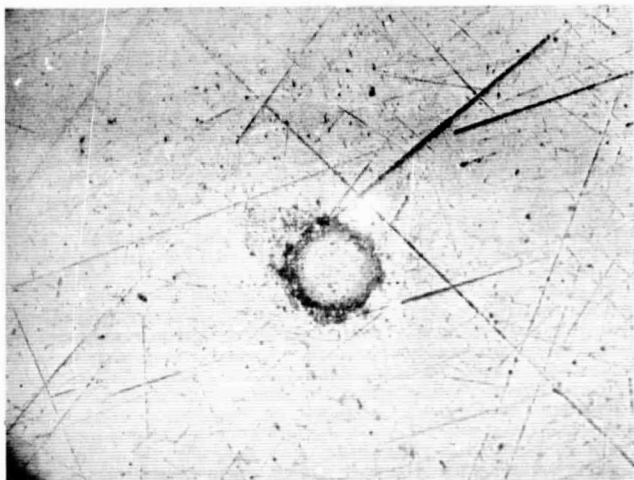


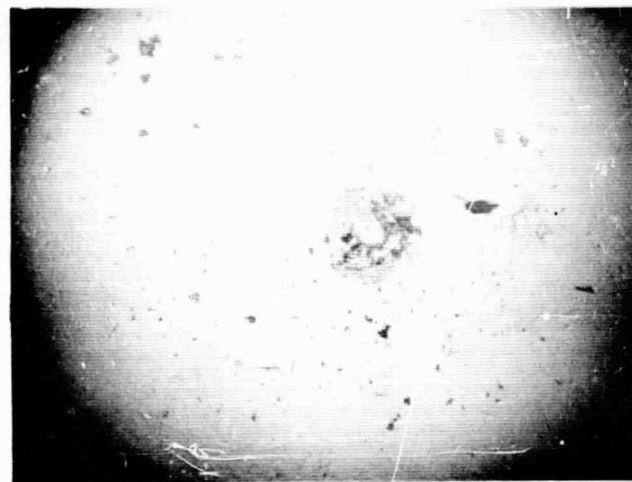
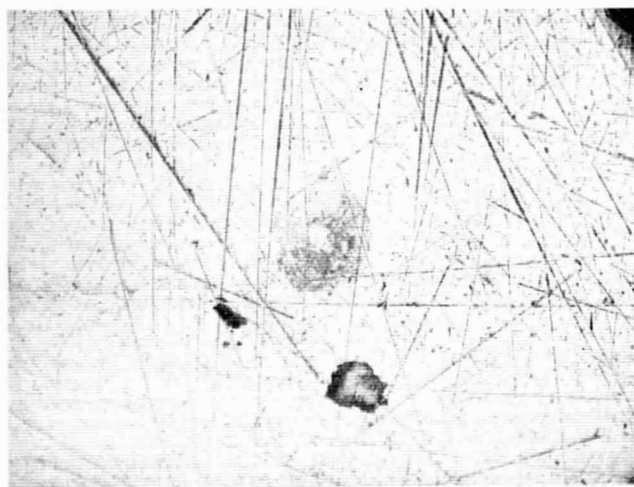
Fig. 49 Drawing of the Shaped Test Specimens

Test Not Run

-219-

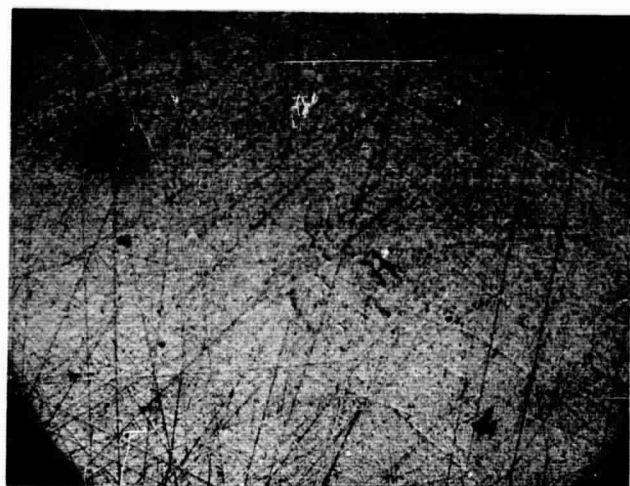


a) Amplitude 1.2 mils/in.

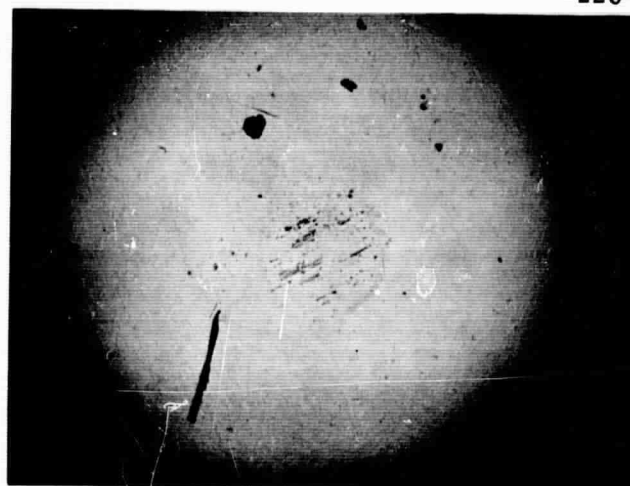


b) Amplitude 1.7 mils/in.

Fig. 50 Photograph of surface damage:
M-2 vs M-2; 80°F; Load, 2#;
200 cps; Pure Pitch; 75x.

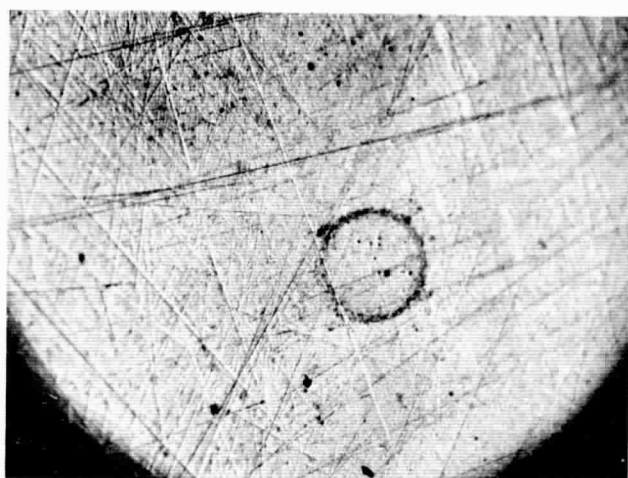


Flat

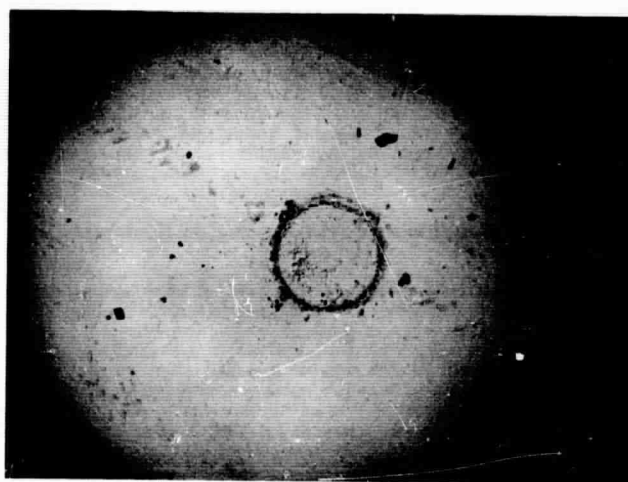


Ball

a) Amplitude .6 mil/in

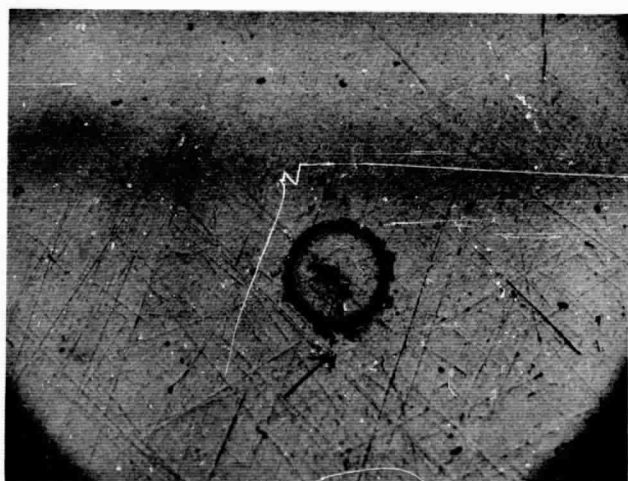


Flat

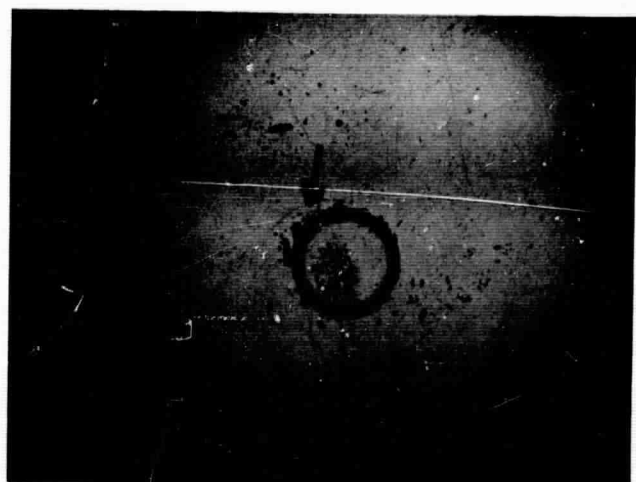


Ball

b) Amplitude 1.2 mil/in



Flat



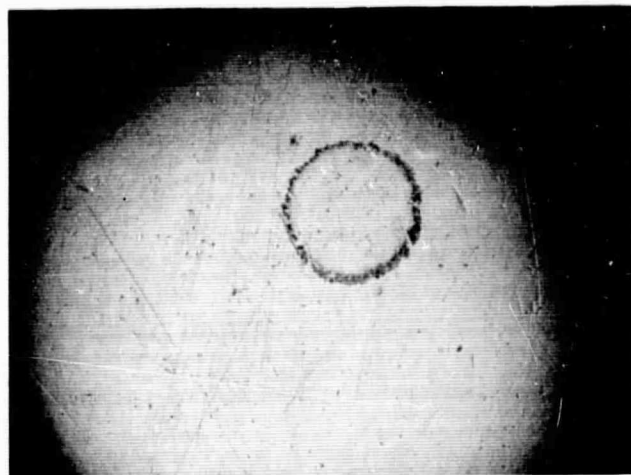
Ball

c) Amplitude 1.7 mil/in

Fig. 51 Photograph of surface damage:
M-2 vs M-2; 80°F; Load, 15#;
200 cps; Pure Pitch; 75x.

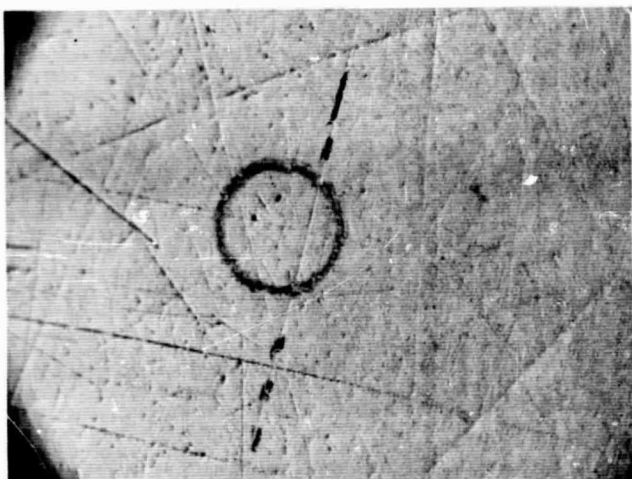


Flat

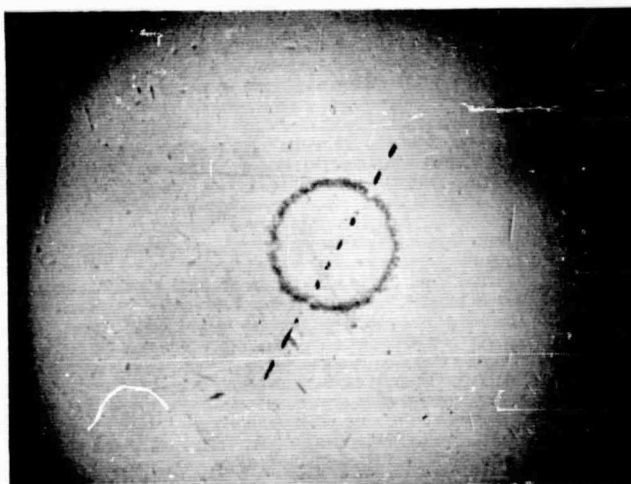


Ball

a) Amplitude .6 mil/in

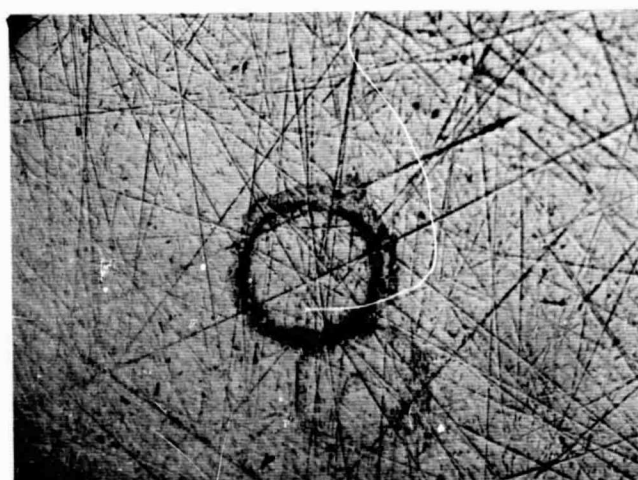


Flat

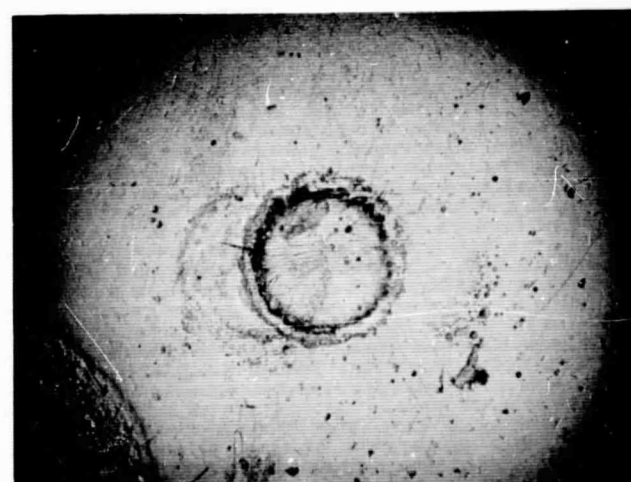


Ball

b) Amplitude 1.2 mil/in



Flat



Ball

c) Amplitude 1.7 mil/in

Fig. 52 Photograph of the surface damage:
M-2 vs M-2; 80 F; Load, 30#;
200 cps; Pure Pitch; 75x.

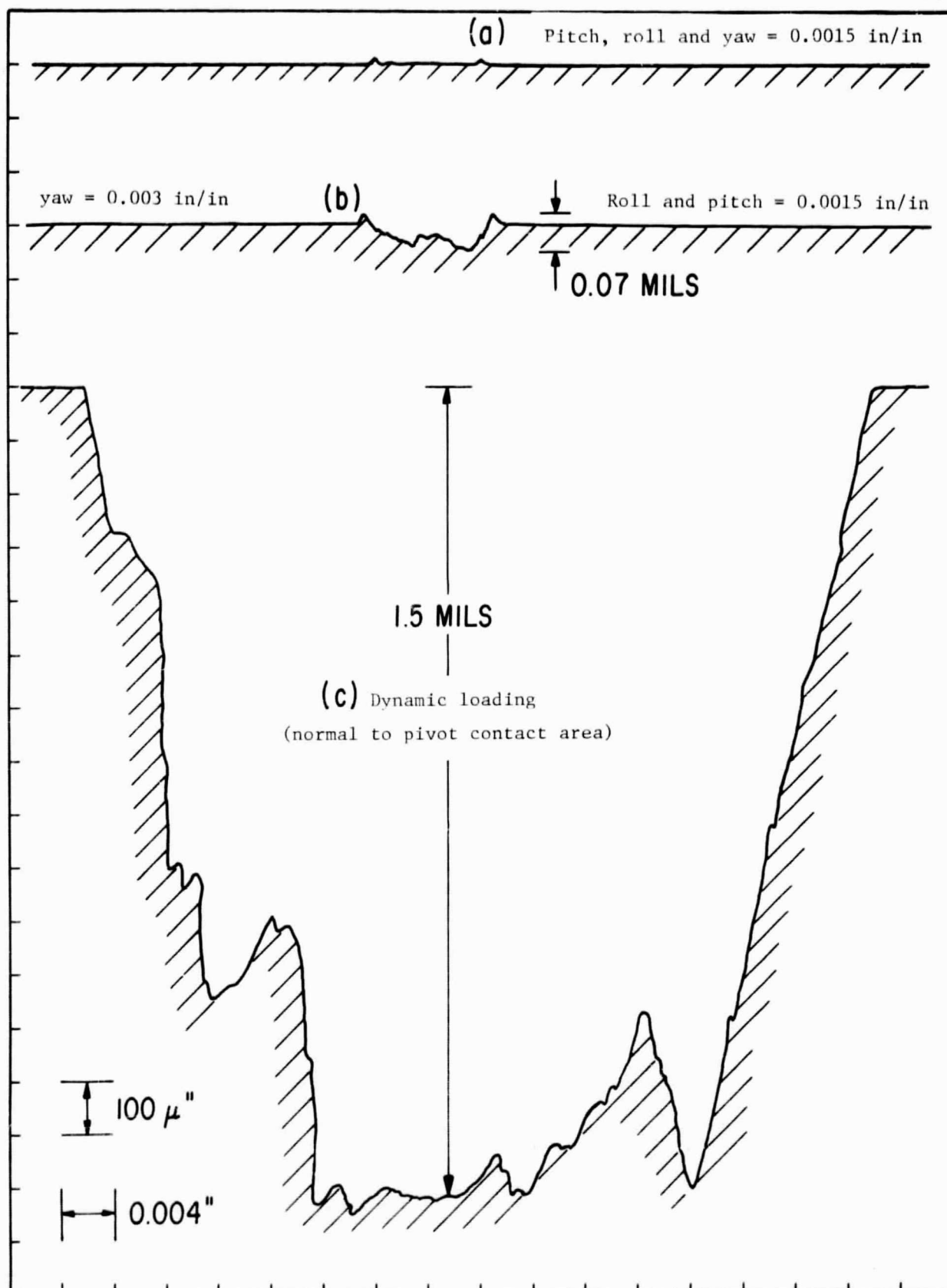


Fig. 53 Surface profile: Traces of the damaged area under conditions of pure pitch, yaw and dynamic load.

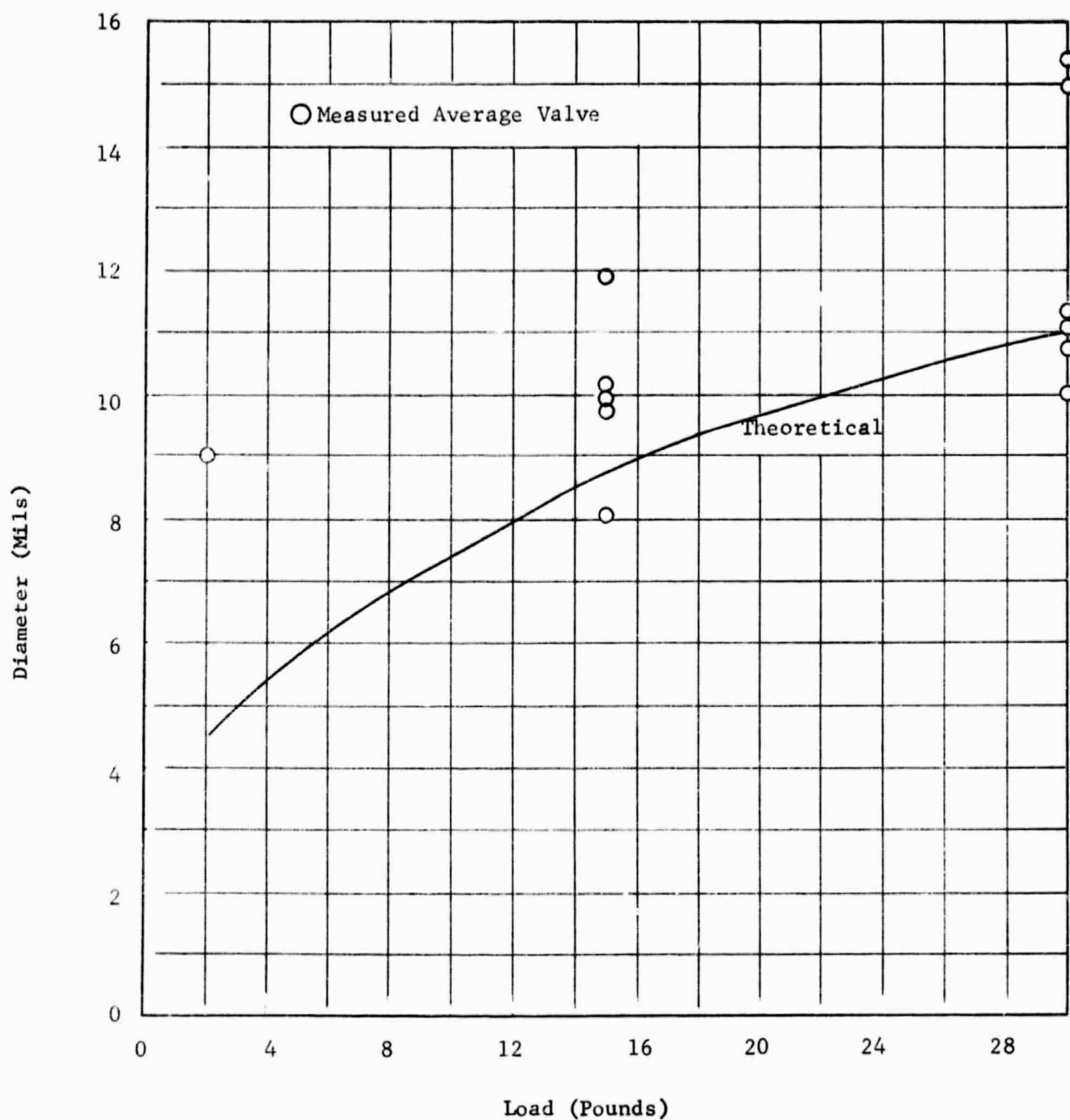
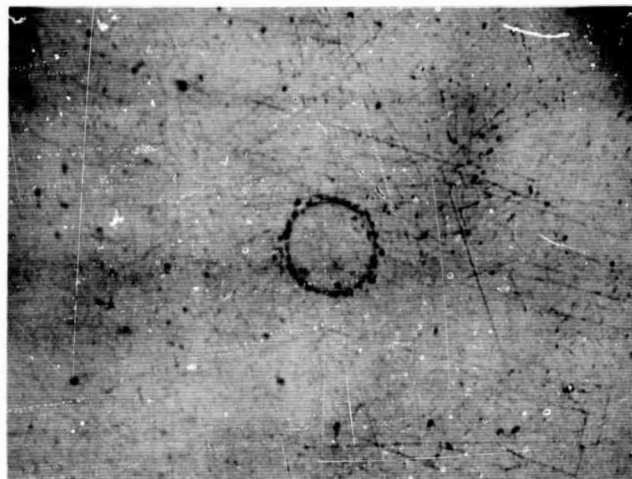
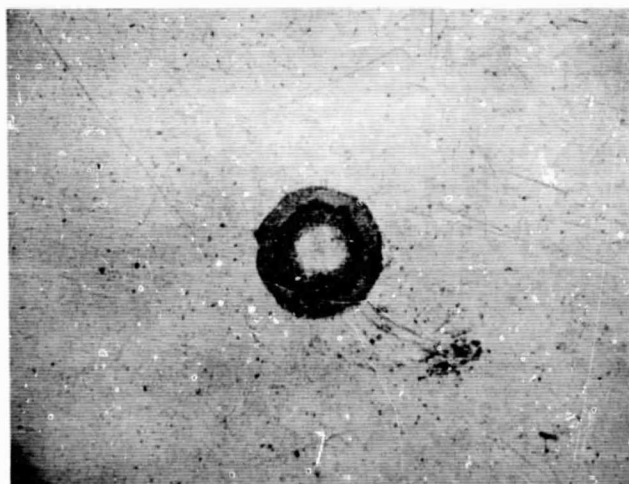


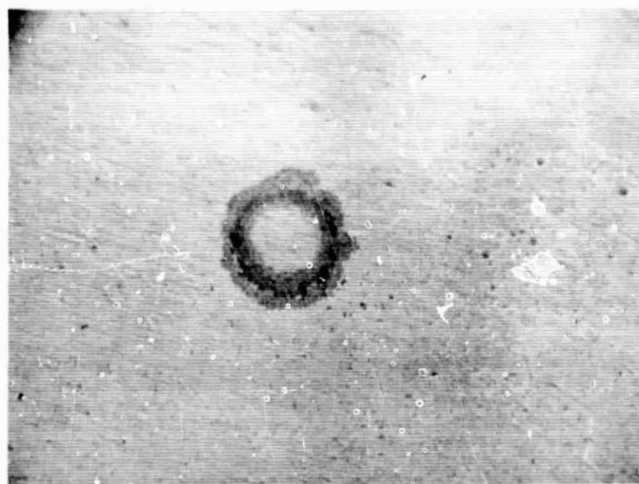
Fig. 54 Effect of Load on the Contact Area Ball on flat, M-2 Tool Steel vs. M-2 Tool Steel



a) Amplitude 1.6 mil/in
Load 15[#]; M-2 Tool Steel Flat



b) Amplitude 3.2 mil/in
Load 15[#]



c) Amplitude 3.2 mil/in
Load 30[#]

Fig. 55 Photograph of surface damage:
M-2 Tool Steel; 80 F; 200 cps;
Pure Yaw; 75x.

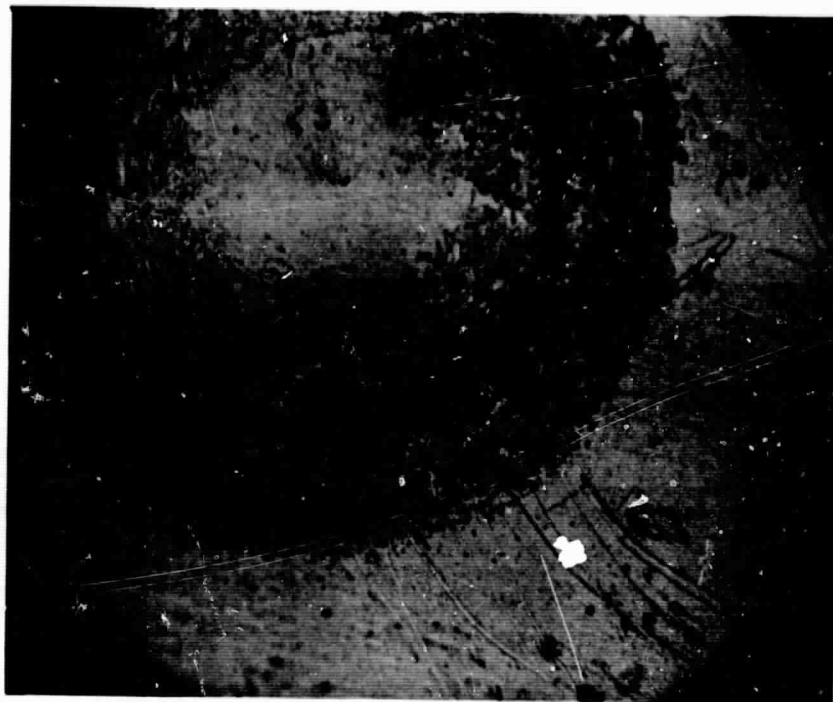
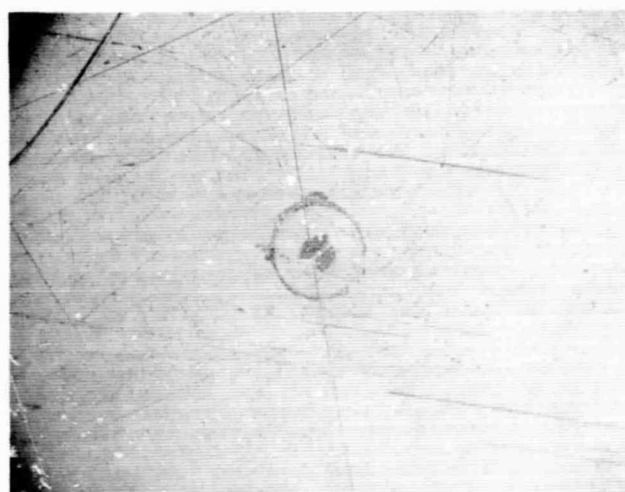


Fig. 56 Photograph of the surface damage:
M-2 vs M-2; 200 cps; Load, 15[#];
Pure Yaw; Amplitude .25 mil/in;
Mag 150x.



a) Pitch, 1.7 mil/in; Roll .59 mil/in;
Temp. 400 F



b) Pitch, 1.7 mil/in; Yaw, .48 mil/in;
Temp. 80 F

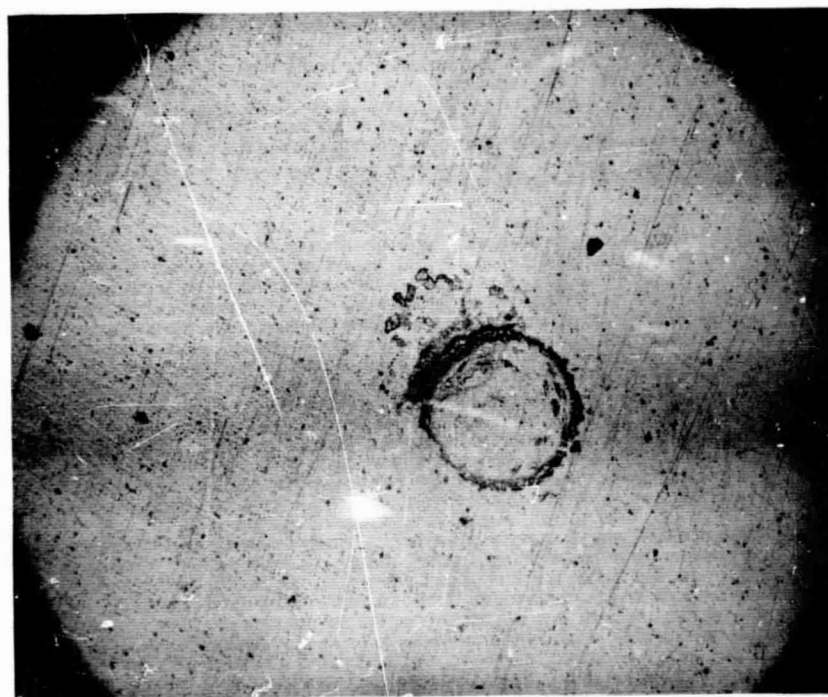


c) Pitch, 1.7 mil/in; Roll, .59 mil/in;
Yaw, .48 mil/in; Temp. 400 F

Fig. 57 Photograph of surface damage with combined motions:
M-2 vs. M-2; 200 cps; Load, 15[#].

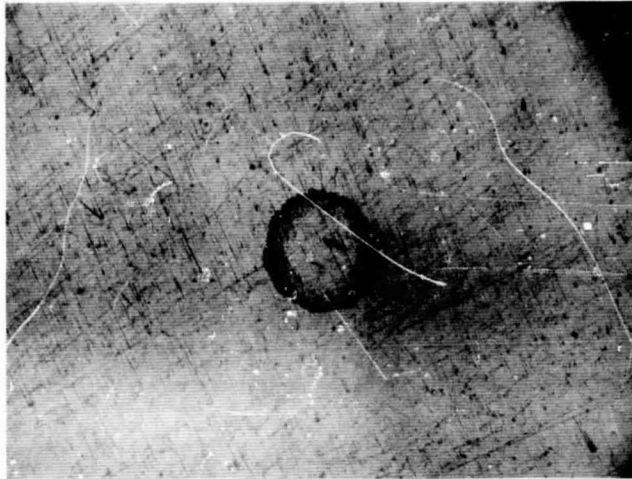


a) 15[#] Load



b) 30[#] Load

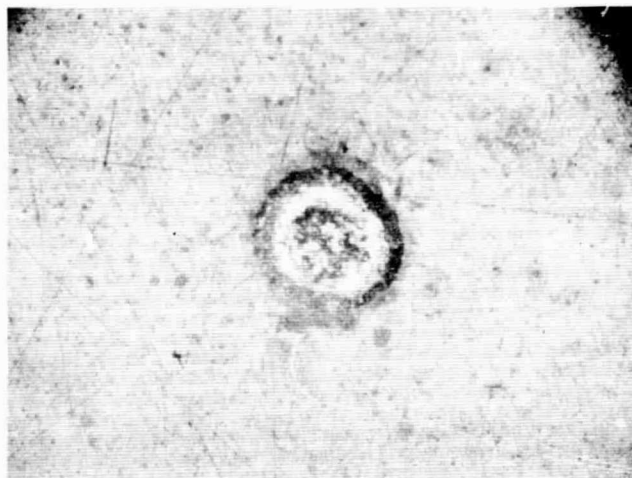
Fig. 58 Photograph of surface damage at high frequency:
M-2 vs M-2; 1000 cps; 80 F; Pure Pitch;
Amp. 1.7 mil/in.



a) 80 F



b) 400 F



c) 1000 F

Fig. 59 Photograph of Surface Damage: M-2; 1000 cps; Pitch, 1.7 mils/in.; Roll, .59 mil/in.; yaw, .24 mil/in.; Load, 15 lbs.; 75X.

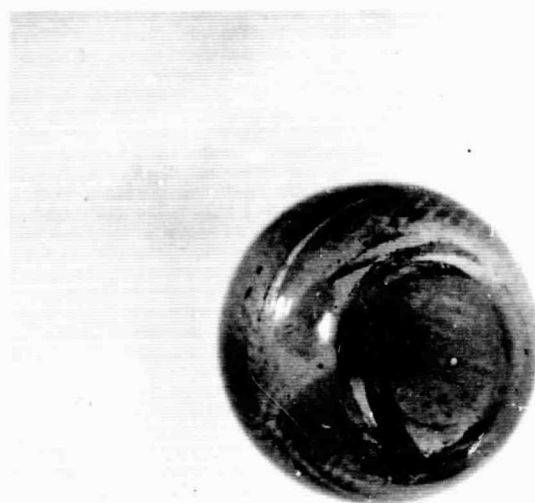
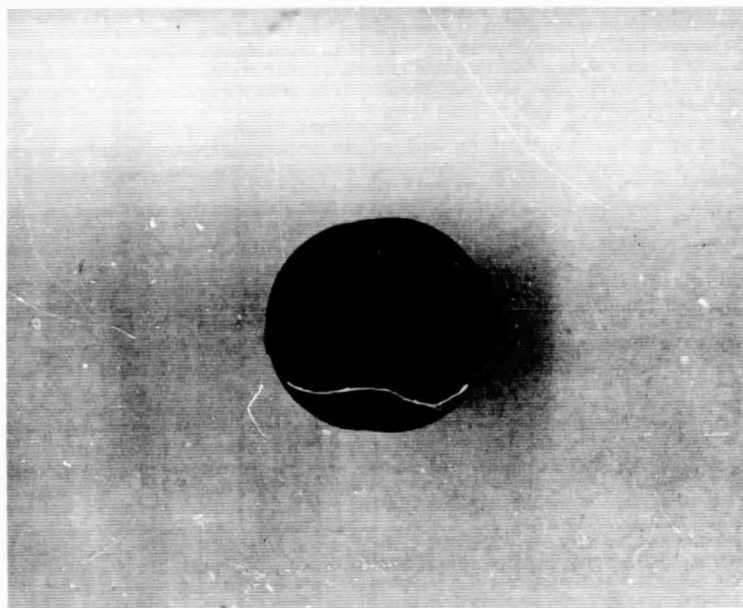
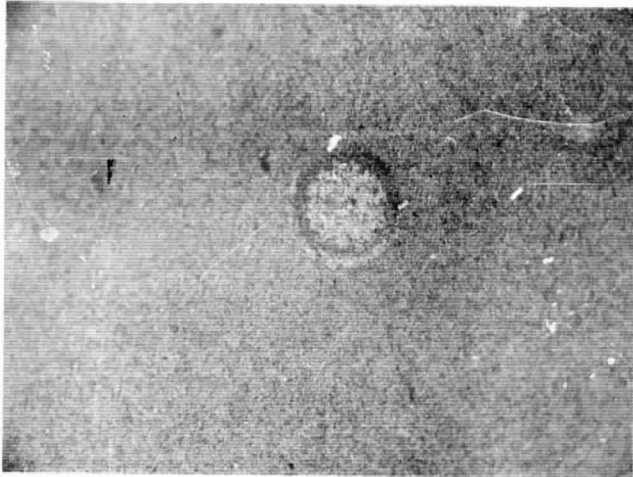


Fig. 60 Photograph of surface damage:
M-2 vs M-2; 1000 F; 1000 cps;
Load, 15#; Pitch, 1.7 mil/in;
Roll, .59 mil/in; Yaw, .48 mil/in;
Mag 3x.

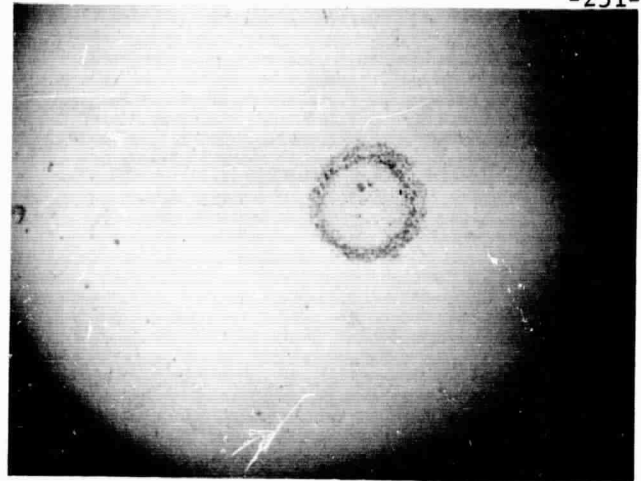


a) Flat
.59 mil/in

Fig. 61 Photograph of surface damage:
K162B vs K162B; 200 cps; 80 F;
2 $\frac{1}{2}$ Load; Pure Pitch; Mag 75x.

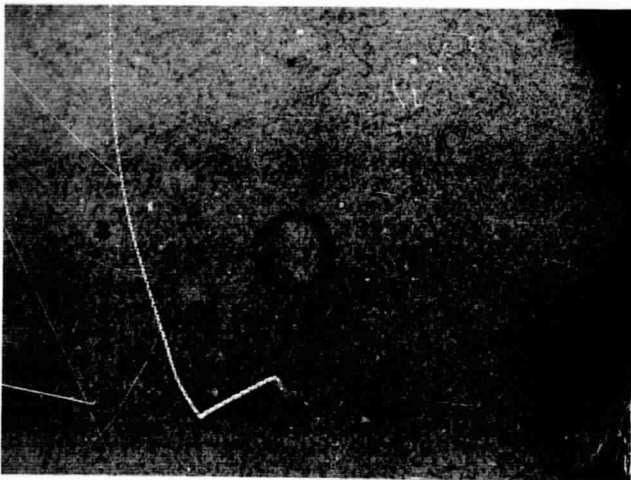


Flat

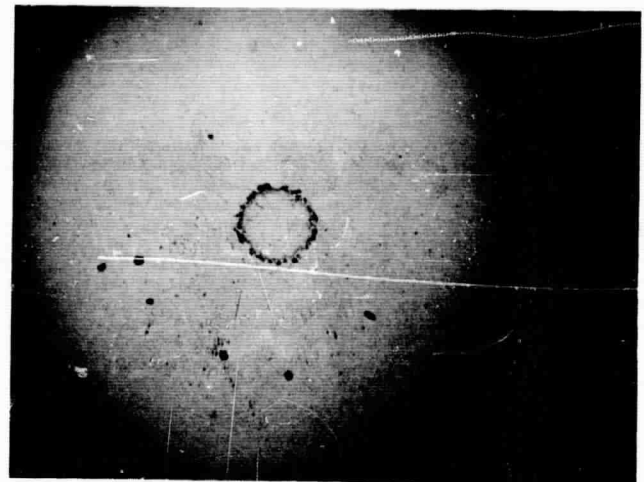


Ball

a) .59 mil/in amplitude

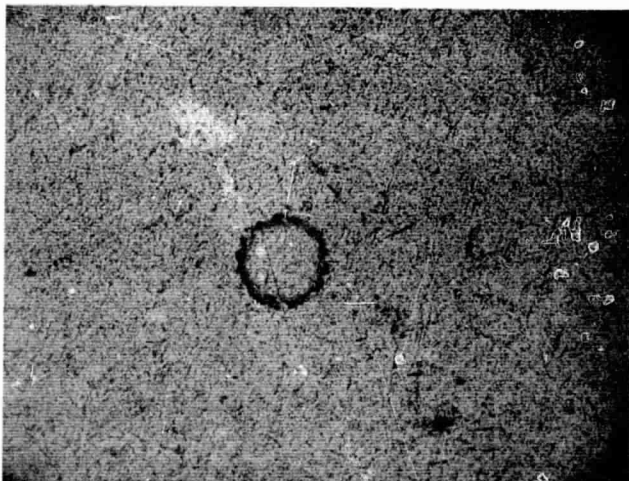


Flat

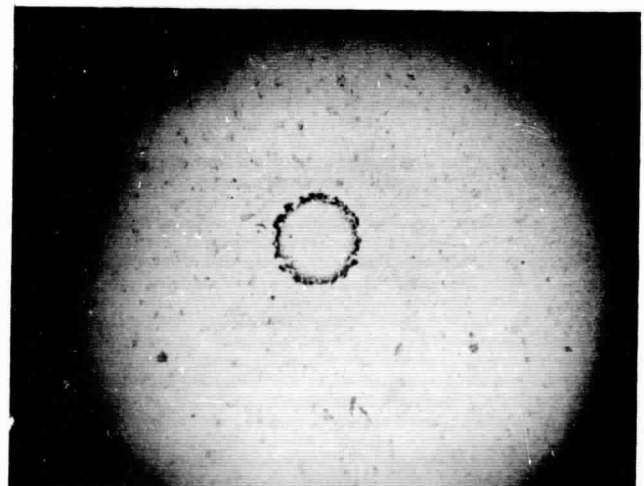


Ball

b) 1.2 mil/in amplitude



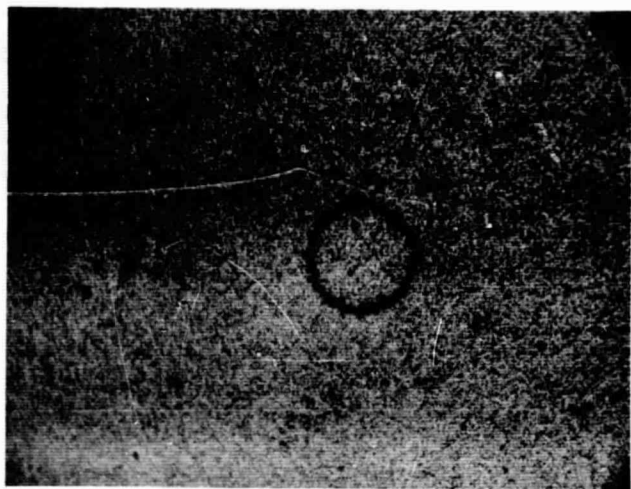
Flat



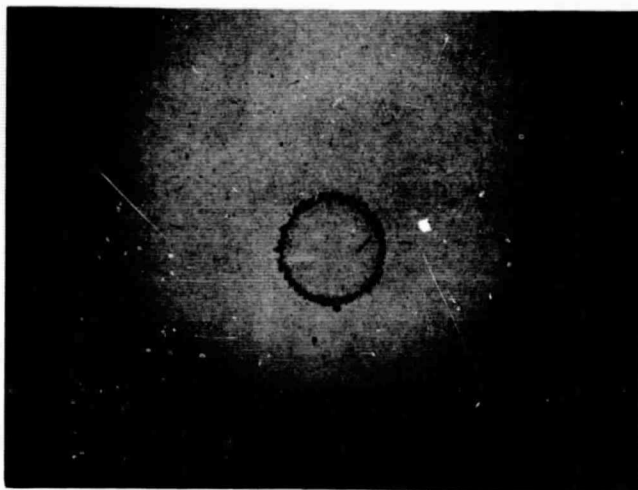
Ball

c) 1.7 mil/in amplitude

Fig. 62 Photograph of surface damage:
K162B vs K162B; 80 F; 15[#] Load;
200 cps; Pure Pitch; Mag 75x.



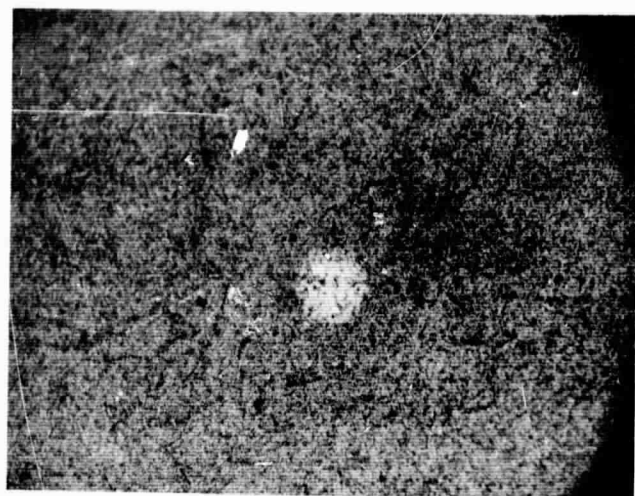
Flat



Ball

b) Amplitude 1.2 mil/in

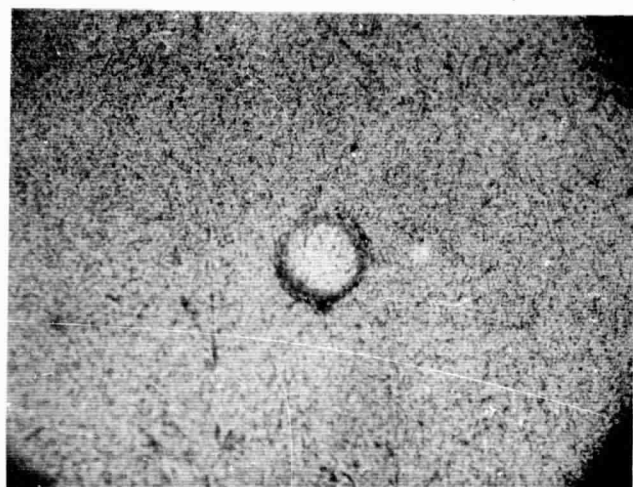
Fig. 63 Photograph of surface damage:
K162B vs K162B; 80 F; 30[#] Load;
200 cps; Pure Pitch; Mag 75x.



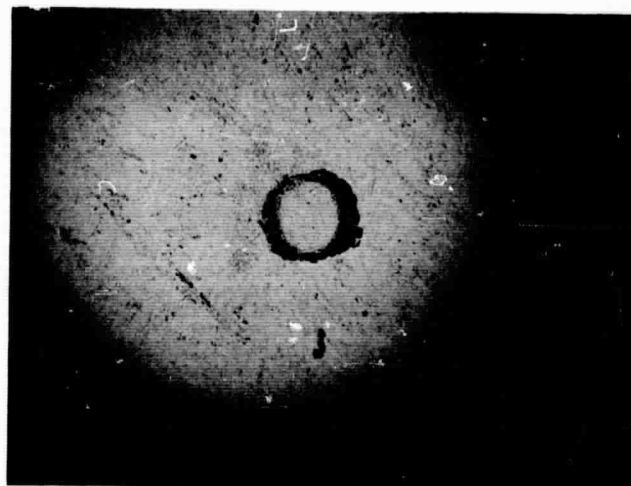
Flat

Ball

a) .59 mil/in amplitude



Flat



Ball

b) 1.2 mil/in amplitude



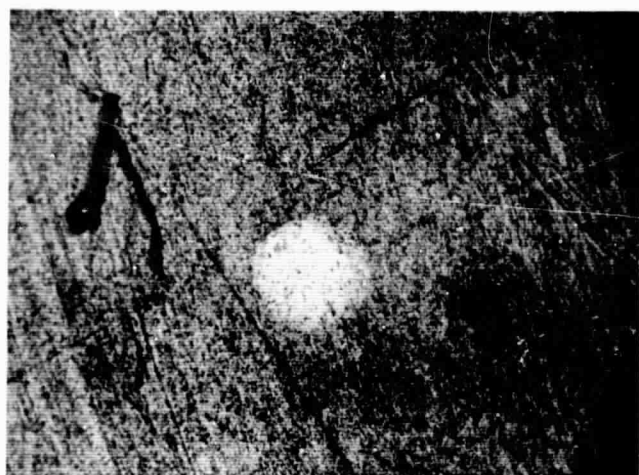
Flat



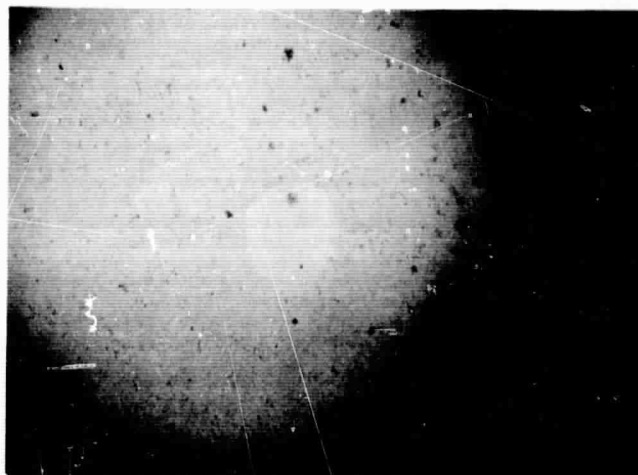
Ball

c) 1.7 mil/in amplitude

Fig. 64 Photograph of surface damage:
K162B vs K162B; 200 cps; 15[#] Load;
Temp. 1000 F; Pure Pitch; Mag 75x.

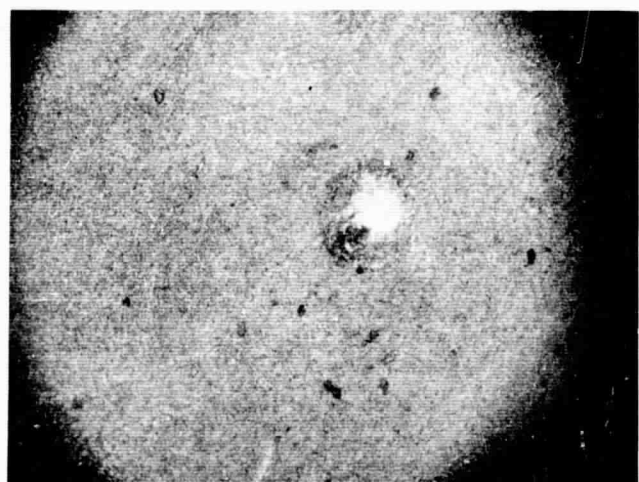


Flat

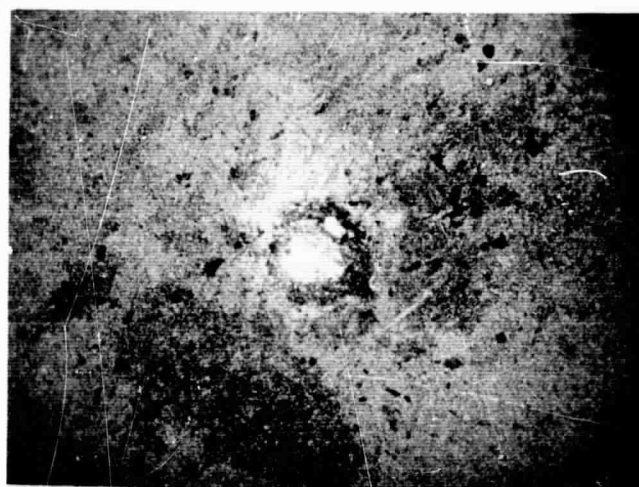


Ball

b) Amplitude 1.2 mil/in



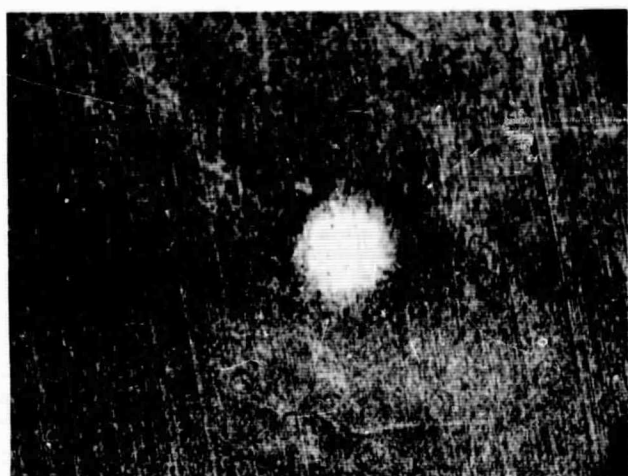
Flat



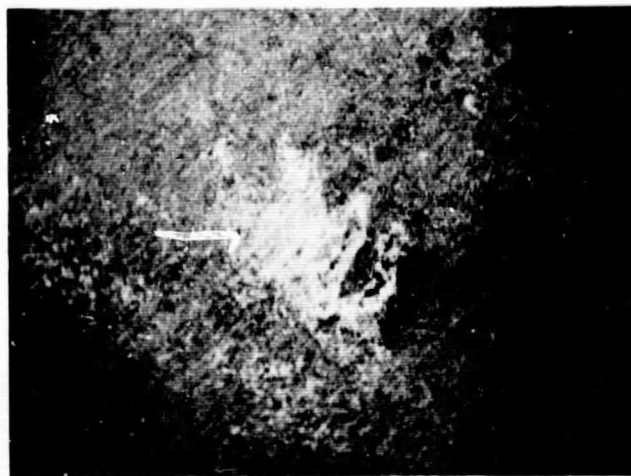
Ball

c) Amplitude 1.7 mil/in

Fig. 65 Photograph of surface damage:
K162B vs K162B; 200 cps; 30⁷/₈ Load;
Temp. 1000 F; Pure Pitch; Mag 75x.



Flat



Ball

Amplitude 1.2 mil/in

Fig. 66 Photograph of surface damage:
K162B vs K162B; 200 cps; 15[#] Load;
1400 F; Pure Pitch; Amplitude, 1.2 mil/in;
Mag 75x.



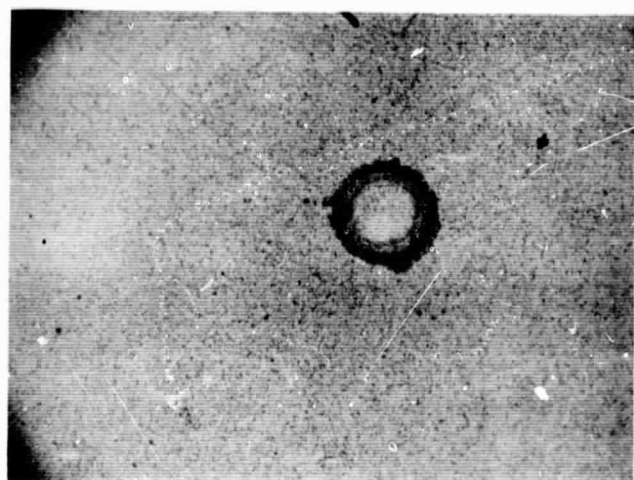
Flat



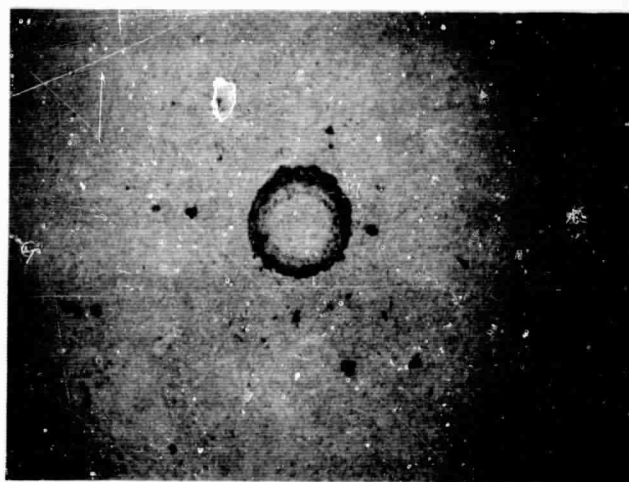
Ball

Amplitude 1.7 mil/in

Fig. 67 Photograph of surface damage:
K162B vs K162B; 200 cps; 15^{lb} Load;
1400 F; Pure Pitch; Amp, 1.7 mil/in;
Mag 75x. .



Flat

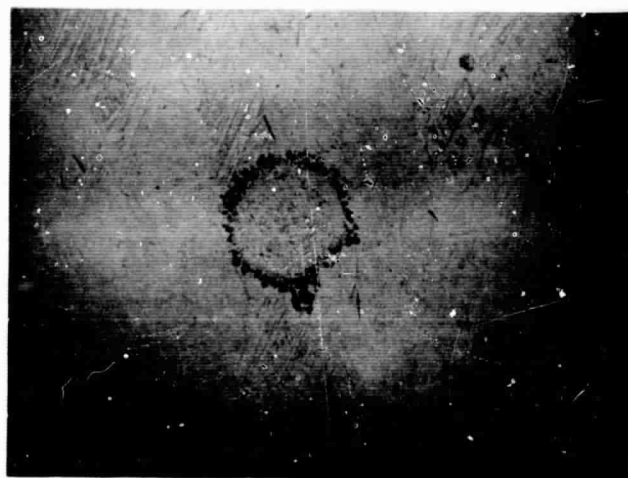


Ball

a) Load 15#



Flat



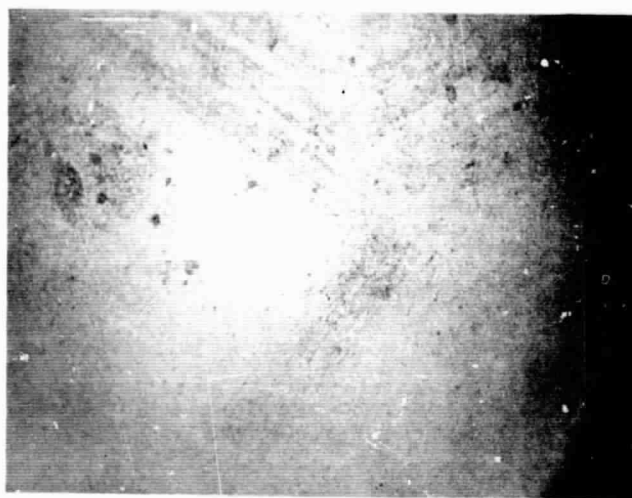
Ball

b) Load 30#

Fig. 68 Photograph of surface damage:
K162B vs K162B; 1000 cps; 400 F;
Pure Pitch, 1.8 mil/in; Mag 75x.

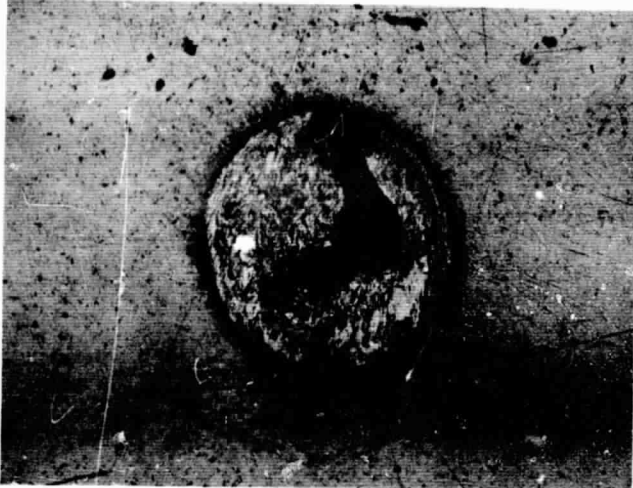


Flat

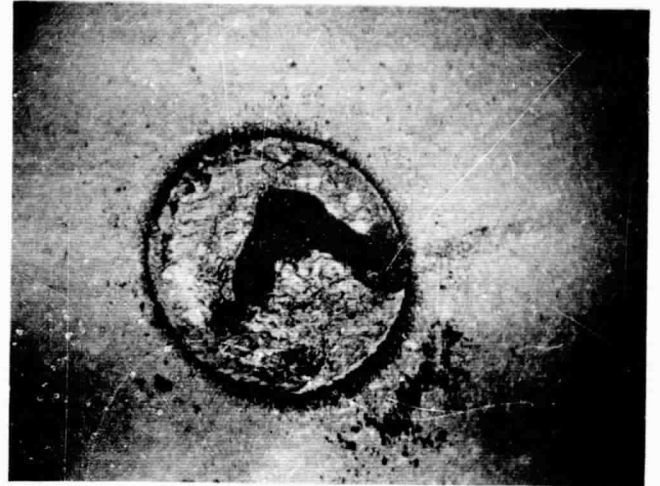


Ball

Fig. 69 Photograph of surface damage:
K162B vs K162B; 200 cps; 1000 F;
Load, 15[#]; Pure Yaw, 3.2 mil/in;
Mag 75x.

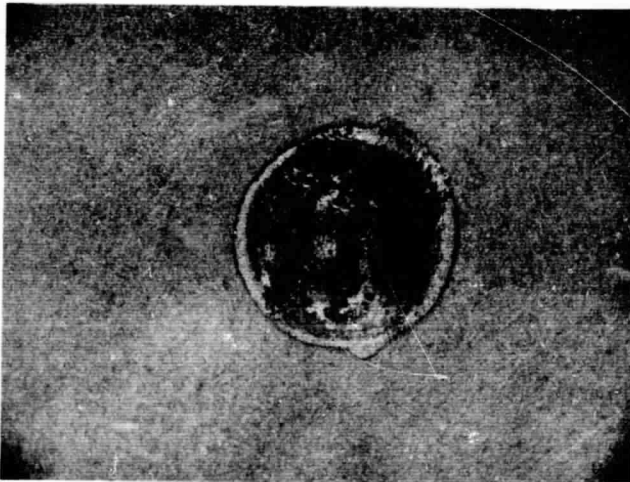


Flat

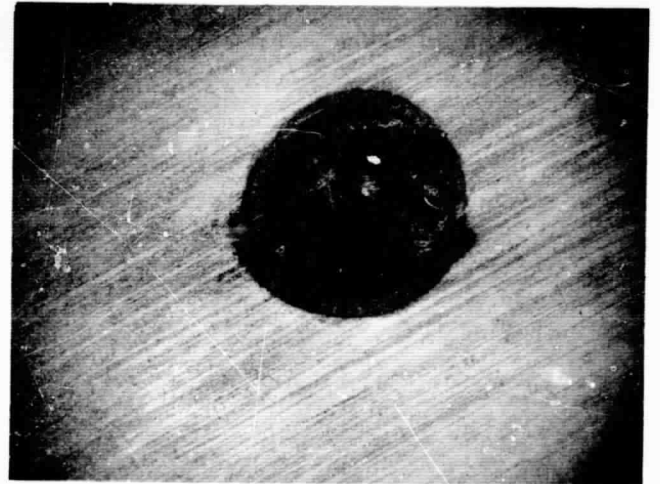


Ball

a) M-2 Tool Steel



Flat



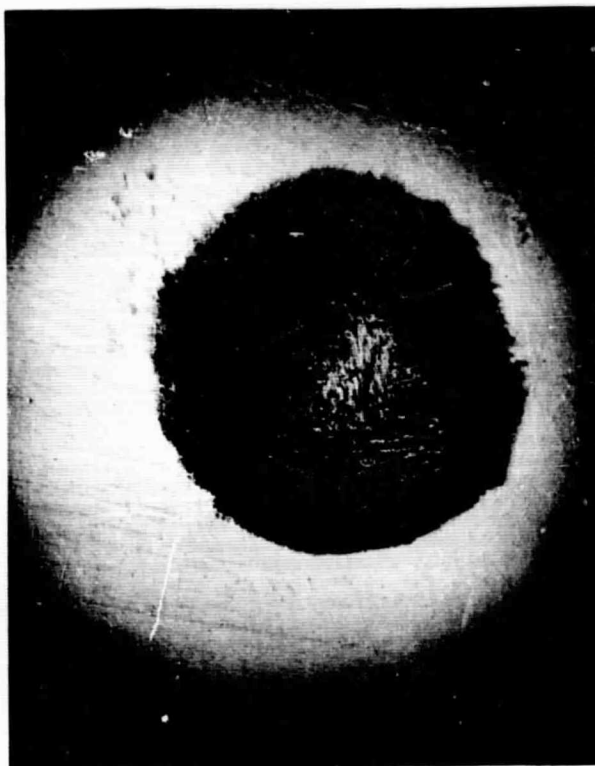
Ball

b) K162 B Carbide

Fig. 70 Photograph of Surface Damage from Dynamic Loading
1000 cps; 80 F; Load 15 lbs.



Flat



Ball

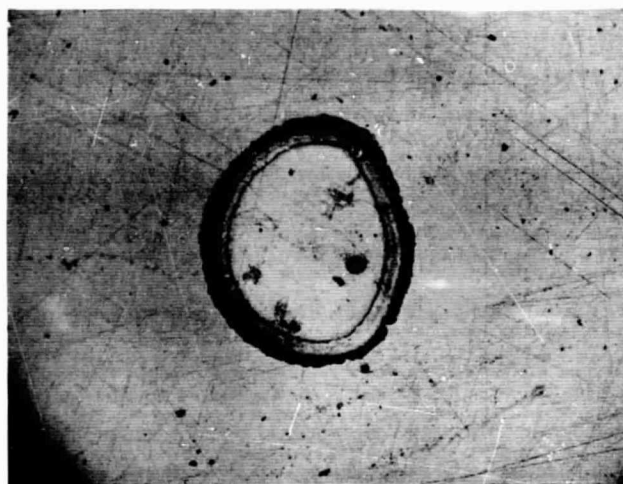
Fig. 71 Effect of turning -
Photograph of surface damage:
M-2 vs M-2; Temp. 400 F.



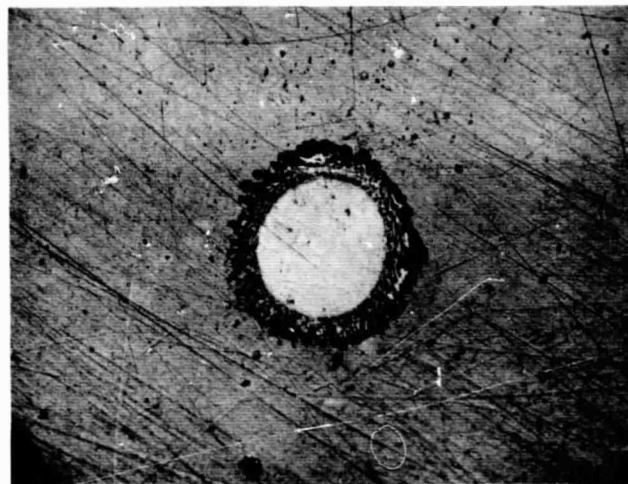
a) Stellite 6 vs Stellite 6



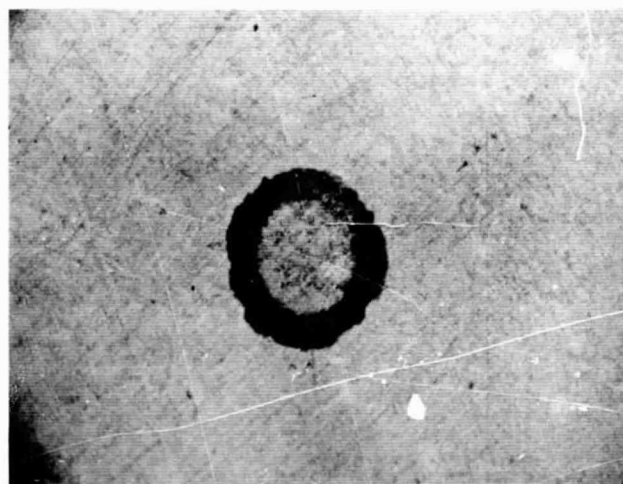
b) 440C vs 440C



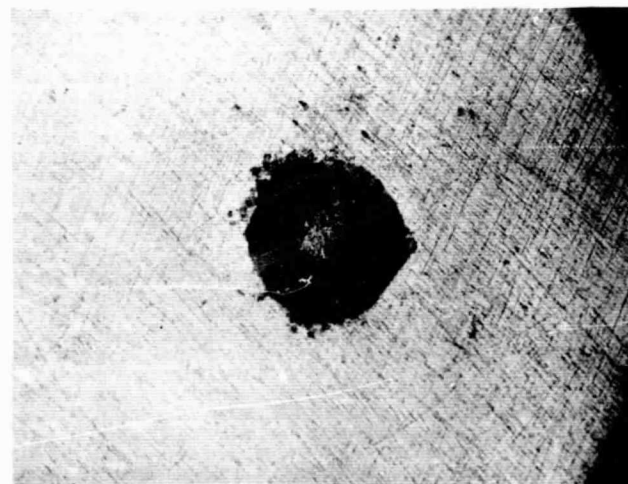
c) SAE 52100 Steel vs SAE 52100 Steel



d) SAE 52100 Steel vs SAE 52100 Steel

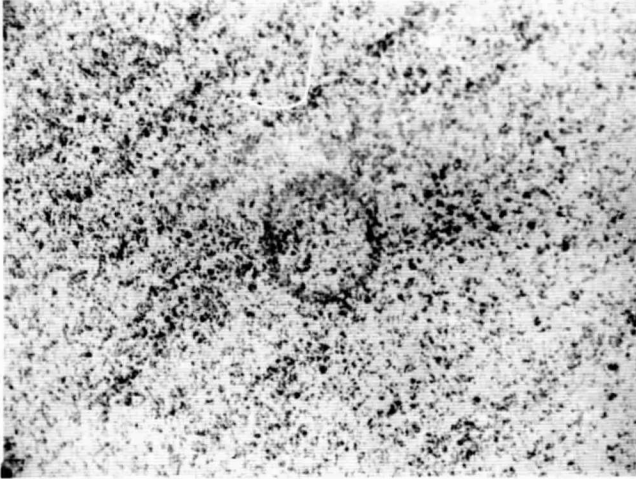


e) Stellite 6 vs Stellite 19

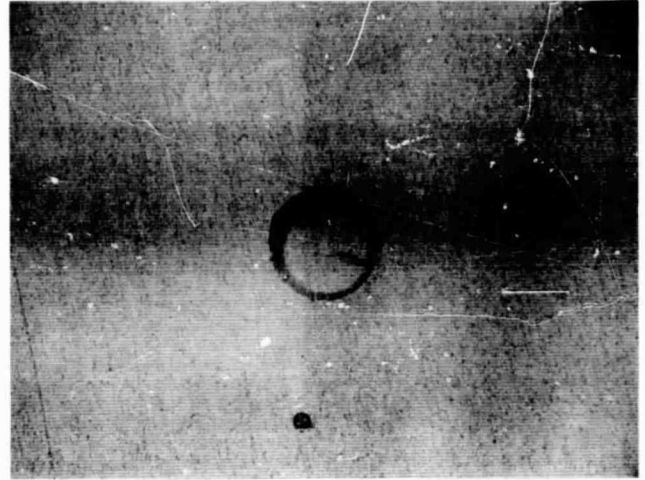


f) Stellite Star J vs Stellite 19

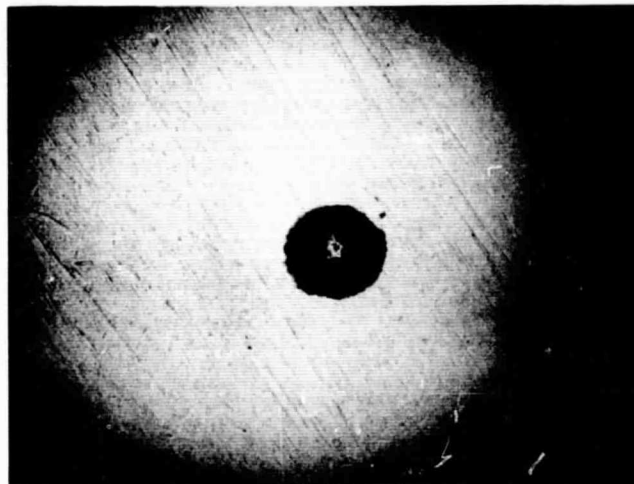
Fig. 72 Photograph of surface damage to Flat:
1000 cps; Temp. 400 F; Load, 15#;
Pitch, 1.7 mil/in; Roll, .58 mil/in;
Yaw, .25 mil/in; Mag 75x.



a) K162 B vs C608

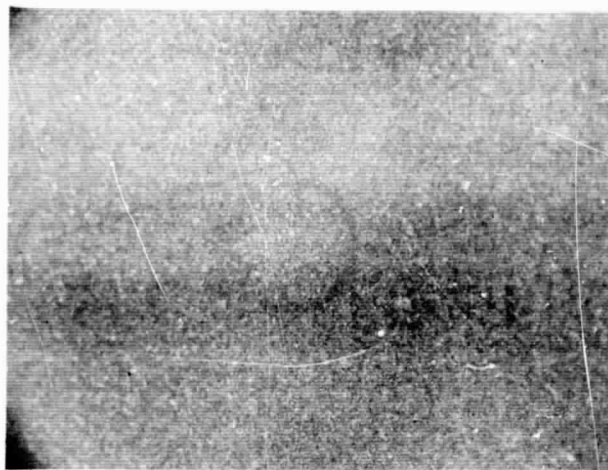


b) K96 vs K96

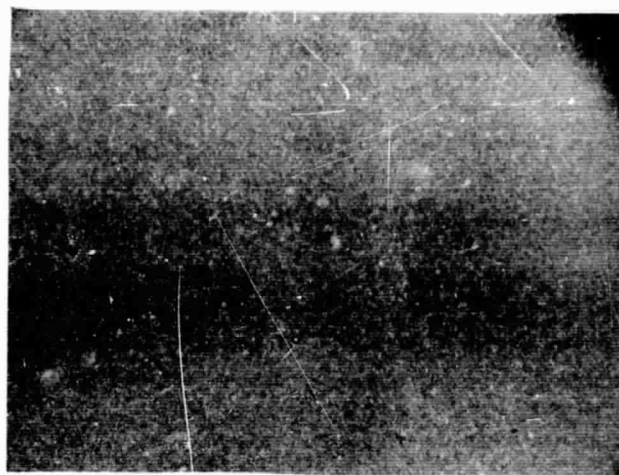


c) K162B vs K162B

Fig. 73 Photograph of surface damage to Flat in material screening tests; 1000 cps; Temp. 400 F; Load, 15#; Pitch, 1.7 mil/in; Roll, .58 mil/in; Yaw, .25 mil/in; Mag 75x.



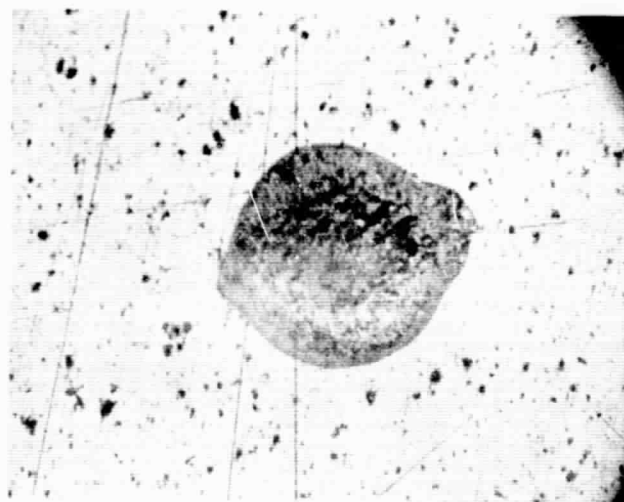
a) Hot Pressed Al_2O_3 vs Cemented Oxide



b) Hot Pressed Al_2O_3 vs Hot Pressed Al_2O_3

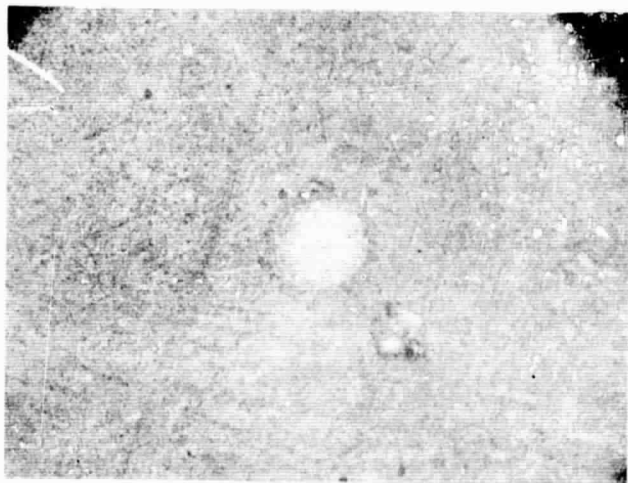


c) Cold Pressed Al_2O_3 vs Cold Pressed Al_2O_3



d) K96 vs Sprayed WC

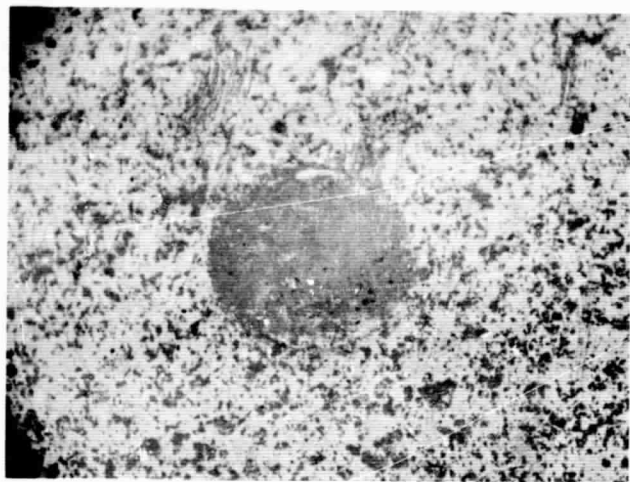
Fig. 74 Photograph of surface damage to flat in material screening tests:
1000 cps; Temp. 400 F; Load, 15#;
Pitch, 1.7 mil/in; Roll, .58 mil/in;
Yaw, .25 mil/in; Mag 75x.



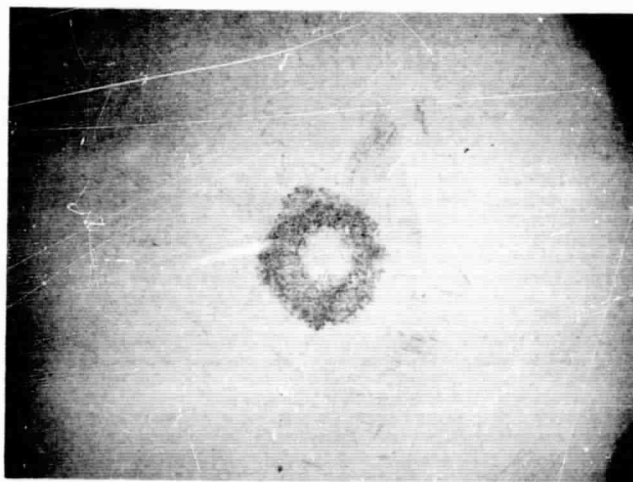
a) K162B Carbide vs K162B Carbide (Flat)



b) Stellite Star J vs Stellite 19 (Flat)

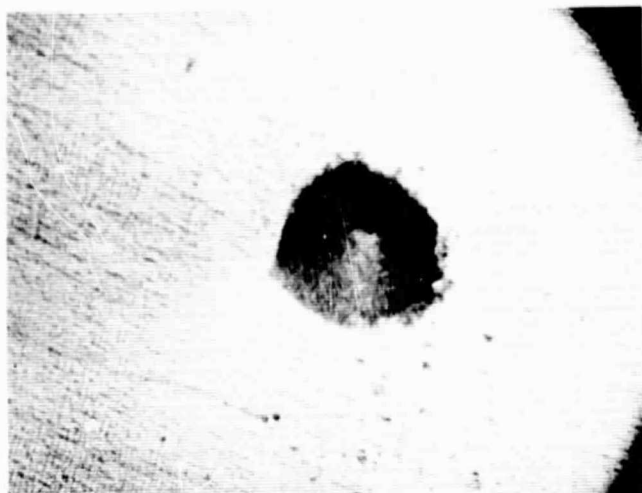


c) Cold Pressed Al_2O_3 vs Cold Pressed Al_2O_3 (Flat)

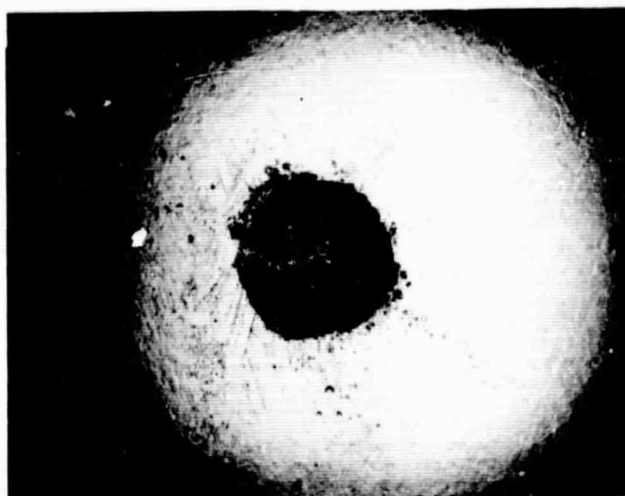


d) Hot Pressed Al_2O_3 vs Hot Pressed Al_2O_3 (Ball)

Fig. 75 Photograph of the surface damage in material screening tests:
1000 cps; Temp. 1000 F, Load, 15#;
Pitch, 1.7 mil/in; Roll, .58 mil/in;
Yaw, .25 mil/in; Mag 75x.

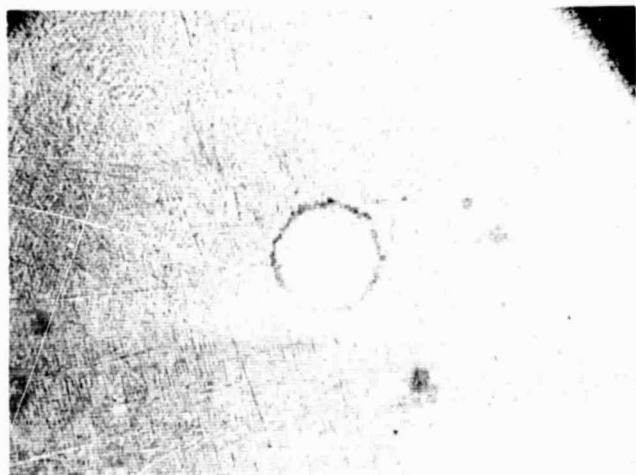


a) WC Coated A-286
Flat

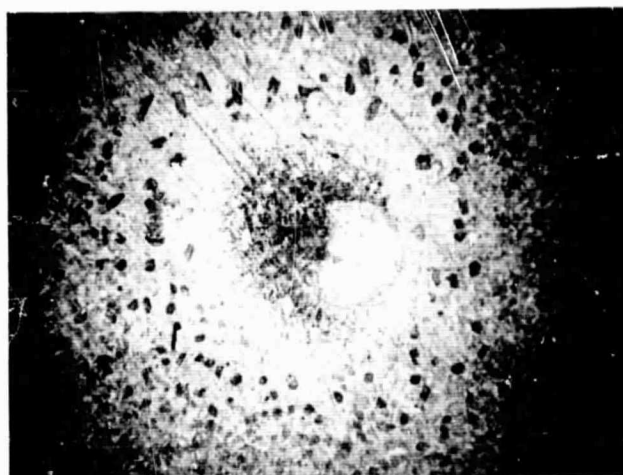


b) K96
Ball

Fig. 76 Photograph of surface damage
in material screening tests:
Material K96 Carbide vs Sprayed WC;
1000 cps; Temp. 1000 F; Load, 15#;
Pitch, 1.7 mil/in; Roll, .58 mil/in;
Yaw, .25 mil/in; Mag 75x.



Flat

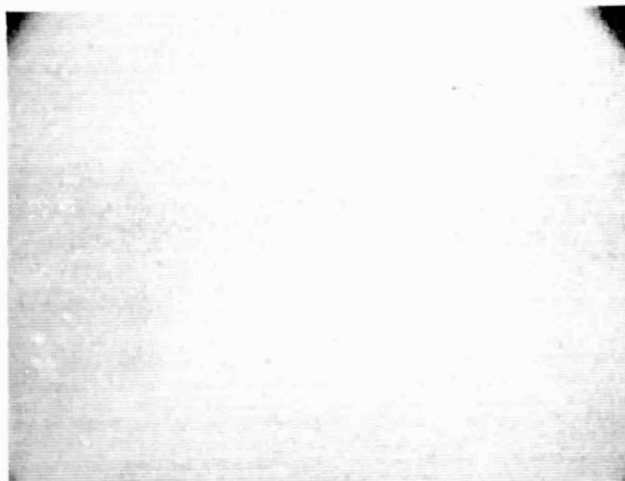


Ball

a) Stellite Star J vs Stellite 19



Flat



Ball

b) K162B Carbide vs K162B Carbide

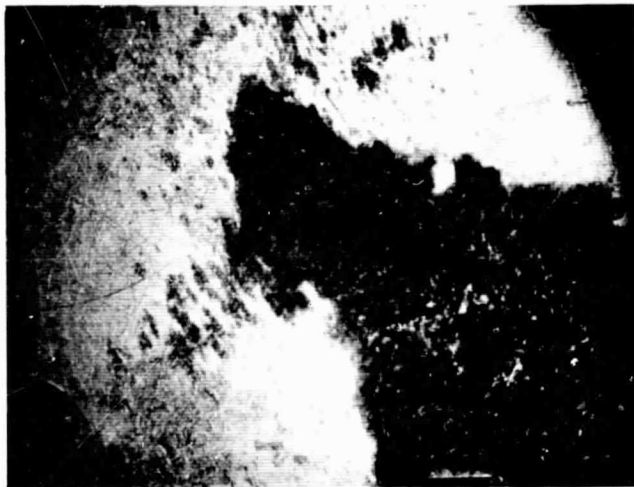
Fig. 77 Photograph of surface damage
in material screening tests:
1000 cps; Temp. 1400 F; Load, 15#;
Pitch, 1.7 mil/in; Roll, .58 mil/in;
Yaw, .25 mil/in; Mag 75x.



a) Socket
Mag 3x



b) Ball
Mag 3x



c) Mag 75x

Fig. 78 Photograph of surface damage:
M-2 vs M-2; Temp. 400 F; 1000 cps;
Load, 15#; Pitch, 1.7 mil/in;
Roll, .59 mil/in; Yaw, .25 mil/in.

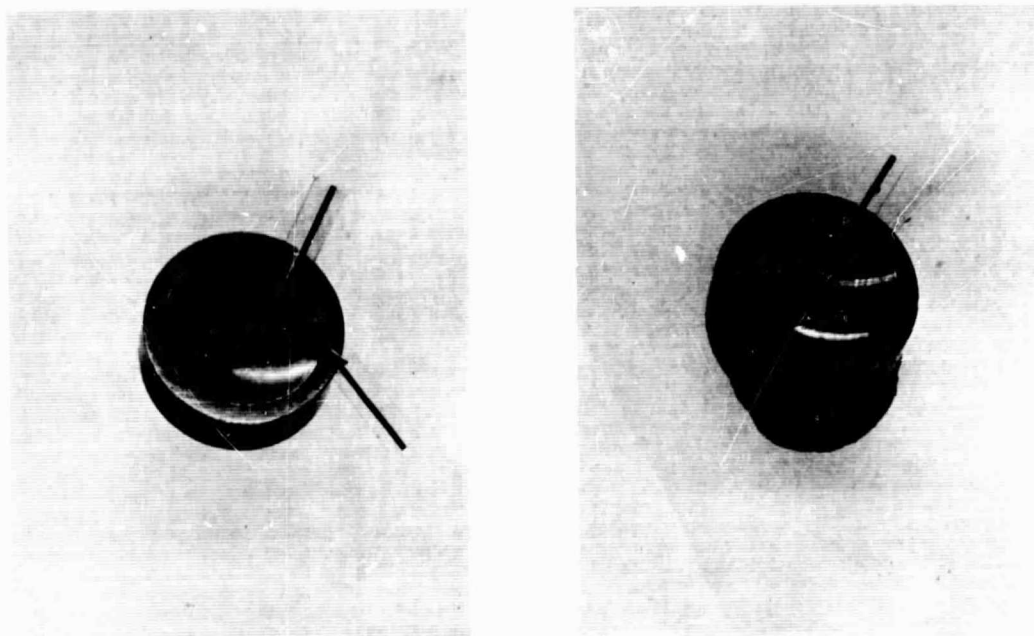


Fig. 79 Photographs of surface damage for two tests:
M-2 vs M-2; 1000 F; Load, 15#; Radius, .256"
1000 cps; Pitch, 1.7 mil/in; Roll, .59 mil/in;
Yaw, .25 mil/in; Mag 3x.

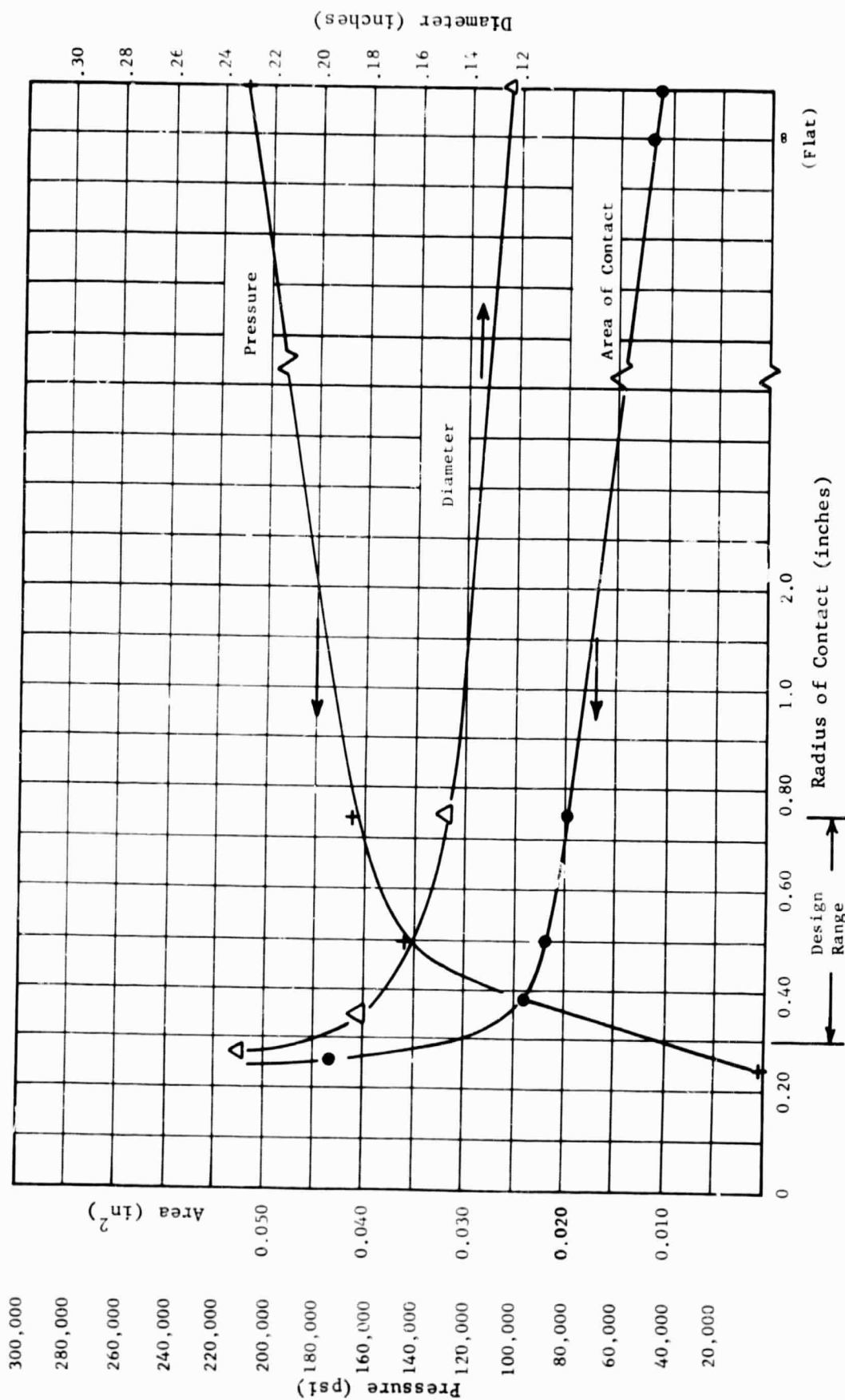
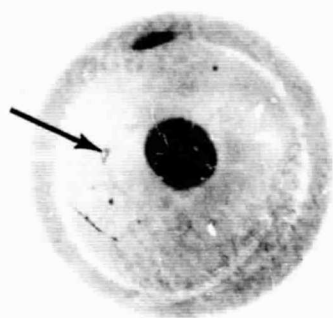
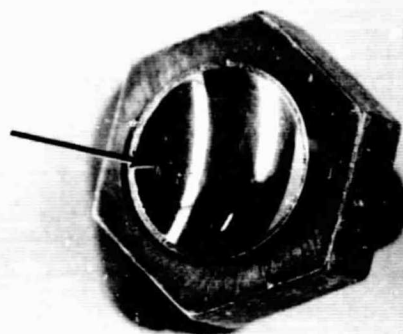


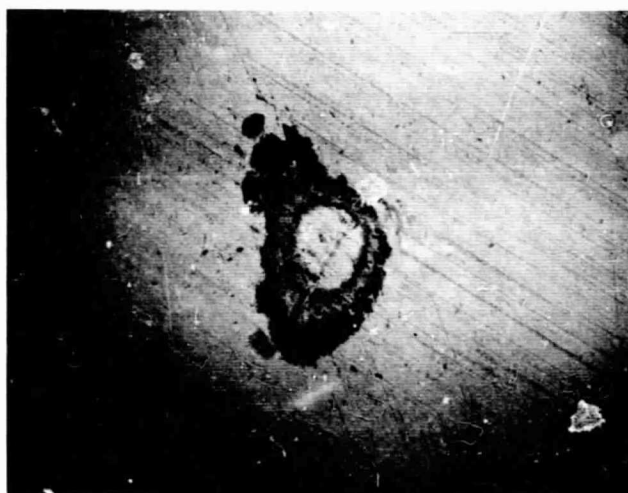
Fig. 80 Effect of Radius of Contact of Socket Area and Pressure Load #15
1/2 in (.250 radius) Ball



a) Ball
3x Mag

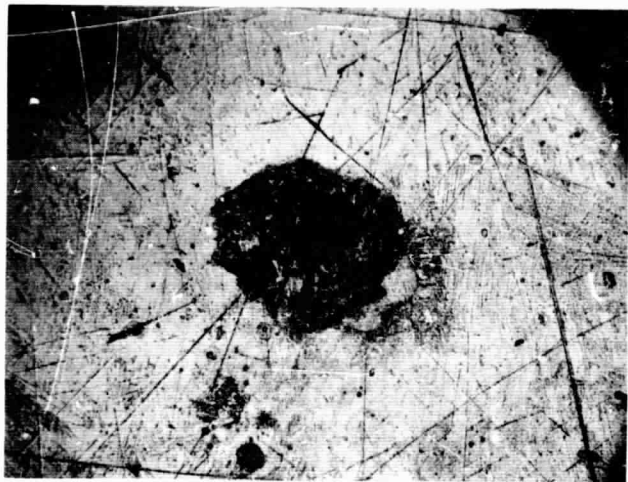


b) Socket
3x Mag

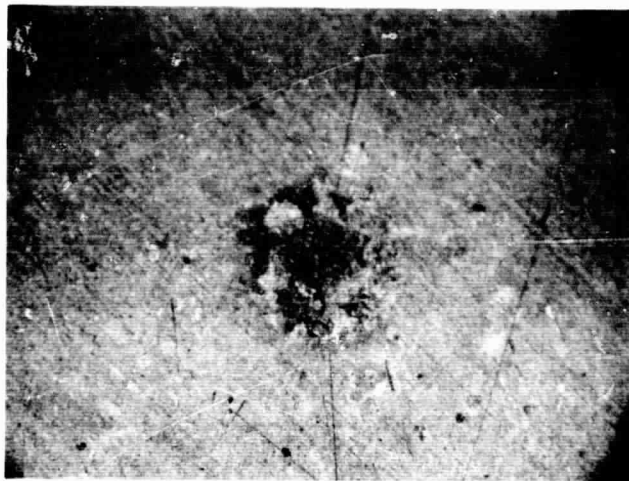


c) 75 x Mag

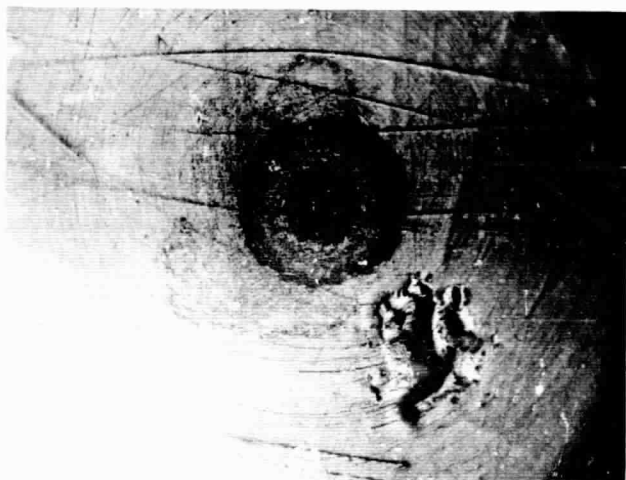
Fig. 81 Photograph of surface damage:
M-2 vs M-2; 1000 cps; 400 F; Load, 15#;
Radius, .375"; Pitch, 1.7 mil/in;
Roll, .59 mil/in; Yaw, .25 mil/in.



a) Radius .375"
Temp. 400 F



b) Radius .375"
Temp. 1000 F

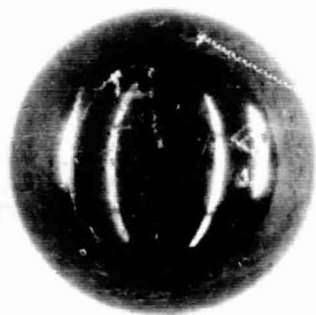


c) Radius .750"
Temp. 400 F

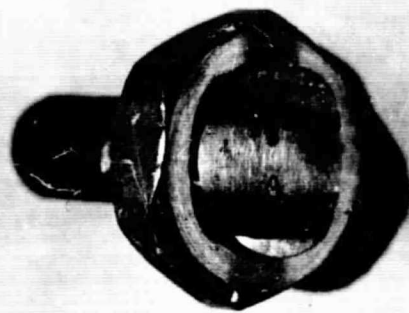


d) Radius .750"
Temp. 1000 F

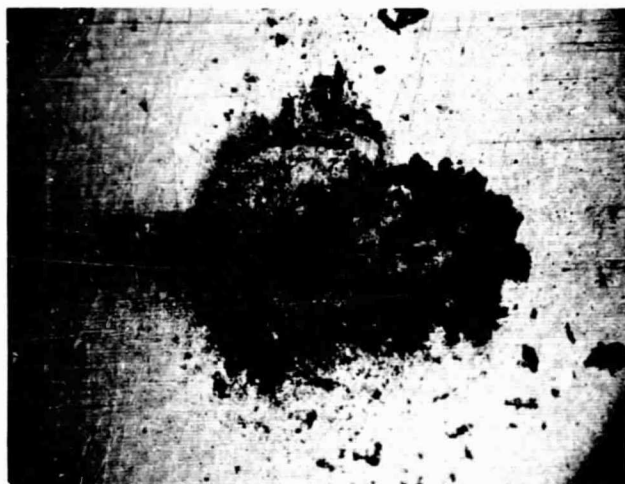
Fig. 82 Photograph of surface damage:
M-2 vs M-2; 1000 cps; Pitch, 1.7 mil/in;
Roll, .59 mil/in; Yaw, .25 mil/in;
Mag 75x



a) Ball
3x Mag

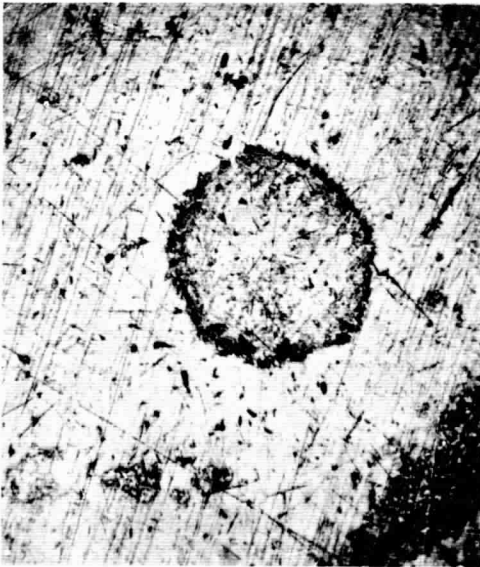


b) Cylindrical Socket
3x Mag

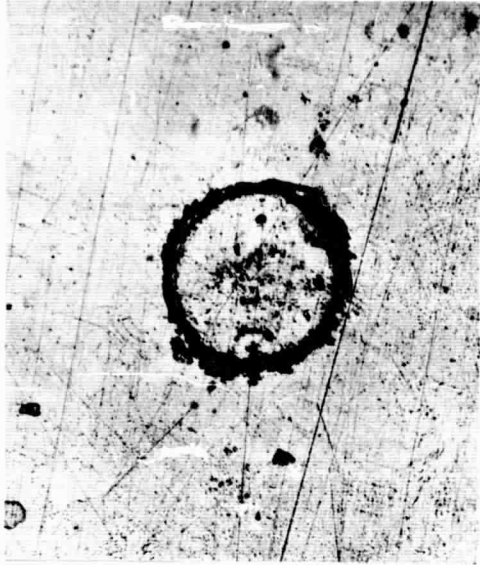


c) Socket
75x Mag.

Fig. 83 Photograph of surface damage:
M-2 vs M-2; Radius, .256 cylinder;
Temp. 1000 F; Load, 15#; Pitch, 1.7 mil/in;
Roll, .59 mil/in; Yaw, .25 mil/in.



a) Ball



Flat



b) Ball



Socket (radius .375")

Fig. 84 Photograph of the surface damage for the tool steel-tool steel Combination after 12 hour operation in forming gas at 500F. 100x Mag



a) Ball



b) Ball

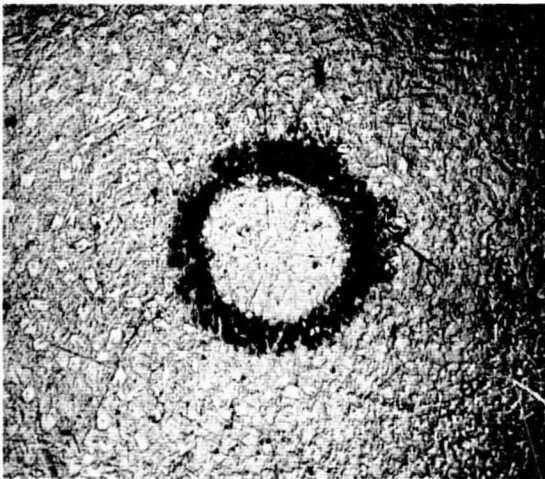


Flat

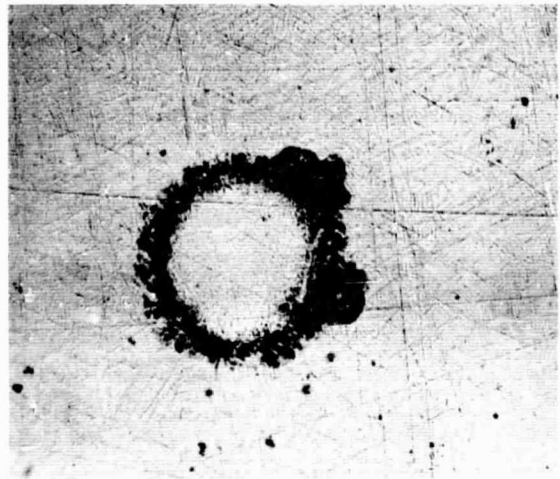


.375R Socket

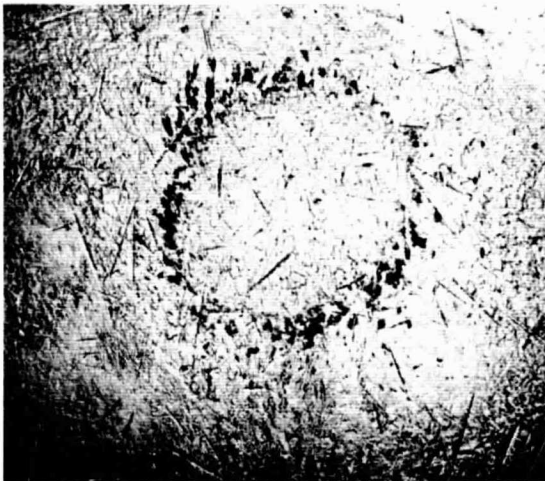
Fig. 85 Photographs of the surface damage for the tool steel-tool steel
Combination after running 12 hours in forming gas at 900°F
Mag 100x



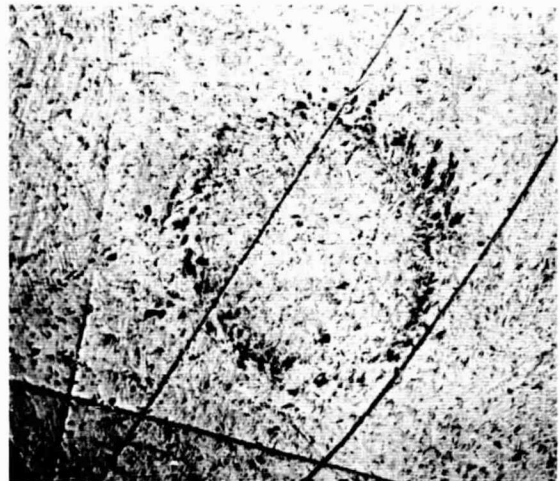
a) Stellite Star J Ball



Stellite 19 Flat

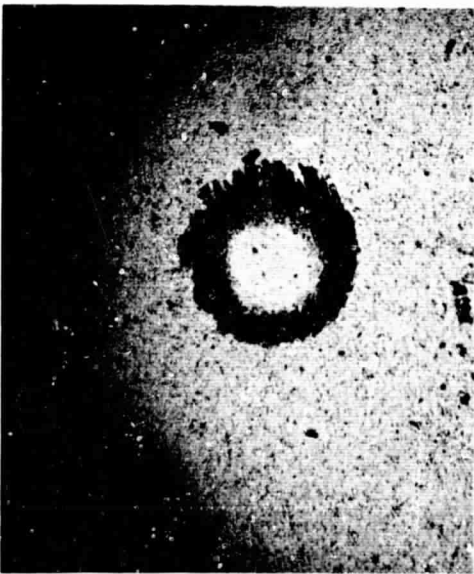


b) Stellite Star J Ball

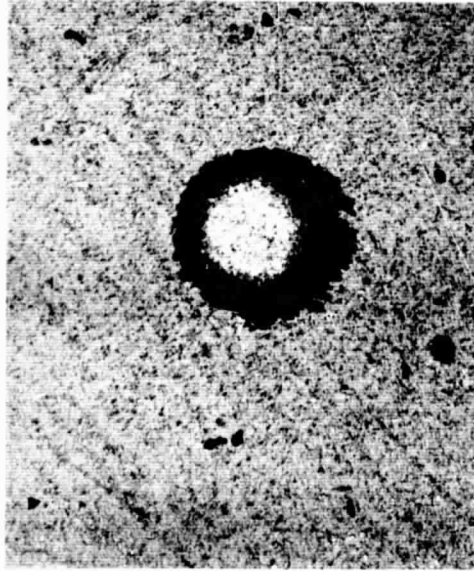


Stellite 19 Socket (.375R)

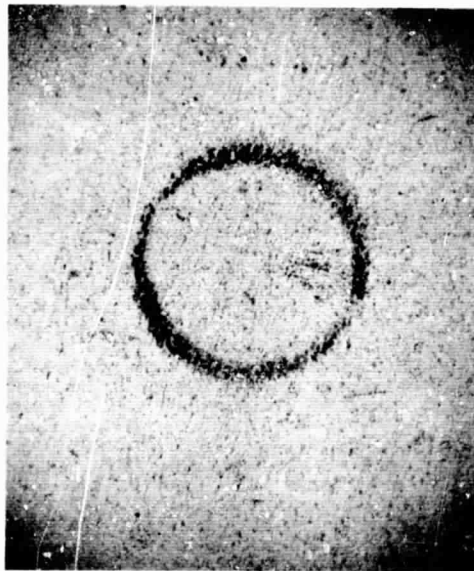
Fig. 86 Photographs of the surface damage for the Stellite-Stellite Combinations after 12 hours running in forming gas at 900F. Mag 100x



a) Ball



Flat

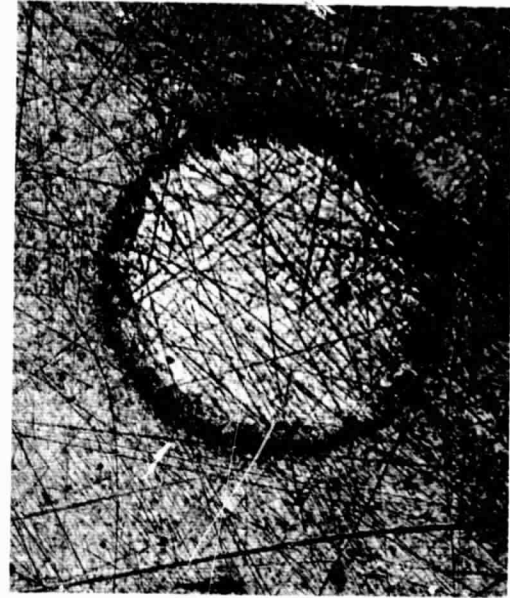


b) Ball



Socket (.375P)

Fig. 87 Photograph of the surface damage for the carbide-carbide (K162B) combination after 12 hours at 900F. Mag 100x.



a) 900°F Ball

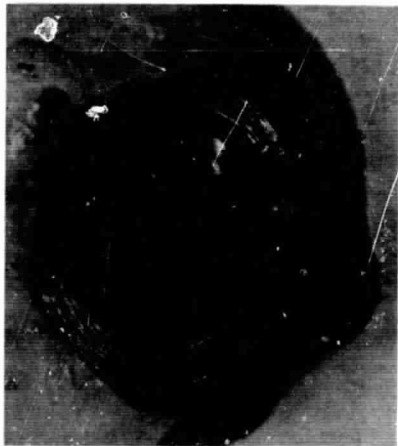
Socket



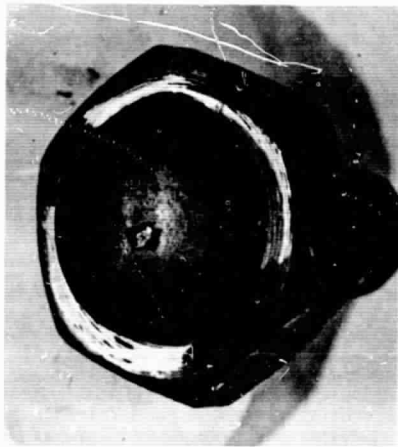
b) 500°F Ball

Socket

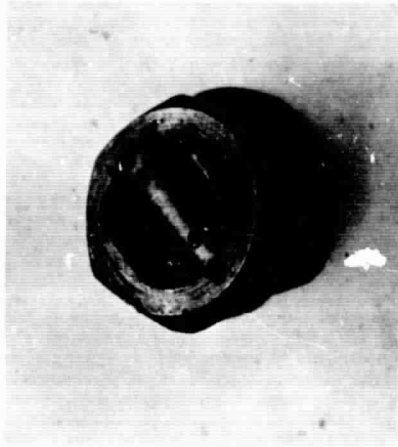
Fig. 88 Photograph of the surface damage for the tool steel-tool steel combination run for 12 hours in air. Specimen shape .250 radius ball vs .375 radius socket. Mag 100x



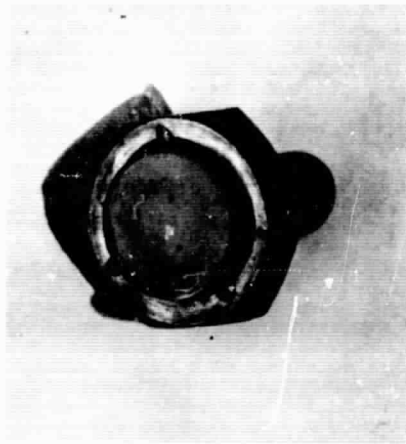
a) .750 Radius Tool Steel



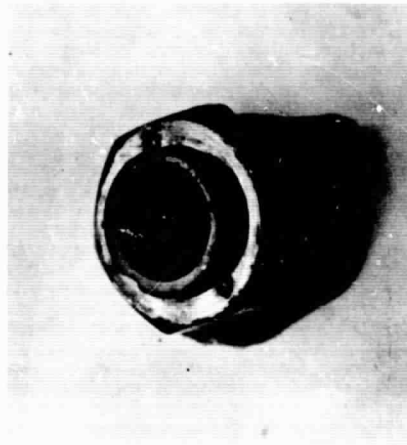
b) .256 Radius Tool Steel



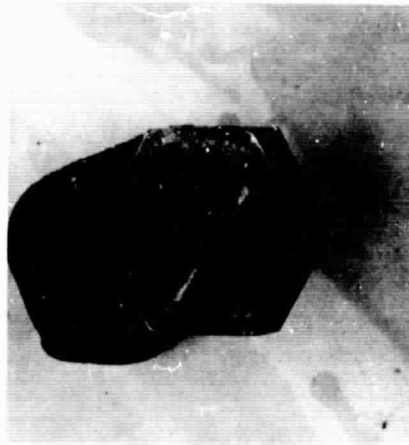
c) .256 Cylinder Tool Steel



d) .750 Radius Carbide



e) .256 Radius Carbide



f) .256 Cylinder Carbide

Fig. 89 Photographs of the surface damage of the carbide and tool steel combinations after approximately 2000 hours of testing at 900F.

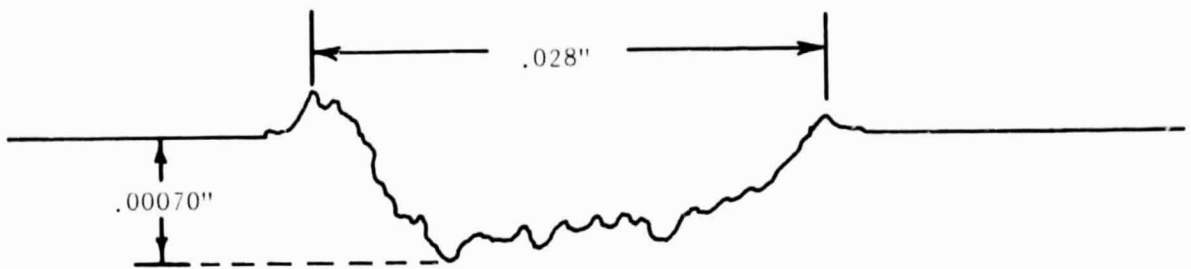
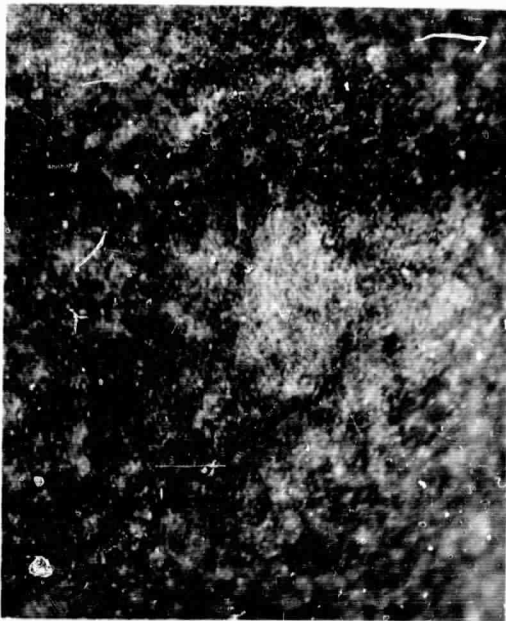
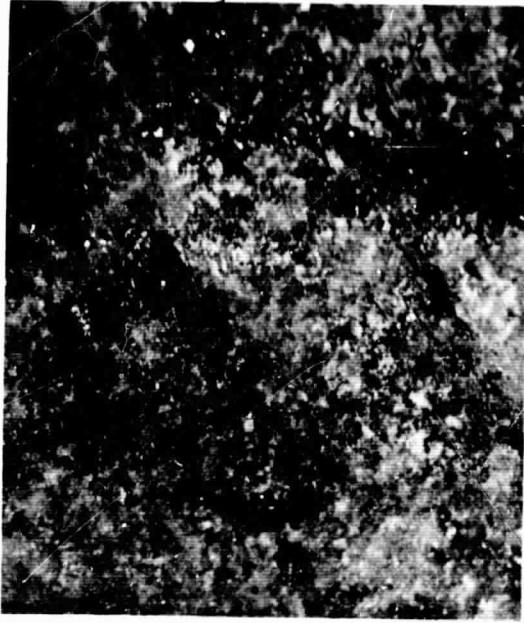


Fig. 90 Talysurf Trace of the Damaged Area
M-2 Tool Steel vs. A-286, 1950 hours



Ball

a) Fused Fluoride

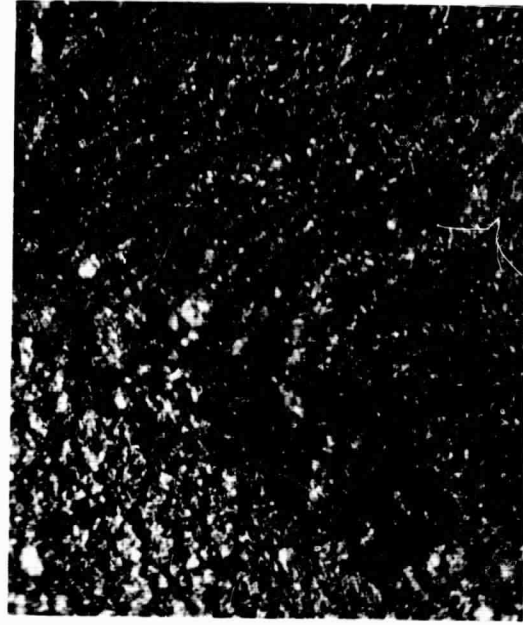


Socket



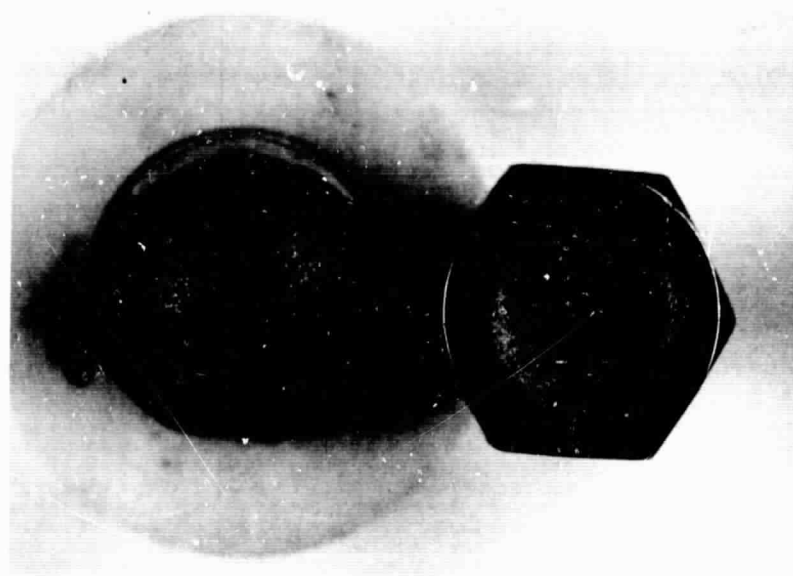
Ball

b) MoS₂ - Silicate



Socket

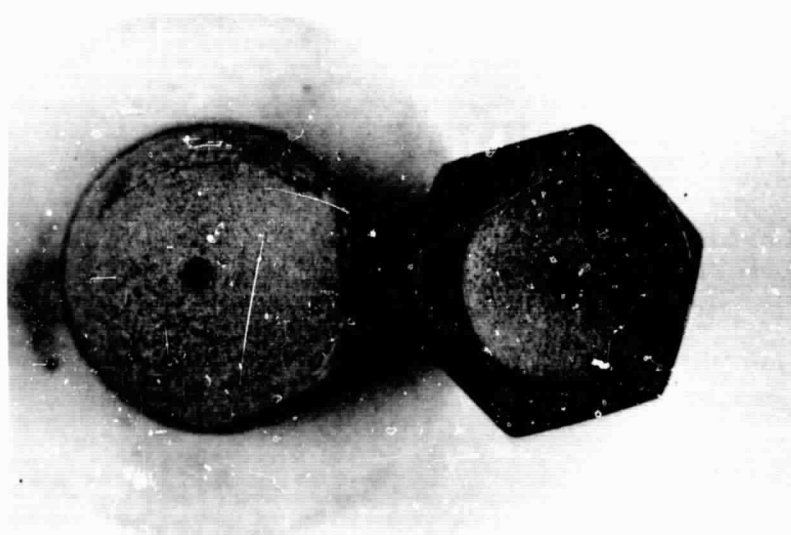
Fig. 91 Photographs of the surface of the Solid Film Lubricants in the contact area after 3.6×10^8 cycles. Temp 500F Mag 200x



Ball

Socket

a) MoS_2 500



Ball

Socket

b) MoS_2 900

Fig. 92 Photographs of the test specimens at the conclusion of the Lubricant tests. Mag. 3x; Time 100 hours; 3.8×10^8 cycles.

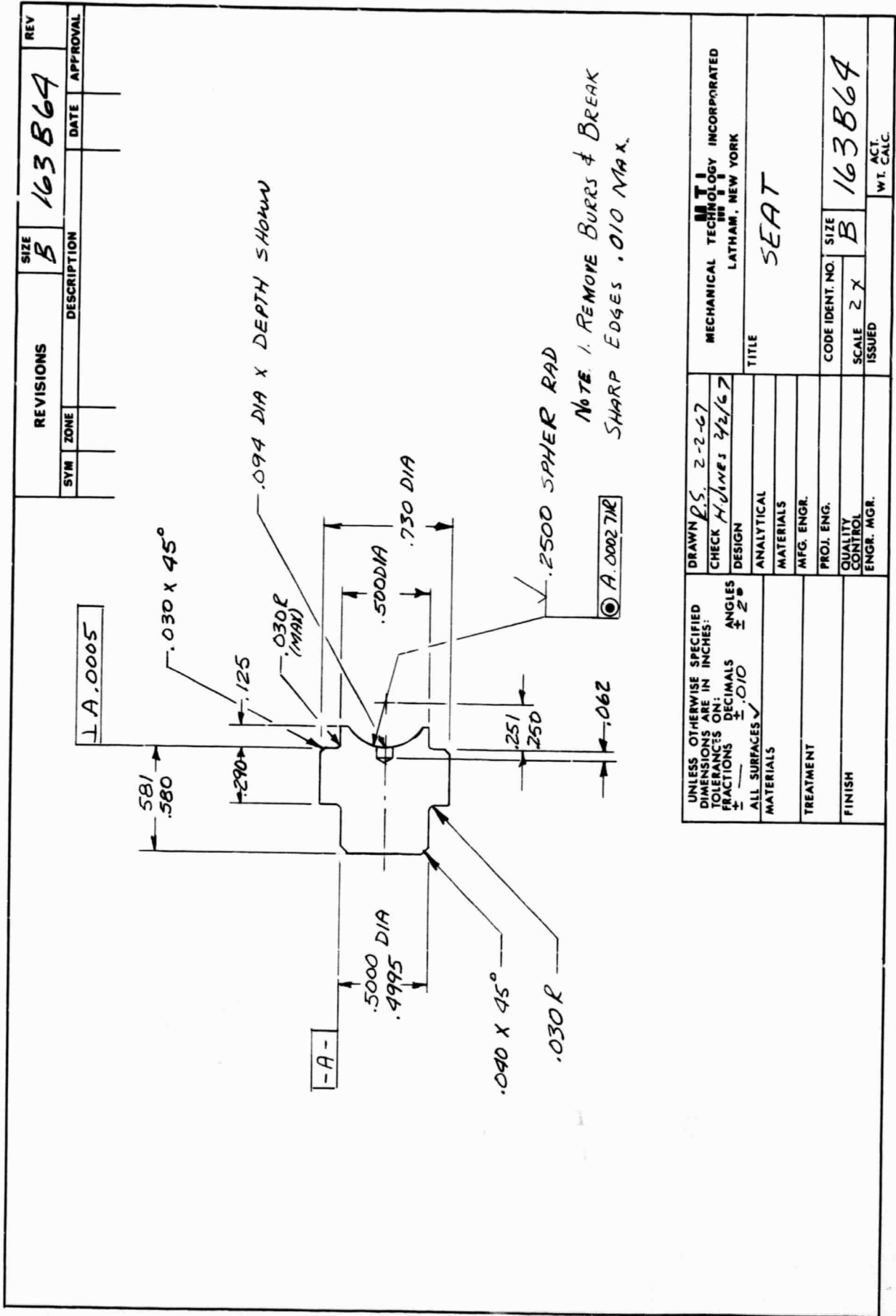


Fig. 93 Drawing of the Conforming Socket

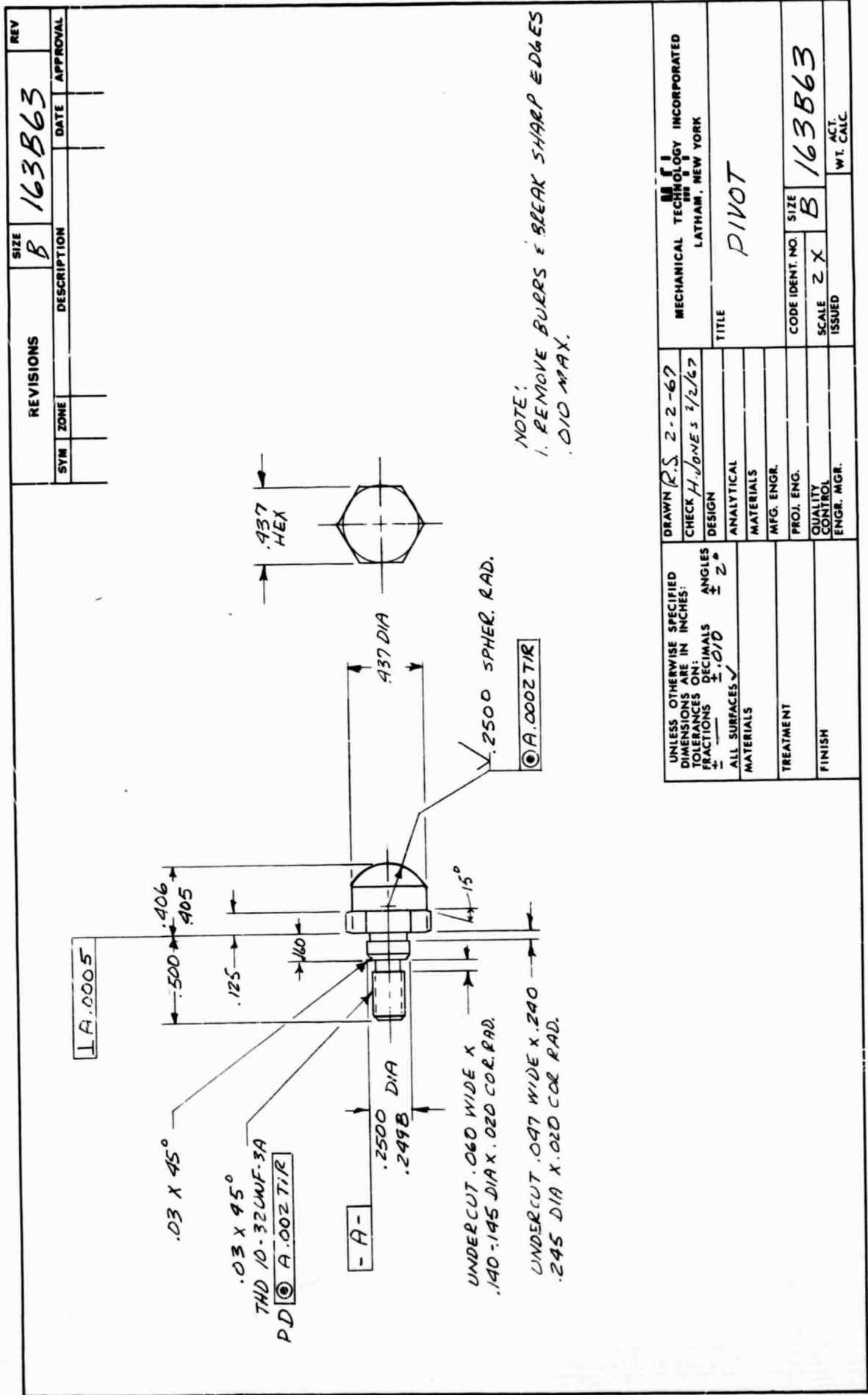


Fig. 94 Drawing of the Conforming Pivot

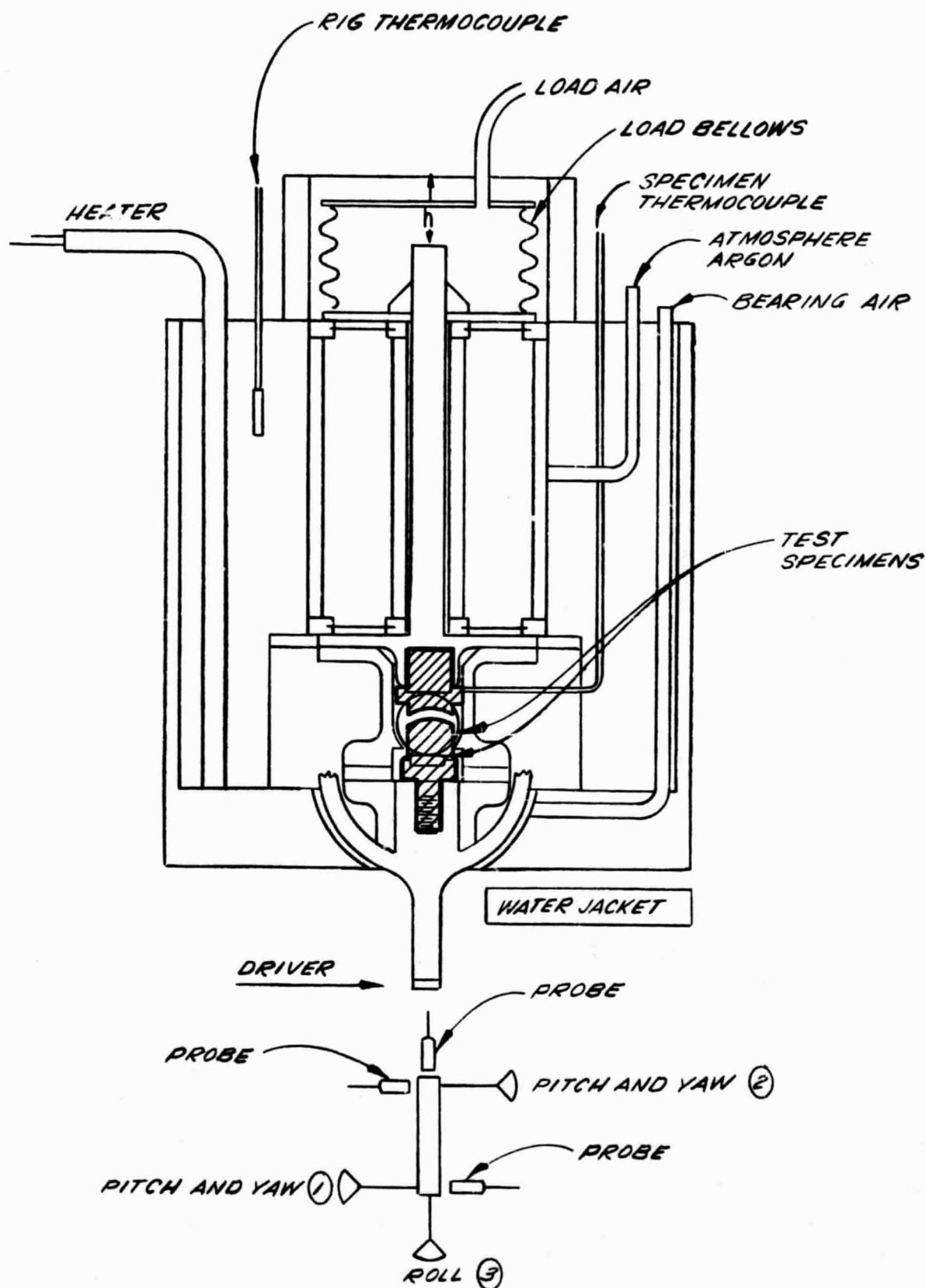
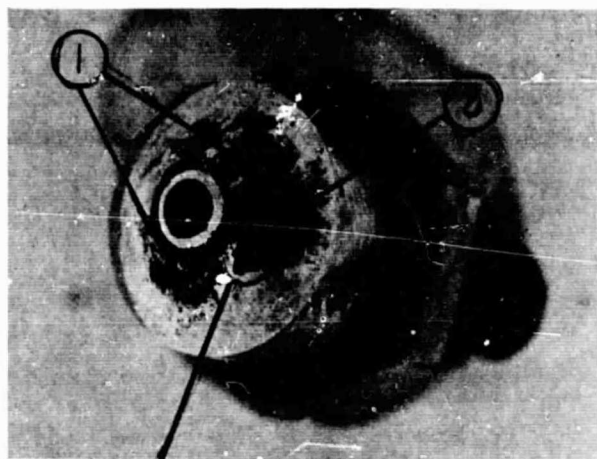


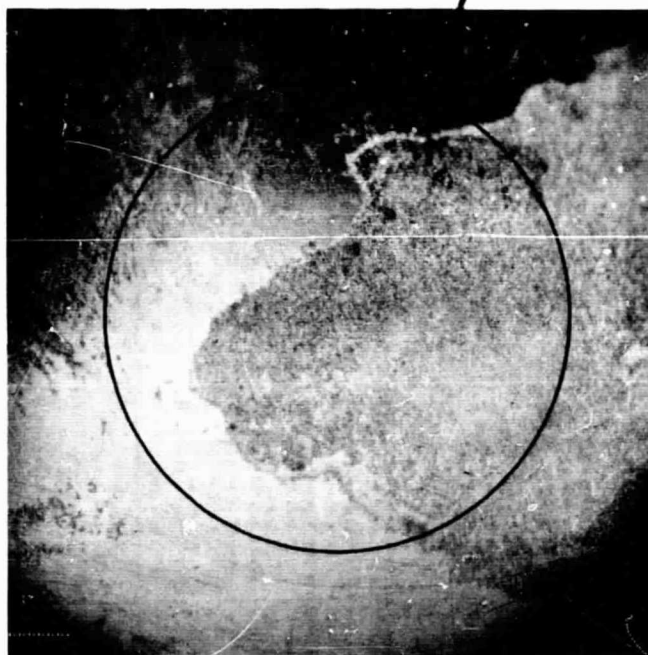
Fig. 95 Schematic of Test Rig



(a) Socket

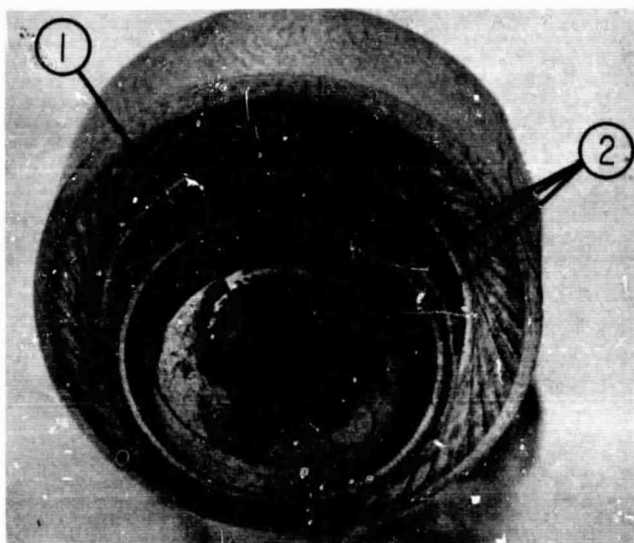


(b) Ball

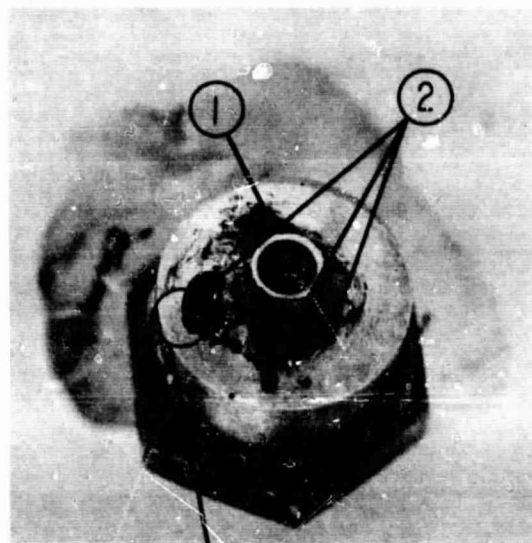


(c) Enlargement of Damage Area on Ball

Fig. 96 Photographs of the surface damage for tungsten carbide vs. A-286 steel flame sprayed with tungsten carbide; Conforming geometry; Specimen 003



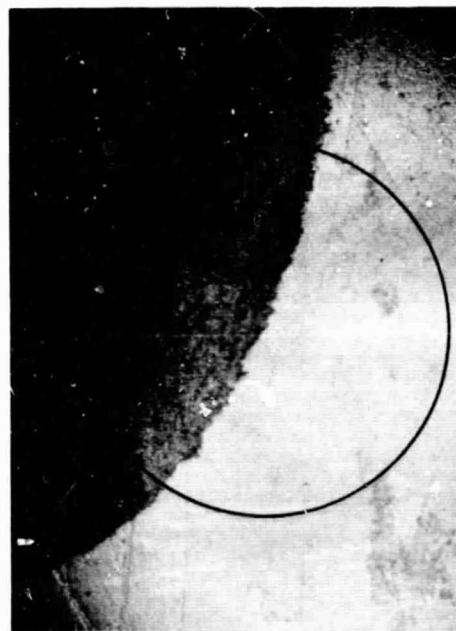
(a) Socket



(b) Ball



(c) Enlargement of Damage Area
in Socket

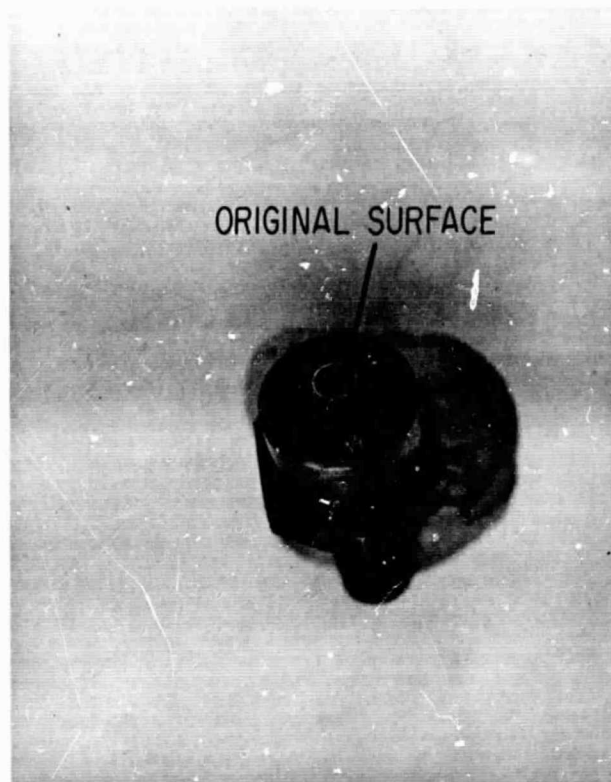


(d) Enlargement of Damage Area
in Ball

Fig. 97 Photographs of the surface damage for tungsten carbide vs. A-286 steel flame sprayed with tungsten carbide; Conforming geometry; Specimen 004

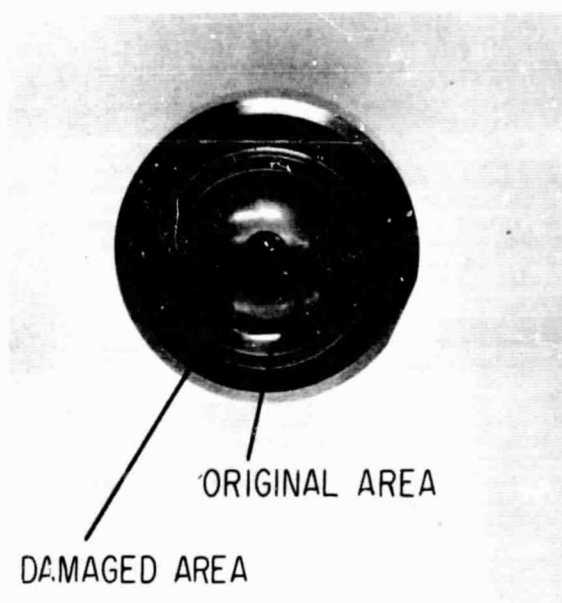


(a) Socket

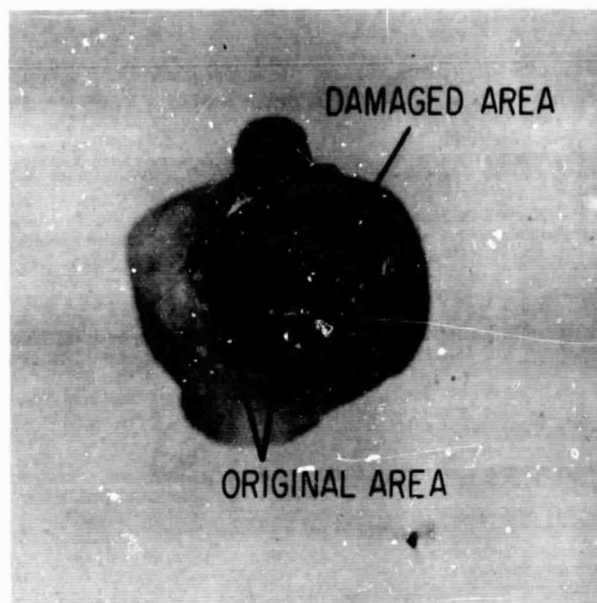


(b) Ball

Fig. 98 Photographs of the surface damage for tungsten carbide vs. A-286 steel flame sprayed with tungsten carbide; Conforming geometry; Continuation of Specimen 003; Mag 3x.



(a) Socket



(b) Ball

Fig. 99 Photographs of the surface damage for tungsten carbide vs. A-286 steel flame sprayed with tungsten carbide; Conforming geometry; Specimen 004; Mag. 3x.

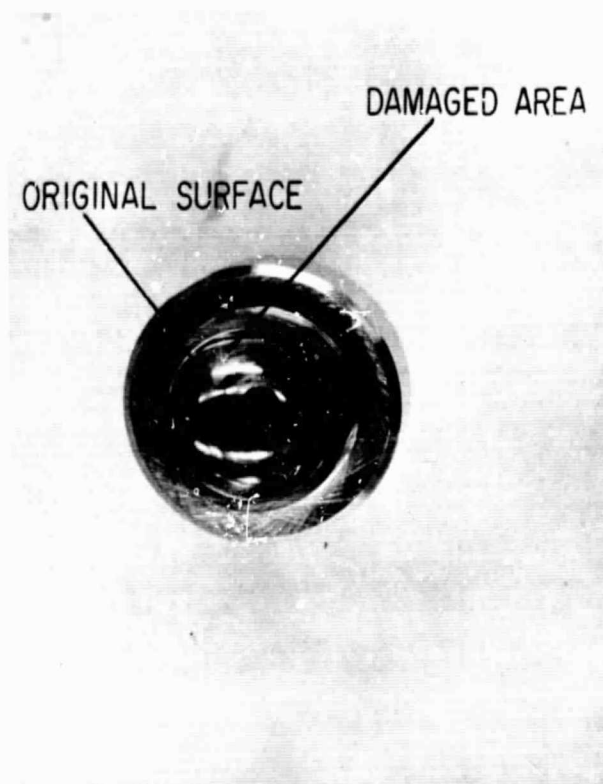


(a) Socket

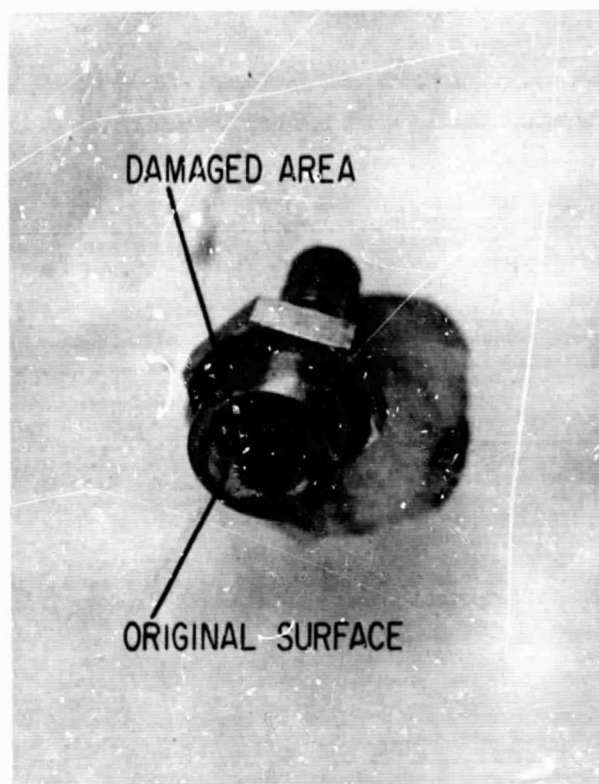


(b) Ball

Fig. 100 Photographs of the surface damage for tungsten carbide vs. A-286 steel flame sprayed with tungsten carbide; Conforming geometry; Specimen 005; Mag. 3x.



(a) Socket



(b) Ball

Fig. 101 Photographs of the surface damage for tungsten carbide vs. A-286 steel flame sprayed with tungsten carbide; Conforming geometry; Specimen 001; Mag. 3x.

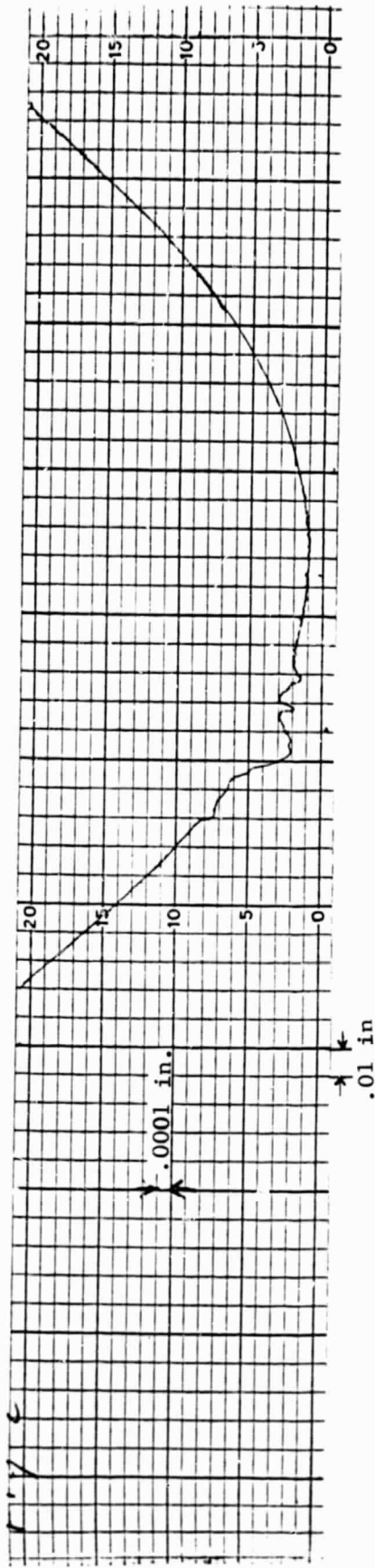


Fig. 102 Talysurf Trace of the SOCKET Using the Straight Line Datum Attachment
(004 Specimen Set)

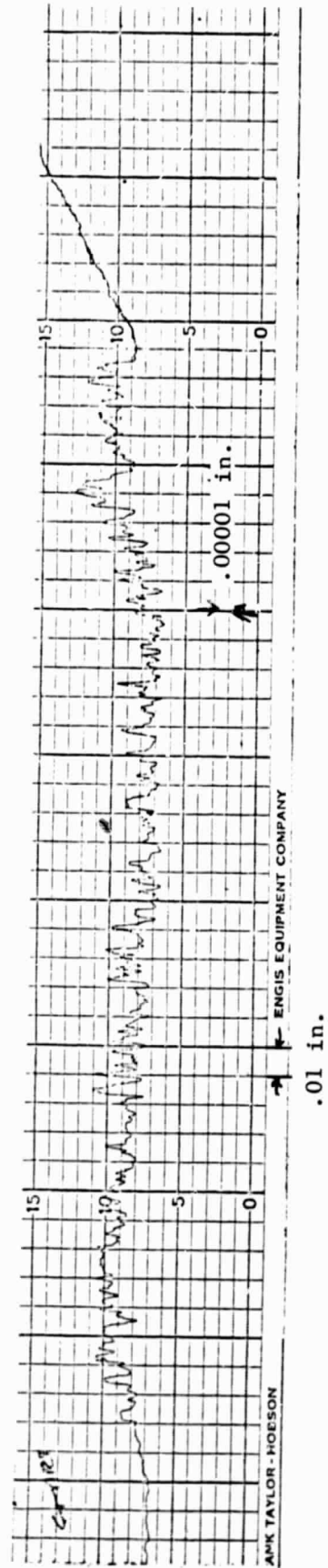
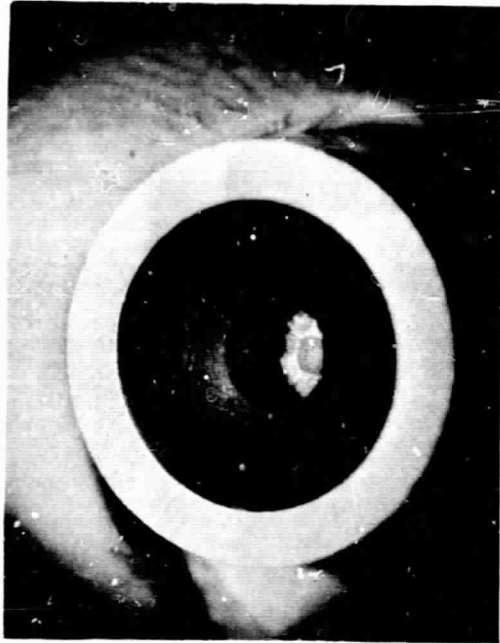
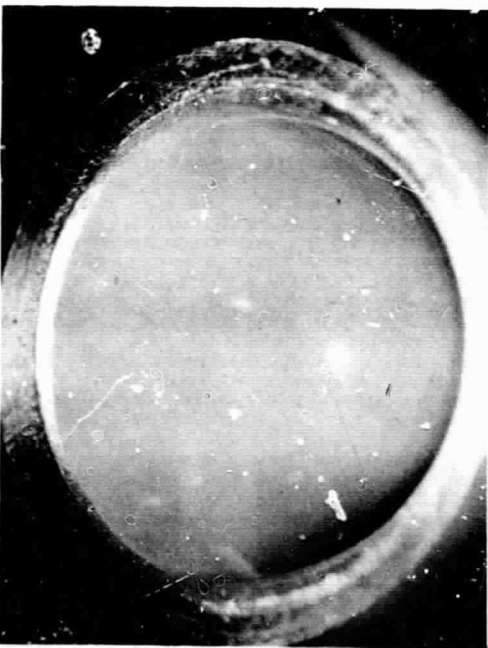
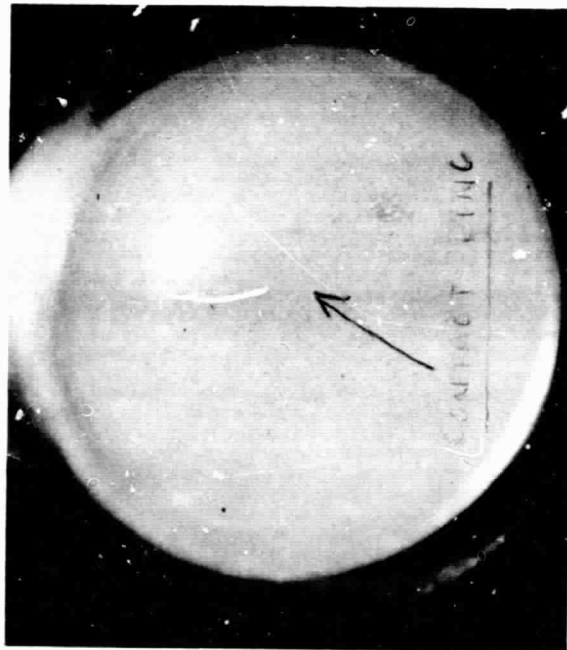


Fig. 103 Talysurf Trace of the Surface of the Ball Specimen Using the Curved Datum
Attachment (004 Specimen Set)

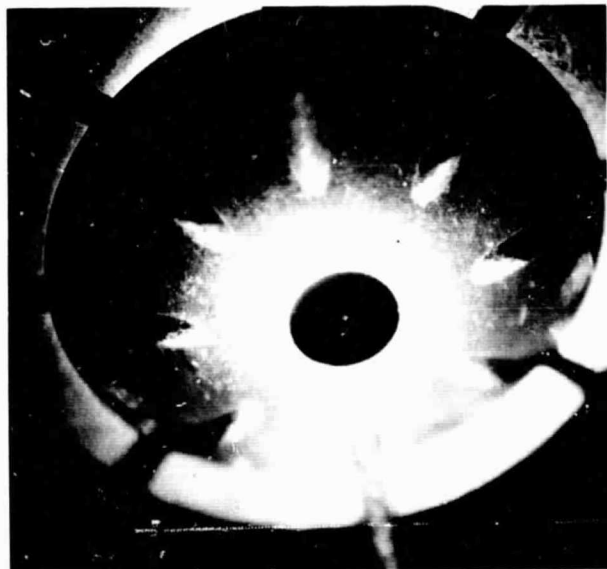
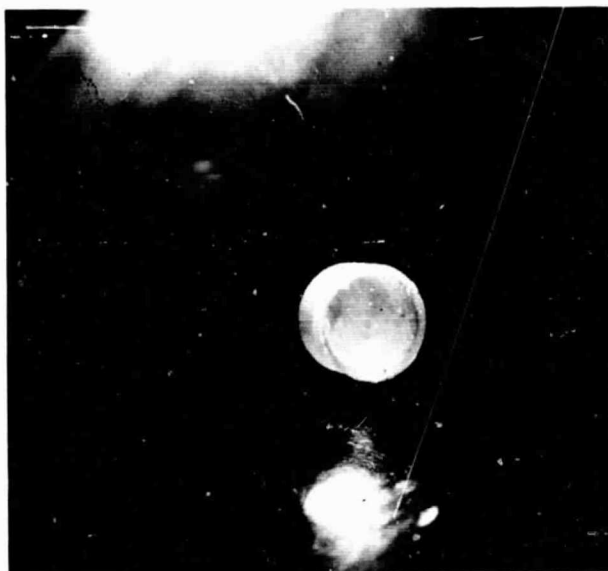


a) Before Test

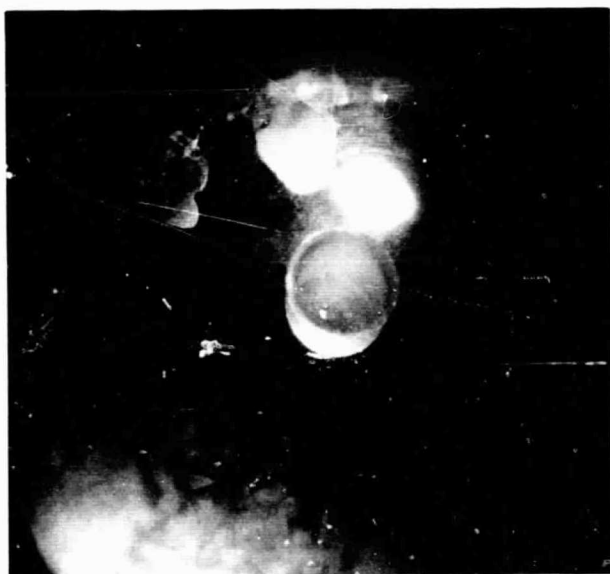


b) After 100 Hour Test

Fig. 104 Photograph of the sapphire vs. tungsten carbide pivot. Specimen No. 1 & 3; Non-conforming geometry; Mag. 6x.



a) Before Test



b) After Test

Fig. 105 Photograph of the sapphire vs. tungsten carbide pivot. Specimen No. B & D; Conforming geometry; Mag 6x.

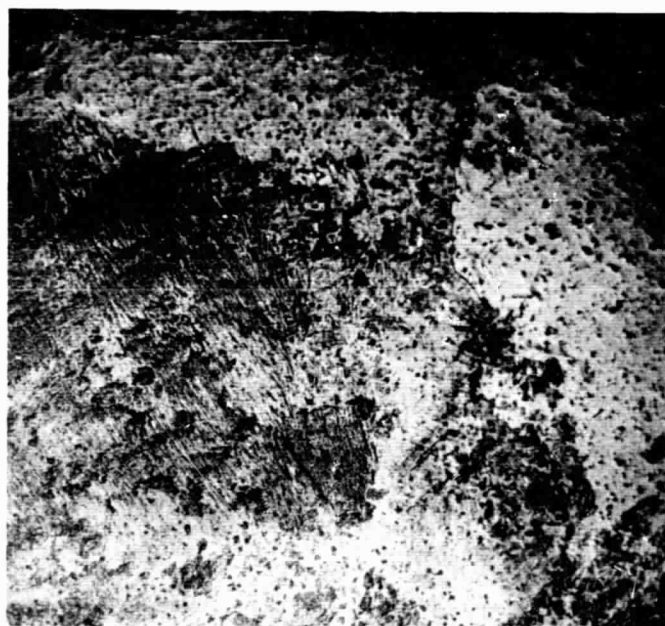
Not Cleaned



a) Hole Edge



b) Groove Edge



c) Socket Surface

Fig. 106 Photograph of the sapphire vs. tungsten carbide pivot. Specimen No. B & D; Conforming geometry; Mag. 100x.

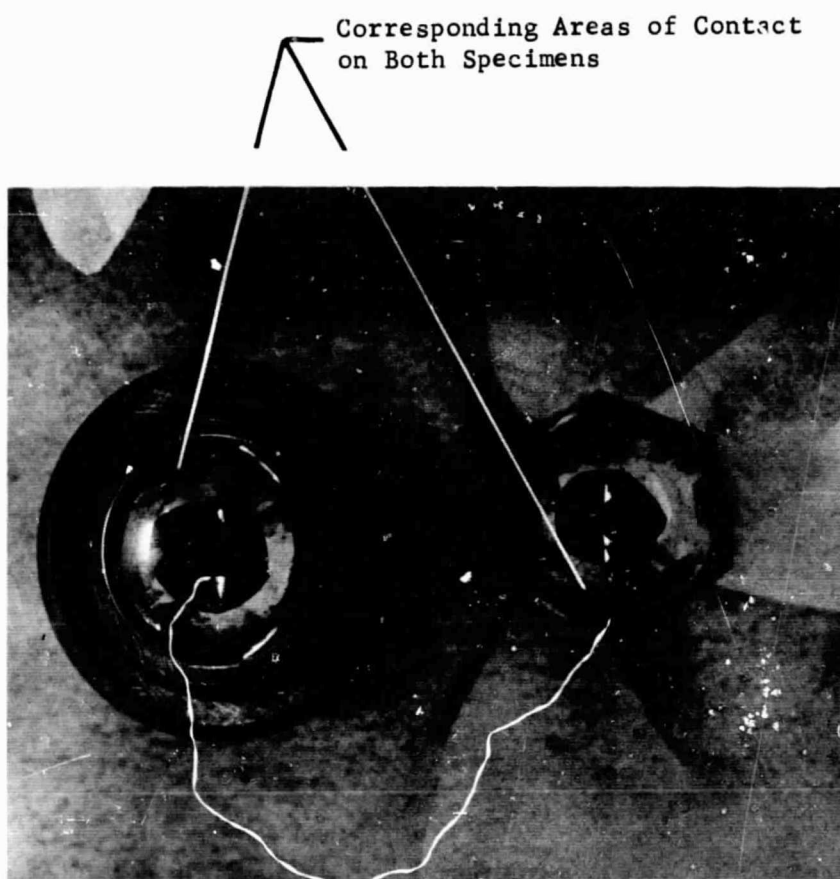


Fig. 107 Photograph of the BRU conforming geometry. Tungsten carbide vs. Tungsten carbide; Specimen No. 113; Mag. 3x.

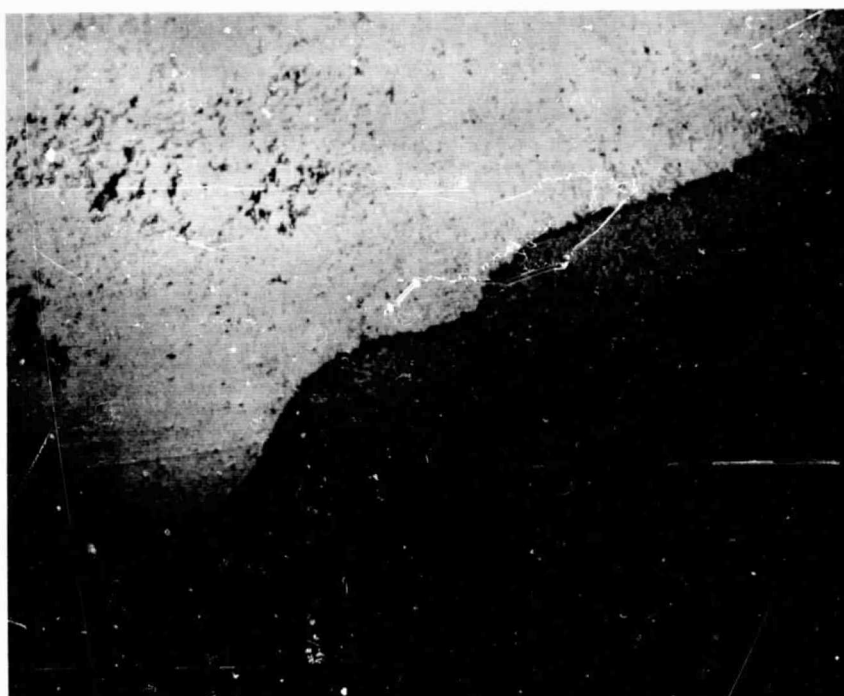


Fig. 108 Photograph of the BRU Conforming Geometry
Tungsten Carbide vs. Tungsten Carbide; Specimen
No. 113; Mag. 100X.

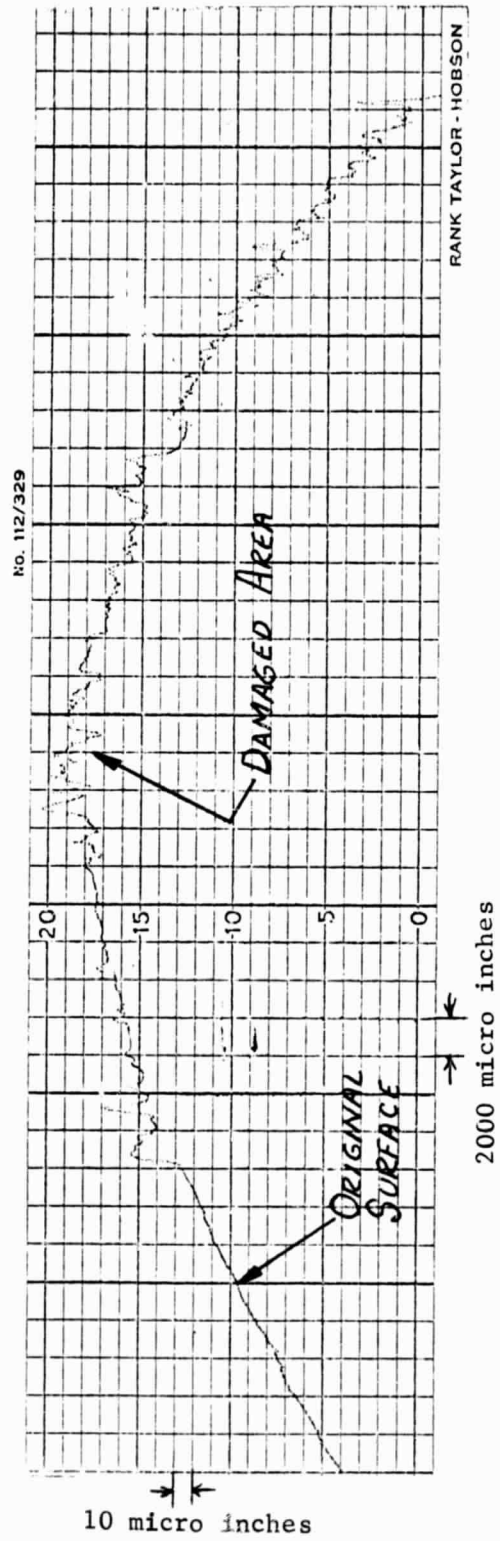
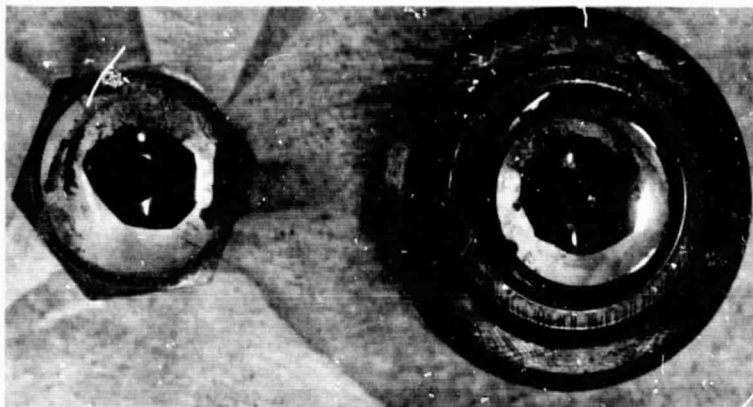
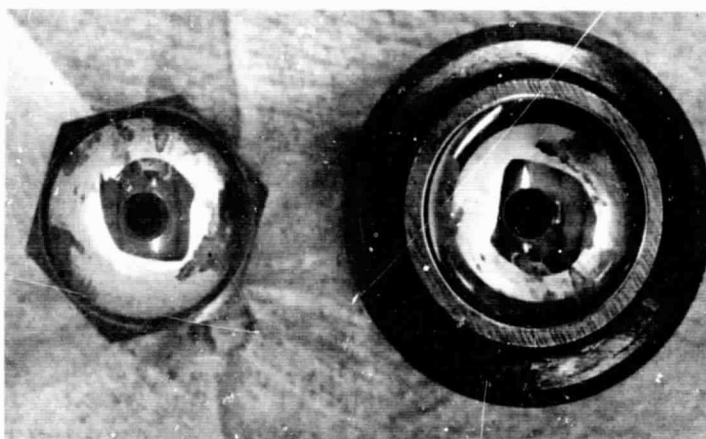


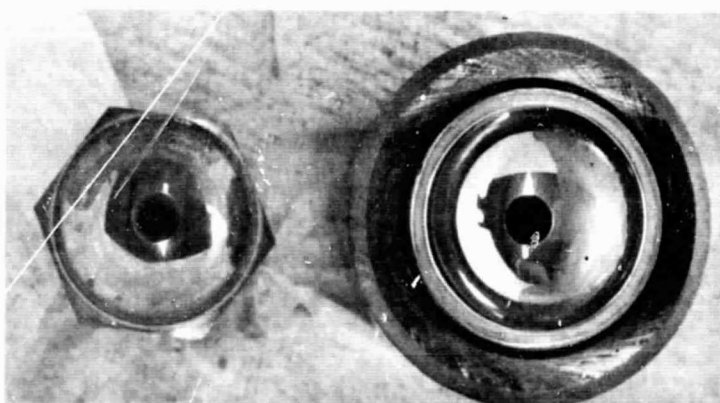
Fig. 109 Talysurf Trace of the 8 x 113 Carbide Ball Specimen After Test



a) Specimen 111



b) Specimen 114

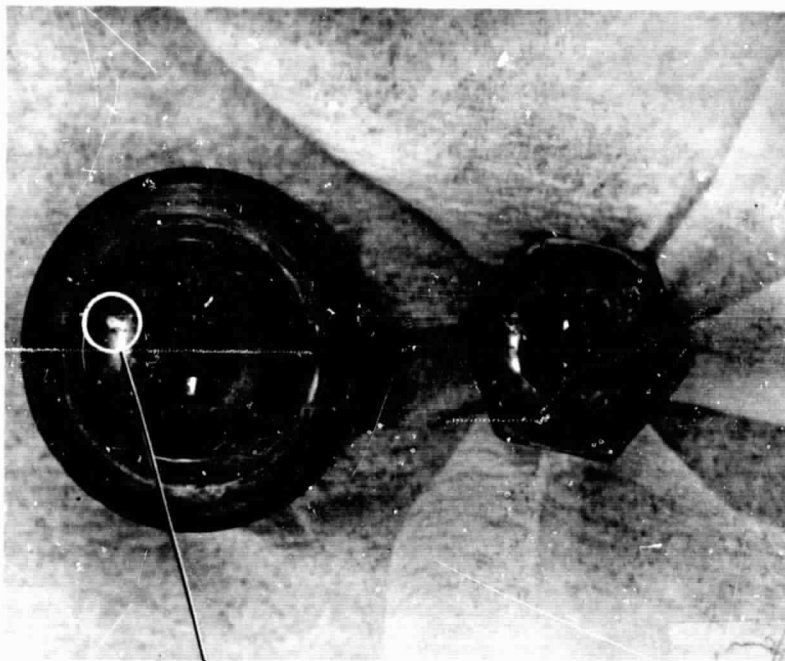


c) Specimen 115

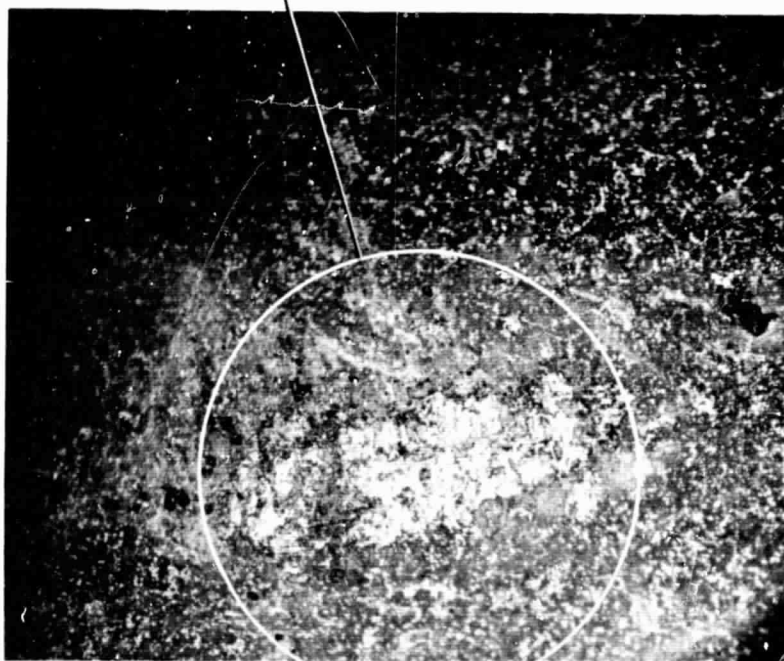
Fig. 110 Photographs of the BRU Conforming geometry. Tungsten carbide vs. Tungsten carbide; Mag. 3x.



Fig. 111 Photographs of the BRU Conforming geometry, Specimen No. 5;
M-2 Tool Steel vs. M-2 Tool Steel; Mag. 3x.

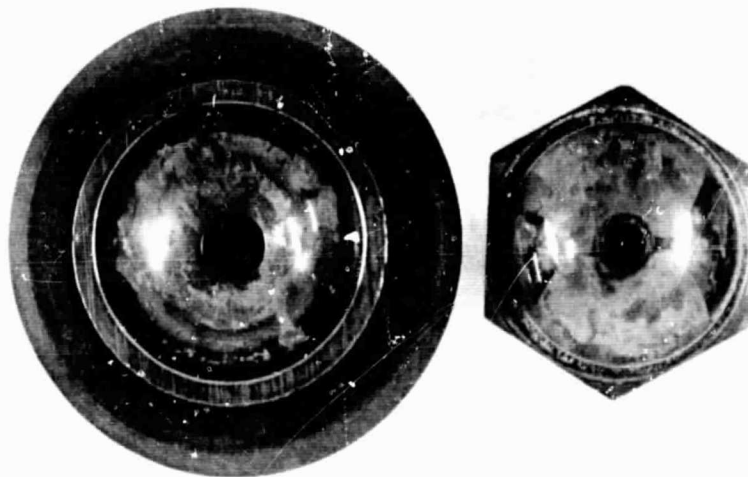


a) Socket and Pivot (3x)

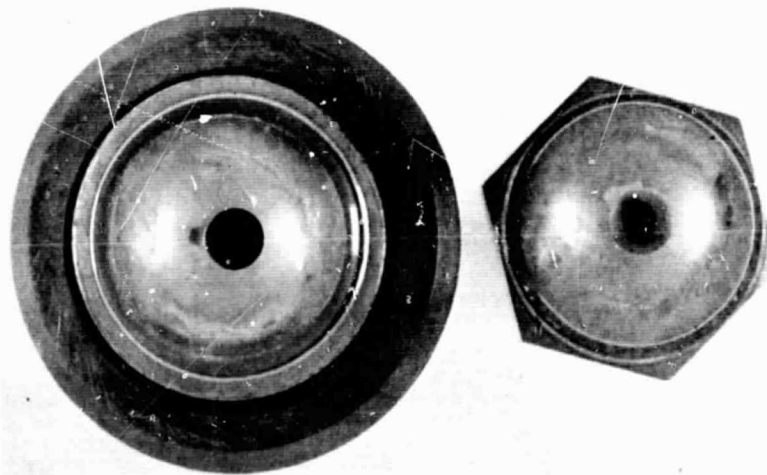


b) Pivot (100x)

Fig. 112 Photographs of the BRU Conforming Geometry; Specimen No. 3; M-2 Tool Steel vs M-2 Tool Steel.

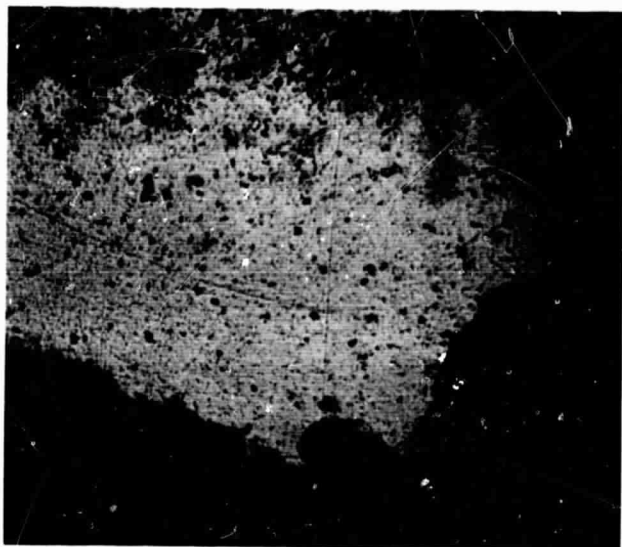


a) 111 Specimen Number

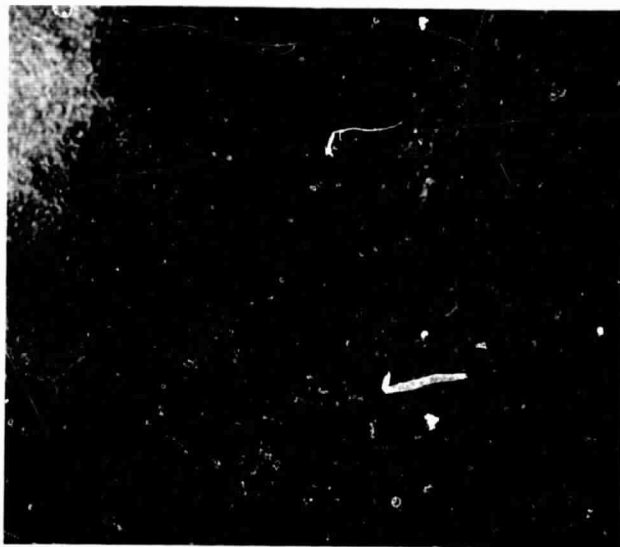


b) 115 Specimen Number

Fig. 113 Photographs of the Carbide BRU Pivot Specimens
After the 1000 Hour Test at 500°F. Mag. 3x.



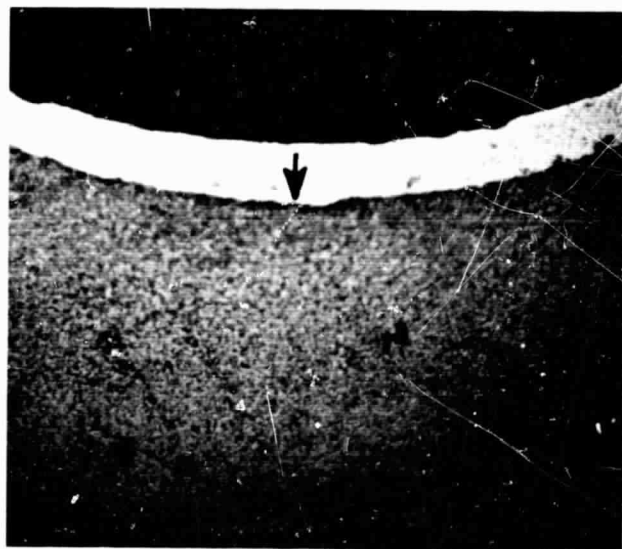
a) Ball



b) Ball



c) Socket



d) Socket Edge

Fig. 114 Microphotographs of the Surface Damage of the 115 Carbide Specimens After 1000 Hours of Testing at 500°F. Mag. 100x.

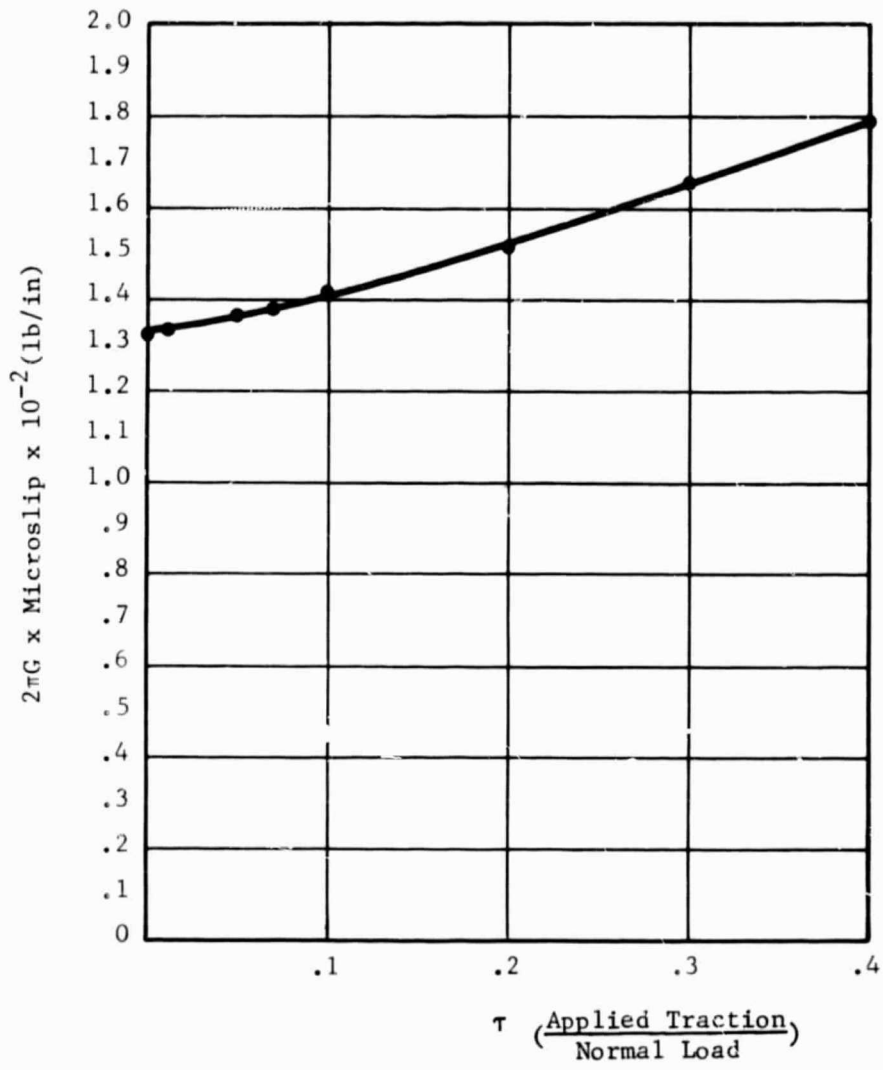


Fig. 115 Effect of τ on Microslip For The Steel - Steel Combination. Load 30 lb.

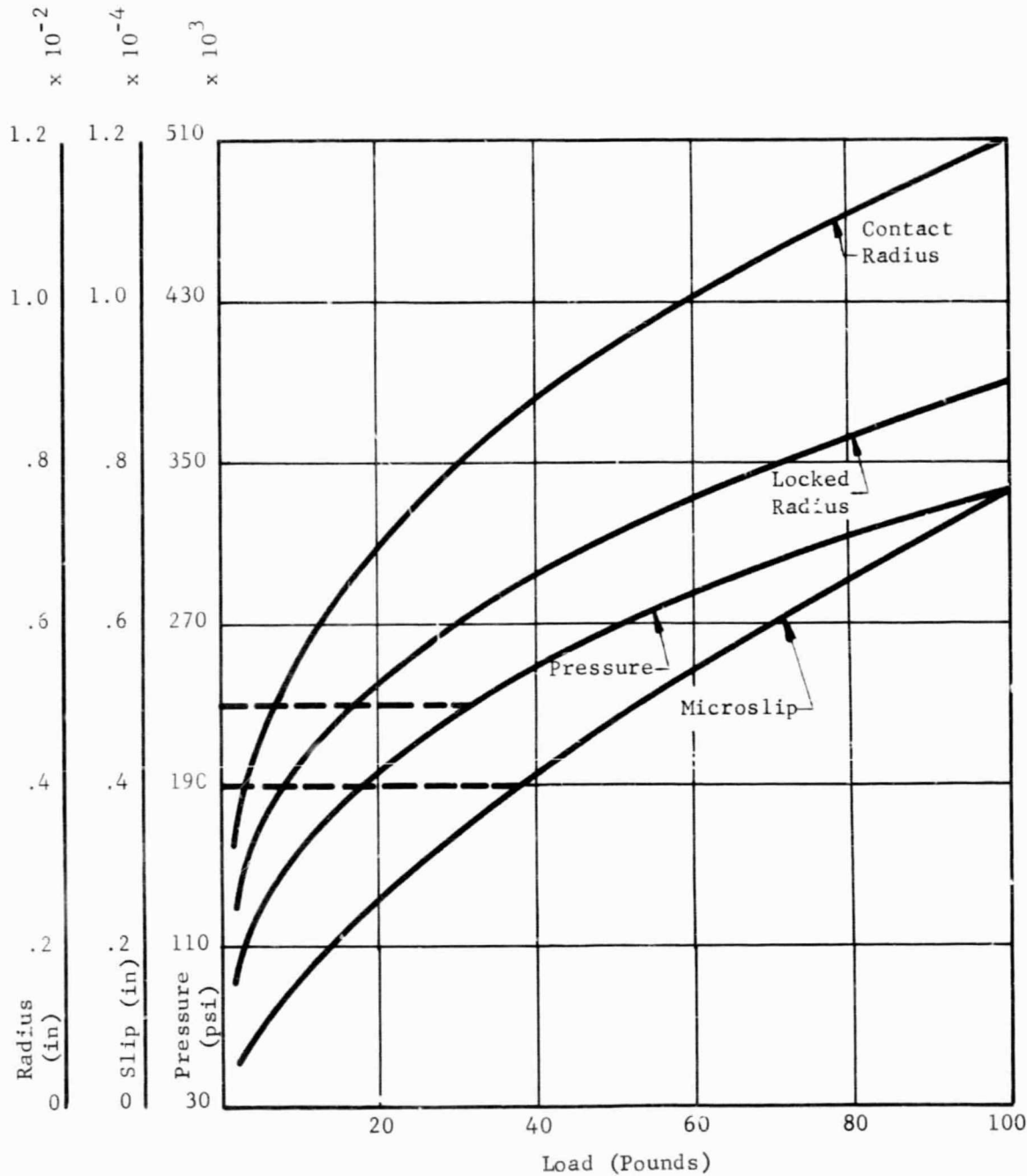


Fig. 116 Pivot Design Curves Steel vs Steel Radius of Pivot: .125"; Radius Socket: .1625"

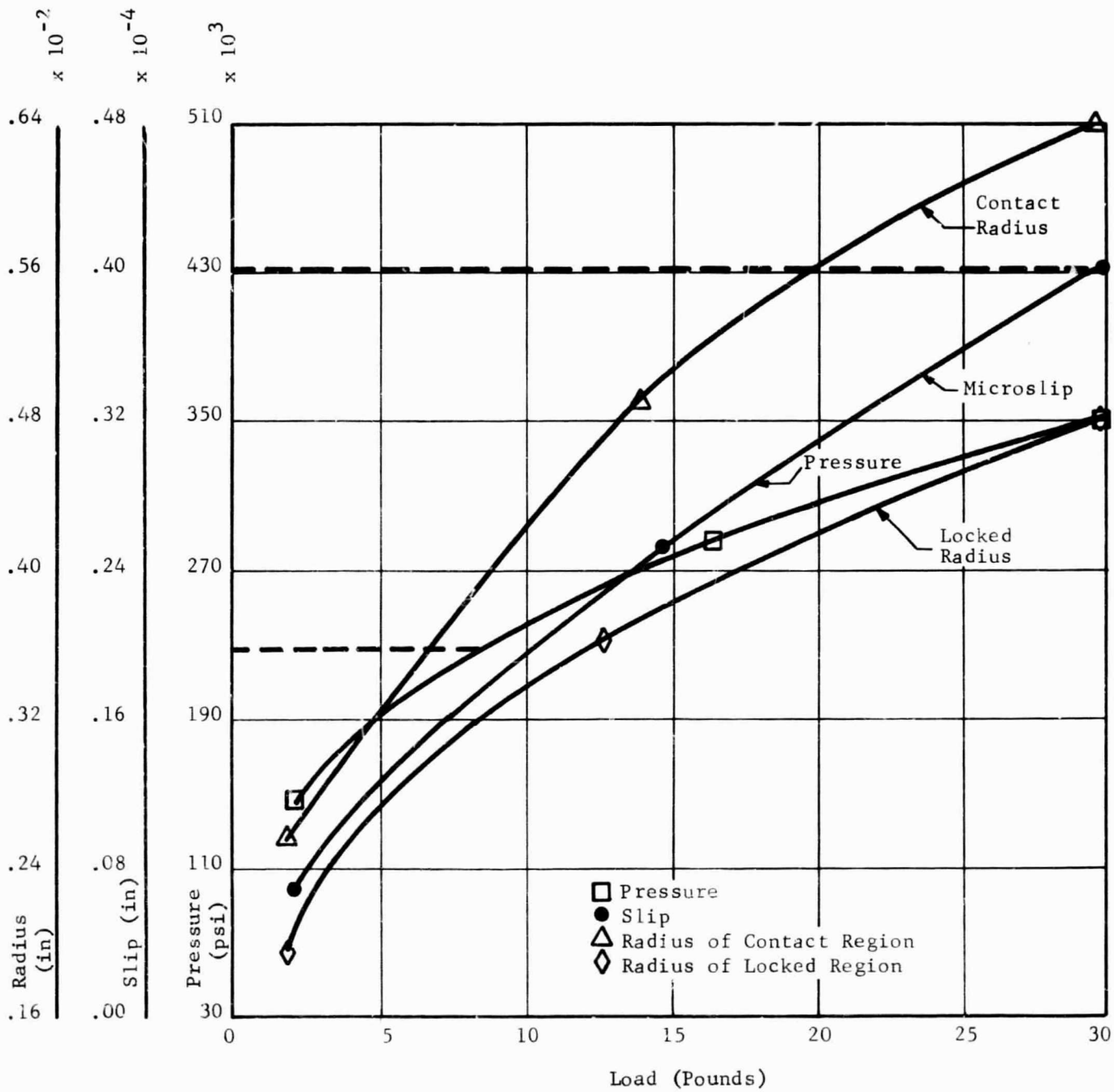


Fig. 117 Pivot Design Curves Kl62B Carbide vs Itself
Radius of Pivot: .125"; Radius of Socket: .1625"

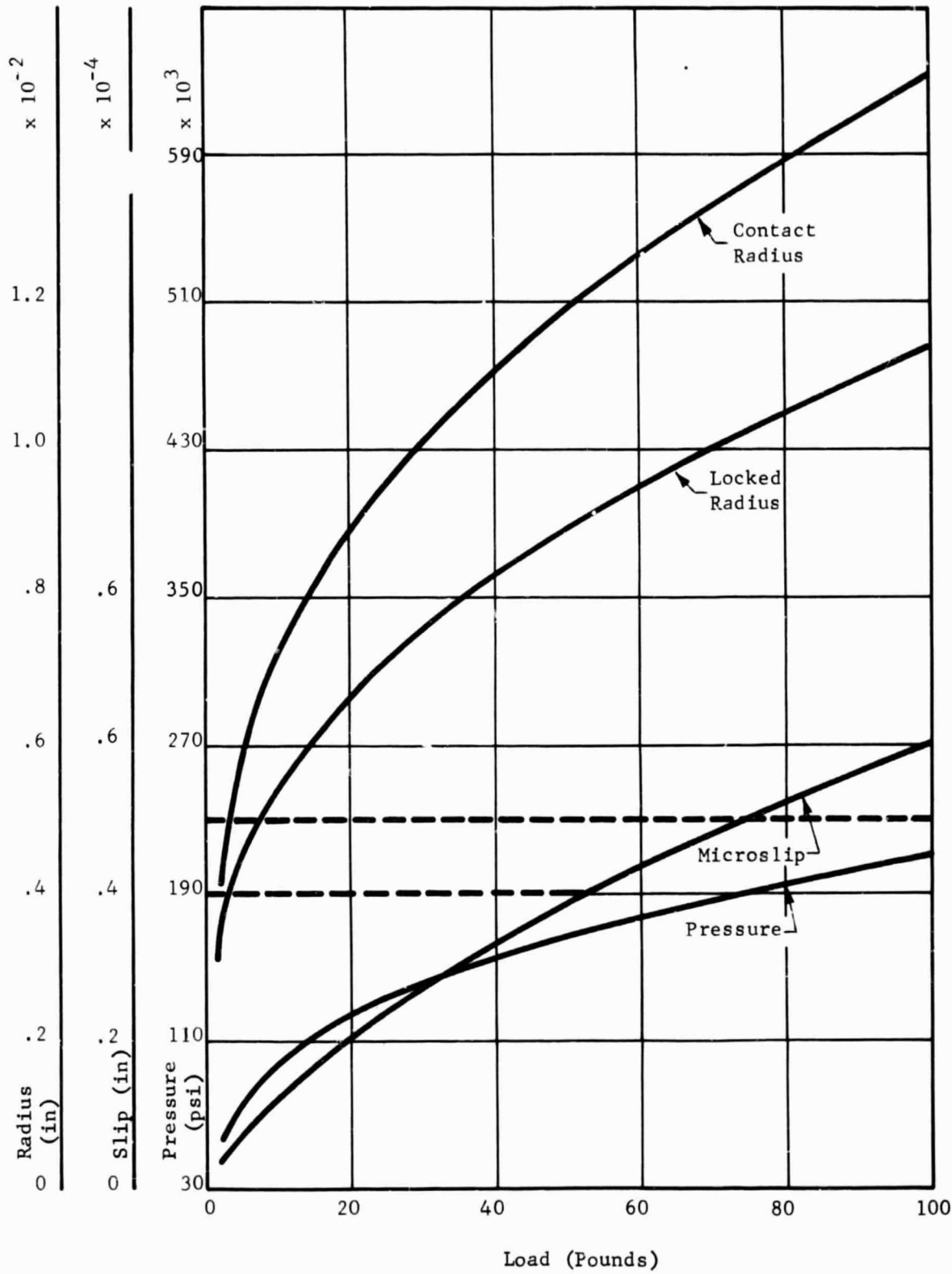


Fig. 118 Pivot Design Curves Steel vs Itself Radius of Pivot: .250"; Radius of Socket: .375"

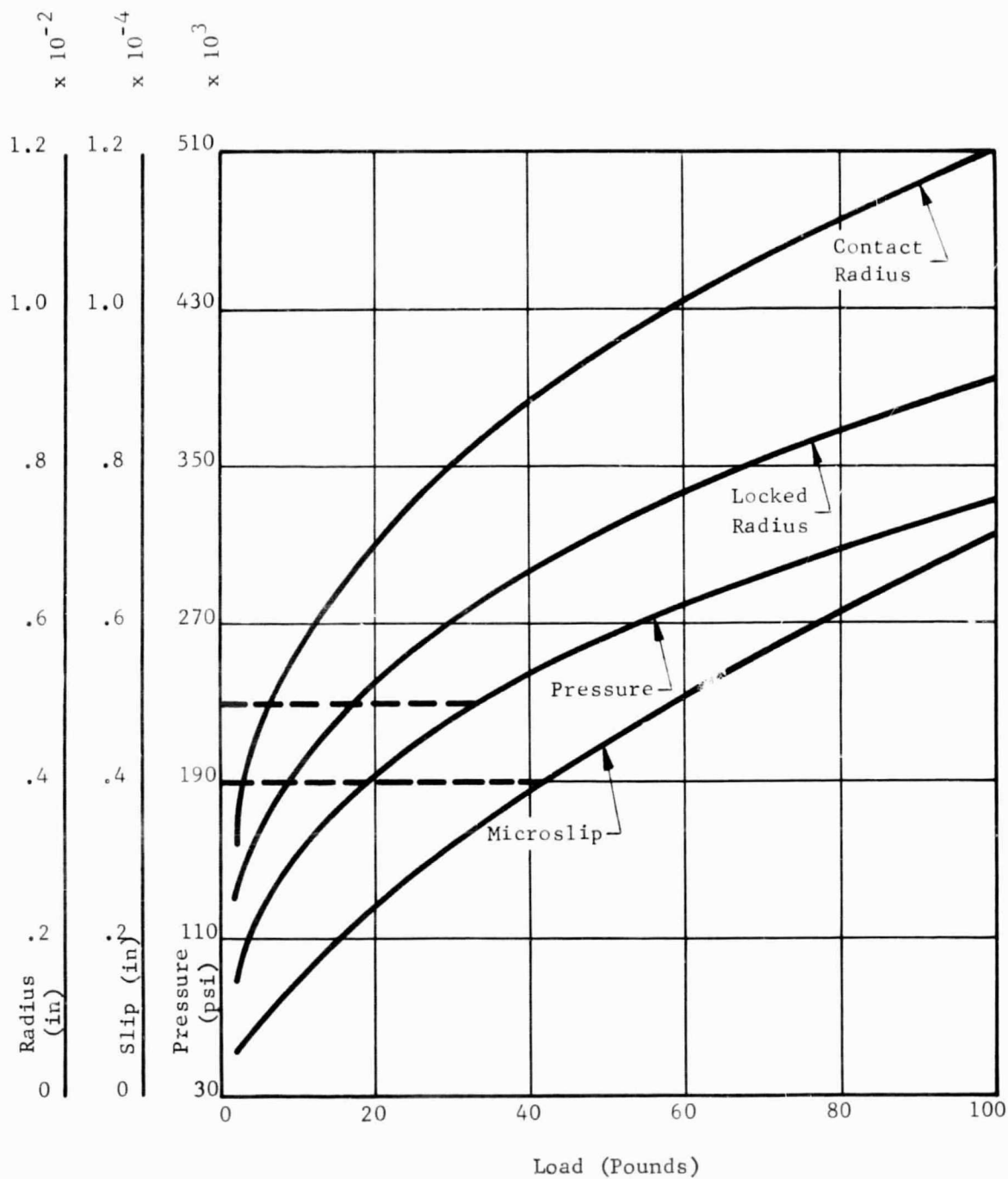


Fig. 119 Pivot Design Curves Kl62B vs Itself
Radius of Pivot: .250"; Radius of Socket: .375"

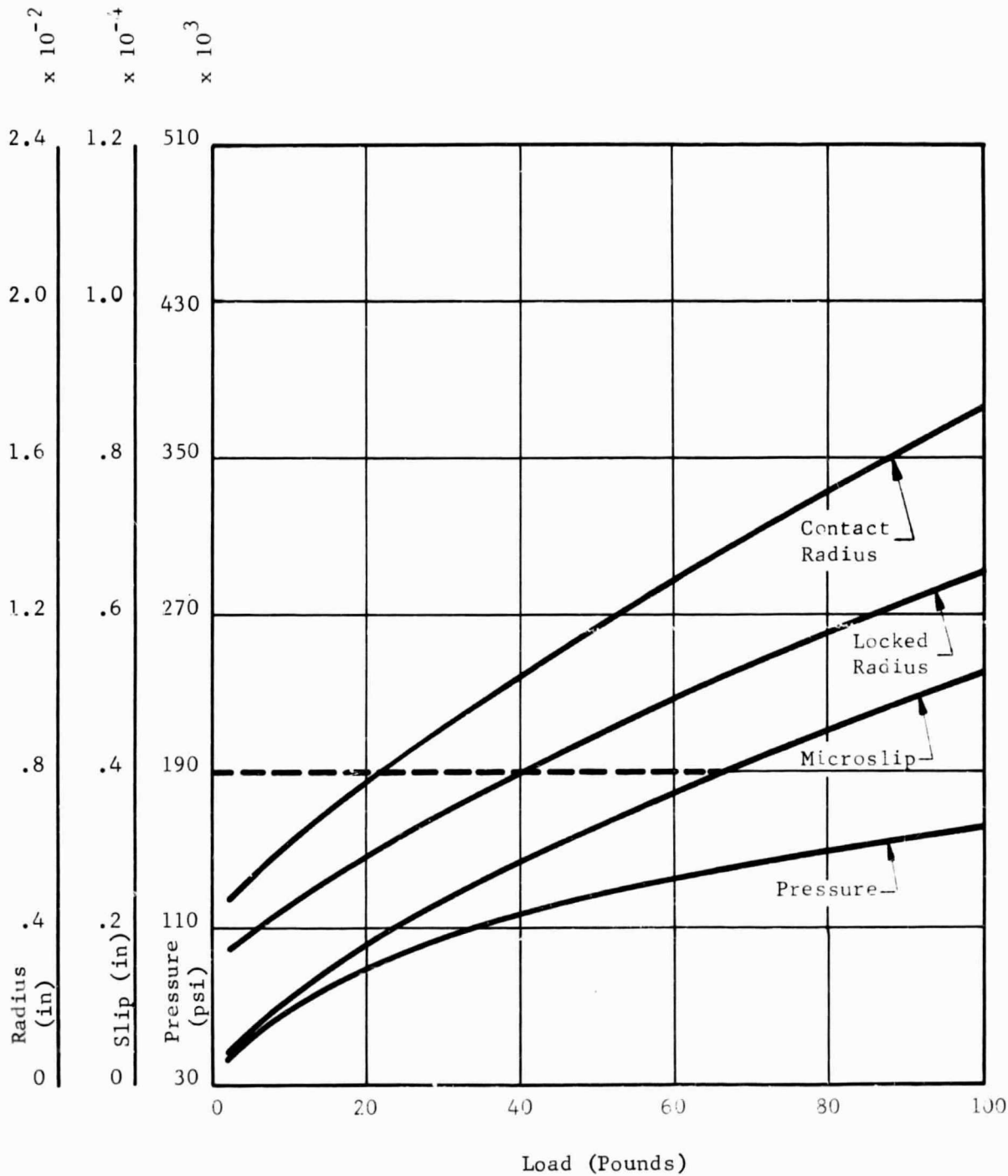


Fig. 120 Pivot Design Curves Steel vs Itself Radius of Pivot: .375"; Radius of Socket: .5625"

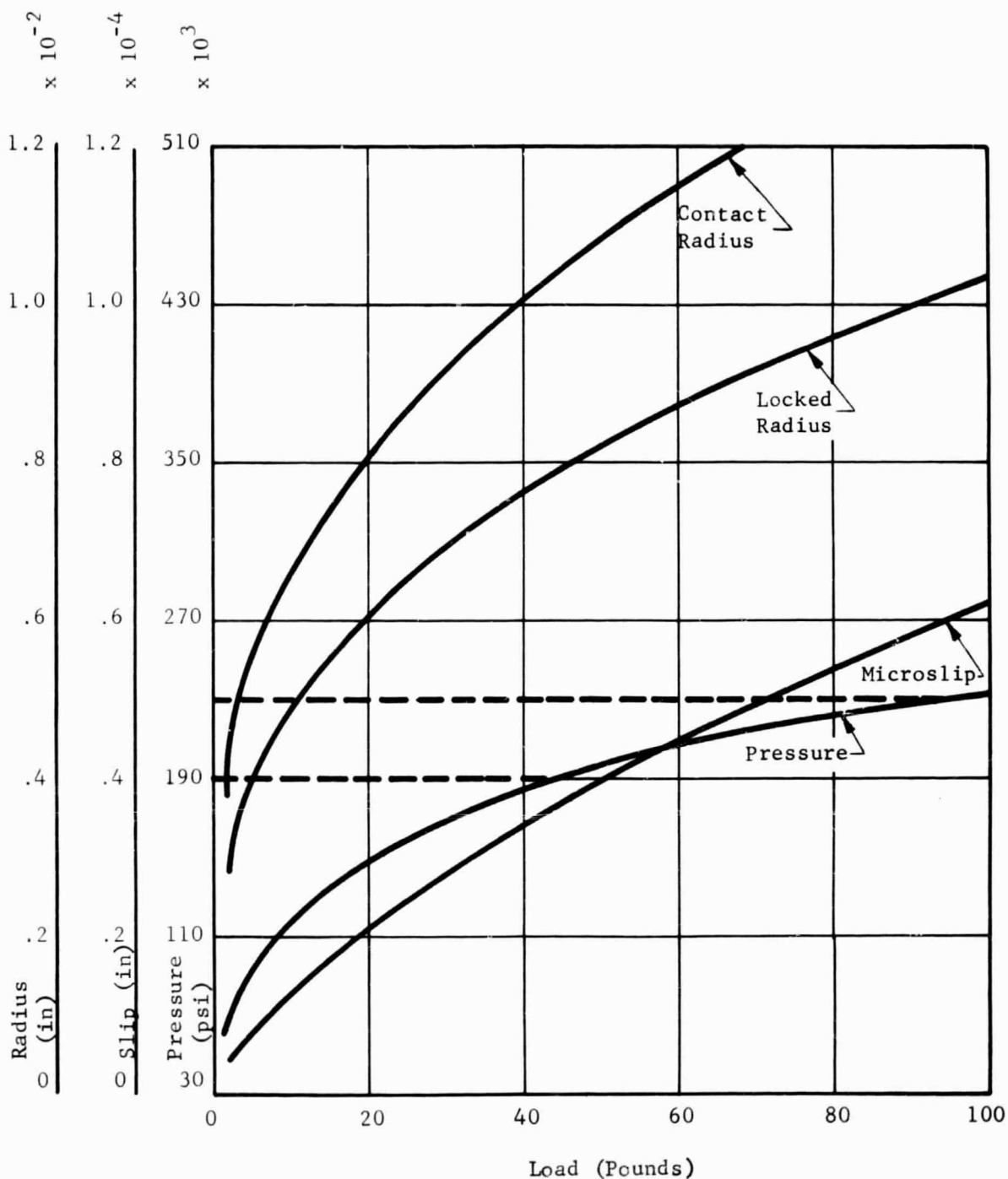


Fig. 121 Pivot Design Curves K162B Carbide vs Itself
Radius of Pivot: .375"; Radius of Socket: .5623"

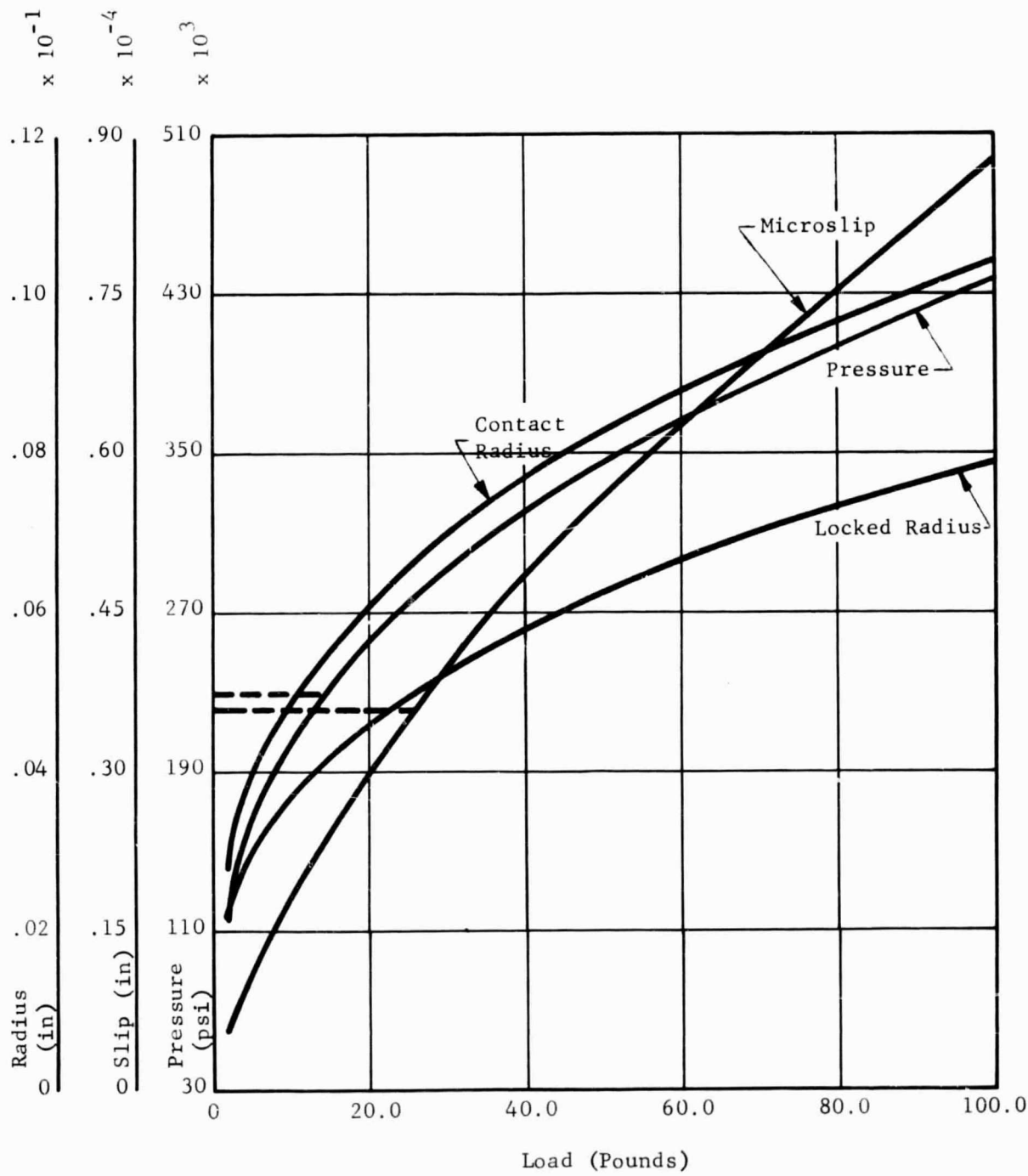


Fig. 122 Pivot Design Curves Steel vs Itself Pivot
Radius: .250"; Socket Radius: (Flat)

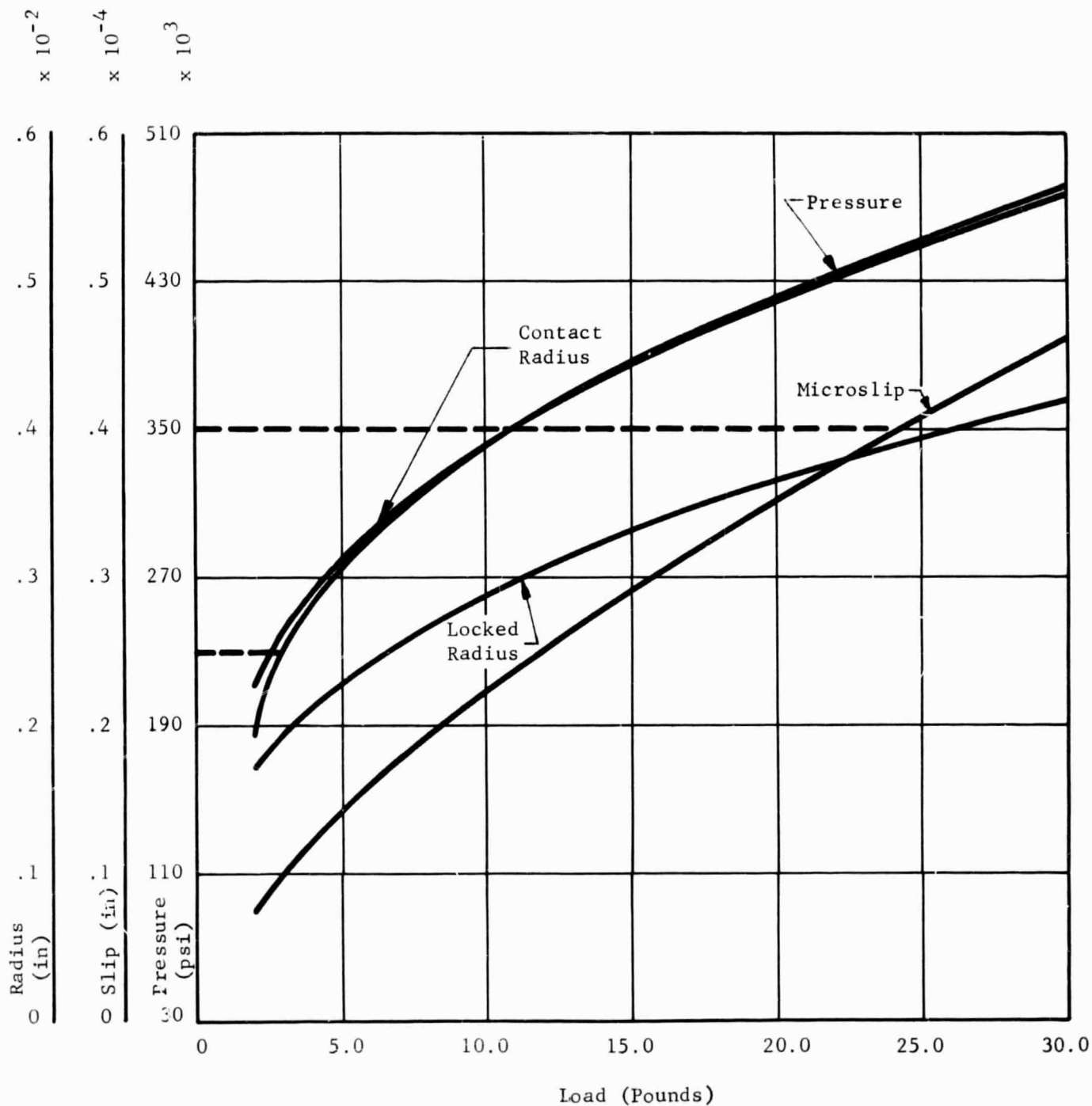


Fig. 123 Pivot Design Curves - Kl62B Carbides vs Itself
 Radius Pivot: .250"; Radius of Socket: (Flat)

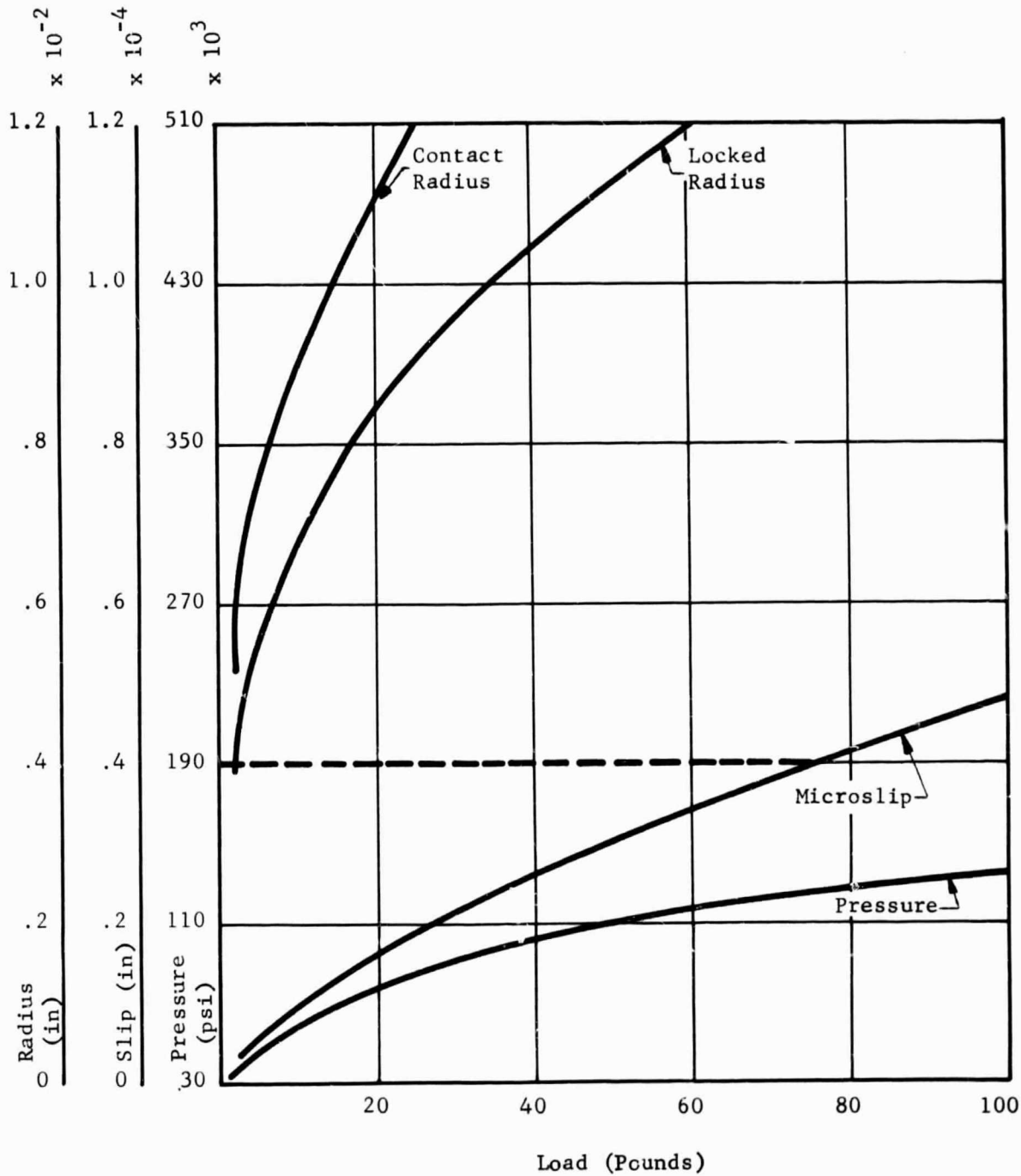


Fig. 124 Pivot Design Curves Steel vs Itself Pivot
Radius: .250"; Socket Radius: .300"

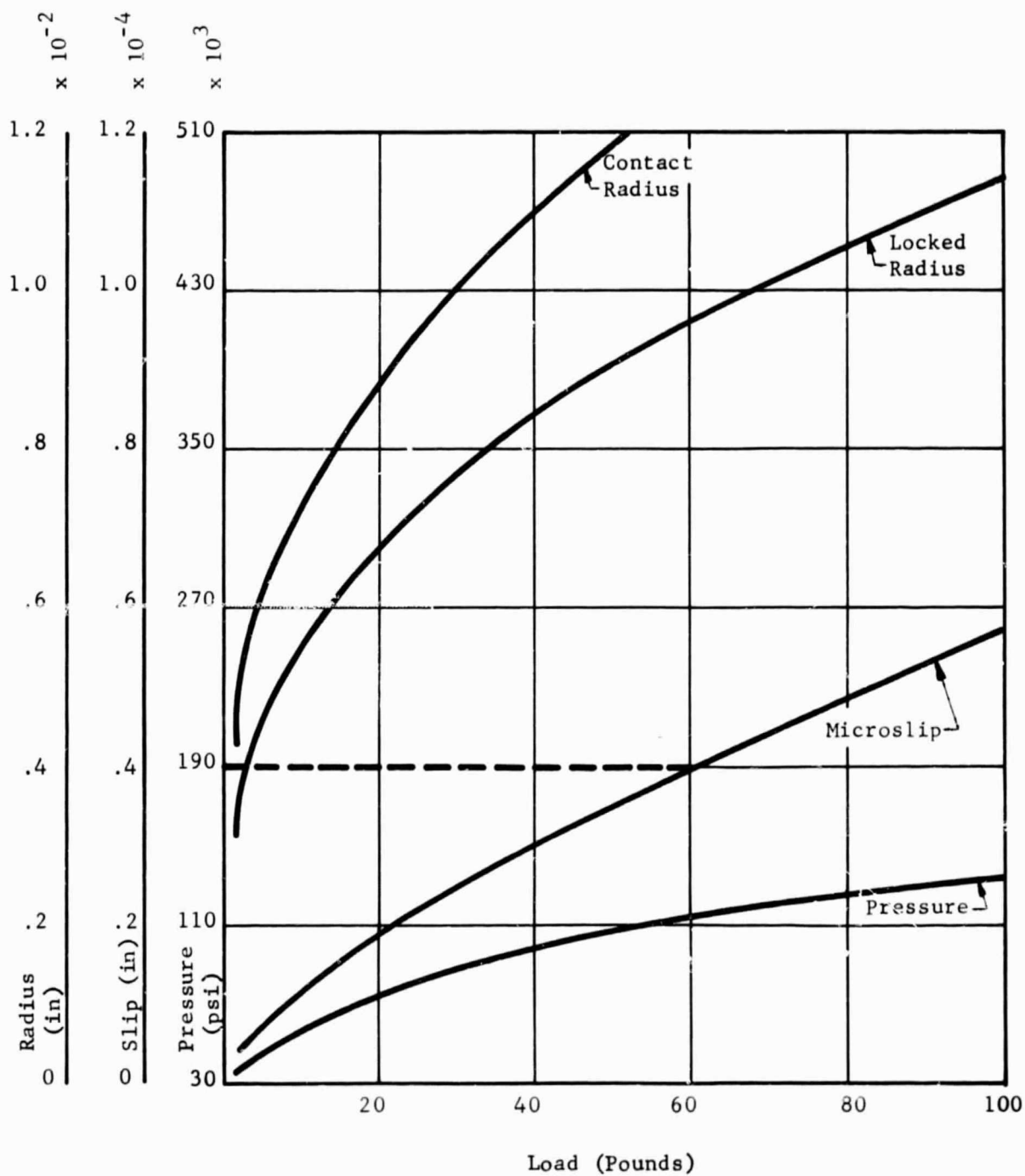


Fig. 125 Pivot Design Curves K162B Carbide vs Itself
Pivot Radius: .250"; Socket Radius: .300"